Università degli Studi di Ferrara

DOCTORAL COURSE IN

PHYSICS

CYCLE XXXIV

COORDINATOR

Prof. Luppi Eleonora

Test of Lepton Flavour Universality using the $B_s^0 \to D_s^- \tau^+ \nu_\tau$ with 3 prongs τ^+ decays and validation of the new opto-electronics for the RICH Upgrade at the LHCb experiment

Scientific-Disciplinary Sector (SDS): FIS/01

Ph.D. Candidate:
Dr. Giugliano Carmen

Supervisor:
Dr. Vecchi Stefania

Co-Supervisor:
Prof. Fiorini Massimiliano

Years 2018/2022

Contents

Introduction

The Standard Model (SM) of particle physics is the most consolidated and successful theory for the description of fundamental particles and their interactions. It has been thoroughly validated since all particles it predicts have been directly observed, and the features of the fundamental interactions it encompasses have been described with accuracy. Despite its extraordinary success, the SM is not believed to give a complete picture of nature because there are many unsolved issues: the presence of neutrino masses, the presence of several free parameters, the hierarchy problem, the lack of a quantum description of gravity, and of an explanation for the many astronomical and cosmological evidences of dark matter and dark energy in the Universe. To overcome this impasse two main lines of experimental research are currently pursued. The former considers direct searches to produce new particles or measure new interactions among ordinary particles following the prediction of New Physics scenario beyond the SM. The latter, exploits precision measurements of known phenomena to highlight possible deviations from the SM predictions. This approach, has contributed to the current formulation of the SM and is pursued in this thesis. In particular, one of the subjects of this thesis is the test one of the assumptions of the SM referred to as Lepton Flavour Universality (LFU). The LFU states that the electroweak couplings are independent from the lepton flavour and differences originate from the different lepton masses. Deviations from LFU would be a clear sign of New Physics. Tests on LFU can be performed by studying the semileptonic decays of $b-$hadrons by comparing branching fractions to final states with different lepton species by defining the observable

$$R(H_c) = \frac{\mathcal{B}(H_b \to H_c \tau \nu_\tau)}{\mathcal{B}(H_b \to H_c \mu \nu_\mu)},$$

with H_b and H_c a $b-$ and $c-$hadron, respectively.

Experimental results on LFU tests have been obtained by Belle, Babar and LHCb and show tension with the SM of about $3.4\,\sigma$ when considering the combination of the measurement of $R(D)$ and $R(D^*)$.

To contribute clarifying the experimental picture of LFU test this thesis documents the preliminary studies for the $R(D_s)$ measurement reconstructing the $B_s^0 \to D_s^- \tau^+ \nu_\tau$ *signal* decay through the $\tau^+ \to \pi^+\pi^-\pi^+(\pi^0)\bar{\nu}_\tau$ and the $D_s^- \to K^+K^-\pi^-$ decays. In order to achieve the best experimental precision, the ratio is computed by considering a normalisation channel, *norm*,

which presents the same visible final state of the signal and calculating the following ratio

$$R(D_s) = \frac{\mathcal{B}(B_s^0 \to D_s^- \tau^+ \nu_\tau)}{\mathcal{B}(norm)} \times \frac{\mathcal{B}(norm)}{\mathcal{B}(B_s^0 \to D_s^- \mu^+ \nu_\mu)} = \mathcal{K} \times \alpha.$$

The value α can be computed by using external inputs, *i.e.* by measurements performed by independent analyses, while $\mathcal{K}$ is the measured observable and is defined as:

$$\mathcal{K} = \frac{N_{sig}}{N_{norm}} \times \frac{\epsilon_{norm}}{\epsilon_{sig}} \frac{1}{\mathcal{B}(\tau^+ \to \pi^+\pi^-\pi^+(\pi^0)\nu_\tau) \times \mathcal{B}(D_s^- \to K^+K^-\pi^-)},$$

where N_{sig} (N_{norm}) and $\epsilon_{sig}(\epsilon_{norm})$ represent, the signal (normalisation) yield and selection efficiency, respectively.

The LHCb experiment has successfully operated during Run1 and Run2 publishing many interesting measurements on several subjects and contributing to more precise tests of the SM. To achieve even higher precision results, especially in some specific $b-$hadron decays, the LHCb detector is undergoing a major upgrade to better exploit the luminosity delivered by the LHC. The goal is to operate at the luminosity of $2\times10^{33}\text{cm}^{-2}\text{s}^{-1}$, 5 times larger than the past run conditions. This requires an upgrade of most of the LHCb detectors and of the readout to cope with the 40 MHz readout rate and the higher level of radiation hardness foreseen during the incoming Run3 in 2022. This thesis provide also a detailed description of the upgrade and commissioning of the Ring Imanging Cherenkov (RICH) subdetectors. For the RICH upgrade, the former Hybrid Photon Detectors (HPDs) are being replaced by Multi Anode Photon Multipliers (MaPMTs), the optics of the RICH nearest to the beam collision is being modified, and the electronics is being replaced. The new front-end electronics are based on the CLARO chip, FPGAs digital board, and Giga Bit Transceiver (GBT) chip for data transmission and front-end configuration.

Chapter 1

The LHCb experiment at LHC

The Large Hadron Collider beauty (LHCb) experiment at the European Centre for Nuclear Research (CERN) is one of the main experiments studying the flavour physics with high precision. LHCb was built to study CP violation and rare decays of hadrons containing b quarks by exploiting the high cross section of b quarks production available in the proton-proton collisions at the Large Hadron Collider (LHC). These studies not only help to deeply test the Standard Model (SM) of particle physics and increase the precision of the SM parameters, but have also the aim to perform indirect searches for New Physics (NP) effects. The detector features in terms of vertex and momenta resolution, trigger, and high charm cross section allowed the experiment to be a considered also a charm factory and to perform leading measurements within the charm physics.

1.1 Large Hadron Collider

The LHC [1] at CERN is a superconducting circular particle accelerator devoted to accelerating and colliding protons and heavy ions. It is located in the former Large Electron-Positron (LEP) collider cave and consists of a 27 km tunnel in which there are two rings of superconducting magnets with accelerating structures to boost the energy of the particles along the way. The tunnel is located between 45 m and 170 m below the ground surface, between Geneva airport and the Jura mountains, spanning the Swiss-French border. The LHC is the highest energy collider ever built and it is mainly designed to provide proton-proton collisions with a center-of-mass energy of 14 TeV, with an unprecedent instantaneous luminosity of 10^{34} cm^{-2}s^{-1}. As said before, in addition to the proton-proton collisions, the LHC is also designed to provide lead ion collisions at a center-of-mass energy of 2.76 TeV per nucleon and a peak luminosity of 10^{27} cm^{-2}s^{-1}.

1.1.1 The accelerator complex

Thanks to the chain of accelerator machines it is possible inject to LHC protons with an energy of 450 GeV and further accelerate them to an energy of 7 TeV.

The proton source is a simple bottle of hydrogen gas, then an electric field allows to get protons, stripping the hydrogen atoms of their electrons. Figure 1.1 shows the path followed by the protons: they are first injected into a linear accelerator (LINAC2), which accelerates the protons to the energy of 50 MeV, then they are accelerated by the Proton Synchrotron Booster (PSB) and by the Proton Synchrotron (PS), up to the energy of 1.4 and 25 GeV respectively. The Super Proton Synchrotron (SPS) is then used to reach 450 GeV, and inject the protons into the LHC as bunches of 1.15×10^{11} protons. LHC provides to accelerate bunches thanks to radio frequency (RF) cavities which accelerate the beam by 485 KeV at each turn. The time distance between two consecutive bunches is a multiple of 25 ns, corresponding to a collision rate of 40 MHz. Since there are some dead times and delays due to the beam dump and to the filling pattern the collision frequency is approximately 30 MHz.

The LHC is also made up of superconducting magnets: dipoles and quadrupoles, which allow to keep the beams in the circular ring and to focus the beams, respectively. Further corrections are enabled by the usage of sextupoles, octupoles, and decapoles. The nominal strength of the magnetic field is 8.33 T and is generated by an electric current of 11.700 A for each dipole. The entire magnetic system is based on the niobium-titanium (NbTi) Rutherford cables technology and works at a temperature of 2 K, obtained using the superfluid helium. Since the space in the tunnel is limited, a twin-bore design is used (Fig. 1.2), in such a way that it is possible to use only one cryogenic structure with proton rings in the same cryostat, but this ultimately requires the presence of oppositely oriented magnetic fields to allow the coexistence of two proton beams along the same circumference. The two beams are kept on parallel orbits and are brought together in a single beam pipe only near the interaction points (IP).

The LHC complex system also requires vacuum systems: one for the insulation of the cryo-magnets, another one for the helium distribution, and a beam vacuum. The requirements for the beam vacuum are very stringent to guarantee the beam lifetime and to minimise the background at the experiments. The typical vacuum at cryogenic temperatures in the IP requires a pressure around in the range 10^{-10} to 10^{-11} mbar.

The beams with protons rotate for many hours in the LHC beam pipes and are focused in four interaction points (the yellow dots in fig. 1.1), in correspondence of the particle detectors in order to analyse the products of the collisions. The accelerator complex includes also other facilities like Antiproton Decelerator and the Online Isotope Mass Separator (ISOLDE), and feeds different physics project like the CERN Neutrinos to Gran Sasso (CNGS) and the Compact Linear Collider test area.

1.1.2 Luminosity

One important parameter in particle experiments at colliders is the *instantaneous luminosity* $\mathcal{L}$ which relates the cross section of a given process, σ_{event}, with the number of expected events N per unit of time in the collisions.

$$\frac{dN_{event}}{dt} = \mathcal{L} \cdot \sigma_{event} \,. \tag{1.1}$$

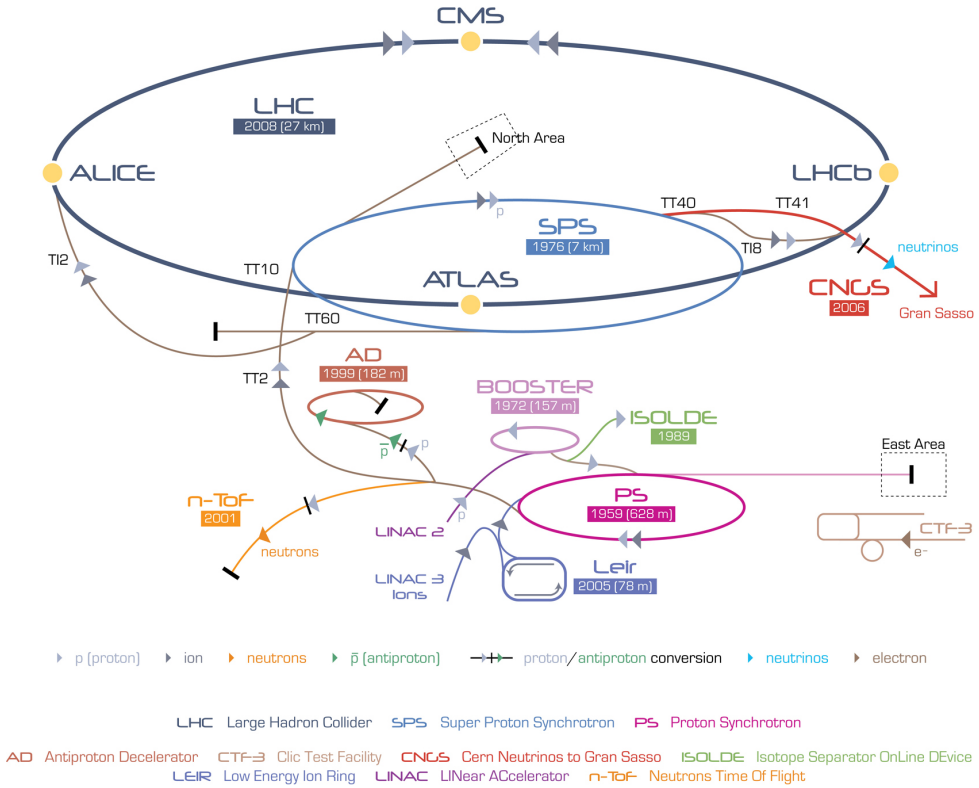

Figure 1.1: The CERN accelerator complex.

For LHC, within some approximations, the instantaneous luminosity can be written as function of the accelerator parameters as

$$\mathcal{L} = \frac{N_p^2 n_b f_{rev}}{A_{\perp}^{eff}} \tag{1.2}$$

with N_p the number of protons per bunch, n_b the number of bunches per beam, f_{rev} the revolution frequency, while $A_{\perp}^{eff}$ is the effective transverse colliding area, which can be estimated from the overlap of the beam spatial distributions. Since the number of protons is not constant with the time due to the beam collisions and the scattering within the beam pipe, the luminosity decrease with a lifetime of $\mathcal{O}(10\,\text{h})$. To minimise the effects of luminosity decay, allowing the same operation condition of the trigger during a fill and to reduce the systematic uncertainties due to changes in the detector occupancy, LHCb implemented a luminosity levelling procedure. This procedure consists of adjusting the transverse overlap of the beams at LHCb, thus constantly redefining the effective colliding area [2], the effect can be seen in fig. 1.3.

This choice allowed LHCb to limit the number of collisions per bunch crossing and the pile up, simplifying the reconstruction of secondary vertices due to the decay of long-lived heavy hadrons. The reduced instantaneous luminosity helps limiting the radiation damage of the detectors, and in particular the innermost detector that surrounds the collision region.

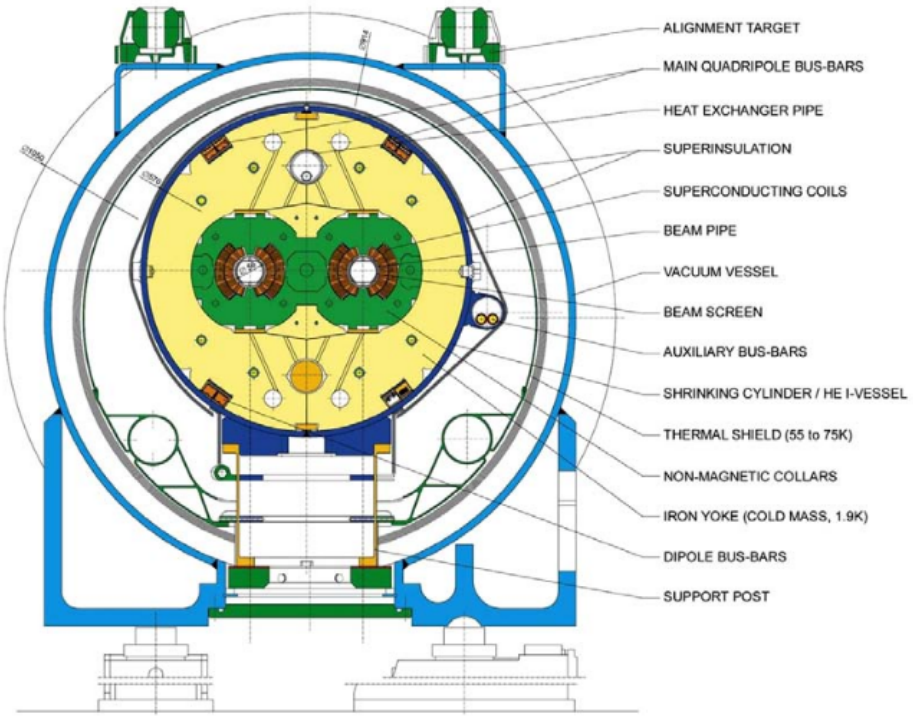

Figure 1.2: Section of the LHC superconducting dipole magnet.

1.1.3 LHC Run1 and Run2

The first injections of beams started in September 2008, but an accident occurred which forced to stop the LHC for more than one year for repairs. The operations restarted in November 2009 with collisions at a centre-of-mass energy of 900 GeV, then raised up to 7 TeV in 2010 and 2011 and 8 TeV in 2012 and January 2013. The 2010-2013 data taking period is referred to as Run1. After the end of Run1, the LHC stopped for detector upgrade and maintenance operations, and restarted in 2015, with collisions at a centre-of-mass energy of 13 TeV. The phase that started in 2015 until 2018 is referred to as Run2. The integrated luminosity recorded by the LHCb experiment in each data-taking year is displayed, together with the beam energy, in Fig. 1.4. In each year, the recorded luminosity corresponds to a fraction between 87% and 94% of the total integrated luminosity delivered by the LHC.

1.1.4 LHC experiments

As mentioned, the beams interact at four different points along the ring, where the largest experiments are located in order to study the the products of the high-energy collisions. As illustrated in the fig. 1.1 in a clockwise order there are

- ATLAS: *A Toroidal LHC ApparatuS* a general-purpose detector whose targets are precision measurements of SM, the search and the study of the Higgs boson, and mechanisms due to new physics. Its length is 44 m, has a 25 m diameter and it is the biggest experiment

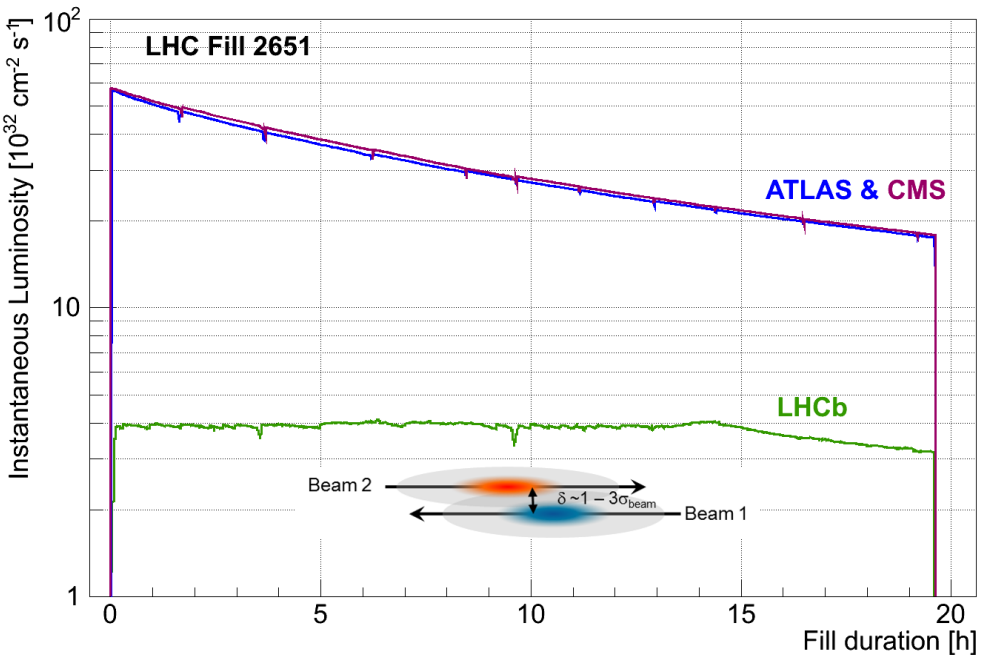

Figure 1.3: Development of the instantaneous luminosity for ATLAS, CMS and LHCb during LHC fill 2651. After ramping to the desired value of $4\times10^{32}\mathrm{cm}^{-2}\mathrm{s}^{-1}$ for LHCb, the luminosity is kept stable in a range of 5% for about 15 hours by adjusting the transversal beam overlap. The difference in luminosity towards the end of the fill between ATLAS, CMS and LHCb is due to the difference in the final focusing at the collision points.

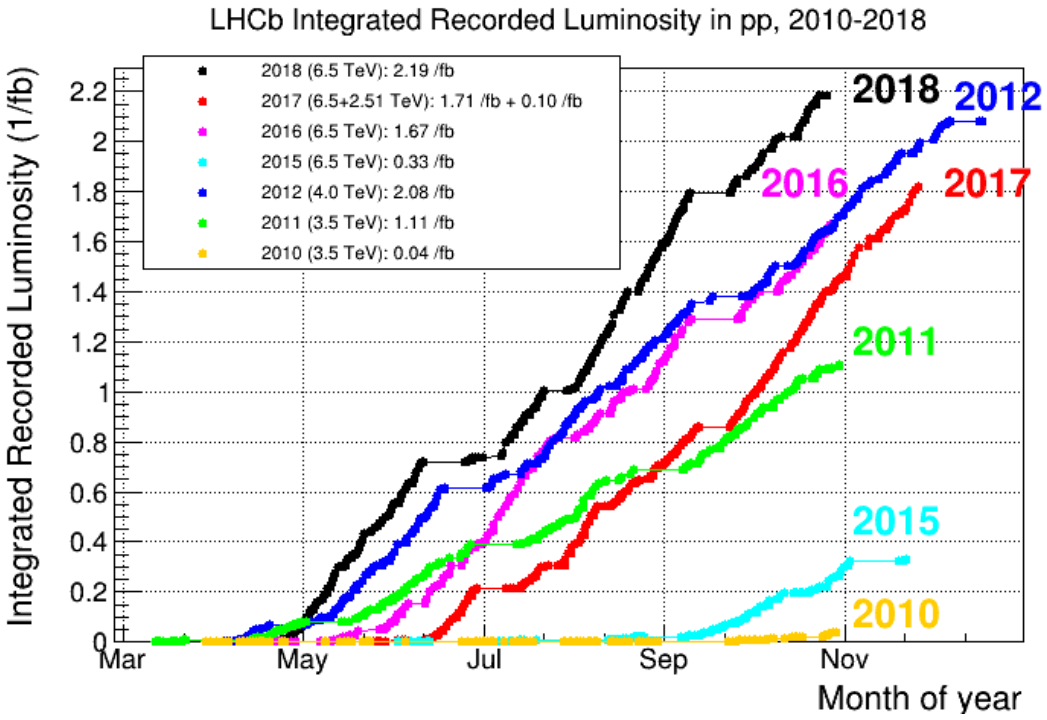

Figure 1.4: Integrated luminosity of *pp* collisions recorded by the LHCb experiment in each data-taking year. The beam energy, corresponding to half of the centre-of-mass energy $\sqrt{s}$, is shown in parenthesis.

at LHC with a weight of 7000 tons.

- ALICE: *A Large Ion Collider Experiment* an ion-ion collision experiment whose purpose is to explore the initial state of matter. To form the quark-gluon plasma are required high energy densities, which are achieved by colliding lead ions with $\sqrt{s} = 2.67$ TeV at a peak luminosity of $\mathcal{L} = 10^{27}$ cm^{-2}s^{-1}.

- CMS: *Compact Muon Solenoid* is a general-purpose detector as ATLAS. It takes its name from the huge superconducting solenoid which generates an internal magnetic field of 3.8 Tesla, about 10^5 times the magnetic field of the Earth. CMS has a compact design because of its relatively small size considering its weight: about 14.000 tonnes for 15.00 meters of diameter and 28.7 meters of length.

- LHCb: *LHC-beauty* is described in the following section 1.2.

1.2 LHCb experiment

The LHCb experiment was built to perform precision measurements of the decays of hadrons containing b and c quarks. The experimental program of the LHCb also foresees measurements of the electroweak sector of the SM, of interaction cross-sections of protons with gases and heavy-ion collisions. At the LHC, the $b\bar{b}$ pairs are produced, at leading order, by *gluon-guon fusion* and *quark-quark fusion*.

The $b\bar{b}$ production cross-section of $b\bar{b}$ pairs at high energies is large for small polar angles with respect to the direction of the beam axis, as shown in Fig. 1.5. For this reason the LHCb experimental apparatus was designed as a single-arm forward spectrometer, in contrast with the ATLAS and CMS detectors, also referred to as General Detector Purpose (GDP), which cover the central region.

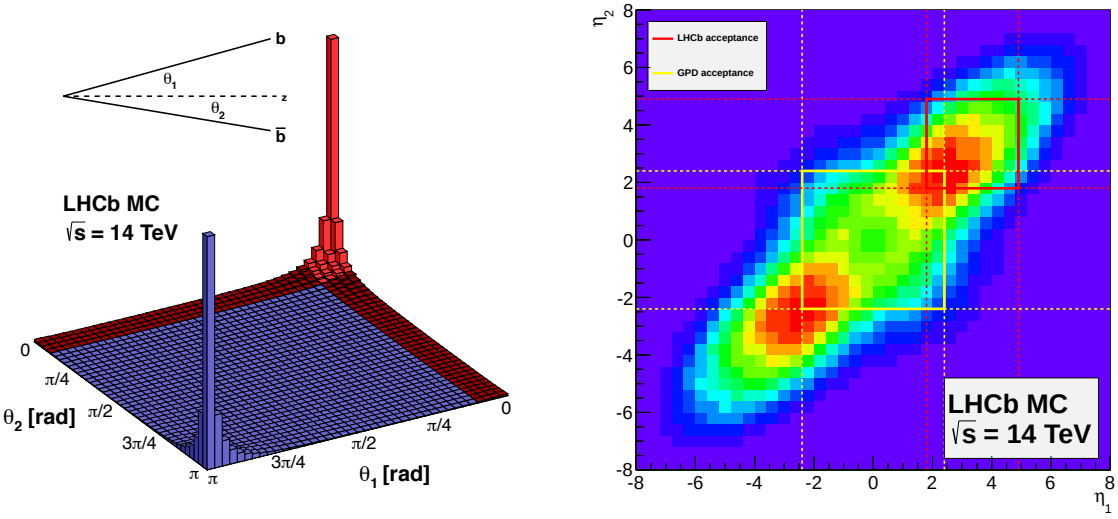

Figure 1.5: (Left) Production cross-section of $b\bar{b}$ pairs as a function of their polar angle with respect to the beam axis, for pp collisions simulated with `PYTHIA8` [118] at a centre-of-mass energy of 14 TeV. The LHCb acceptance is in red [3]. (Right) Two-dimensional pseudorapidity plot of $b\bar{b}$ production phase space in simulated pp collisions at $\sqrt{s} = 14$ TeV with the LHCb acceptance is highlighted in the red square while the General Purpose Detector (GDP) acceptance is in yellow.

The coordinate system of LHCb is right-handed: the $z-$axis is defined along the anticlockwise-beam direction, the $x-$axis points to the centre of the LHC ring, and the $y-axis$ points upwards, perpendicular to the LHC plane. The LHCb detector covers the angular region between 10 mrad and 300 (250) mrad in the $x-z$ ($y-z$) plane with respect to the beam axis. Introducing the pseudorapidity, $\eta \equiv -\ln[\tan 2\theta]$, being θ the angle between a particle momentum and the beam axis, the angular coverage corresponds to the region $2 < \eta < 5$. This design, enables the detector to collect about 27% of the b quarks and 24% of the $b\bar{b}$ pairs produced in the pp collisions, the corresponding geometrical efficiency of general-purpose detectors like CMS and ATLAS are around 49% and 41% for b quarks and $b\bar{b}$ pairs, respectively. However, the number of collected decays at equal instrumented solid angle is much larger, with significant cost benefits. The small solid angle covered also allows for a sequential arrangement of the detectors along the beam direction.

1.2.1 The LHCb subdetectors layout

Figure 1.6 shows a schematic representation of the experimental apparatus from the side. Most detector subsystems are assembled in two halves, which can be moved out horizontally for assembly and maintenance purposes, as well as to provide access to the beam-pipe. They are referred to as the detector A- and C-sides. From the interaction point, which defines the origin

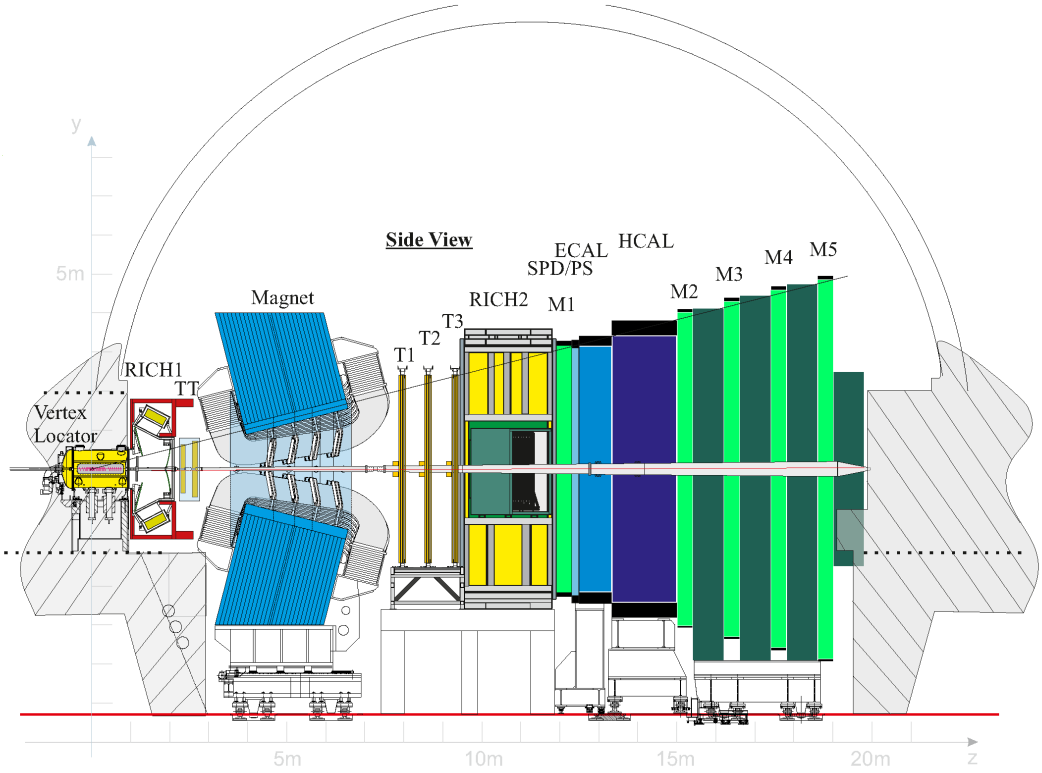

Figure 1.6: Side view of the LHCb detector in the non-bending $y-z$ plane with its subdetectors along the beam $z-$axis.

of the LHCb coordinate system, along z axis, the following sub detectors are placed:

- the vertex locator (VELO), it is a vertex detector based on silicon-strip technology, it surrounds the pp interaction region and it is aimed at the precise measurement of the primary and secondary vertices due to pp interactions and the heavy flavor hadrons decays, respectively;
- a ring-imaging Cherenkov detector (RICH1) providing particle identification information (PID) for charged particles with momentum in the range 2–60 GeV/c;
- the Tracker Turicensis (TT), is a large-area silicon-strip tracking detector placed upstream of the magnet, that is also used to reconstruct the tracks produced by long-lived particles decaying outside the VELO acceptance;

- a warm dipole magnet installed in a rectangular yoke with a window inside. It provides a vertical field with bending power 4 Tm, needed to measure the momentum of charged particles. The field direction is regularly reversed during the data taking in order to provide useful samples to perform cross-checks and reduce systematic uncertainties;
- three tracking stations (T1, T2, T3) placed downstream the magnet, are made of two technologies: silicon strips in the region closest to the beam pipe and straw drift tubes in the outer one;
- a second ring-imaging Cherenkov detector (RICH2) providing PID information for charged particles with momenta in the range 15-100 GeV/c;
- a scintillating pad detector (SPD) separated by a thin plate of lead from the pre-shower detectors (PS). This subdetectors are used to distinguish electrons from photons and hadrons, respectively;
- an electromagnetic calorimeter (ECAL) to identify electrons and photons and to measure their energy;
- an hadronic calorimeter (HCAL) that stops the hadrons and provides a rough estimate of their energy;
- five muon stations (M1–M5), composed of alternating layers of iron and multiwire proportional chambers, are used to identify muons. The first one is placed before the Calorimeters and the last four downstream.

Both the Calorimeters and the Muon detector provide information that are used at the low-level trigger L0 to filter useful events.

1.2.2 Tracking system

The LHCb tracking system is composed of the VELO, the TT and the three tracking stations (T1-T3). The purpose of the system is to provide the trajectory of charged particles traversing the detector material. Everything is complemented with a warm dipole magnet which bends the charged particles trajectory, allowing the measurement of their momentum.

Vertex locator

The VELO is installed inside the LHC vacuum vessel to minimise the materials in front of the first measurement and achieve the best vertex resolution. Its main purpose is to measure precisely the trajectories of the charged particles, the position of the primary vertices (PVs) of the pp collisions, and the displaced secondary vertices, especially those originated by $b-$ and $c-$hadron decays that are displaced by of order of magnitude of 1 cm.An excellent vertex resolution is crucial for time-dependent CP violation measurements of B_s^0 mesons, dominated by the fast $B_s^0 - \bar{B}_s^0$ mesons oscillations, and in general to suppress the large background due to particles produced at the PV.

The VELO covers a length of 1 m and is made up of 46 semicircular silicon modules arranged perpendicularly with respect to the beam direction, as shown in Fig. 1.7. Except for the first

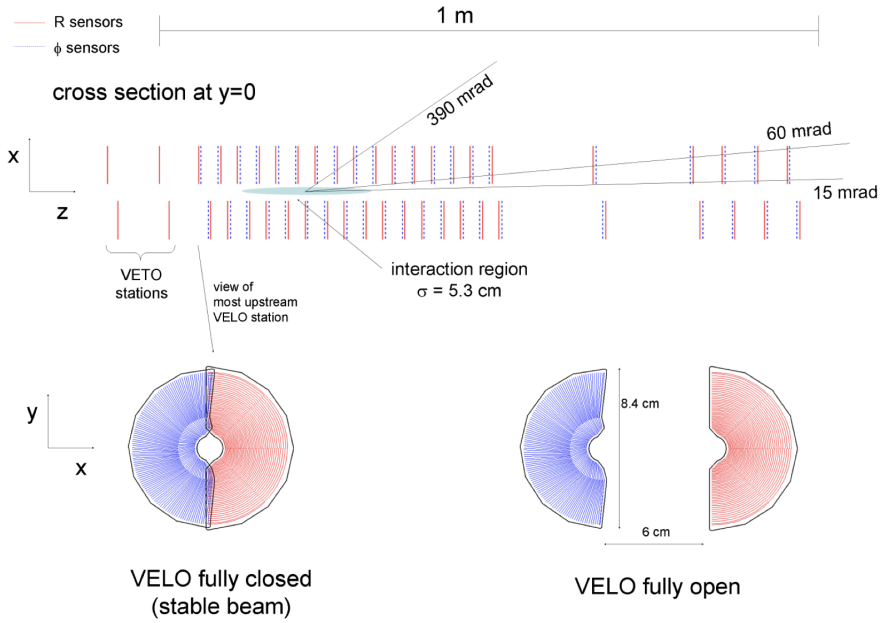

Figure 1.7: Schematics of VELO system. In the bottom part of the figure are represented the closed and open positions.

four module, consisting of one type of sensors, all the others are made up of two overlapping radiation-resistant sensors, with a thickness of 300 μm, whose sensitive area starts at 8.2 mm and ends at 41.9 mm from the beam, respectively. Each pair of sensors is specialised to measure the radial distance from the beam with semicircular-shaped strips, R sensor, or to measure the azimuthal angle with strips oriented approximately in the radial direction, ϕ sensor. The modules are mounted in a configuration which allows to remove ambiguities in the reconstruction of the tracks and to decrease the number of ghosts which are the reconstructed tracks that do not correspond to the passage of any particles. Since the distance of the sensitive area of the VELO modules from the beam is smaller than that required for safety, the VELO sensors are mounted on a remote-controllable positioning system that allows to move them when the beams are not stable in order to avoid damages to the sensors. The two configurations, VELO open and VELO closed are shown in fig. 1.7.

The two halves are mounted in an $AlMg_3$ box (RF-box) which has the function of separating the LHC beam-pipe vacuum from the VELO and shielding it from the electromagnetic effects induced by the high-frequency beam structure. Indeed the thickness (300 μm) and the material were chosen to minimise the multiple scattering of the tracks before reaching the VELO, since this degrades significantly the resolution of the impact parameter. The two boxes present a highly corrugated shape to allow the two detector halves to overlap in the VELO closed configuration, as shown in Fig.1.8. All tracks inside the LHCb acceptance pass through at least three modules. The tracks reconstructed in the VELO are used to determine the PV with the best spatial

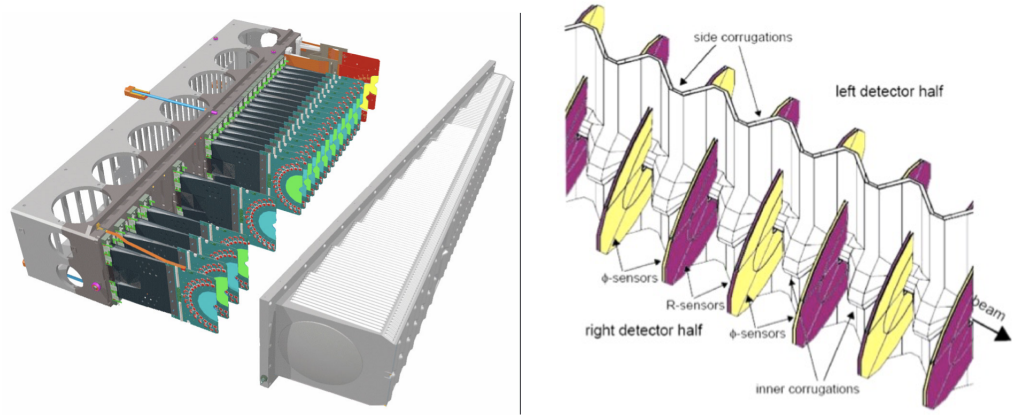

Figure 1.8: (Left) Module support and (Right) inner view of the RF-boxes, with the detector halves in the fully closed position. The edges of the boxes are cut away to show the overlap between the sensors of the two halves. R- and ϕ-sensors are coloured in yellow and purple, respectively. [4]

resolution of about 4 μm at the optimal track angle. The impact parameter, *i.e.* the distance between the track's point of closest approach to the PV and the PV itself, is measured with a resolution of 44 μm in the transverse direction for particles with transverse momentum of 1 GeV, that reduces to 15 μm for larger transverse momentum [5].

Tracker turicensis

The Tracker Turicensis (TT) is located upstream the magnet, it covers the full LHCb angular acceptance and it is composed by four planar layers of silicon micro-strips organised in two pairs, the TTa and TTb stations. The stations are separated by about 30 cm along z. All the layers consist of 500 μm thick, 9.64 cm wide and 9.44 cm long silicon sensors carrying 512 readout strips each one with a pitch of 183 μm. To remove some ambiguities in the reconstruction of the tracks, the first and the last layers are organised in vertical strips measuring the x coordinate whereas the two central layers are rotated by $\pm 5^\circ$ with respect to the vertical (fig. 1.9). Since the tails of the dipole magnetic field extend up to the region where it is installed, it provides a rough measurement of the particles momenta without reconstructing the tracks segments downstream of the magnet. This feature is used to predict the rough expected trajectories of the tracks in the T–stations, thus reducing the number of upstream- and downstream-tracks combinations that have to be fitted during the collision-event reconstruction.

Magnet

The dipole magnet match the detector angular acceptance and it is placed between the TT and the T-stations. It is made up of two inclined saddle-shaped coils as can be seen in fig. 1.10. The magnetic field produced bend the charged particles in the $(x-y)$ plane providing an integrated field of about 4 Tm, measured with an accuracy of $4 \cdot 10^{-4}$, and a non uniformity

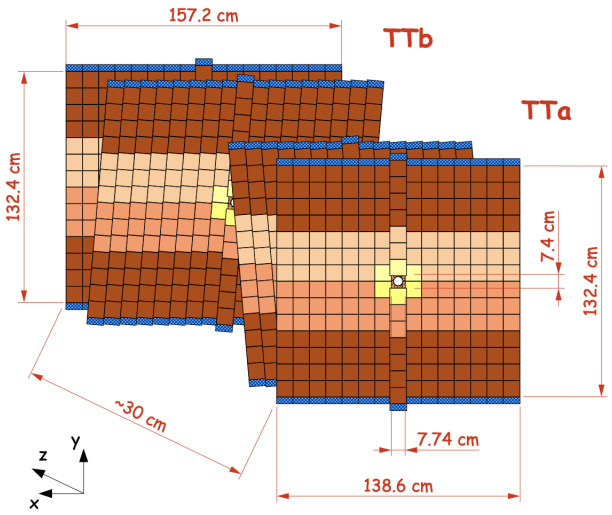

Figure 1.9: Scheme of the TT subdetector. Different readout sectors are indicated by different shadings [6].

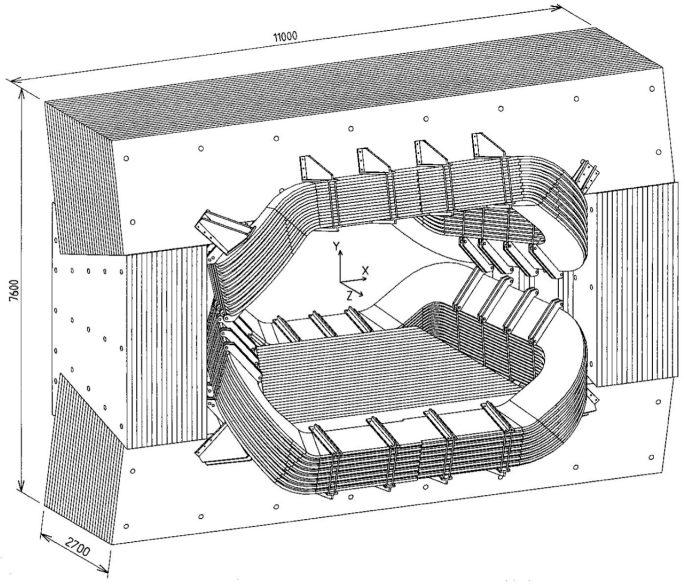

Figure 1.10: Layout of the LHCb magnet

of the order of 1%.

During the data taking the magnet polarity is periodically reversed to keep under control systematic effects due to possible left-right asymmetry. Therefore each year of data taking consist of two dataset labelled as $MagUp$ and $MagDown$.

T–stations

The three tracking stations (T1-T3) are placed downstream the magnet and cover an area of about (6×5) m^2. They are divided in two parts: "Inner Tracker" (fig. 1.11) and "Outer Tracker"

(fig. 1.12) depending on their distance from the beam line. The two parts are implemented with two different technologies: four silicon micro-strip planes for the "Inner Tracker" placed like in the TT, and four planes made up of two rows of staggered straw-tube drift chambers detectors, operating in proportional-counter regime, covering the larger polar angles for the "Outer Tracker". The border between the two parts is determined by the requirement that the detector occupancy is lower than 10% and the single-hit detection efficiency in each layer is larger than 99%. In the Inner Tracker the dimensions of each sensor are 7.6 cm × 11 cm, while

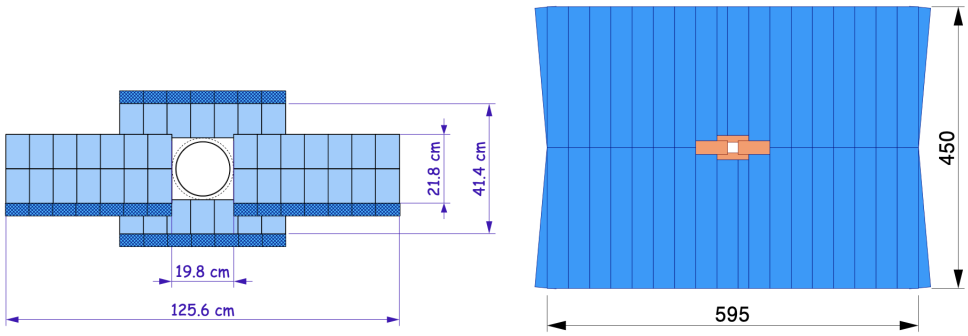

Figure 1.11: Scheme of the IT subdetector: (Left) front view of a layer of the inner tracker, (Right) front view of one of the T–stations. The inner tracker is drawn in orange and the outer tracker in blue [6].

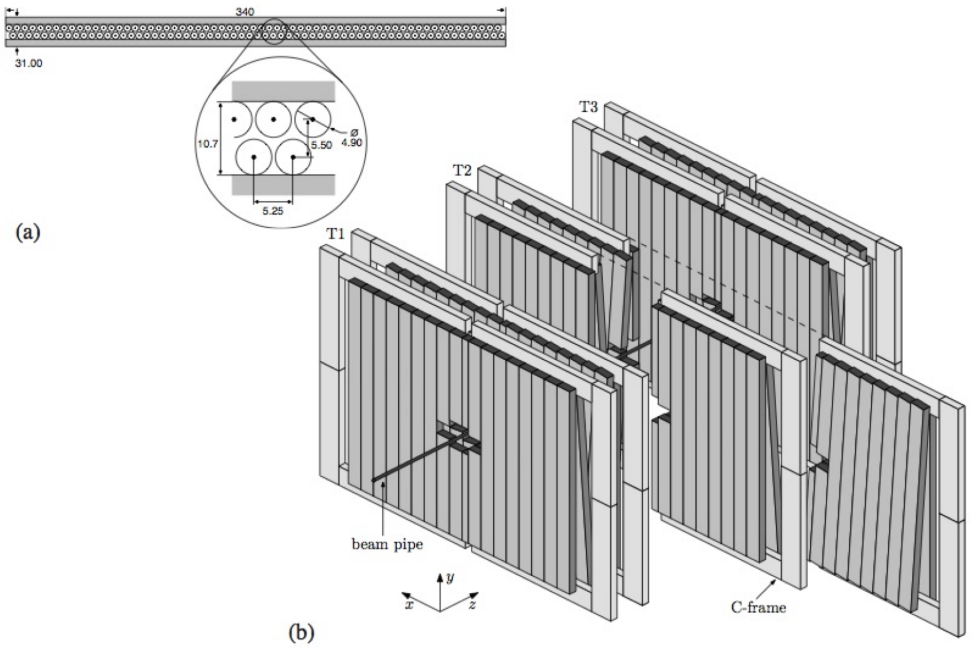

Figure 1.12: Scheme of the OT subdetector. (a) Section of an OT detection plane. (b) Arrangement of OT straw-tubes chambers modules in planes and stations. Each station can be opened for maintenance, as shown for the second station [7].

the straw tubes of the Outer Tracker are 2.4 m long, have 4.9 mm inner diameter and are filled

with a gas mixture of $Ar/CO_2/O_2$ (70%/28.5%/1.5%) to guarantee drift time below 50 ns. The anode wire is made of golden-plated tungsten and is operating at 1500 V with respect to the tube of Kapton-XC coated with Aluminium. The straws wall is 80 μm thick thus to ensure that the total thickness of each T-station is just 3.2% of a radiation length. This kind of technology allows a spatial resolution of about 200 μm in each detection plane.

1.2.3 Tracking performances

Figure 1.13 shows a scheme of the different types of tracks in the LHCb detector. Among the

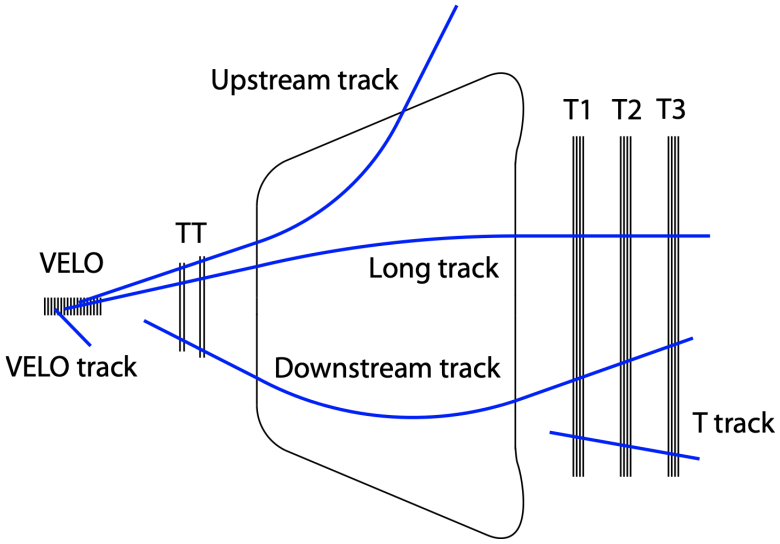

Figure 1.13: Representation of different types of tracks in the LHCb detector.

tracks, those hitting all the tracking detectors (VELO, TT and T-stations) are referred to as long tracks. The long tracks are widely used in physics analyses since they have the best momentum resolution (in the range 0.5-1.0% for momenta within 20 and 100 GeV/c). Long tracks also have good resolution of the impact parameter respect to a PV ($\sigma_{IP} \sim 15 + 29/p_T$ μm, being p_T measured in GeV/c, see fig. 1.14) and the resolution on the PV position depends strongly on the number of tracks used to reconstruct the vertex.

The downstream tracks are reconstructed using only hits in the TT and in the T-stations, since they have no hits in the VELO. They are usually associated to tracks from the decay of long-lived particles such as K_S^0 and Λ .

The upstream tracks are usually low-momentum tracks that are deviated outside the T-stations acceptance and are reconstructed only using VELO and TT hits. From the small curvature acquired due to the residual magnetic field in the TT region it is possible to assign the momentum, though with low resolution of about 15%.

VELO tracks, containing hist only in the VELO, are useful to reconstruct the primary vertices and correspond to particles generated with high angles. T-tracks, containing hits only in the T-stations, are mainly generated by secondary interaction. Whereas a track reconstructed

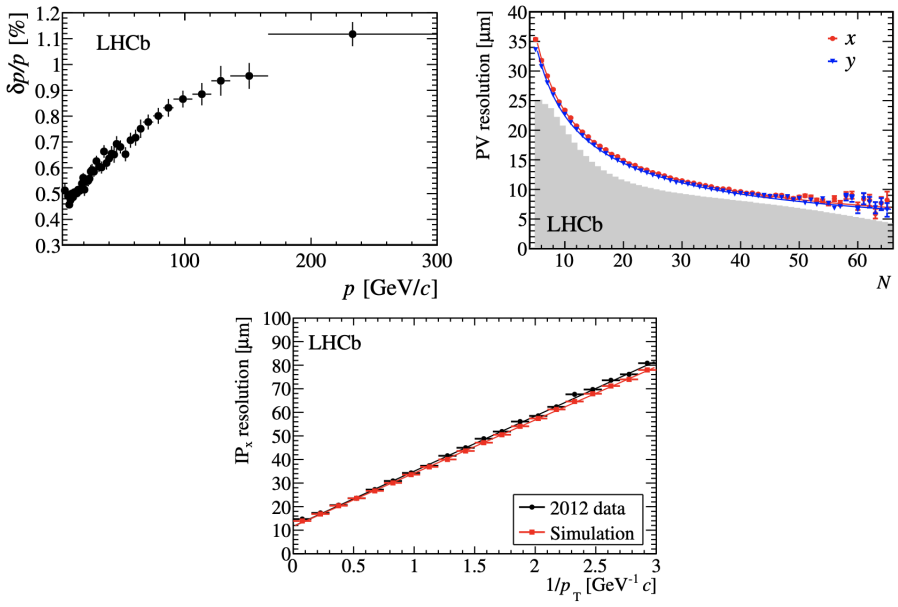

Figure 1.14: (Top left) Relative momentum resolution as a function of momentum, for long tracks reconstructed from the decay of J/ψ particles. (Top right) Primary vertex resolution in the x and y directions, for events with one reconstructed PV, as a function of tracks multiplicity. (Bottom) Resolution of the x projection of the impact parameter with respect to the primary vertex, as a function of $1/p_{\mathrm{T}}$ [2].

by a random combinations of hits it is identified as *ghost*. To quantify the probability that a track is a ghost, a multivariate algorithm has been developed.

During the reconstruction procedure first are reconstructed the long tracks and then using the remaining tracks are reconstructed the downstream and the upstream tracks. The procedure is articulated in three main step:

- Pattern recognition of the VELO hits, to create segments matching the hits lying on a straight line. The VELO track constitute the seed for the long track. In the tracking stations a segment matching hits in T1 and T3 is created and, following the hypothesis of a parabolic trajectory, are calculated the possible hits in T2. If the hits are found are added to segment in the T stations and then combined with the seed segment found in the VELO.

- A Kalman filter [19] is run on each track candidate taking into account scattering and ionization effects [20], and to precisely measure the momentum and the charge corresponding to the particles which left the track.

- Removal of duplicate tracks, by checking the percentage of shared hits among two tracks. The quality of a track is evaluated by measuring the $\chi^2/ndof$ in the kalman filter.

Figure 1.15 shows the tracking efficiency as a function of the momentum in 2011 and 2012.

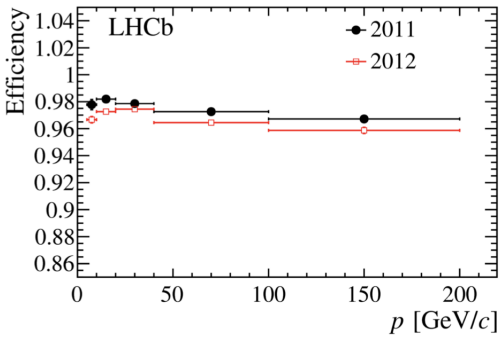

Figure 1.15: Tracking efficiency as a function of the momentum. The tracking efficiency represents the probability for a particle to be reconstructed using hits along its trajectory.

1.2.4 Particle identification

The particle identification (PID) is one of the fundamental requirement for the LHCb experiment since it plays a key role in the identification of signal decays and suppression of background. The PID rely on the use of the RICH detectors, the two calorimeters and the muon detector system.

Cherenkov detectors

The two Ring Imaging CHerenkov detectors, RICH, exploit the Cherenkov effect. A particle propagating through a material (radiator, with refractive index n) with a velocity larger than the light in the medium $v > c/n$, emits photons in a cone of aperture θ around its direction propagation that depends on the particle's velocity in terms of c, β, $\cos\theta = \frac{1}{n\beta}$, see fig. 1.16.

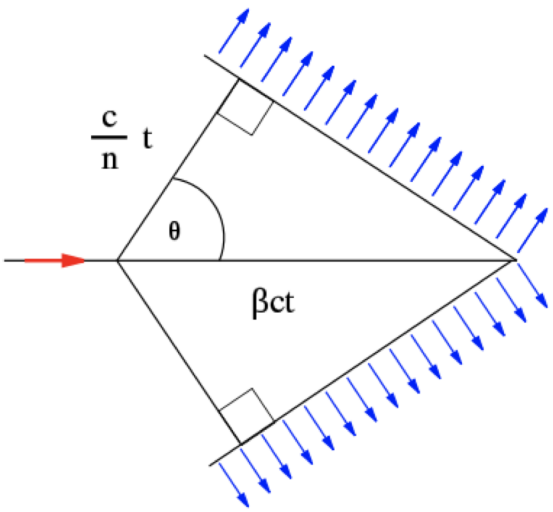

Figure 1.16: Schematic of the Cherenkov radiation emission process.

Through a system of mirrors the Cherenkov photons are focused on a plane instrumented with photon detectors. The light cones are projected in rings whose radius depends on θ.

Combining the measurements of β and of the momenta it is possible to infer the particle's mass, and thus identify it.

To separate hadrons over the wide momentum range (1-150 GeV/c) two RICH detectors with different radiators materials are installed. Figure 1.17 shows side views of both the detectors. The RICH1 detector is placed upstream of the magnet between the VELO and the TT, to cover

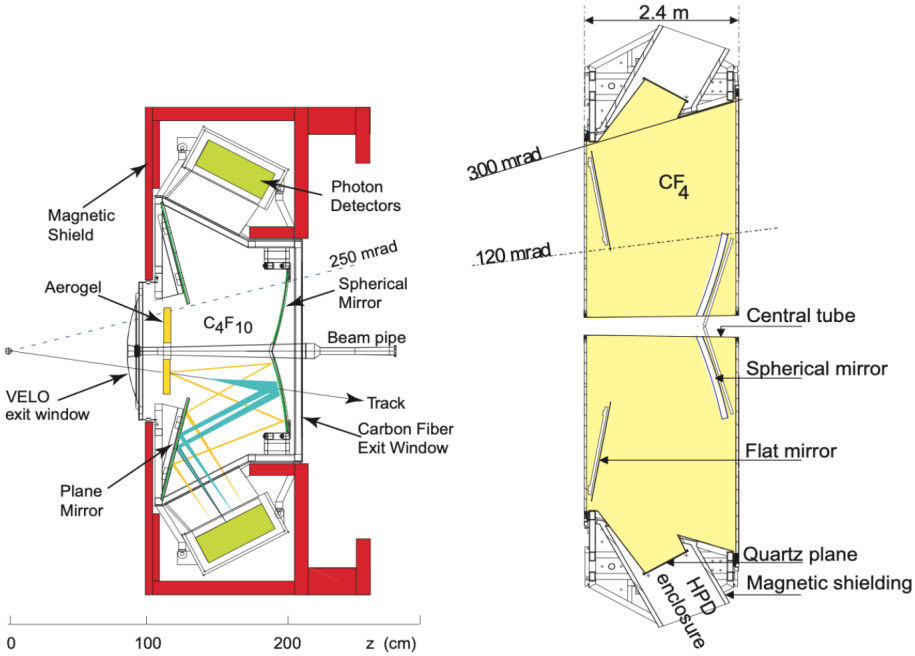

Figure 1.17: Schematic side views of (Left) RICH1 and (Right) RICH2 detectors.

the low momentum range between 2 - 60 GeV/c, and is filled with C_4F_{10}. During Run1, a layer of silica aerogel was also placed in the RICH1 to detect particles with low momentum but was removed before Run2 given its limited performances.

The RICH2 detector is located after the tracking stations, covers the [12,120] mrad range in the horizontal plane and up tp 100 mrad in the vertical plane and the momentum range from 15-100GeV/c, and it is filled with CF_4.

In fig. 1.18 (Left) is shown how the Cherenkov angle saturates at the value of $\theta_c = arccos(1/n)$ by considering different radiators. Whereas fig. 1.18 (Right) shows the Cherenkov angle as a function of particles momentum using information from the C_4F_{10} for the particles detected within the LHCb acceptance.

The photons are detected by an array of hybrid photon detectors (HPDs) with photochathode efficiency optimised for the 200-600 nm wavelength. The HPDs are placed inside iron boxes to shield the effects of the magnetic field on the focal plane of a system of spherical and planar mirrors. In the RICH system the particle identity is determined by matching tracks (produced by VELO and TT) to rings on the photodetector planes and determining the most probable candidate particle for each track/ring. The RICH pattern recognition exploits a maximum likelihood method to fit the association of all measured photon hits, using the Cherenkov angle, with all measured charged particles tracks. A typical event in RICH1 is shown in fig 1.19,

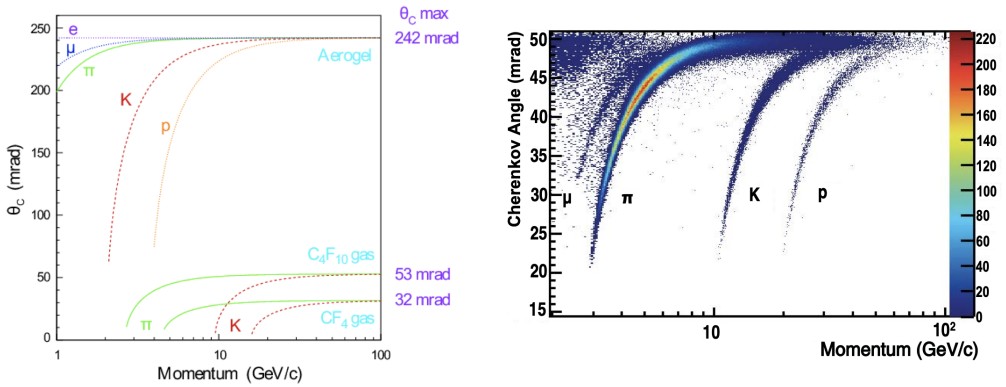

Figure 1.18: (Left) Cherenkov angle as a function of particle momentum for the RICH radiators and for different particle masses and (Right) for isolated tracks, defined as tracks whose Cherenkov ring does not overlap with any other ring, in the C_4F_{10} radiator[4, 8].

the number of photoelectron detected, hits in the rings, depends on the radiator and track momentum. In RICH1 there are both small diameter, densely populated rings from the C_4F_{10} (hits $\leq$ 30 and radius $\simeq$ 5 cm) and large sparsely populated rings from the aerogel (hits $\leq$ 6 and radius $\simeq$ 15 cm).

Calorimetric system

The calorimetric system is located downstream the RICH2 and provides identification and measurement of the energy and position of electrons, photons and hadrons. The entire system consists of four subsystems and is divided in two modules. The first calorimetric module consist of SPD and PS. They are two scintillator pads with an active surface of 7.6 m wide and 6.2 m high, interleaved with a layer of lead whose thickness corresponds to 2.5 radiation lengths, X_0, and ~ 0.06 hadronic interaction lengths λ_I.

Since photons don't deposit energy upstream the lead layer is it possible to distinguish them from the electrons using the SPD.

The calorimetric system is then composed by ECAL and HCAL assembled by alternating tiles of plastic scintillator and absorber. The ECAL cover the full LHCb angular acceptance, is placed 12.5 m downstream the interaction point and is 7.8 m wide and 6.3 m high. The absorber is made of lead, for a total thickness corresponding to $25X_0$ and $1{,}2\lambda_{int}$. The energy resolution achieved is $\sigma(E)/E = 1\% \bigoplus 10\%/\sqrt{E/GeV}$ [9]. The first term is due to a constant contribution, while the second is the statistical uncertainty on the energy deposit.

The HCAL is placed 13.3 m downstream the interaction point and is 8.4 m wide and 6.8 m high. Due to space limitations, this design only covers 5.6 λ_I. The energy resolution achieved is $\sigma(E)/E = 9\% \bigoplus 69\%/\sqrt{E/GeV}$ [9].

All the detectors are read using photomultipliers transmitting the light through wave-shifting fibres. Different segmentations are used for the scintillator tiles in the SPD, PS, and ECAL depending on the distance from the beam pipe. The region with the highest occupancy is the inner one, as can be seen in Fig. 1.20.

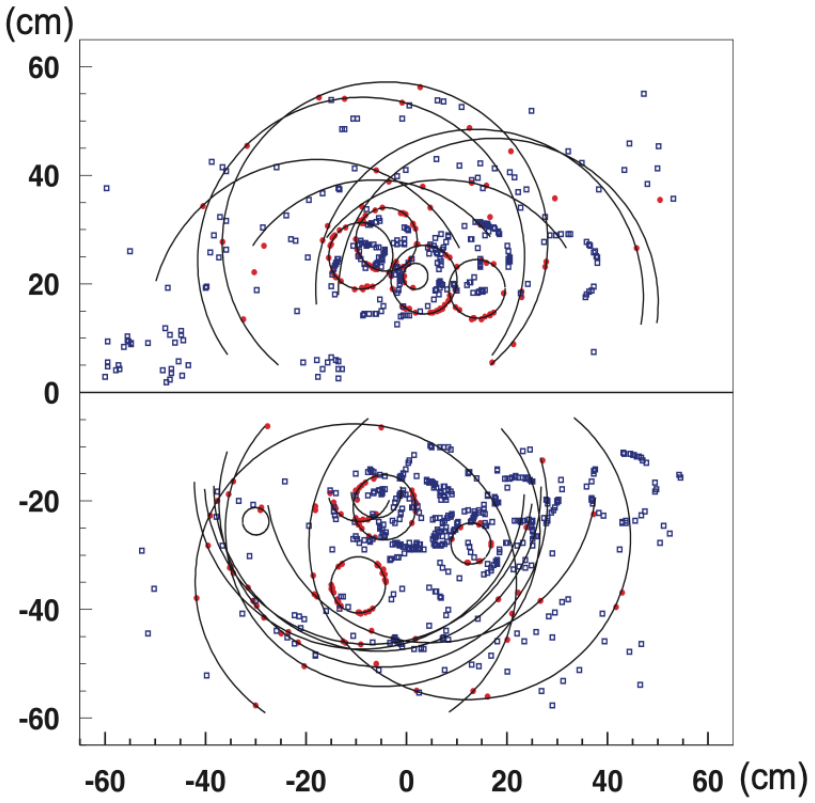

Figure 1.19: Typical LHCb event in RICH1 with Cherenkov rings interpolation. The small (large) ring radii in RICH1 originate from the C4F10 (aerogel) radiator. The solid red rings indicate particles passing through the whole detector and the blue dotted rings indicate the particles for which no match is found in with tracks in the VELO and TT detectors.

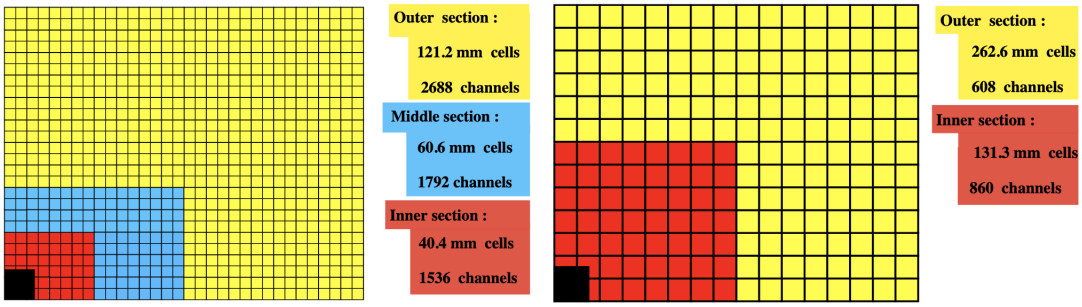

Figure 1.20: Segmentation of one quadrant (left) of the SPD, PS and ECAL and (right) of the HCAL. The black sector, corresponding to the beam pipe, is outside of the LHCb acceptance.[4]

The energy deposits in the various detectors from different types of particles are shown in fig. 1.21. The photons do not leave hits in the SPD station, but interact with the lead converter, creating an electromagnetic shower in the PS and ECAL. The electrons have the same behaviour as the photons at the PS and ECAL level, but also leave hits in the SPD detector. The π^0 neutral hadron can be classified as merged if reconstructed from a single cluster in ECAL or resolved

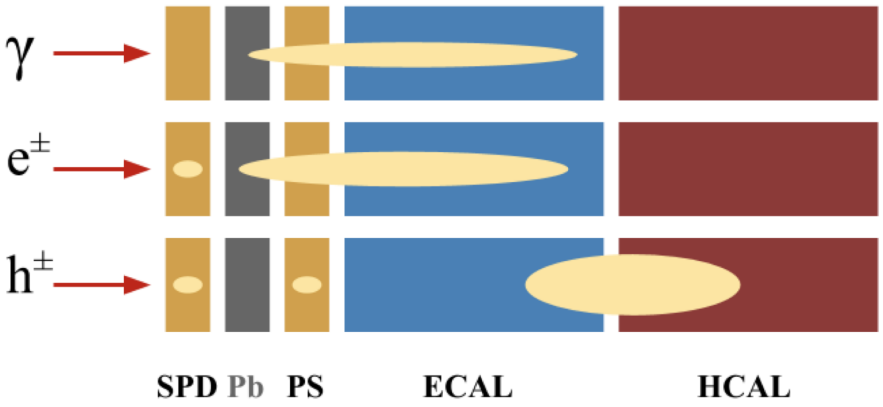

Figure 1.21: Representation of typical electromagnetic and hadronic showers and their interaction with the different detectors of the calorimetric system.

when reconstructed from two photons. Eventually hadrons are typically Minimum Ionising Particles (MIPs) in the SPD, PS, and in the ECAL (in the latter the energy deposit can be very variable). Basically all the energy is released in the HCAL.

1.2.5 Muon system

The muon system distinguish muons from hadrons and provides a quick measurement of the muon transverse momentum with 20% of resolution that is used in the hardware trigger (L0) [18] (fig. 1.22). It consist of 5 muon stations covering the acceptance range of [20, 306] mrad in the horizontal plane and [16, 258] mrad in the vertical plane. The stations are named M1-M5, the

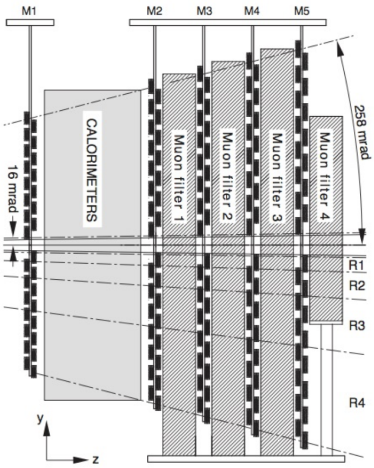

Figure 1.22: Side view of the muon system along the beam axis.

last four are placed downstream of the HCAL and are interleaved with iron absorber to stop hadrons not fully absorbed by the HCAL. The system given by calorimeters plus muon stations has an interaction length of about $20\lambda_I$ meaning that only muons with momentum greater than

6 GeV/c reach the last station. The station M1, is placed upstream the calorimeters and is used to improve the measurement of the transverse momentum in the hardware trigger.

The muon stations are made of multiwire proportional chambers and GEM detectors (only in the innermost region of M1, to cope with the higher radiation levels) with a digital readout on segmented cathodes (PAD). The pad granularity depends on the distance from the beam pipe to guarantee low occupancy and enough momenta resolution for the trigger L0. The pads are organised in projective towers with respect the interaction point for the L0 trigger. The transverse momentum of a muon candidate with hits in a tower in all five stations is computed using the coordinates of the pads in M3, M2 and M1 stations and assuming it is produced at the nominal interaction point.

1.2.6 PID variables

All the information collected by the PID detectors are combined to perform a particle identification of each track. The methods used to cope this task are two. The first considers likelihood functions $\mathcal{L}$ for each particle type, computed on the information from RICH detectors and calorimeters. Each track is initially assumed to be a pion, then the likelihood under different identity hypotheses (electron, muon, kaon, proton) is compared to the first one. The logarithm of the likelihood ratio, referred to as "delta-log-likelihood", $DLL(x) \equiv \log \mathcal{L}(x) - \log \mathcal{L}(\pi)$, is used as discriminant variable. The performance of the delta-log-likelihood variable in distinguishing kaons from pions is shown in Fig. 1.23.

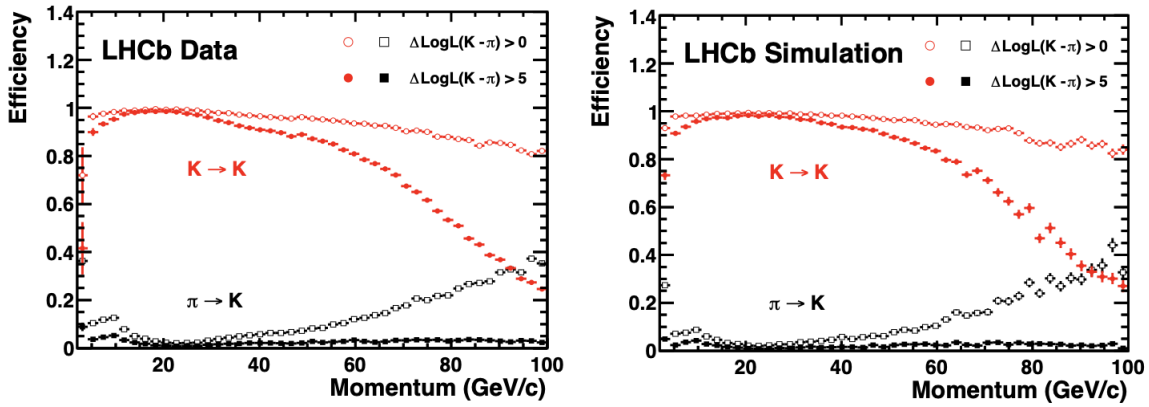

Figure 1.23: Efficiency and probability of mis-identification as kaons for true pions (black) and kaons (red) as a function of the particle's momentum for different cuts on $DLL(K-\pi)$. On the left is shown the results on data, from calibration samples, while on the right the expectations from simulation [17].

The second method relies on neural networks trained on simulated events and tested on calibration samples from data, using the TMVA toolkit [125]. These variables are named `ProbNN`, are defined between 0 and 1, are computed for each particles and can be interpreted as probabilities for a given charged particle to be identified as π, K, μ, p, e. This method shows improvements for muons and electrons, which are not well distinguished by the RICH detectors

but has limited discrimination between pions and kaons.

1.3 Trigger

Recording all the collision events occurring in the LHCb detector is technically impossible given the 10 MHz rate of visible interactions, therefore a trigger is needed to decide which event should be recorded in a mass storage. The system needs to be fast to quick decide which events to save. The task is fulfilled thanks to a series of steps:

- Level-0 Trigger (L0): it's an hardware based trigger, it is implemented with electronics, executed in a synchronous way with the bunch crossing rate of LHCb (40 MHz) and reduces the rate to 1 MHz;
- High Level Trigger (HLT1): it's a software based trigger which filters the reconstructed events passing the L0 trigger based on inclusive selections reducing the rate of events to 150 kHz;
- High Level Trigger (HLT2): it's a software based trigger which processes the output of the HLT1 and performs a more precise event reconstruction selecting the events based either on inclusive or exclusive requirements and produces an output rate of 12.5 kHz that are saved to permanent storage.

Starting from Run2 the detector alignment and calibration was implemented online so that the HLT2 software trigger could run on offline quality reconstruction events. This lead to a big experimental improvement in both reducing possible systematics related to differences between online and offline reconstruction and removing the need for a data reprocessing. Figure 1.24 shows the trigger scheme employed starting from Run2.

Hardware trigger

The L0 trigger exploits information available from the subdetectors, and consists of two units: L0-Calorimeter and L0-Muon L0-Calorimeter is divided itself into `L0Hadron`, `L0Photon` and `L0Electron`. The first records information from the HCAL system which is divided in clusters of 2×2 cells, in order to contain most of the energy released by a single particle and to avoid to receive energy deposits from different particles. The transverse energy associated to a cluster is computed as:

$$E_T = \sum_{i=0}^{3} E_i \sin\theta_i$$

being E_i the energy deposited in the $i-th$ cell and θ_i the angle between the beam and the line connecting the nominal collision point to the centre of the cell, while the sum considers the detector layers. In case there is an energy deposit in the ECAL it is added.

The `L0Photon` and `L0Electron` take information coming from the ECAL and allow to estimate the energy of electrons and photons. An event is triggered only if at most 2 or 4 PS hits

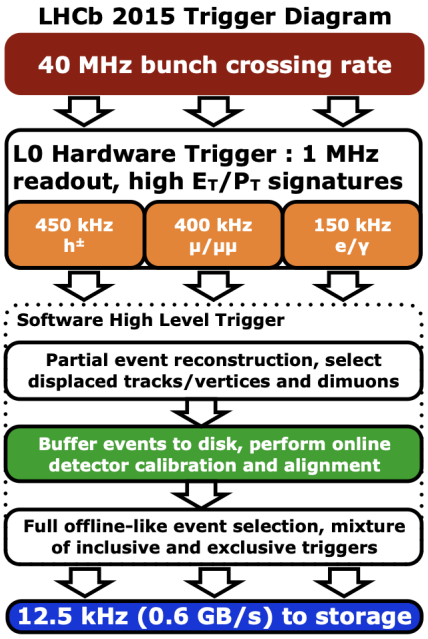

Figure 1.24: Trigger scheme of the LHCb experiment during Run2 (2015–2018).

are fired by the cluster in the outer and in the inner region, respectively. Photons and electrons are then distinguished considering the presence of hits in the SPD cells aligned with the PS ones. Only events with energy greater than 3.7, 2.4 and 2.8 GeV for hadrons, electrons and photons, respectively, are retained. Furthermore, to reduce the events with too high multiplicity, is also used a cut on the number of hits.

The `L0-Muon` system exploits the hits detected in the Muon stations and extrapolates the direction of the corresponding tracks starting from the collision point. In each muon station is determined an area called field of interest near the extrapolated hit, this area also takes into account trajectory variations due to multiple scattering, considering that its momentum in the x direction is larger than 0.6 GeV/c. If at least one of the hit is found in the field of interest, the signals in the stations M1 and M2 are employed to estimate the transverse momentum of the muon. At the end, an event is retained only if the muon with largest transverse momentum of a muon is greater than a threshold (typically 1.5 GeV/c) and/or there are more candidates and the square root of the product of the two larger transverse momenta $\sqrt{p_T(\mu_1)p_T(\mu_2)}$ is larger than the threshold (about 1.3 GeV/c).

The combination of the information is provided by L0-Decision Unit (DU) which make a logical OR to create the global L0 trigger decision. The decision is taken in 4 μs from the pp collision considering all the delays due to the time needed by the particles to travel through the whole detector, the electronics and the cable transmission. All the system is implemented on the FPGA technology and provides a rough estimate of the greatest transverse momentum of muons, electrons, photons and hadrons of the event. All the events fired by the L0-trigger are written to the disk of the Event Filter Farm (EFF) which is a dedicated computer cluster consisting of 1.700 nodes with 27.000 physical cores and 10 PB of data storage.

1.3.1 Software trigger

The EFF responsible of the HLT which is divided in two steps: HLT1 and HLT2. The first-stage performs a complete reconstruction of the tracks in the VELO to find the primary vertices (PVs) produced in the *pp* collisions. All the tracks having large impact parameter (IP) with respect to all of the PVs are extrapolated to the TT detector and matched with its track segments. In this way is possible to estimate roughly the particles momentum. Moreover, if this is larger than a preset threshold, more than 3 GeV/c, the track is extrapolated through the magnetic field and then connected with the signal deposited in the T-stations. Then, it is fitted using a Kalman filter [19], to take into account multiple scattering and corrects for the energy losses due to the passage of the track in the material detector. At this point, different algorithms are run to perform different selections e.g. to combine pairs of selected tracks or to connect them with the information from the muon stations. Each set of reconstruction and selection algorithms is named "trigger line".

The HLT2, uses the information coming from all the detectors and performs a full reconstruction of the event. Thanks to the trigger lines it is possible to categorise the event of interest, using selections based on the kinematics and PID information of the candidate particles and on the topology of the decays.

1.3.2 Trigger categories

The events selected by the trigger system can be classified according to the following non-mutually exclusive categories:

- TOS (trigger on signal): events for which the presence of the signal is sufficient to generate a positive trigger decision.
- TIS (trigger independent of signal): the "rest" of the event is sufficient to generate a positive trigger decision, being the rest defined through an operational procedure consisting in removing the signal and all detector hits belonging to it.
- TOB (trigger on both): events that are neither TIS nor TOS; neither the presence of the signal alone nor the rest of the event alone are sufficient to generate a positive trigger decision, but rather both are necessary.

All the events that belong to both TIS and TOS categories are instead referred to as $TIS\&TOS$ and are used to define the trigger efficiency at offline selection level which relies on data samples.

1.4 Software

Figure 1.25 shows a schema of the LHCb dataflow. The first software to be used, in case of collision, is `MOORE`, which is deputed to the trigger duties. The events are then reconstructed with `BRUNEL` and those containing interesting decays are selected with the stripping selections implemented in `DaVinci`. `DaVinci` is also used to produce "ntuple" in `ROOT` format, ready to

be analysed. The simulation, instead, flows through GAUSS which runs three steps: *pp* collision, simulated with PYTHYA8 [118], decay of resulting particles with EVTGEN [122] and their propagation through the detector with GEANT4 [117]. The GEANT4 output is then digitised with BOOLE and then the workflow is identical to that of the data.

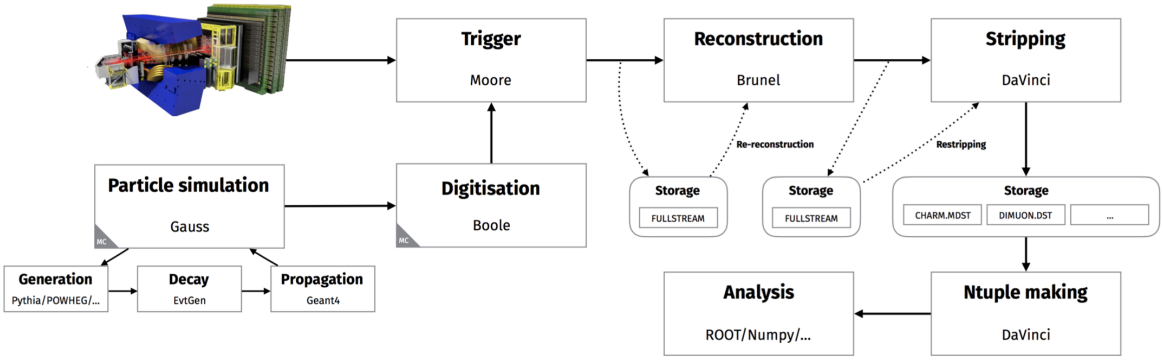

Figure 1.25: Data and simulation workflow.

1.5 LHCb upgrade

During Run1 and Run2 LHCb has recorded an overall integrated luminosity of about 9 fb^{-1}, that allowed to perform a large number of high precision measurements in the context of heavy flavour physics, obtaining leading and outstanding results as the first observation of the $B_s^0 \to \mu^+\mu^-$ [10, 11], the measurement of a flavour changing neutral current anomaly in the $B_0 \to K^*\mu^+\mu^-$ decay [12, 13], the observation of pentaquark states [14] in the $\Lambda_b^0 \to J/\psi p K^-$ decay, and the observation of tetraquark states [15, 16].

Nevertheless many key measurements remain statistically limited with experimental precision not directly comparable to the uncertainties of the theoretical predictions [13]. Moreover the LHCb physics programme involve also exploration studies which includes experimental observables that will shed light on the lepton sector, and in topics beyond flavour physics. The main limitation is given by the LHCb readout trigger architecture which limits the running luminosity. For this reason, to allow data operation at an increased luminosity of 2×10^{33}cm^{-2}s^{-1}, LHCb is currently completing a major upgrade in which the detector readout will be performed at 40 MHz instead of the previous 1 MHz. The aim is to collect at least 50 fb^{-1} of data by the end of 2028, which will allow measurements in some key decays with precision comparable with theoretical predictions. In order to sustain this changes, the readout has been replaced and to face up to the increased radiation hardness and higher values of occupancy mainly all the sub-detectors have been upgraded.

1.5.1 Trigger and readout upgrade

The Run1-Run2 readout and triggering scheme represents a limitation factor for the trigger effectiveness at Upgrade conditions. Figure 1.26 shows as the trigger yield on many hadronic

channels already saturates at the current luminosity of LHCb. In the upgraded version of the

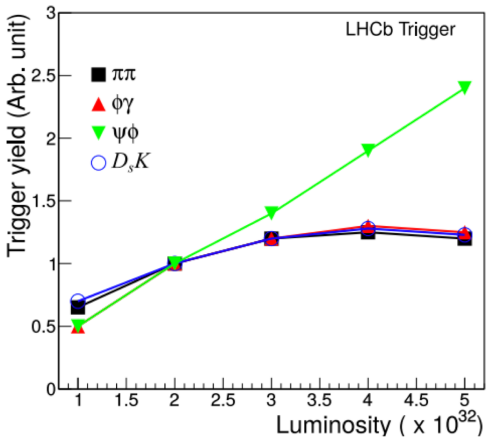

Figure 1.26: Trigger yield as function of the instantaneous luminosity for different decays of B mesons.

LHCb experiment (see fig. 1.27), the hardware trigger will be replaced with a software-based Low Level Trigger (LLT) which use information from the calorimeter system and muon. The foreseen output rate of LLT will be in the range of 15-30 MHz. Without the L0 trigger the front-end electronics will be able to run sending data synchronously at 40 MHz to the back-end electronics (mainly composed by FPGAs and high bandwidth bidirectional optical links with a common protocol). An uniform infrastructure based on the so-called PCIe40 cards [21–23] will be used for data readout, slow and fast control. The data will be buffered to disk, and a software trigger will perform the first selection and reconstruction with an output rate to store of 2-5 GB/s.

1.5.2 Detector upgrade

The new version of the LHCb experiment is shown in fig. 1.28. As already pointed out, for the upgrade an higher radiation tolerance and granularity are request, in particular for the tracking subdetectors. The upgraded VELO [24] will be placed closer to the beam axis, the radiation lengths will be reduced from 4.6% to 1.7% radiation lengths, and the strip technology will be replaced with pixels. These changes will improve of 40% the the impact parameter resolution, with a better tracking efficiency for low momentum particles and provide a better decay time resolution. The tracking stations will be replaced with the Upstream Tracker (UT), placed upstream of the magnet, and the Scintillating Fiber tracker (SciFi), downstream of the magnet [25]. The former will be composed of four tracking layers exploiting the silicon strip technology. The latter will consist of twelve layers instrumented with 2.4 m long scintillating fibres with diameter of 250 μm, arranged on a vertical direction. The fibres will readout by Silicon Photon Multipliers placed on the top and bottom of the layers cooled at the temperature of -40°C to decrease the radiation damage and the dark noise. The combinations of both UT and SciFi with the information collected in the VELO will reduce the number of ghost tracks by a

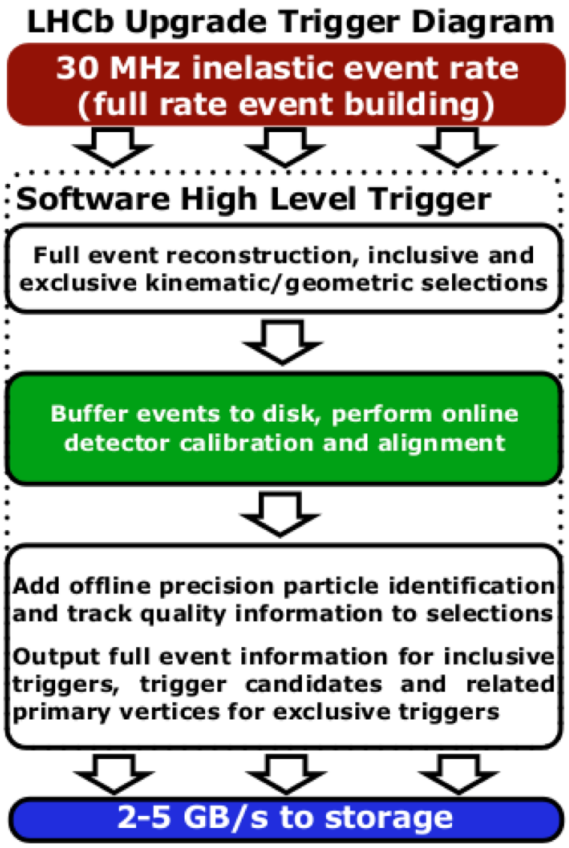

Figure 1.27: Run3 trigger scheme of the LHCb experiment.

factor 50-70%[26]. The RICHs upgrade will be discussed in the next chapters. The calorimeters and the muon chambers, will not undergo big upgrades apart by the replacement of the front-end electronics and the removal of station used in the old L0 trigger only.

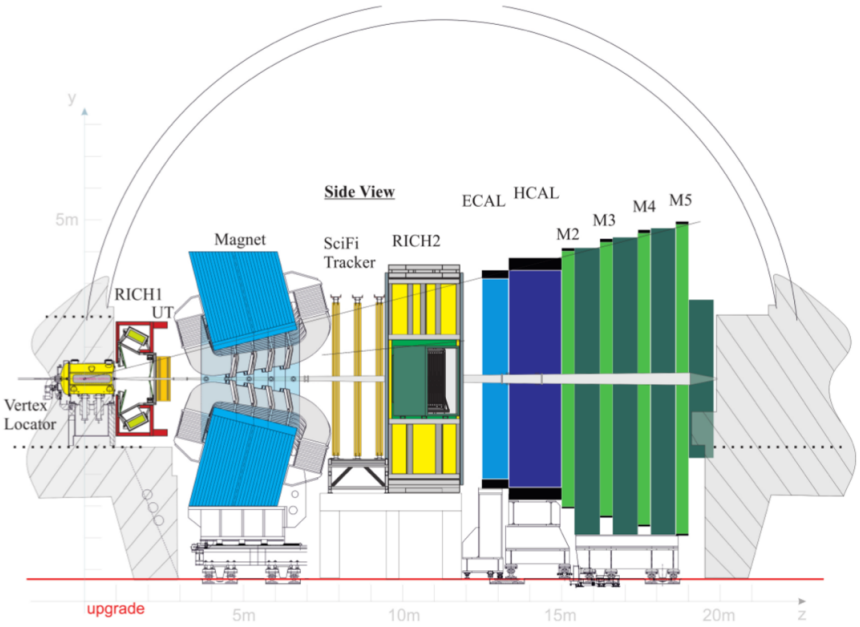

Figure 1.28: Side view of the upgraded LHCb experiment.

Chapter 2

The LHCb RICH Upgrade

To cope with the five-fold increase in instantaneous luminosity foreseen in Run3, and the need to read-out the full LHCb detector at 40 MHz, the complete photon detection and electronics chain in both RICH detectors has been replaced. In particular, the HPDs are replaced by Multi-Anode PhotoMultipliers Tubes (MaPMTs), a new front-end electronics is installed. The optics and the mechanics are also redesigned to reduce the peak occupancy and to provide a new support structure housing the photon detectors.
The new photon detector tubes are described in sec. 2.1, then the building block of the new front-end electronics, *i.e.* the CLARO chip, is introduced in sec. 2.2. The Elementary Cell (EC), a module where the new MaPMT photodetectors are allocated is described in sec. 2.3. The digital boards, the column structure, and the photon detector regions are described in secs. 2.4, 2.5, and 2.6. The mechanics and optics are treated in sec. 2.7, while in sec. 2.8 an overview of the experimental control system is given. Eventually, the calibration of the photon detectors and of the front end electronics, and the expected performances of the detector are discussed (secs. 2.9 and 2.10).

2.1 Multi-anode PhotoMultiplier Tube

The design of the upgraded photon detection chain has been optimised to cope with the non-uniform occupancy expected in the RICH system. For this reason the photon detection planes consist of two regions having different granularity. The new photomultipliers are Multi-anode Photo-Multiplier Tubes (MaPMTs) manufactured by Hamamatsu. Two MaPMT types are mounted in the RICH detectors depending on the occupancy and the possibility to reduce the number of the instrumented channels. Based on these criteria, the whole RICH1 and the central region of RICH2 are equipped with Hamamatsu R13742 MaPMTs (custom version of R11265), while the outer region of RICH2 has been equipped with Hamamatsu R13743 (custom version of R12699). Both the types of MaPMTs are composed by a matrix 8×8 anodes and with a 0.8 mm thick UV glass entrance window: the R13742 is 1-inch photon detector with a pixel size of 2.88×2.88 mm^2, ideal for the high occupancy areas of the RICH system, while the R13743 is a 2-inches device, with a pixel size of 6×6 mm^2. Each MaPMT is equipped with a Super

bi-alkali photocathode, the R13742 has 12 stages of dynodes while in the R13743 the number of dynodes is 10. The standard gain of MaPMT is optimised for single photon detection, and corresponds to 10^6 e^- at 1 kV operating voltage. A gain spread of 1:3 is tolerated between pixels of the same device. Moreover, a gain spread of 1:3 is also expected between different MaPMTs but can be compensated by adjusting the device bias voltage. The photo-electron collection efficiency rate is 90% at the first dynode stage. The Dark Count Rate (DCR) is less than 2.5 kHz/cm^2. In fig. 2.1 are shown the MaPMTs installed in the LHC Run3 RICH detectors. The

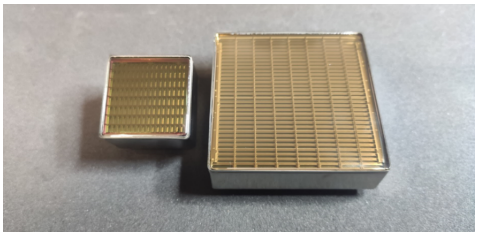

Figure 2.1: Hamamatsu MaPMTs the R13742 (R-Type) on the left and R13743 (H-Type) on the right.

RICH1 is equipped with 1920 R13742 while the RICH2 with 768 R13742 and 384 R13743. This MaPMTs have been selected among 3550 units after a Quality Assurance procedure (performed in Padova and in Edinburgh) to verify the real specifications. The parameters gathered during the Quality Assurance phase are used both to accept the MaPMT and to optimise the positioning of the units in the photon detector planes. The MaPMTs production was completed in 2018 and a series of test-beams allowed to gather complementary results [28]. A full Run3 module, composed of 12 MaPMTs, was installed inside RICH2 and operated during the last year of data taking before Long Shutdown 2. During such test, a background source named Signal-Induced-Noise (SIN), delayed with respect to the incoming photon, was observed for the first time in the outer pixels of the R13742 units. Then the SIN has been thoroughly studied and characterised due to the possible pile-up effects in the high occupancy region of RICH1 [30]. The main mitigation strategy to lower the SIN contribution consists in lowering the HV while keeping a good detection efficiency. Furthermore Hamamatsu designed and produced a sub-set of units to limit the occurrence of such effect. A total of 200 SIN-mitigated units have been delivered and quality assured to be installed in the high occupancy region of RICH1.

2.2 Front-end electronics: the CLARO ASIC

The CLARO [27] is an application specific integrated circuit (ASIC), consisting of 8 channels, designed to process input signals in the range from 30 ke^- up to 20 Me^-. Each of the 8 channels is equipped with an amplifier and a discriminator: the first is an analog device which converts the channel current input pulses into voltage signals and feeds them to the discriminator, the latter compares the signal at the amplifier output to a programmable threshold. When the set threshold is exceeded, it generates a digital pulse at the output of each channel. The output signal of each channel is of about 2.5 V and the pulse duration, typically 1-25 ns, depends on

the amplitude of the input signal which passed the threshold. A simplified scheme of a channel can be seen in fig. 2.2. Effects like crosstalk among the channels have been minimised reducing the input impedance of the front-end amplifier.

In order to cope with the high average hit rate, which is expected to be more than 10^7 hits/s per pixel, especially in the high occupancy region of RICH1, a fast radiation-hard electronics is required, together with low power consumption to ease the need for cooling. According to the FLUKA [29] simulations of the experiment, the worst-case values corresponding to an integrated luminosity of 50 fb^{-1}, after applying a safety factor of 2, are 3×10^{12} 1 MeV n_{eq}/cm^2 for the neutron fluence, 1.2×10^{12} HEH/cm^2 for the high-energy hadrons fluence, and 200 krad for the total ionising dose, respectively. These reasons lead to design the CLARO capable of processing signals and recovering the baseline in less than 25 ns, with a power consumption of 0.7-2.5 mW/channel, depending on the number of hits per second to drive the output to the digital board, and able to tolerate up to 2 kGy. The configuration register of the CLARO is 128-bit long which can be accessed by a Serial Peripheral Interface (SPI). The register is protected from bit flip called Single Event Upsets (SEUs) by a Triple Modular Redundancy (TMR). With the TMR three copies of the configuration register are kept in separate cells at different locations in the chip. In this way if one register copy is compromised due to a SEU, the other two cells correct the register configuration. The first 96 bits of the register are used to configure the 8 channels and the remaining bits to control the global features of the ASIC. Each CLARO channel is therefore adjustable with a 12 bits configuration register, with a possibility to read/write (R/W), as presented in table 2.1.

Table 2.1: Configuration bits of CLARO channels.

Bit Position	Name
0:5	Threshold
6:7	Attenuation
8	Input Enable
9	Hysteresis Disable
10	Test Pulse Disable
11	Offset Enable

The first six bits are used to set 64 steps of threshold of the discriminator from 0 to 63. The next two bits corresponds to attenuation which reduces the channel gain by the factor of $(1/2)^n$ (*e.g* a factor 0 means no reduction and both bits disabled, while a factor 1 means reduction of 1/2 and 6-bit disabled and 7-bit enabled). The threshold steps are regulated according to the attenuation, with 0 attenuation, the usual threshold step is 30 ke^- and ranges up to 2 Me^-. The 8-bit position enable switches the channel on/off (0/1). Even the hysteresis is a parameter which can be switched on/off with the corresponding bit (9-bit position) and activates when the CLARO comparator triggers. The hysteresis is used to avoid output oscillations in channels with thresholds set too close to the baseline. The test pulse bit enable the injection of charge from the internal capacitors to perform characterisation tests. The last bit of the twelve can be used as offset of the threshold by setting an amount of 32 steps and allows to access negative

threshold values. The threshold zero corresponds to the central part of the Digital Analog Converter (DAC) threshold scale, in this way it is possible to use the DAC to cancel the offset at the discriminator input. The actual threshold are calibrated with test signals injected at the input through a dedicated test capacitor.

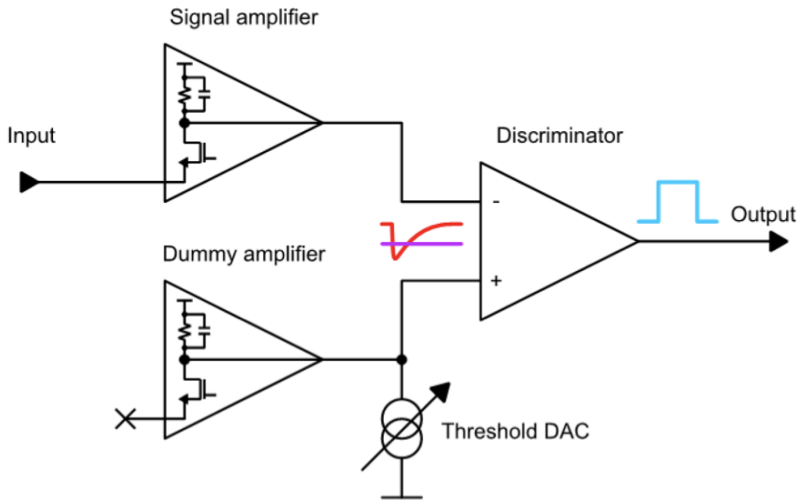

Figure 2.2: Scheme of a CLARO channel.

2.3 The Elementary Cell

The EC represents the core module of the LHCb RICH Upgrade as it hosts the MaPMT photodetectors and the readout system. To allow a different granularity two different types have been foreseen: E-type (EC-R) and H-type (EC-H). In fig. 2.3 a view of the EC-R is shown.

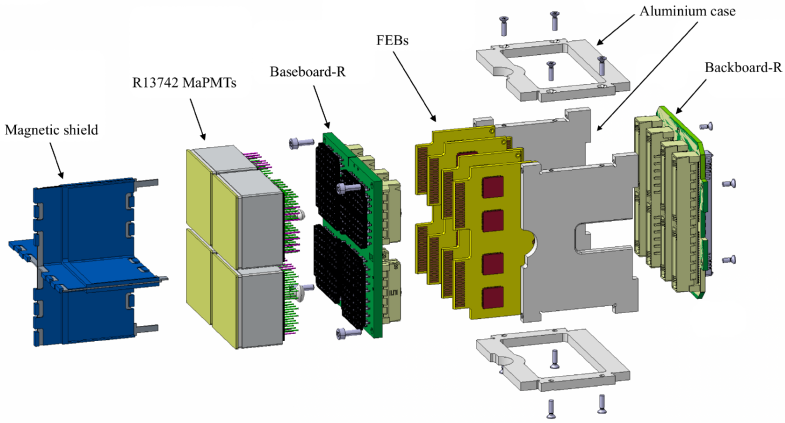

Figure 2.3: Schematic view of the R-type elementary cell.

An EC-R reads 4 R13742 MaPMTs for a total of 256 pixels in about 2×2 square inches. The MaPMTs are plugged into a baseboard, hosting four 3 MΩ resistive dividers in parallel

to bias the dynodes of each MaPMT. A dedicated connector brings the high voltage to feed each divider. The last two dynodes of the chain can be powered by a dedicated supply line in the occupancy region, where the current draw is higher and can induce non-linearity effects in the MaPMT gains. In the RICH1 EC-R, a magnetic shield made of mu-metal, is allocated in front of the MaPMT, to attenuate the magnetic field by a factor of about 20. In fig. 2.4 the effect on the counting efficiency of the magnetic shield is shown. The baseboard propagates

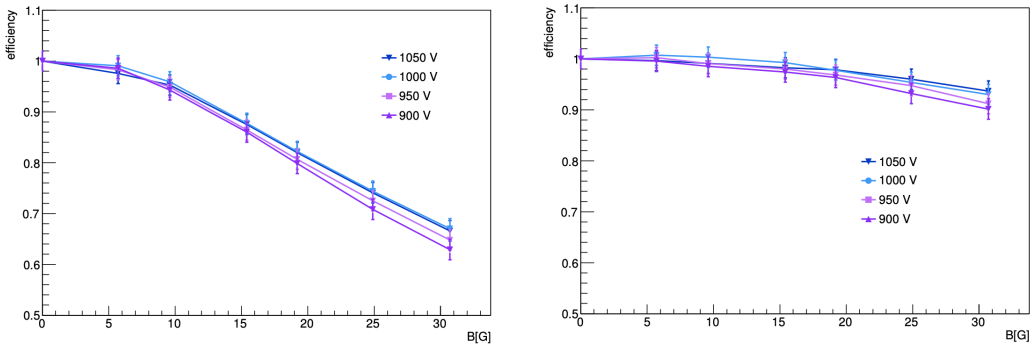

Figure 2.4: Counting efficiency as a function of the longitudinal magnetic field for an edge pixel, at different values of HV, for an EC-R (Left) without and (Right) with the magnetic shield.

the signal to the connectors on the other side, where are plugged-in four Front End Boards (FEBs), each FEB has four CLARO on each side to convert the anode signal into a digital pulse. Then a backboard connected with the FEBs routs the signal to the Photon Detector Module Digital Boards (PDMDB). The mechanical support for the electronic components consist of an aluminium case, it also allows thermal transfer by conduction, where the heat dissipation from the voltage dividers is favoured by copper layers placed internally to the baseboard. Also temperature probes are installed and routed to the PDMDBs: two per baseboard, one per FEB and two per backboard. In total the RICH1 has been equipped with 480 EC-R while only 192 are used in the central region of RICH2. The EC-H, see fig. 2.5, is designed to read the R13743 MaPMT, in this case only two FEBs are used with half the CLARO channel disabled and five temperatures probes installed. As said before, due to granularity consideration, the ECs-H are used in the peripheral region of RICH2. As for the MaPMTs, Quality Assurance procedures have also been carried out for the ECs. A dedicated setup and test protocol, described in detail in section 3.1, have been developed and installed in two facilities, one in Ferrara and the other in Edinburgh.

2.4 Photon detector module digital boards

The signals coming from the MaPMT channels feed into the FEBs and then into PDMDBs. The PDMDB transports the digitised photon detector signals away from the high radiation region of the detector without introducing dead-time and preserving the photon detection efficiency. Furthermore, the design of the board is highly constrained by the layout of the photon detection plane, the confined space, the presence of the magnetic field, the radiation environ-

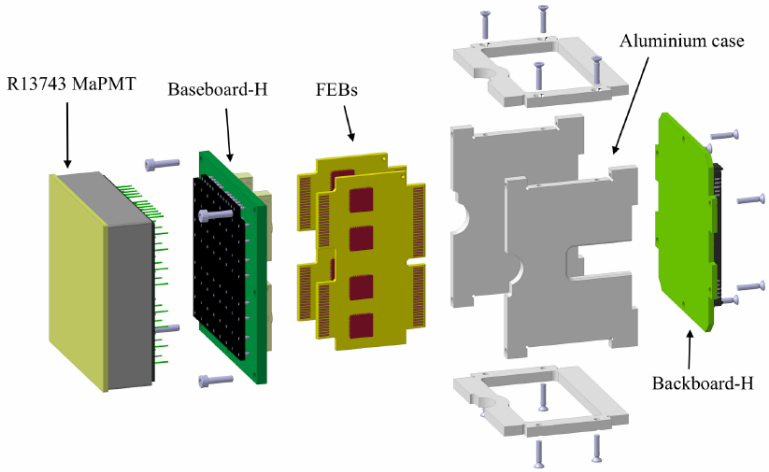

Figure 2.5: Schematic view of the H-type elementary cell.

ment, and the compatibility with the data acquisition infrastructure that is common to all the LHCb subdetectors. Those reasons brought to the use of the FPGA as it is a flexible way to format the data and to interface between different electrical signalling standards of the front-end ASICs and giga-bit optical link (GBT) chipset. Two variant of the PDMDB are used (see fig. 2.6) in correspondence of the different granularity of the photon detectors planes. Two PDMDB-Rs are mounted back to back, coupled to a group of four EC-R, while a single PMDB-H is coupled to a group of four EC-Hs. The module consisting of four ECs and one or two PDMDBs is called Photon Detector Module (PDM). On each PDMDB is allocated a TCM (Trigger and Control Module), a 3×6 cm^2 plug-in module that provides the interface for the fast and slow controls data exchanged between a PDM and the LHCb global online system. The TCM hosts a VTRX (optical transceiver) and GBTX (giga-bit optical link) chips operating in bidirectional forward-error-correction mode, and through the GBT links is able to distribute synchronously the LHC clock to the Front End (FE) electronics. Moreover, it implements the various protocol required for the configuration of the PDM using the Slow Control Adapter GBT System (GBT-SCA) that is connected to the GBTX sc e-port operating at 80 MHz. The DTM is a 3×6 cm^2 plug-in module that provides the high speed transmission interface for the PDM receiving data from FPGA. On each board there is the same number of FPGAs and DTMs, in particular three on PDMDB-R and two on PDMDB-H. The physical link consist of the VTTX optical transmitter with each channel connected to a GBTX ASIC, each operating in transmission mode. One GBTX receives its 40 MHz reference clock from the TCM and generates a 160 MHz clock routed to the FPGA, and a locally routed 40 MHz clock that serves as the reference clock for the second GBTX. The DTM GBTX data transmission e-links that are connected to the FPGA operate in a rate mode of 160 MHz. The PDMDB motherboard acts as a bridge for the signals between the ECs and the TCM and the DTMs. The board also incorporates local power regulation for the FPGAs as well as for the active components on the ECs, TCM, and DTMs using CERN FeastMP-CLP DCDC converters. The only active components on the motherboard, apart from

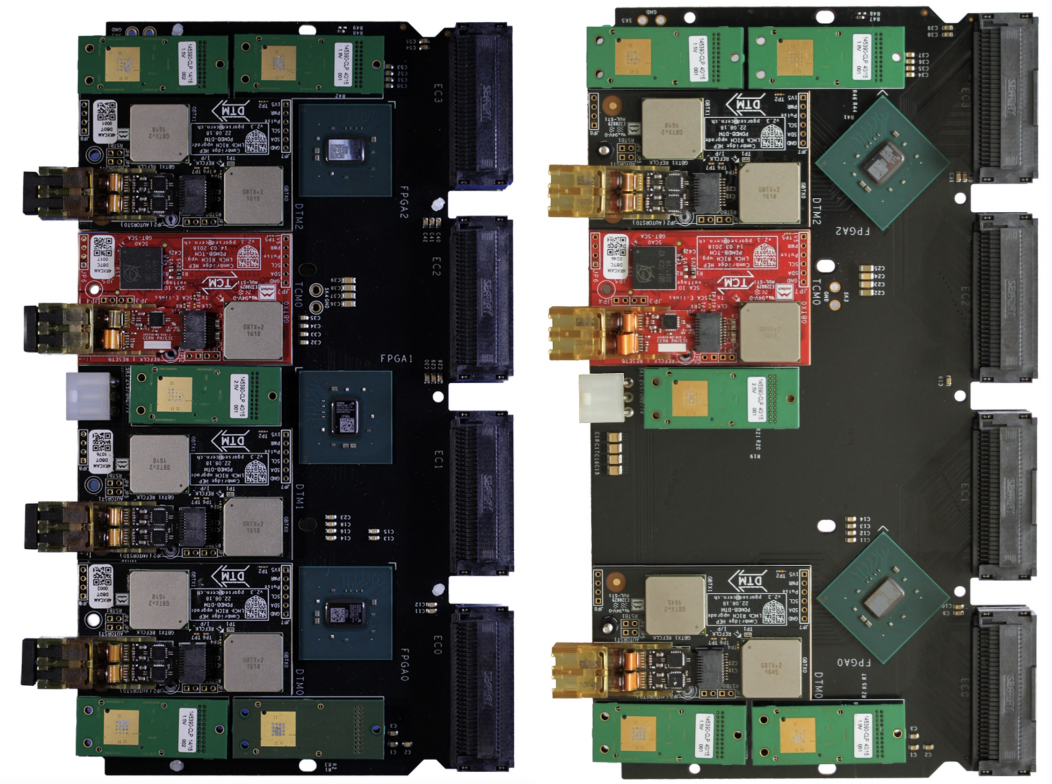

Figure 2.6: Picture of (Left) PDMDB-R and (Right) PDMDB-H.

the DCDC converters, are the FPGAs which receive the 2.5 V LVCMOS digital GBT frame and the packing of the bits into the frame is performed in the FPGA logic.

2.4.1 Leveling plate

The active components mounted on a PDMDB are a significant source of heat therefore they are cooled by an aluminium plate that provide the thermal coupling of them with the internal structure of the columns. The procedure developed and followed to ensure the thermal exchange is referred to as Leveling Plate. In fig. 2.7 is shown the overview of all the components that need to be mounted on the PDMDB to ensure proper heat exchange between cooling and components generating heat. In particular, thermal pads are placed on the FPGAs, GBTs, and VTTX to guarantee not only the thermal isolation but also the thickness required between the PDMDB and the aluminium plate. Spacers and screws are use to anchor the PDMDB with the plate on the column.

2.5 Photon detector columns

Depending on which part of the RICH is arranged, two types of PDMs can be classified: PDMs-R and PDMs-H. The first consist of four ECs-R and two back-to-back PDMDBs-R, installed in the whole RICH1 and in the central region of the RICH2. The latter is made up of ECs-H, and one PDMDB-H, and it is installed in the peripheral regions of RICH2. Each RICH

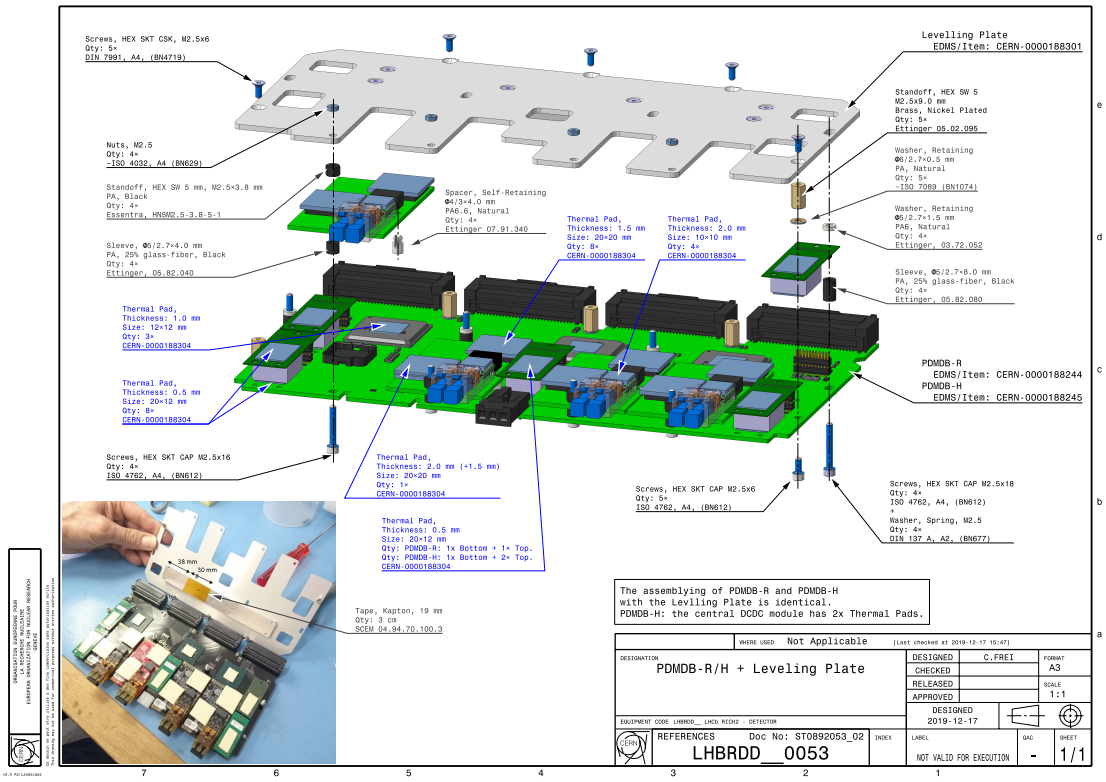

Figure 2.7: Leveling Plate scheme.

detector contains six PDMs assembled on a T-shaped aluminum structural element, referred as T-bar. The T-bar provides a precise reference for the positioning of the ECs and PDMDBs. The length is about 1.6 m, the width 55 mm and the depth 40 cm. In fig. 2.8 the CAD view of the T-bar and a fully populated RICH2 column is shown. The ECs are mounted at the front of the T-bar by screws, and their connector are located into the openings of the T-bar, and plugged into the corresponding PDMDB connectors. Also the PDMDBs are fixed to the T-Bar by screws.

To facilitate the installation, handling and maintenance, and considering the low hit rate expected in the corresponding regions, two ECs have not been mounted in the upper and lower part of the RICH1 columns, containing 22 ECs instead of the 24. For the same reasons, the column placed upstream of each MaPMT plane, detecting Cherenkov photons coming from particles at lowest pseudorapidity, has 20 ECs. Whereas, RICH2 columns, are fully populated have four PDM-Hs interleaved by two PDM-Rs. To guarantee that each column is at temperature below 30°C , a cooling is provided in the column by a fluorinate coolant (3M Novec 649) circulating into ducts placed into the spine of the T-bar. The geometry and the fact that the cooling flows back and forth into the ducts offer a uniform temperature distribution.

Moreover, each column requires services as Low Voltage (LV), High Voltage (HV), data and TFC (Timing and Fast Control)/ECS (Experimental Control System) optical fibres, and monitoring devices for the DCS and DSS (Detector "slow" Control System). Two different designs have been produced depending from the different orientation of columns, horizontal

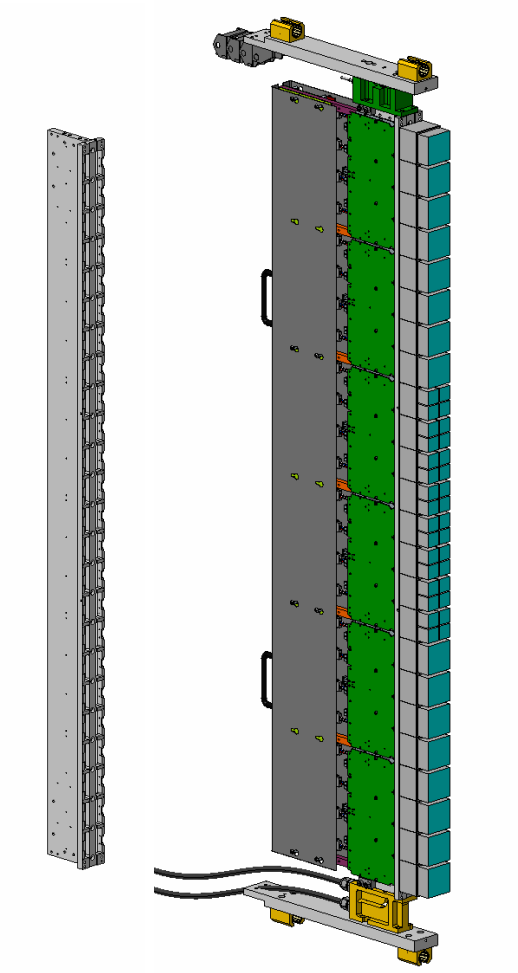

Figure 2.8: (Left) CAD view of the T-bar. (Right): CAD view of the RICH2 column populated with the photon detector modules.

in RICH1 and vertical in RICH2. Each PDMDB needs a primary supply of about 7V and a secondary supply of 2.5V allowing to power cycle individual boards via GPIO operations and the current consumption of a PDMDB-R (PDMDB-H) is approximately 2.5A (1.5 A) when fully configured. The LV supply is provided by two Wiener Maraton channels for RICH1 columns, while one channel is used for RICH2 columns. Dedicated distribution boards, located at one end of the column, provide the 2.5 V supply by means of DCDC regulators. Then, each MaPMT is supplied by a high voltage (900 V) and an intermediate voltage (90 V) to power the last dynode, aiming to mitigate possible non-linearity effects in the MaPMTs installed in the high-occupancy region, and allowing to monitor the anode current that should be kept below 100 μA per MaPMT. The HV supplies, for each column, are provided by common floating ground A1538DN CAEN boards, while the distribution of the voltages and ground from one PDM to the corresponding four ECs is implemented through dedicated HV distribution boards.

To avoid ground loops, each column is electrically insulated: a copper braid connects the LV ground of the column to the safety ground of the detector. Optical fibres transmit data and control the PDMDBs, all of them have two TFC/ECS, moreover, PDMDB-R has six fibers while

PDMDB-H has four fibers to transport data to the TELL40 boards. Then 12 fibers connect the optical links to the individual connectors on the PDMDB.

2.6 Photon detectors regions

The RICH1 columns are 22 arranged side by side in groups of 11, the first array, made of 11 columns is placed below the beam pipe, the other above. Both the arrays are placed in horizontal with respect to the plane perpendicular to the beam pipe. In fig. 2.9 is shown a RICH1 column, in each column are allocated the optical fibers, the low-voltage distribution the built in supports for the services to the MaPMTs and the associated electronics.

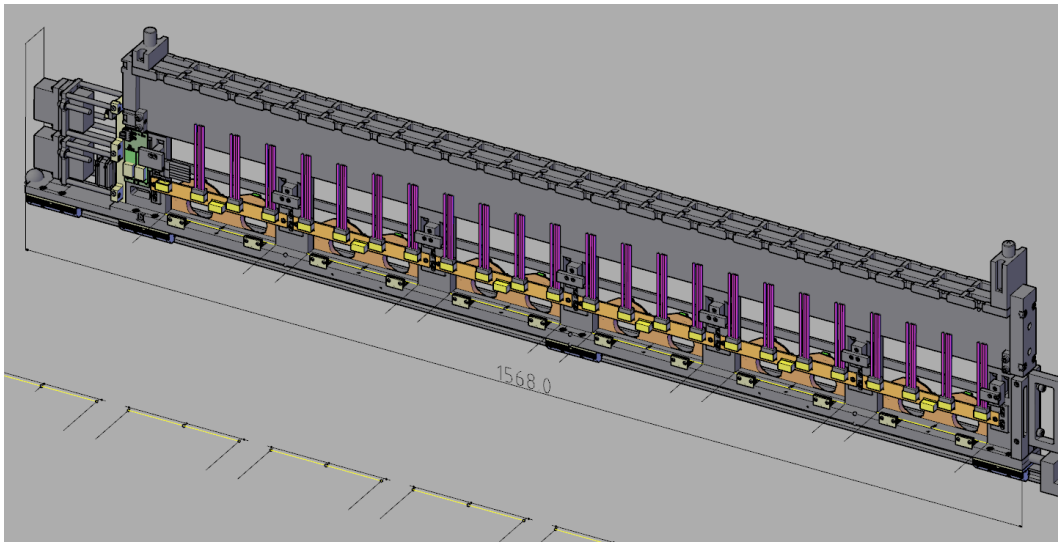

Figure 2.9: CAD model of a column in the RICH1 configuration. Copper-carried services (low-voltage, high-voltage, and thermometry) enter the column through connectors at the extreme left of the column. Cooling and data fibres enter from the right. the MaPMTs are mounted on the top surface, there alignment pins are also shown. On the bottom face of the column are mounted carriages to support the column from a rail. Cassettes for winding optical fibres are shown in orange.

The arrays are placed on rails to allow easy removal for maintenance, and are held at correct angle and aligned on the *MaPMT chassis*. In fig. 2.10 is shown the chassis installed on the Up side of the RICH1.

The RICH2 is made of aluminium profiles, placing twelve columns each side by side with about 1 mm between them, see fig. 2.11.

Such structures are named racks and are installed into the magnetic shields on the LHCb A-side and C-side in a vertical position almost perpendicular to the LHC beam. Also this racks have rails which guarantee the translation, perpendicular to the focal plane, of each column of the complete photon detector system. Under the racks are located two cooling manifolds: one to distribute the coolant to each column in parallel the other to collect back the fluid. On the upper side of the racks, are placed the cables to route the optical fibres and the electric cables to the patch panel located above the racks. The patch panel is the interface where all services are

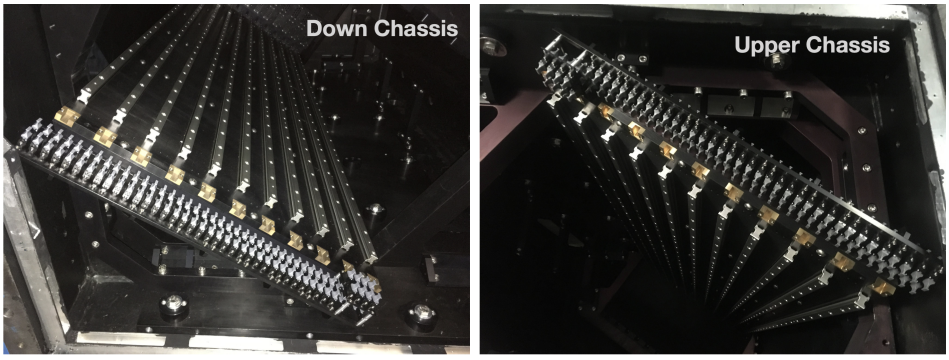

Figure 2.10: Support structure for the RICH1 columns, the MaPMT chassis, showing the rails and alignment structures. The chassis is mounted to the soft-iron magnetic shielding that surrounds the MaPMT region.

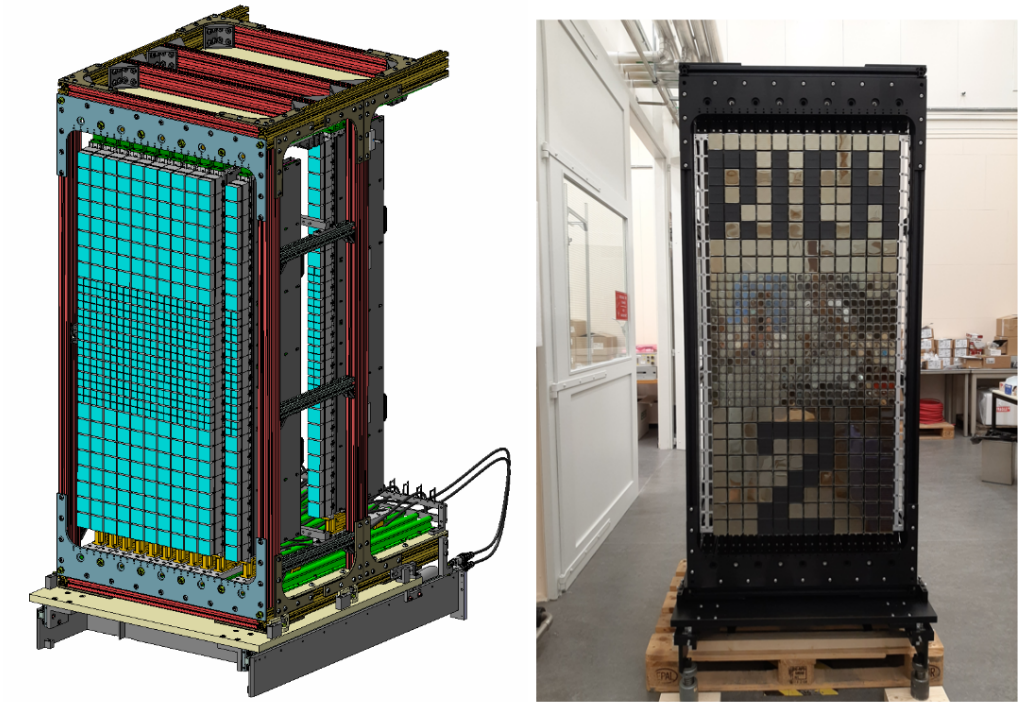

Figure 2.11: CAD view (Left) and photograph (Right) of the fully assembled and commissioned RICH2 A-side photon detectors array.

connected to the columns, it provides to all the connections: safety ground, LV, HV, DCS, DSS, TFC/ECS and data transfer. To ensure dry atmosphere with a good dielectric environment, and to minimise the risk of condensation Nitrogen is flushed permanently into the enclosure. In fig.2.12 are shown the CAD view and the photo of the photon detection system in the A-side enclosure.

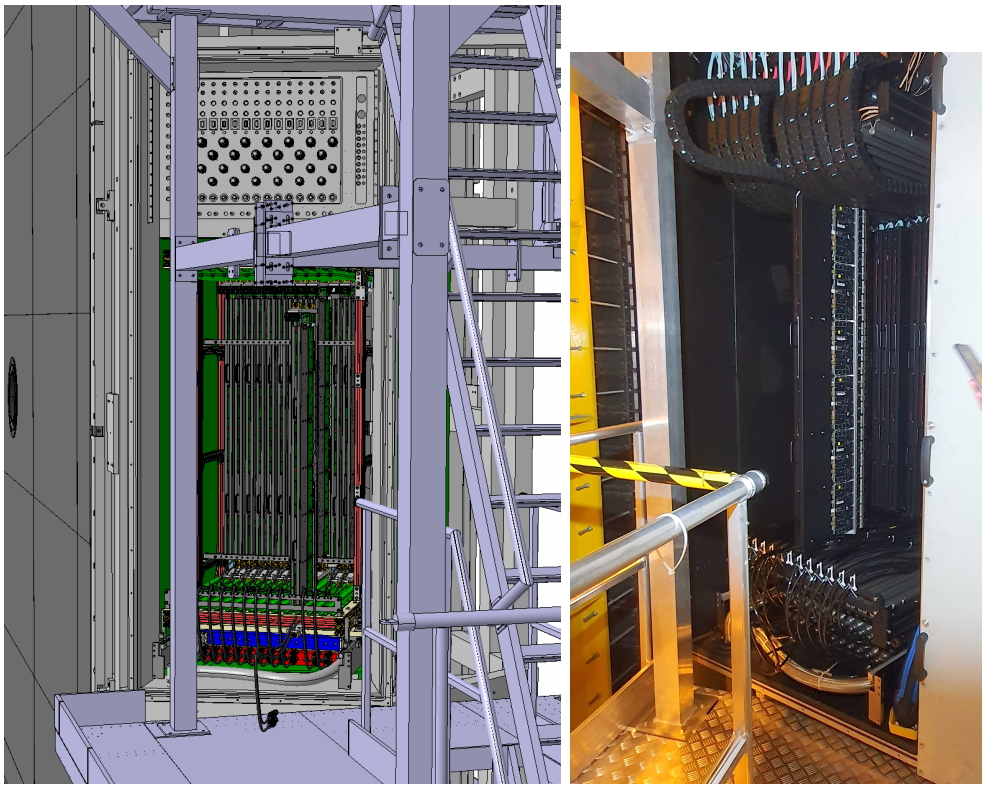

Figure 2.12: CAD view (Left) and photograph (Right) of the RICH2 photon detection system inside the A-side enclosure.

2.7 Mechanics, Optics and Gas enclosure

The new RICH1 has the same angular acceptance of the previous one and it will provide π/K PID from approximately 2 – 30 GeV/c (with K separation obtained from veto mode below the kaon threshold of 9.3GeV) and π/p separation from approximately 10 – 60GeV/c. To face up the hit occupancy foreseen in the Run 3 the optical layout has been modified with respect to the precedent version: the occupancy has been halved by increasing the focal length of the spherical mirrors by a factor $\sqrt{2}$, moving the photo detector plane further away from the beam line. Moreover, the re-arrangement of the spherical mirror configuration led to the decreasing of the emission point uncertainty improving also the Cherenkov angle resolution due to the reduced aberrations of the spherical mirrors. The old and the upgraded versions are visible in fig. 2.13.

The design philosophies of the original RICH1 detector are retained. The material budget within the acceptance retains lightweight carbon-fibre spherical mirrors with all other components of the optical system located outside the acceptance; the total radiation length of RICH1 is ∼4.8% X_0. Planar (flat) mirrors reflect the image from the tilted spherical mirrors onto the photon detector planes. The Photon detector planes occupy an active area of 605 mm wide by 1199 mm long. The photodetectors are shielded from the fringe field of the LHCb dipole, which unshielded is 60 mT in the region of RICH1. Each photo detector plane is shielded with a box, one is placed above and the other one below the beam pipe and it will reduce the magnetic

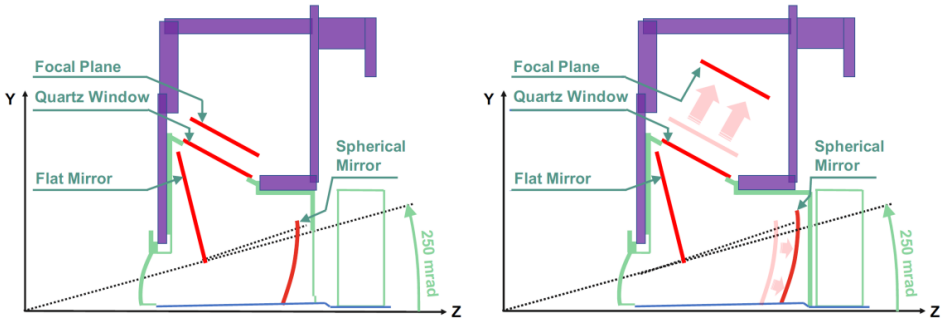

Figure 2.13: The optical geometries of (Left) the original and (Right) the upgraded RICH1 where the photodetector plane (Focal Plane) is moved further away from the beam-line to take advantage of the increased focal length of the spherical mirrors.

field experienced by the MaPMT to about 2.5 mT. The main part of these boxes is mounted on the on the wall/floor and two side elements that can be removed to allow for MaPMT column extraction and insertion in situ. Within the magnetic boxes, the MaPMTs are mounted within additional local mumetal shielding and are able to work efficiently in fields of 3 mT.

2.7.1 Gas enclosure

To ensure gas and light tightness a gas enclosure is required as shown in fig. 2.14.

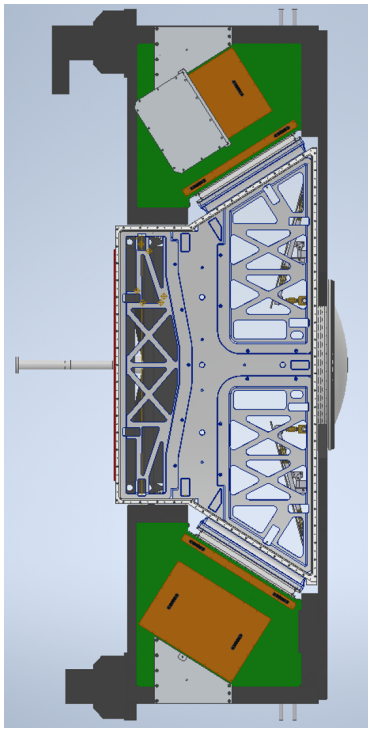

Figure 2.14: CAD layout of the RICH1 gas enclosure.

The gas used will be the C_4F_{10} at differential pressure of ± 3 mbar with respect the outside

environment and the total gas volume is approximately 3.8 m^3. The enclosure is a box with six sides bolted and epoxy-sealed at their edges and internally sealed with flexible silicon sealant to ensure leak tightness. The upstream and downstream faces seal the RICH gas and provide a liga are sealed by quartz windows to allow Cherenkov radiation to pass trough and hit the photo detector planes. The side panels are designed to maximise the access for installation of the internal optical components. The overall weight of the gas enclosure is about 1130 kg.

2.7.2 Mirrors

The spherical mirrors composed by carbon fiber are arranged into four quadrants centred around the beam line and are used to focus the Cherenkov light on the photon detector planes. For the RICH1 upgrade new planar mirror segments have been manufactured and assembled into two planes composed by eight rectangular mirrors each with dimension 370 mm×440 mm, positioned outside the detector acceptance above and below the beam line. Each mirror is made of carbon fiber with an aluminium and magnesium fluoride coating optimised for the angle of incidence of the Cherenkov photons resulting from the upgraded RICH1 optics and for the MaPMT quantum efficiency. The mirrors are bonded at their center to a polycarbonate mount, bolted into machined pockets on four rigid aluminium support frames.

2.8 Experimental Control System, monitoring and dataflow

The configuration, control, monitoring, archiving, operation and running of the RICH subdetectors are foreseen by the RICH ECS. The ECS is a uniform and homogeneous control system developed within the JCOP framework provided by CERN [31]. The RICH ECS is built on the top of the WinCC-OA [32] Supervisory Control And Data Acquisition(SCADA) tool, and is divided in three domains: the High Voltage system (HV), the data acquisition system (DAQ) and the DCS. The domains are integrated in a Finite State Machine (FSM) that can take automatic actions like switching on/off the low voltage system and the MaPMT high voltage system, and is able to monitor constantly the electronics, the detector environment and the condition of the cooling system to ensure safe operations. The safety of the detector hardware is paramount at every operation. Indeed, thanks to a large number of temperature and humidity sensors placed on the BaseBoards, BackBoards, FEBs, cooling manifolds and in the photon detector enclosure, it is possible to monitor the temperature both when the detectors are operational both when are switch off, via the SCA chip, located on the PDMDBs, and Embedded Local Monitoring Board(ELMB), in the gas enclosure, respectively. The resolution achieved is of about 0.5°C, and is provided by the SCA with a current of 100 μA. The combination of each sensor/current source, read by SCA, has been calibrated in the laboratory and then mapped inside the DSC WinCC-OA project. A safe switch-on procedure is implemented, where automatic configuration of the SCA chip at power-up allows the read out of the temperature sensors without any action of the operator. If the automatic configuration fails the detectors are returned to a safe state (OFF). Finally a smaller number of sensors are connected to the Detector Safety System (DSS)

running on a PLC system with many redundancies and represent the last line of defence of detector safety. The DCS takes also care to record the information related to the temperature and the pressure of the Cherenkov radiators in the Conditions Database and can be extracted by the LCHb event reconstruction index in order to calculate he refractive index of the gas radiator.

A live configuration to operate properly and establish a predictable dataflow is required for the FE and the Back End (BE) electronics. The control system is segmented in subsystem capable to scale up to thousands of FE and hundreds of BE devices and it is composed by one PDMDB, one SOL40, and one TELL40. The SOL40 provides, via 48 optical links, a clock of 40MHz and TFC commands to the PDMDBs through their TCMs. All the commands, like writing registers or generating test pulse are decoded by the combination of a GBTx and an SCA ASICs. The TELL40 takes FE data by the PDMDB, via unidirectional optical links, through DTMs.

TFC links are monitored to spot issues on the receivers side, through the reading of the Received-Signal-Strength-Indicator (RSSI) and of the Master GBTx Forward-Error-Correction (FEC) counters. The commands related to the TFC allow to enable communication, initialise temperature sensors, load the firmware on the FPGAs on the PDMDB and set the CLARO thresholds.

2.9 Photon detectors and frontend electronics calibration

The most important parameter of the RICH system is the single photon detection efficiency, which is driven by intrinsic properties of the MaPMTs such as the photocathode quantum efficiency, the collection efficiency at the first dynode and the single photon gain. Also the anode signal digitisation, provided by CLARO channel via a programmable threshold, contributes to the detection efficiencies.

Calibration procedures using the DAC scans are implemented to minimise the inefficiencies due to the threshold setting, to monitor the single photon gain variation with time and ageing, and the CLARO channels stability. The DAC scan is a measurement performed on the FE electronics to check the linear response of the channels to an input signal as a function of the channel threshold. It is performed sending n pulses with equal amplitude to each of the CLARO channel inputs, registering the number of times the channels have been switched on, and increasing the signal amplitude. The result of this test is an error function distribution, this being the reason why this test is also referred to as "S-Curve", fig. 2.15, instead of a step distribution due to the electronic noise. The derivative of an S-curve is a Gaussian distribution centred on the transition point, which is the number of electrons injected in the CLARO channel input corresponding to the half of the maximum height of the s-distribution. The width of such gaussian is the spread of the charge, also called noise, and is represented by the width of the curve slope. Both these parameters are obtained by fitting the S-curve with a translated error function distribution. By repeating the DAC scan at different threshold it is possible to determine the conversion between the threshold DAC code and the corresponding charge for each set of attenuation and offset bits. In fig. 2.16 a DAC scans performed on a RICH2 column

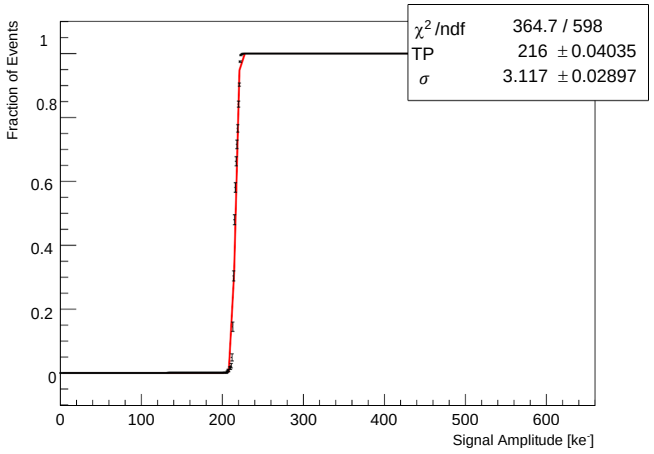

Figure 2.15: S-Curve distribution for a CLARO channel. The parameters of interest are obtained by fitting the curve.

acquiring ten thousands events, while keeping the HV in state off and not illuminating the system, is reported. In all the set of attenuation and offset bits considered, linearity between the threshold setting and the injected charge has been found.

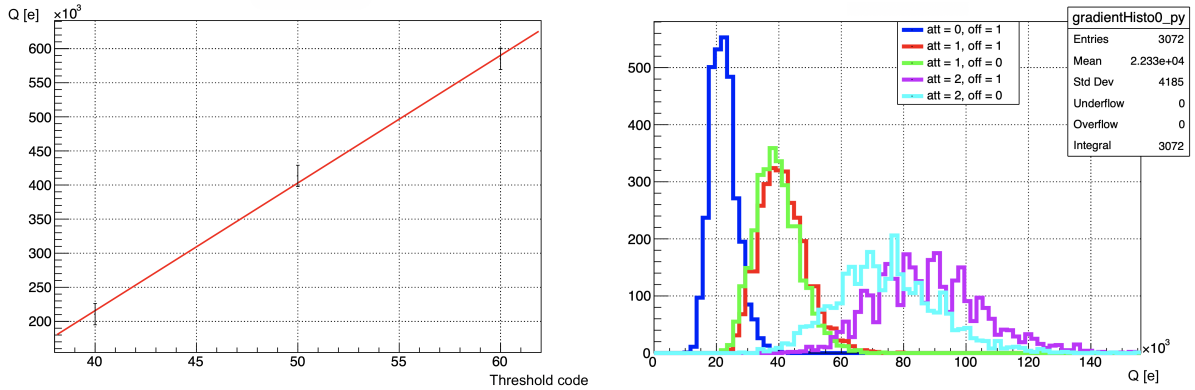

Figure 2.16: (Left) Calibration of a single CLARO channel with offset bit enabled and no attenuation. The charge corresponding to a threshold DAC code (th) is determined by the linear relation $Q = Q_0 + Q_{\text{th}} \cdot \text{th}$. (Right) Distribution of the charges corresponding to one threshold step (Q_{th}) for a RICH2 column in different conditions of offset and attenuation.

To maximise the single-photon efficiency, threshold scans are performed to find the set of FE working points, *i.e.* optimal threshold, attenuation, and offset bits. This test, differently from the DAC scan test, is performed with the MaPMT powered on and using a LED as signal source for the CLARO channels. During the test, the CLARO input signal coming from the MaPMT, operating in a single-photon regime, is constant in amplitude meanwhile the channel threshold changes with a given set of attenuation, offset, and HV. The final distribution, see fig. 2.17 corresponds to the integral of the single photoelectron spectrum, and the parameter of interest is the Working Point (WP) of the CLARO channel, *i.e.* the minimum between the pedestal and the first single photoelectron peak. The Threshold Scans are performed at the MaPMTs

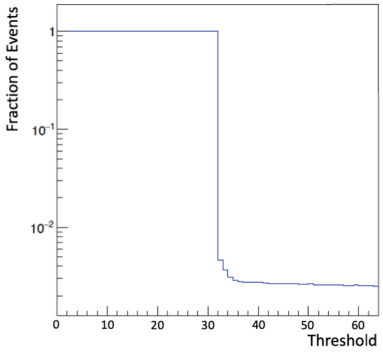

Figure 2.17: Threshold scan distribution.

operative voltage of 950 V, 1000 V, and 1050 V to analyse the variation of the MaPMTs gain with the voltage. The expected result is a shift of the working points to higher threshold values for increased voltage. Each scan starts at threshold 0 and ends at threshold 63. After several test, has been found that the best operational conditions can be obtained for zero attenuation and with the offset bit enable, in order to identify the pedestal for all the channels.

As will explained in the sec 3.1 the strategy adopted to obtain the working points consist into considering channel threshold five steps above the pedestal. In fig. 2.18 is shown the distribution of the threshold settings for the RICH2 channels, converted in absolute charge as determined through DAC scan for the RICH2 channels. From the quality assurance performed on the photo detectors is possible to compare the information related to the single photon peak (G) distribution of the anodes to the threshold setting at different HV. Being the standard deviation σ_G of the single photon distribution proportional to the gain as $\sigma_G \sim G/4$, these working points gives a good threshold efficiency.

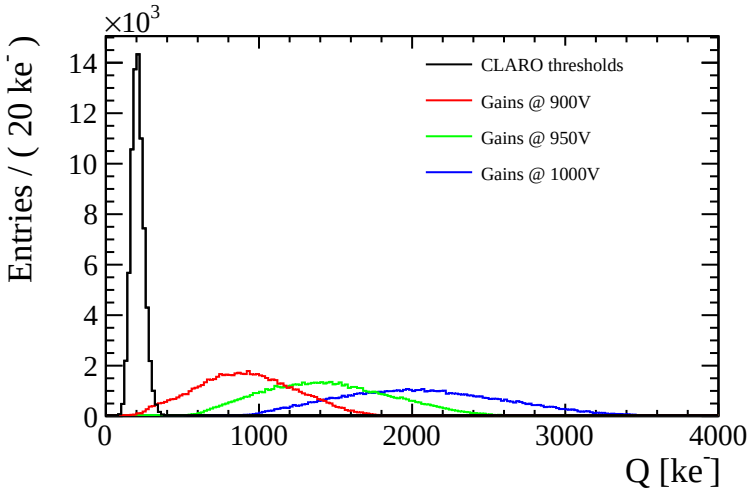

Figure 2.18: Distribution of RICH2 CLARO thresholds converted in absolute charge (black), with a mean of 207.58 ± 0.16 ke^- and a standard deviation of 39.64 ± 0.10 ke^-, reflecting the spread of the pedestals distribution. The threshold settings can be compared to the pixel gains at 900 V (red), 950 V (green) and 1000 V (blue).

Since they provide the integral pulse height spectrum, the threshold scans are also used to estimate the single-photon peak for each channel, thus allowing to implement the monitoring of gain variations with MaPMT ageing.

Other tests performed to characterise and calibrate the MaPMT are the so-called Dark Counts Rate (DCR) and the SIN test. The first is the measurement of the rate of events generated by spontaneous emission of electrons in total lack of light, given by the thermal emission from the photocathode. Given a MaPMT, the DCR at time interval Δt is defined as:

$$DCR = \frac{Number\ of\ events}{\Delta t}$$

The measurement of the DCR allows to identify the noisy anodes in the MaPMT and to verify the uniformity of the MaPMTs. The SIN test is performed to study a further source of MaPMT noise already introduced in sec. 2.1. In this test, the light signal is generated by a laser pulse. A typical spectrum for a pixel affected by SIN is shown in fig.2.19. The peak in the 100-125 ns

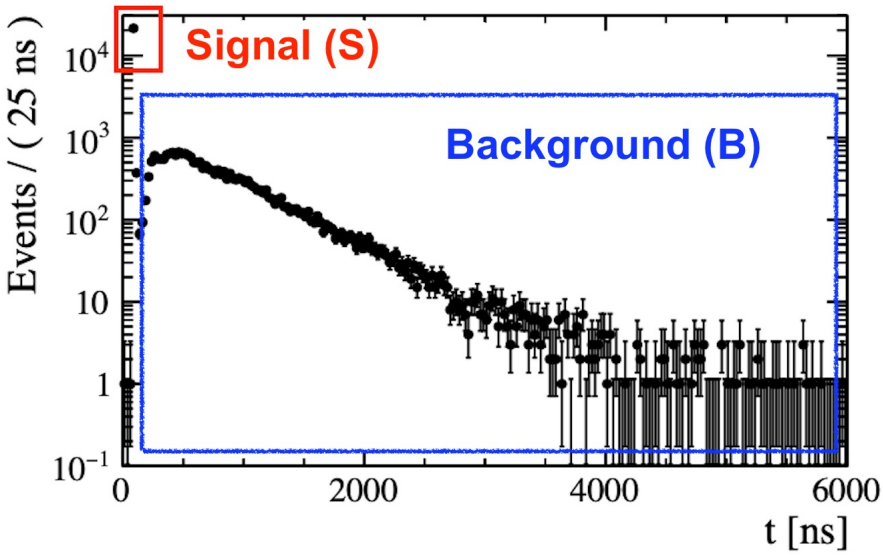

Figure 2.19: SIN spectrum: in red the Signal and in blue is unlighted the background contribution given by the SIN.

time slots is the primary laser signal, the negligible number of events on the left of the signal peak are dark counts, while the tail on the right, up to few μs is dominated by SIN pulses. These processes are due mostly to the ionisation of the residual gas inside the tube caused by the interaction with electrons, generating feed-back ion to the photocathode, or to other sources of signal-correlated noise such as light emission. Information related to the intensity of the SIN for each anode of the MaPMT can be retrieved by considering the SIN ratio, defined as

$$SIN_{ratio} = \frac{noise}{signal + noise}$$

or by computing the signal to noise ratio

$$S/Nratio = \frac{signal}{noise}.$$

In the next Chapter are explained the strategies to mitigate the SIN background.

2.9.1 Time alignment

The prompt Cherenkov radiation and focusing mirror optics lead to the nearly simultaneous time-of-arrival (ToA) of photons from a track in the RICH detector. This feature can be exploited to apply a time gate to the FE electronics excluding out-of-time background and accepting well-defined ToA photon signal. In fig. 2.20 is reported a simulation of the distribution of photon hit times in the RICH1 detector. Theoretically, the signal (S) last about 2 ns due to the spread of primary vertices in LHCb and state the minimal width for the FE time gate. Practically also the combination of CLARO jitter and time walk, the channel variations, the MaPMT transit time spread, and the digital sampling rate at the FE electronics have to be considered, thus the required time gate increase to 3.125 or 6.25 ns. In such scenario, the time gate excludes not only background from beam interactions but also sensor noise such as MaPMT SIN by a factor of 4 to 8, improving also the PID performances of the RICH pattern recognition algorithms.

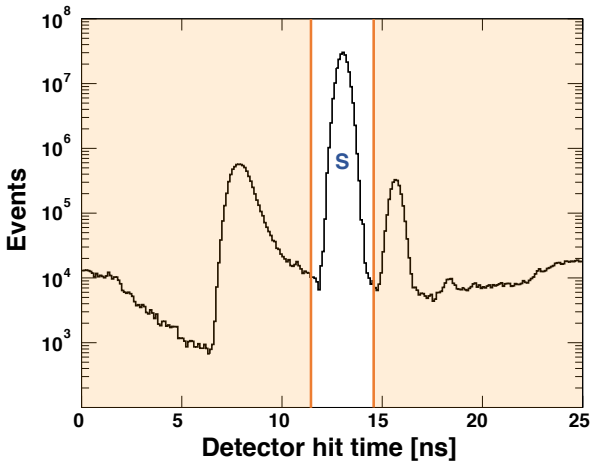

Figure 2.20: RICH1 simulated photon detector hit time distribution showing the signal (S) peak and possible time gate in the front-end electronics of 3.125 ns. On the left part of the signal peak there is the background mainly due to particles crossing directly the photon detector while on the right of the signal peak there's the contribution of the photons with additional reflection.

The time gate is applied using the FPGA mounted on the PDMDBs at a fixed latency with respect to the LHCb clock. The position of the time gate can be additionally fine-tuned with respect to the signal ToA in the RICH detector by adjusting the clock phases of the FPGA and the GBT.

2.10 Expected performances

The performances of the RICH detectors: MaPMT occupancy, PID-efficiency, and the single-photon resolution σ_θ as well its individual components (chromatic, emission point and pixel errors), are evaluated using the LHCb simulation framework within the `GAUSS` application monitoring. The simulation evaluates the MaPMT gain and noise, and the background sources exploiting the values acquired during the quality assurance procedures. Given the assumptions that a photon is emitted from a point along the particle path, at the middle of the radiator length, and that it hits the center of the relevant detector pixel, the Cherenkov angle θ_{C} can be reconstructed.The total Cherenkov angle resolution for a track $\Delta\theta_{\mathrm{C}}$ is given by

$$\Delta\theta_{\mathrm{C}} = \frac{\sigma_\theta}{\sqrt{N_{\mathrm{ph}}}} \oplus C_{\mathrm{tracking}}, \tag{2.1}$$

where N_{ph} denotes the photon yield, the σ_θ is the θ_{C} resolution, the constant factor C_{tracking} corresponds to the tracking resolution, and the $\oplus$ symbol indicates that the two terms are added in quadrature.

For the purposes of the evaluation of the expected RICH performance C_{tracking} is assumed to be equal 0.35 mrad.

2.10.1 Simulation setup and typical output

The simulated data is obtained within a standard Run 3 configuration, corresponding to $\mathcal{L} = 2 \times 10^{33} cm^{-2} sec^{-1}$, using a sample of 10000 $B_s \rightarrow \phi\phi$ decays as typical signal events. The PID performance, after the application of the reconstruction algorithms, is reported for tracks in the LHCb acceptance, with the momentum range of about 2-100 GeV and a transverse momentum larger than 0.5GeV/c. The PID procedure uses, as input, the reconstructed charged tracks from tracking detectors and the digitised RICH hits. Then, Cherenkov photons are generated and their trajectories are traced through the RICH system onto the MaPMT planes. These signals are compared with the `GEANT4` generated photon hits and a likelihood function of the event is generated. This process is performed for all the mass hypotheses and the largest global likelihood is finally selected. The average MaPMT quantum efficiency curve, used as nominal value in the simulation, is shown in fig. 2.21, together with a typical PID performance curve, representing the probability to mistag a pion as a kaon versus the probability to correctly identify the particle as a kaon. The expected occupancy is determined after the digitisation step, implemented through the `BOOLE` application, as a function of the MaPMT identifier and it is reported in fig. 2.22.

Performance study

The increased QE of the MaPMTs leads to an increased photon yield. In particular, to evaluate the photon yield (${N_{\mathrm{ph}}}^{\mathrm{optimal}}$) and the Cherenkov angle resolution has been used a particle gun setup. The particle gun has been configured with 80GeV muons in order to ensure

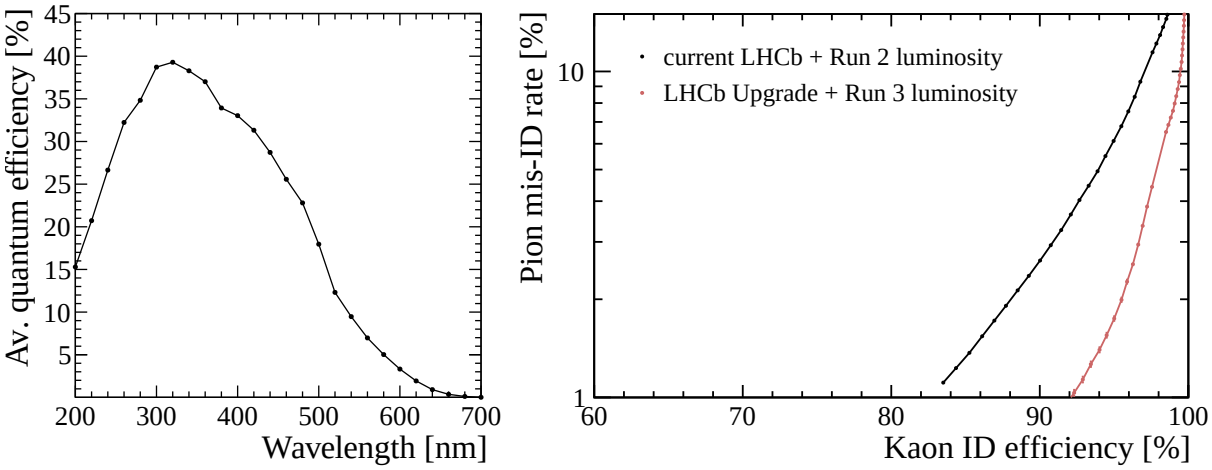

Figure 2.21: (Left) Average quantum efficiency of the MaPMTs used at RICH and (Right)a typical PID performance of the kaon identification obtained from the LHCb software for the configuration described in the text (red). A corresponding curve for the Run 2 conditions (prepared using the simulation with the current LHCb geometry and Run 2 luminosity as reported in Ref. [33]) is shown for a reference (black).

that the tracks are fully saturated and to minimise the uncertainty arising from the tracking system. Moreover, has been implemented the request that the acceptance region where the RICH performance is expected is optimal: *i.e.* the polar angle of the tracks is required to be in the range between 90-180 mrad and 40-90 mrad for RICH1 and RICH2, respectively.

The results are consistent with the signal events with the same requirements on the quality of the tracks corresponding to the ones arising from the particle guns configuration. In table 2.2 are summarised the results and also the typical photon yield ($N_{\mathrm{ph}}{}^{\mathrm{typical}}$) in the signal events, without the track quality requirements, are reported. The typical photon yield values are lower than the optimal ones, mainly due to the limitations in the acceptance due to the beam pipe region.

Table 2.2: Simulated performance of the LHC Run 3 RICH detectors. For RICH2, the values are given for the inner detector regions populated with the R13742 MaPMTs.

	Photon yield		**Cherenkov angle resolution** [$mrad$]				
	$N_{\mathrm{ph}}{}^{\mathrm{optimal}}$	$N_{\mathrm{ph}}{}^{\mathrm{typical}}$	chromatic	emission point	pixel	σ_θ	$\Delta\theta_{\mathrm{C}}$
RICH1	63	59	0.52	0.36	0.50	0.81	0.36
RICH2	34	30	0.34	0.32	0.22	0.52	0.36

The dominant contribution to the total Cherenkov angle resolution per track is due to the tracking uncertainty C_{tracking} assumed to be equal 0.35 mrad, according to the initial assumption and by using the Eq. 2.1.

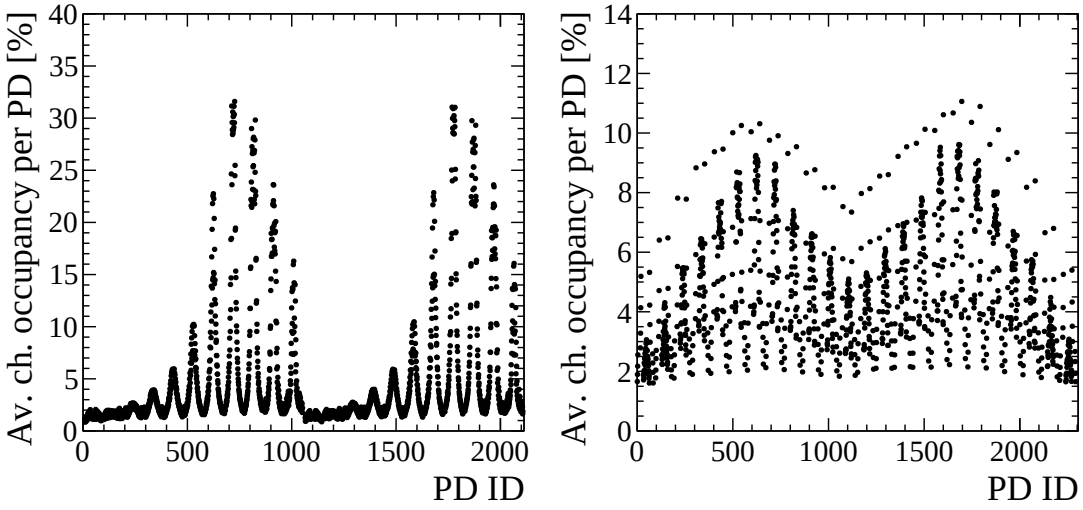

Figure 2.22: (Left) Average detected occupancy per channel for different MaPMTs in the RICH1 and (Right) RICH2 detector. In the axis the PD label indicate the Photo Detector. The values are obtained using the LHCb simulation.

Chapter 3

The LHCb RICH Upgrade: test and commissioning

In this Chapter are described the tests performed on the upgraded detector, in particular, the Quality Assurance test, performed on the ECs in Ferrara, sec. 3.1, the strategies implemented to mitigate the SIN effect, and the RICH commissioning executed in the ComLab at CERN and in the LHCb cavern, sec 3.3. The contents of this chapter related to the ECQA procedures and SIN studies, follow and complete the previous works [28, 30].

3.1 Quality Assurance tests

The Ferrara LHCb Group has been responsible for the quality assurance procedure of the CLARO, of the FEBs production, and, together with the Edinburgh group, of the ECs quality assurance (ECQA). The ECQA procedure required the shipment of all the components to Ferrara and Edinburgh: MaPMTs, metal chassis, FEBs, Backboards, and Baseboards. ECs which successfully passed the QA tests were encapsulated in jars designed on purpose to prevent any damage and then shipped to CERN.

3.1.1 EC assembling

Each EC has been assembled following a well-established procedure. The R-type EC are made up of:

- 4 R13742 MaPMTs
- 1 baseboard
- 4 FEBs
- 1 backboard

while the H-type:

- 1 R13743

- 1 baseboard
- 2 FEBs
- 1 backboard

Both types are assembled in an aluminium case made up of 4 pieces. In fig. 3.1 the components of both types ECs are shown. After the assembling the each EC is introduced in a test station to be tested.

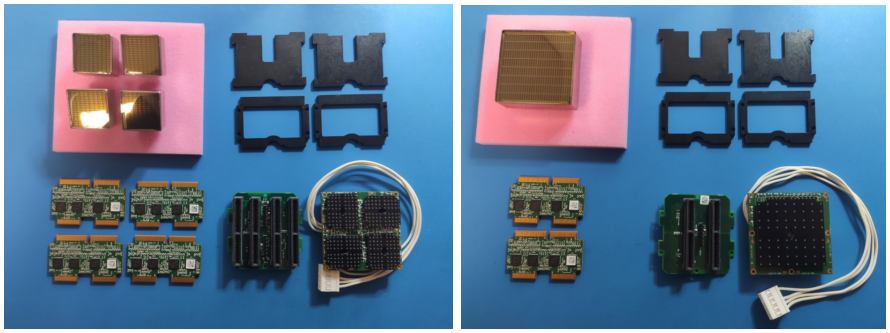

Figure 3.1: Components required to fully assemble of (Left) R-type and (Right) H-type EC.

3.1.2 Test station

The test stations are four: two in Ferrara (Station ID 1 and 2), and two in Edinburgh (Station ID 3 and 4). Each of them is made up of a dark box, a system controller, a Low Voltage power supply, a LED driver, and an HV crate, as shown in fig.3.2. The dark box hosts up to four ECs,

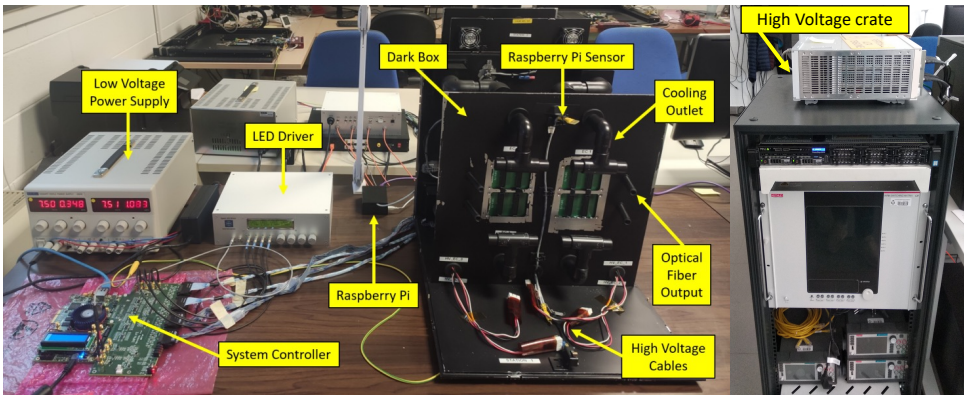

Figure 3.2: The Station 1 test setup present in Ferrara.

in a completely dark environment since the MaPMTs are switched on during the test procedure. The ECs are then connected to four Digital Boards (DBs) with the system controller through eight Universal Asynchronous Receiver/Transmitter (UART) which are physical circuits able to transmit and receive serial data. In particular, each DB is equipped with two UART, one per FPGA. Thanks to the LED driver placed outside the box it is possible to inject, in a controlled way, the light in the box. The box is also instrumented with four optical fibers which are

connected to the LED driver and a mirror to reflect the light on the phototubes. The MaPMTs are connected to the HV crate ISEG ECH 2425, and to the cooling system consisting of a fan system providing a continued airflow. The DBs and the cooling system are powered by the LV power supply, Aim TTi EX354RT8, placed outside the box. The values of temperature and humidity are monitored by a Raspberry Pi system. The entire system is controlled by CENTOS7 OS PC running a DAQ control software designed in 64-bit National Instrument LabVIEW.

To be able to identify each component during the tests, a numbering scheme for the ECQA setup is used (fig. 3.3), according to which the ECs are numbered clockwise from 0 to 3 starting from the top-left. The UART are numerated from 0 to 7 and each of them is connected to two FEBs. The FEBs are referred to as 0 or 1 and their order is inverted for UART connectors rotated of 180° with respect to the others. During the test, each set of ECs placed in the box have been referred to as "Load" to which has been associated a load number. For each station, each load number consists of sequential four-digits, and together with the type of the EC is used to identify the folder where are stored all the data collected during the QA tests, e.g. Load_0010_H_S2 is the folder for the Load Number 0010 of H-type EC tested on the station 2. To distinguish the ECs, once mounted in the box, a numbering is needed: the reference system adopted numbers the ECs from 0 to 3 as shown in fig. 3.3. In case of ECs R-Type the MaPMTs are identified from A to D or from 0 to 3 starting from the top-left and going clockwise. Also

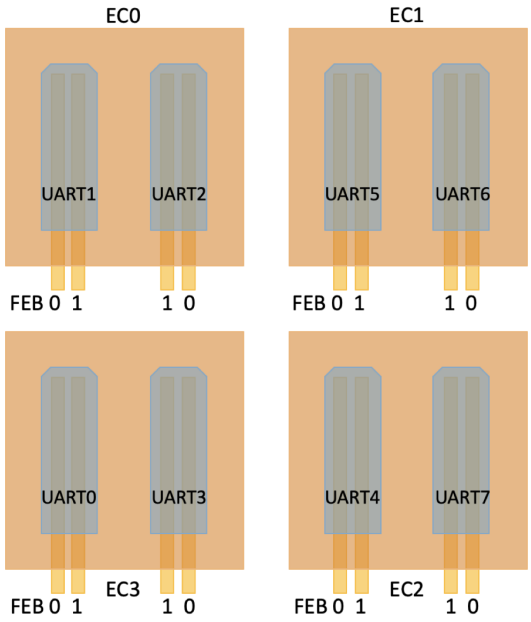

Figure 3.3: Numbering scheme for the ECQA components.

the CLAROs on the FEBs follow a specific numbering scheme that is shown in fig. 3.4. For each Load is essential to store the information related to the QR_Codes which identify the single pieces used to assemble the ECs and the tests response. The QR_Codes folder is created during the assembling procedure, for each one is reported date, time location, operator, Baseboard, FEBs, and Backboard QR codes, Load Number, Station ID, EC position, and eventually, the

QR codes of the MaPMTs. Whereas in the PDF folder are stored all the results of the tests.

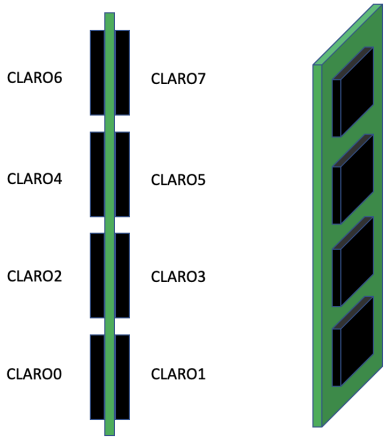

Figure 3.4: Frontal and perspective view of a FEB with CLAROs and their numbering convention.

3.1.3 DAQ software

The core of the DAQ control software is given by low-level python functions performing strictly defined commands. Those python functions are in communication with the the system controller and the DB which execute the commands. The upper hierarchy level is, instead, provided in the LabVIEW environment by a graphical user interface (GUI) in which each python function corresponds to a Virtual Instrument (VI). The first raw version of the DAQ control software has been developed using standalone functions to perform the single quality assurance test on the ECs such as: reading of the ADC channels, S-curve tests, Threshold Scan, SIN and Dark Count Rate measurements. When the connection with the DB is established, the user can set the Load Number, the EC Type and the Station ID. Each VI is able to operate according to the information stored into a configuration file which depends from the input given by the user. The final version of the DAQ has been totally automatised, each step of the test protocol is indicated in the control panel with a tab in which are also shown possible error massages arising during the tests. The user can decide to run the Machine in a *MANUAL* mode, selecting each step one by one using the "MAIN CONTROL" options and confirming the passage from a test to another by pressing the button "CONFIRM STEP" or in *AUTO* mode. When running in AUTO mode are executed all the steps selected by the user in a dedicated panel before to start the test. On the main panel are also displayed the values of temperature and humidity monitored by the two sensors placed in the box. Also the state of the HV system is checked together with the connection to the system controller and the ISEG crate.

3.1.4 ECQA Test protocol

Once assembled, the ECs without the MaPMTs are inserted in the dark box, then the control software enables the connection between each ECs and the PC and power on the CLAROs. To

retrieve in any moment information related to the ECs and the FE electronics, a mapping with the correct association of a CLARO channel to the MaPMT is required. Two mapping files are provided: one for the R-type ECs and one for the H-Type ECs. Each mapping file consist of a header line in which the following values are stored: the channel ID (UART FEB CHIP CHANNEL), its anode (1-64), its MaPMT (A-D), and its EC (0-3). For the H-type Load since only one MaPMT is used there is no need to report the MaPMT column. The tests performed are:

- S-Curve Comm Check: this test is performed to check if there are communication problems with the CLARO. It's a fast DAC scan read by a dedicated `C++` script which verifies that the counts at low signal intensity are less than 5, and the high signal intensity are more than 950, while sending 1000 pulses per DAC step. This check is able to detect oscillations in the distribution given by noisy channels which count more than 1000 counts or dead ones which counts always 0. If it is one of these cases, a text error is generated, the EC is dismounted from the box and the connectors are cleaned using compressed air and the test is repeated. If the problem persists the FEB is replaced and sent back to the FEB quality assurance to be tested.

- Power-cycle, Singe Event Upset and reading of the ADC channels: the first two parts consist of a reset of the CLARO chips and correspond to a first reading of the FPGAs ADC channels. The read out and the ADC channel values are written in a file, called LV_noconfig.txt. The CLARO are configured and the related file, LV_conf.txt, it's written.

- HV measurement (without MaPMTs): this step is performed switching on the HV at 1000V. Once the current is stable, typically after one minute, the backboards currents are measured and registered, together with the voltages od the HV, into a HV_nopmt.txt file. Then the HV is switched off.

- MaPMTs mounting and S-Curve Comm Check: at this point the MaPMTs are mounted in the ECs and their QR codes scanned. To check there are no issues due to the interaction of the MaPMTs with the CLAROs, an S-Curve Comm Check is performed. If the test is successful, the dark box is finally closed otherwise the problem has to be investigated in the way mentioned before.

- HV measurement with MaPMTs: measurement with the HV switched on at 1000 V. All the average values of the currents for the HV channels, monitored in 1 minute time window, and the HV tensions are written in the HV_pmt.txt file. The procedure is repeated also at 1050 V and the related values of the Backborards currents are used to set the the HV current limits in the next test. The measurement ends with the switching off of the HV.

- S-Curve test: a DAC scan performed on all the CLAROs (range 0-725 mV, step 1.2 mV) using six different configurations: Offset bit 0 with threshold 10, 20 or 30, and Offset bit 1 with threshold 42, 52, and 62 with all the channels enabled. The data are acquired and then processed through a `PYTHON` script to find the transition point for each channel. In

case a channel doesn't exhibit a transition point, an error message is generated without blocking the procedure, only at the end of the test the operator can check the data and decide if the corresponding EC should be put aside or not. The script produces six pdf files corresponding to each configuration, two overview histograms representing the transition point and the noise distributions for all the channels of the load, and a txt file, in which all the transition points and the spreads are reported. In fig. 3.5 the transition point and the noise distributions are shown for a given configuration. Furthermore, in this step

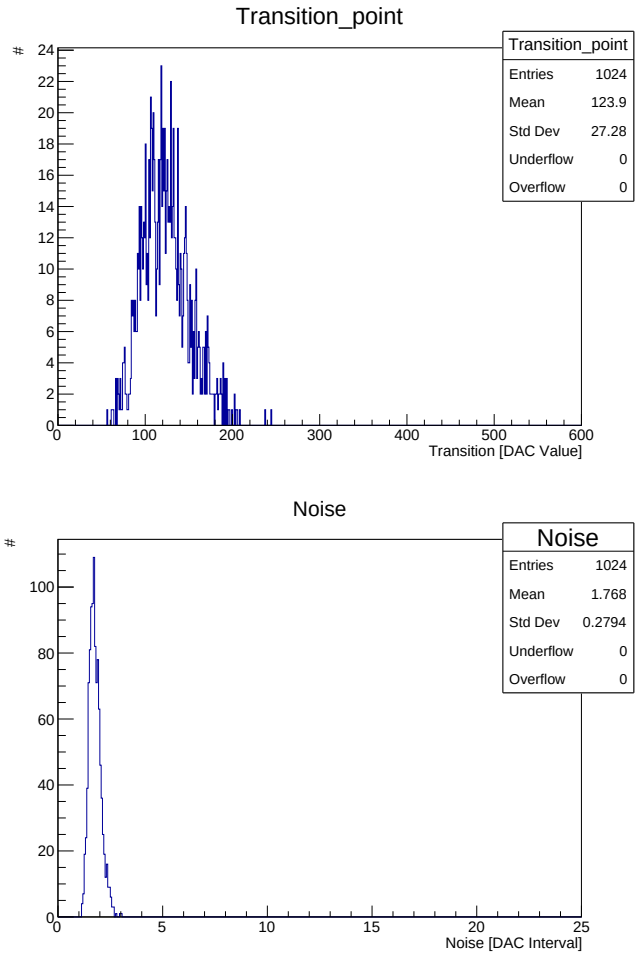

Figure 3.5: Transition point and noise distributions for a full 4 ECs load R-type. On the y-axis is shown the number of channels.

is performed a linear fit to the distribution of the channel transition point at different threshold to extract the slope and the intercept. The first representing the number of ke^- per threshold step, gain of the channel, the latter being the channel offset in ke^-.

- 1050 V stand-by: this stage is the most time consuming since it requires 10 hours. During this time the ECs are left with HV set at 1050 V in order to reduce the electronic noise.

- Threshold Scan test: after the 1050 V stand-by, the HV is set at 1000 V and the threshold scan test is performed. The configurations used are two: all the channels enabled with

offset bit 0 and then with offset bit 1. The pulses sent from the LED driver are 100 k at 100 kHz per threshold step. In case of Offset bit 1, the final working point is obtained by adding five threshold steps to the pedestal value. To check that the threshold has been found in all the channels, an error overview PDF containing 2D histograms 8×8, fig. 3.6 is generated for each MaPMT of the load. This test also produce a 2D histogram for

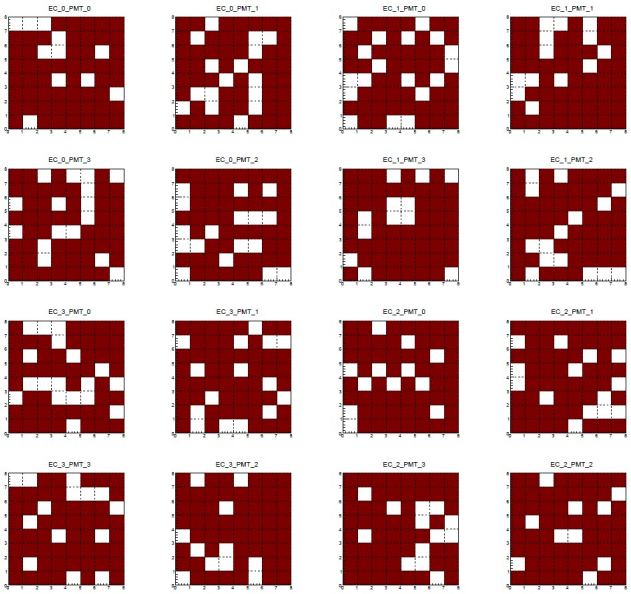

Figure 3.6: 2D histogram error overview for a threshold scan test. This test was performed with the CLAROs Offset bit at 0, therefore most of the channels do not exhibit the pedestal and are marked as defective in this plot.

each MaPMT reporting the found working point per channel as shown in Fig: 3.7. While in fig. 3.8 is reported the single channel Threshold Scan distribution. At the end of the procedure a text file is written reporting for each channel the threshold with Offset bit 1 and with Offset bit 0. A dedicated algorithm has been implemented to calculate the threshold in case of Offset bit 0 since the pedestal, in this condition, is not always visible. The algorithm compares the threshold scan distributions at Offset bit 0 in the range [1,20], and Offset bit 1 in the range [19,42] searching for the threshold value at which the two distributions better overlap. The bin content in the Offset bit 1 distribution, C_1, is compared to the bin content C_0, in the Offset bit 0 distribution, using the formula:

$$\sum_{k=1}^{20} \frac{(C_1 - C_0)^2}{C_1}. \tag{3.1}$$

The values obtained are used to fill an histogram defined in the range[19,42] as shown in fig. 3.9. The threshold corresponding to the minimum of the histogram represents the threshold shift operated by the Offset bit. The test confirm the reliability of the setting with Offset bit 1 with zero attenuation, choosing the WP 5 steps above the pedestal.

- Dark Count Rate measurement: the aim of this test is to measure the rate of counts

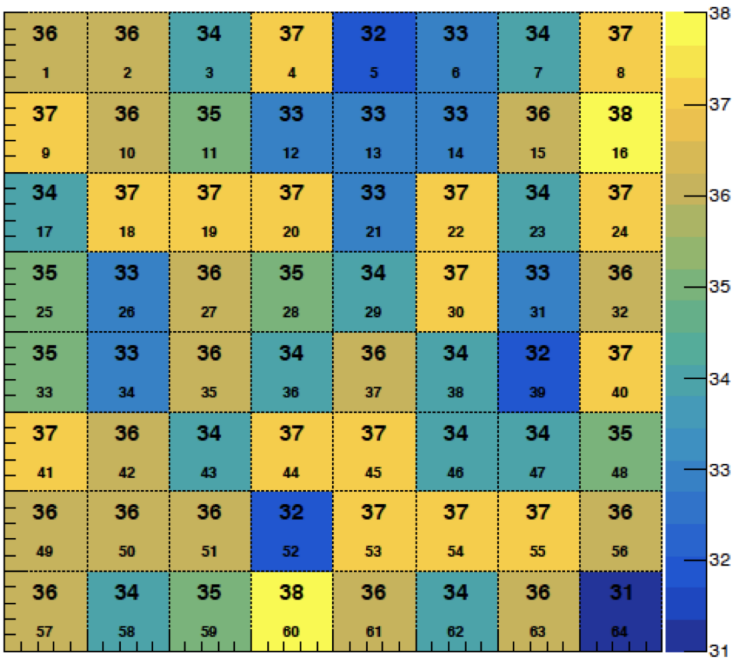

Figure 3.7: 2D histogram showing the found working points for all the channels of the MaPMT 2 (C) of the EC 2, the one placed in the bottom-right position in the dark box.

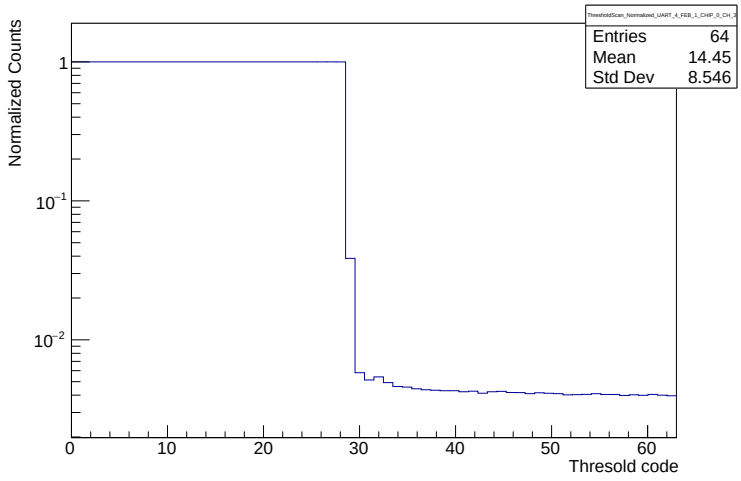

Figure 3.8: Typical Threshold Scan distribution for the CLARO channels in the ECQA procedure. In this case it is shown the 3 channel associated to the CHIP 0 FEB 1 UART 4.

without any light source on the MaPMTs. The test is performed setting the HV at 1000 V and proceeds in two steps. At the beginning the CLAROs are configured with threshold 7 and the DCR is measured in a 100s time window, then a second DCR measurement is performed after loading the optimised threshold in the CLAROs register in the same 100 s time window. The output of the test is processed by a `C++` script which produces 2D histogram plots with the DCR of the MaPMTs to give an overview the uniformity of the DCR for all the MaPMTs and to check that the DCR does not exceed 1 kHz per channel.

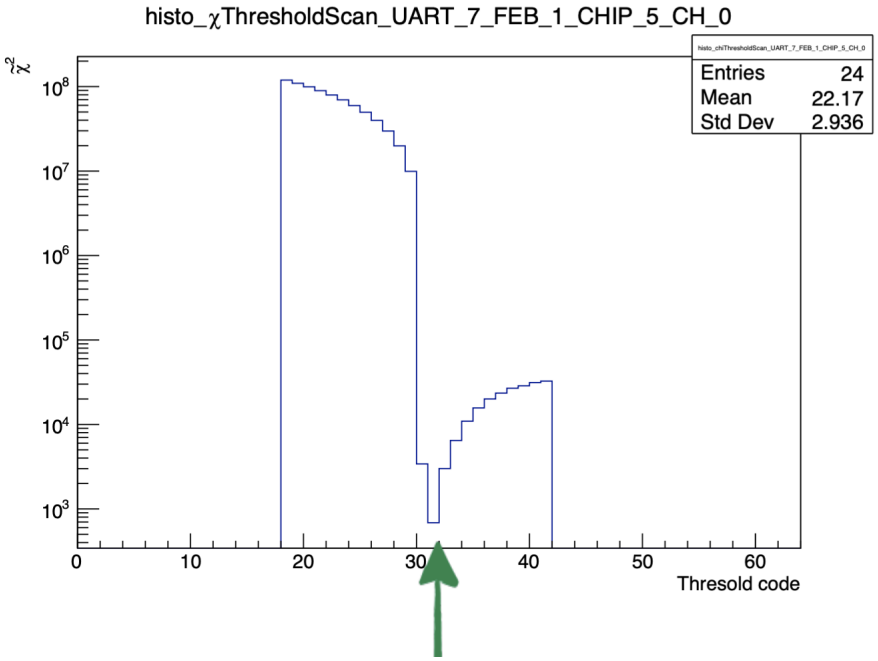

Figure 3.9: Distribution of the values found with the Threshold scan search algorithm for threshold code values in range [19,42]. For this channel, the minimum is found at threshold code 32 meaning that the shift operate by the Offset bit is 32.

- SIN test: eventually the SIN test is performed at 1000 V, 950 V, 900 V and 850 V configuring the CLAROs channel at their optimal thresholds. The relative analysis is performed by a `C++` script which produces the PDF plots containing the MaPMTs 2D histograms and the SIN spectrum for each channel.

The complete test last 12 hours and the final output is a log file which can be checked by the user together with the plots corresponding to each testing step. When the test is successful, the main parameters (EC barcode, data, time, place of test, station ID, EC position in the Load, Load number, EC components, the result of each test performed, ..) are loaded in the LHCb database to be used in the commissioning and the ECs are placed in a plastic jar before being shipped to CERN.

3.2 Mitigation strategies for the SIN

The ECQA provided plenty of data to study with high statistics the SIN background. In particular, here some of the results which are subject of the paper in ref. [30] are reported, as well as the strategies applied to mitigate the effects of such background. The figure of merit considered to asses the effect of SIN on a pixel is the ratio $\mu^p_{SIN} = B_p/S_p$ representing the mean number of SIN pulses for the pixel p under study. This value has been found to be different from a pixel to another one on the same MaPMT, and for the same pixel when considering two different MaPMTs. However, a common pattern of pixels affected by SIN is found: in the figs. 3.10 are shown the time-spectra for four different pixels of the same MaPMT and the map

of the mean number of SIN pulses for all the pixels of tube. From the time-spectra distribution shows that the pixel 28 is not affected by SIN, since the events after the signal are consistent with dark counts (which are of the order of kHz). The other three pixels, instead, show effect of SIN, with different intensities depending on the pixel position within the MaPMT. Whereas, considering the global map related to the pixels on the MaPMT, fig. 3.10 (Right), it is possible to visualise that the SIN effect is essentially concentrated in the top and bottom rows of the MaPMT. The computation of the same map for all the MaPMTs available revealed that the localisation described above is a general feature of SIN even if the absolute value of the figure of merit is not the same since it may differ between different units as reported in table 3.1. The

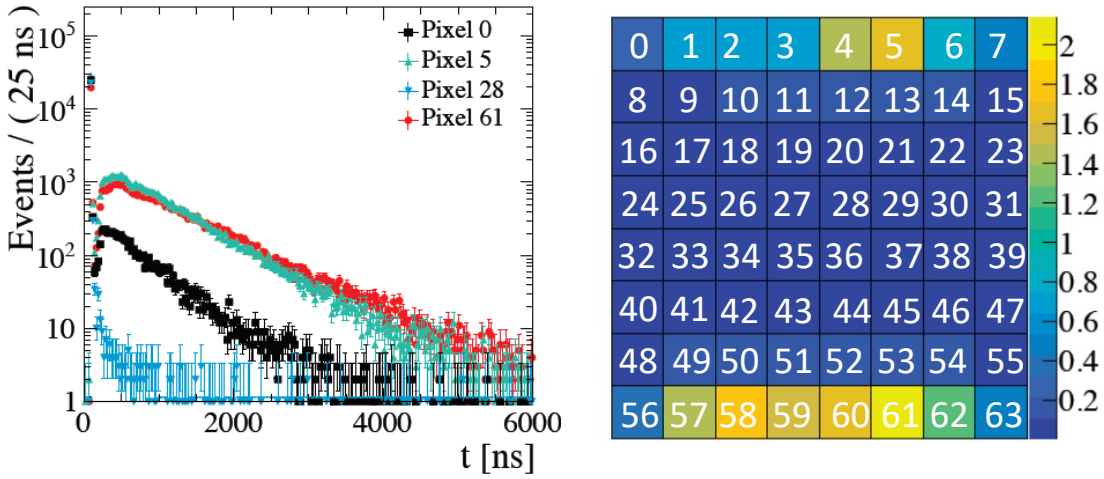

Figure 3.10: (Left) time-spectra in logarithmic vertical scale for four pixels of the same tube. (Right) Map of the mean number of SIN pulses for all the pixels of the tube. The numbering scheme of the pixels foresees that the pixel-0 is top-left, the pixel-7 is the one top right and pixel-63 is bottom-right.

Table 3.1: Mean number of SIN pulses estimated for four pixels on four MaPMTs using the numbering scheme adopted in the 3.10.

MaPMT	μ^0_{SIN}	μ^0_{SIN}	μ^{28}_{SIN}	μ^{61}_{SIN}
FB4439	0.2457 ± 0.0035	1.695 ± 0.013	0.0109 ± 0.0007	2.139 ± 0.018
FB2294	0.0745 ± 0.0012	0.3715 ± 0.0029	0.0076 ± 0.0004	0.491 ± 0.003
FB2312	0.132 ± 0.0017	0.747 ± 0.004	0.0081 ± 0.0004	2.231 ± 0.011
FB4500	0.266 ± 0.004	1.398 ± 0.012	0.0103 ± 0.0007	1.034 ± 0.010

figure of merit has been also used to search for correlations with parameters such as gain and dark count rate. As shown in fig. 3.11, the values related to the pixel 61 of 1400 MaPMTs exhibit no clear correlation with respect to the pixel gain and the mean number of SIN, except a weak increment when considering lower high-voltages. Other tests performed have shown no effect of the SIN on the MaPMT properties and ageing effects. Since this effect has been addressed also to internal light emission due to MaPMT mechanical structure, a new series of MaPMT has been produced by Hamamatsu to reduce the contribution from SIN pulses. The change of the internal mechanical design together with the application of mitigation strategies like the use of an

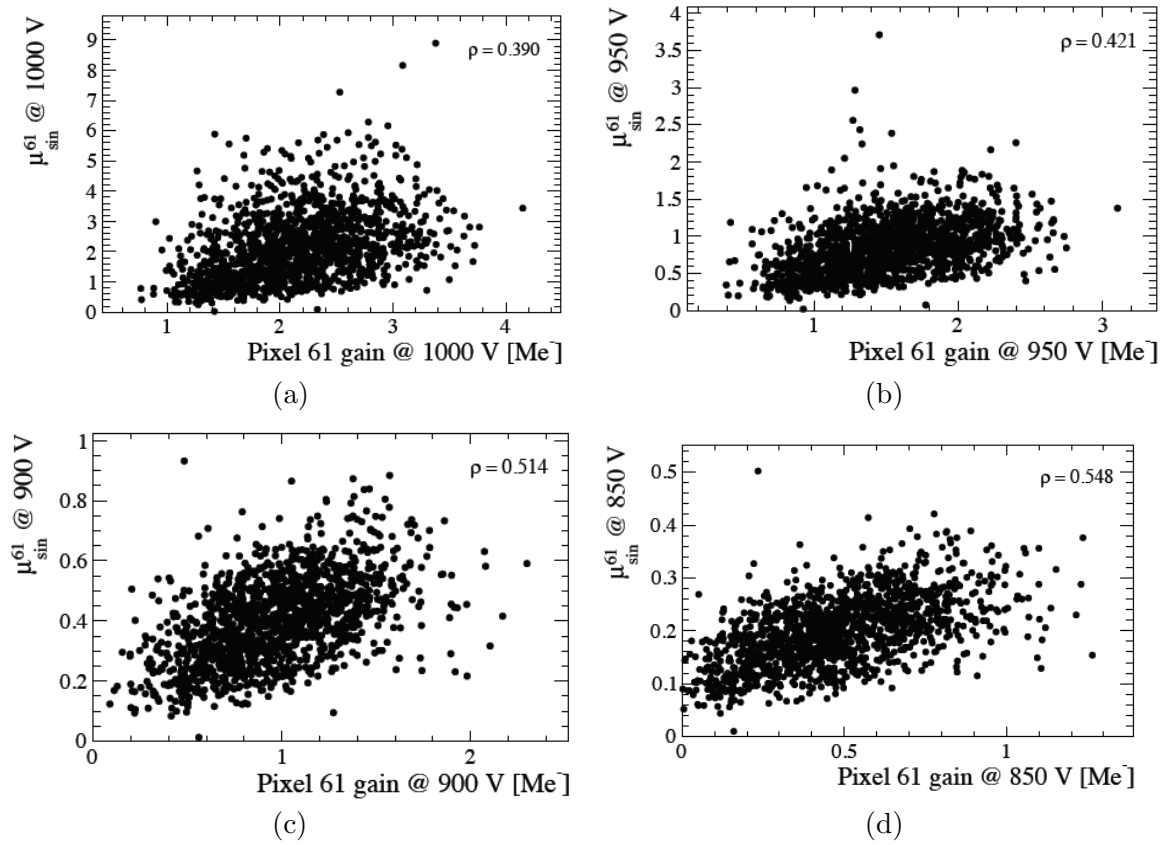

Figure 3.11: Correlation between the pixel gain at (a) 1000 V, (b) 950 V, (c) 900 V and (d) 850 V and the mean number of SIN events at the corresponding HV.

appropriate high-voltage operating point, and the implementation of a nanosecond timegate in the digital board firmware (as discussed in subsec. 2.9.1) will enable excellent PID performances. In fig. 3.12 the comparison of the PID performance obtained considering three different scenarios (the nominal simulation including SIN, the optimised scenario obtained applying the mitigation strategies and the nominal configuration without simulating the SIN effect) is reported. The expected performances have been evaluated by means of full simulation studies deeply described in the [30].

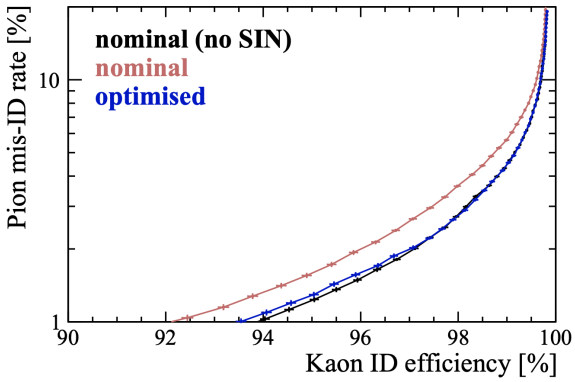

Figure 3.12: Probability to misidentify a pion as a kaon in function of the efficiency of identifying a kaon. In red the nominal scenario, in blue the optimised one obtained by considering the mitigation strategies and in black the nominal scenario obtained without considering the SIN contribution.

3.3 RICH commissioning

Once the components have passed all the quality assurance tests, the last steps, before their installation at the LHCb site, are the column assembling and the commissioning which are performed at the ComLab in Meyrin.

3.3.1 Column assembling

The column assembling follows a well defined procedure stated by the RICH group:

- mounting of the mechanics and the copper brade for the safety ground connection on the Tbar;
- LV and HV cabling;
- mounting of the fibers cassettes and fibers cabling;
- installation of the PDMDBs, already equipped with thermal pads and levelling plate;
- placement of the ECs.

Once is ready the column is stored in the cabinets (see fig. 3.13) till the moment of the commissioning.

Figure 3.13: Cabinets with (Left) RICH1 and (Right) RICH2 columns.

3.3.2 Test station

The tests take place into the test station which consist of a dark box, called Small Simple Box (SSB), fig. 3.14. The SSB is connected to LV, HV, Cooling System services, and a Laser. Four machines are used for: the user operations, the WinCC projects, the GBT servers, and the storing of the data acquired.

3.3.3 Commissioning Test protocol

Before installing a column in the SSB the QR codes of the PDMDBs mounted on it have to be scanned. The data are saved in a file named "PDMDBs.txt" placed in the "/data/RICH1/COL_xx" folder on the pc running the WinCC projects. Then, using a MiniDAQ it is possible to open the panel of the Finite State Machine, the TOP FSM panel, in fig.3.15, select in the ComLab panel (fig. 3.16) the ID of the column, and upload the gain calibration values from the SCA-ADC of each PDMDBs.

After this operation the column is installed in the SSB, the cooling pipes are connected, and the cooling rack is switched on. To verify that the cooling is working properly the values of the

Figure 3.14: Dark box used for the commissioning tests.

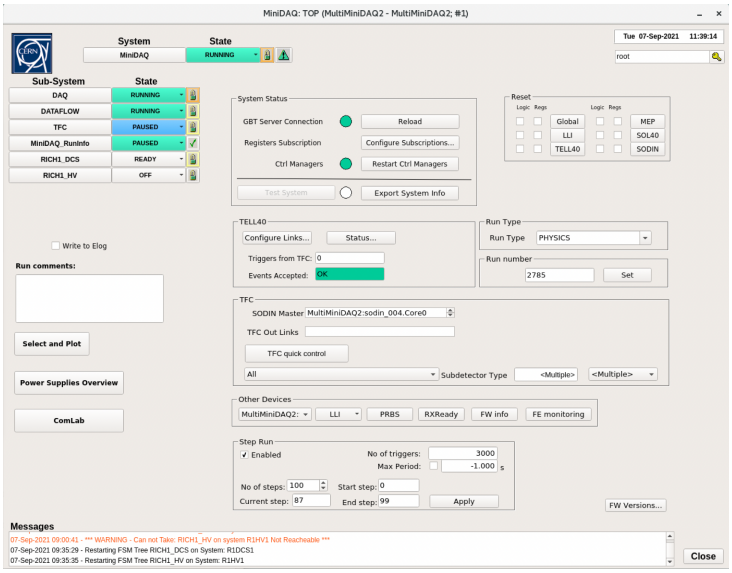

Figure 3.15: Top FSM panel.

pressure in the cooling rack and the values read by the "TESTO" temperature sensor through the "Select and Plot" tool present in the FSM panel can be checked. Then the startup checks, which foresees the switching on of the Low Voltage, can be executed. This operation is ruled by the RICH1_DCS partition on the top FSM panel. If everything is working properly, the LV and the current values should be around 8 V and 6 A, respectively. Otherwise there could be a short in one of the PDMDBs and it is necessary check the MARATON voltage, the LV plug and/or unplug the LV from the PDMDBs. After the LV switching on all the SOL40 links by using a

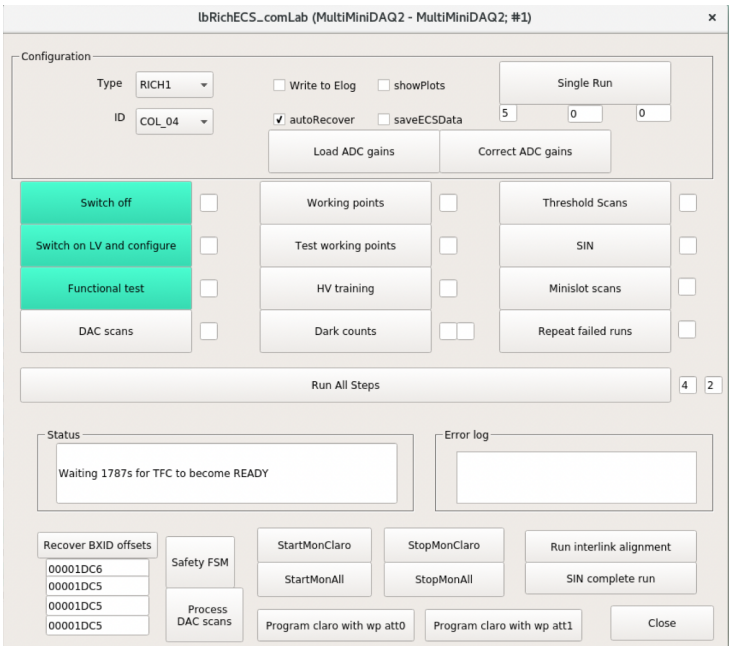

Figure 3.16: ComLab panel.

dedicate panel are checked, as shown in fig 3.17. If each link doesn't show a green light a power cycle is needed or a cleaning of the TFC fibers interested with an apposite tool. At this point

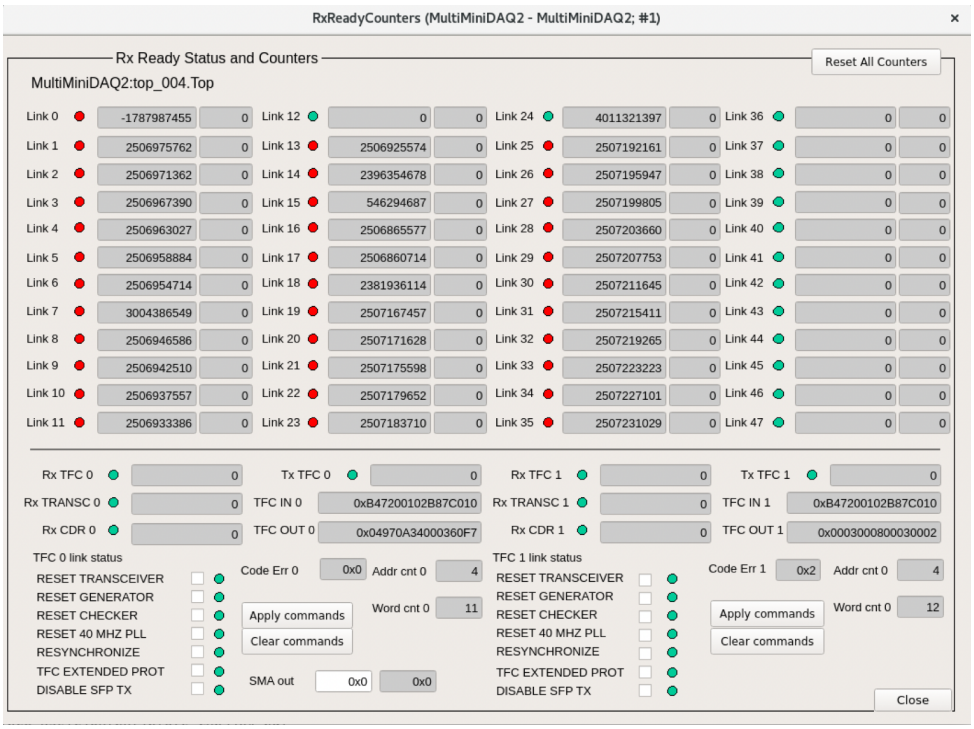

Figure 3.17: SOL40 RxReady. The SOL40 links are numbered from 36 to 47.

the configuration of the PDMDBs is performed by the sending the "CONFIGURE" command from the MiniDAQ partition on the topFSM panel. The configuration foresees the initialisation

and the configuration of the GBTs, FPGAs and of the CLAROs. When all the PDMDBs reach the state "READY" and the total current is around 12-13 A per channel, it is possible to go to the next step. From the top FSM panel all the links TFC and data can be checked as done for the SOL40 links. In the fig. 3.18 the panel related to the TELL40 UP(top_010) is shown, the TELL40 Down (top_018) is similar. If the Received Signal Strength Indicator (RSSI) values, see

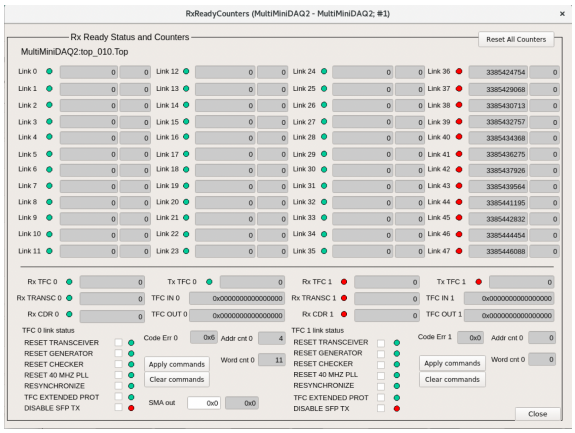

Figure 3.18: TELL40 RxReady, panel related to the TELL40 UP(top_010).

fig.3.19, are below -6 dBm it is required to check that the ECS/TFC fibers are well plugged and clean them with the appropriate tool.

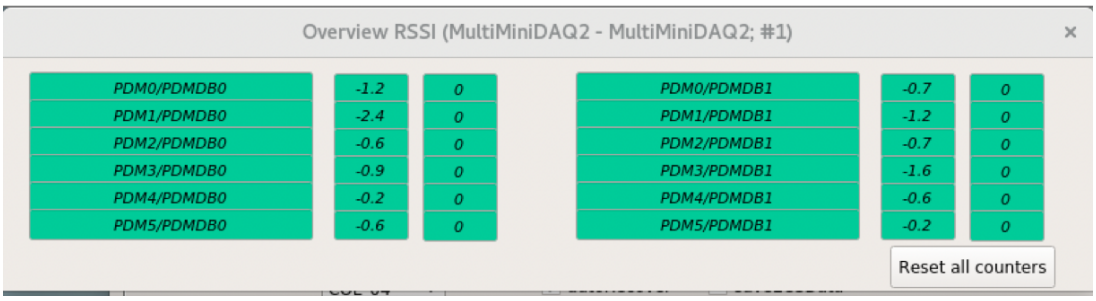

Figure 3.19: RSSI overview.

From the "Power Supplies Overview" tool it is possible to control the temperature of all the sensors which should be around 18.0/19.0 °C, only the SCA sensor should give a temperature around 32 °C. If it is not the case it means that the ADC gain calibration value is not present in the database with all the QA values, and therefore is set to one by default. In this case the value is changed and the database updated by clicking on the "Correct ADC" gains button and saving. The power link is then checked by a dedicated shell command executed on the server hosting the SOL40 and TELL40 cards and running the GBT servers.

Functional test

Once the validation procedure is completed the functional tests can be performed. Such tests foresees four short run to verify the FE configuration, EC assembly and the conditions after the

shipment from the ECQA facilities to CERN. The sequence with the CLAROs are programmed is the following:

1. Threshold=10, Offset=0, Attenuation=0, testPulseDisable=1, HV=0 V; to check that all the channels are OFF;

2. Threshold=10, Offset=1, Attenuation=0, testPulseDisable=1, HV=0 V; to check that all the channels are ON;

3. Threshold=10, Offset=0, Attenuation=0, testPulseDisable=0, HV=0 V . This run is used to perform the automated interlink time alignment and the centering of the BXID offset in the acquisition window;

4. Threshold=10, Offset=0, Attenuation=0, testPulseDisable=1, HV =1000 V to check that all the channels are counting.

The expected hitmap of the steps (1-3-4, being the output of the 2 equal to the 3) for the MaPMT placed top left in the column (PDM0 EC1 PMT0), are shown in fig. 3.20. Such output is provided for all the ECs and PMTs. If one of the above functional tests fails, the procedure

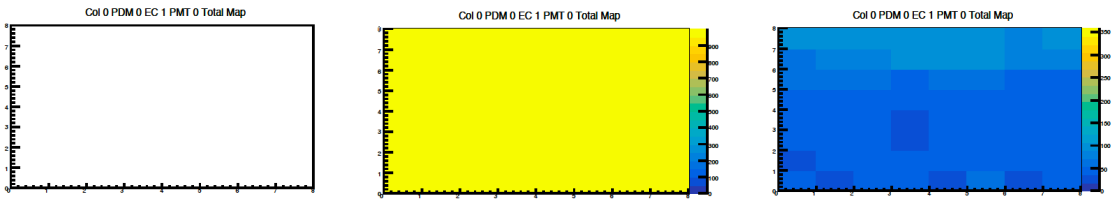

Figure 3.20: Total hitmap of the MaPMT placed on the top left of the column in case of (Left) all channels off; (Center) channels on and test pulse enabled; (Right) channels on with HV on.

is interrupted, and, depending on which step failed, the PDMDB firmware needs to be reloaded and/or the EC needs to be unplugged and plugged again to check both the connectivity of the PDMDB with the EC and the EC itself.

Automated test

Once the functional test have resulted successful it's possible to start the automated procedure using a WinCC-OA user interface. The FE registers (MasterGBTx, SCA, GPIO, DAC, DTM-GBTx, CLARO and ADC) are constantly monitored to check the status of the FE and of the ECs as well as the connection of the OCP-UA servers. The procedure provides also auto-recover actions and the writing of log files containing information related to errors and eventual missing runs. The output and the processed files are saved in folders which structure is the same for each column. The sequence in which the tests are performed is the following:

1. PDMDBs configuration: during this step the LV is switched on. If the SOL40 and TELL40s links are not locked, an error is issued and the test is interrupted. The recover procedure

consist in a power cycle, after that the PDMDBs are configured, and all the counters in the SOL40 and TELL40s related panels are reset.

2. functional tests and time alignment as described above;

3. DAC scans to fully calibrate the CLAROs. The runs are taken with 1000 pulses per step using different attenuation and offset settings:

   - Offset=1, Attenuation=0;
   - Offset=1, Attenuation=1;
   - Offset=0, Attenuation=1;
   - Offset=1, Attenuation=2;
   - Offset=0, Attenuation=2.

   For each configuration we perform three DAC scans at different values of CLARO threshold; the output of the analysis provides, for each combination of attenuation and offset, the values of the transition point, the gain of the channel and the offset. The aim of this test is to verify that:

   - the width of the S-Curves is a narrow distribution centred at ∼1 DAC step. If it's not the case it is the clear sign of a high level of noise in the system so it needs to be addressed;
   - there is no outlier in the distribution of the zeros of the CLAROs: this may lead to awkwardly high threshold setting;
   - there is no outlier in the threshold step distribution: this may correspond to very different charge calibration for some channels

   In fig. 3.21 are shown the distribution of the charges corresponding to one threshold step and to the zero threshold for all the channels of a RICH1 column.

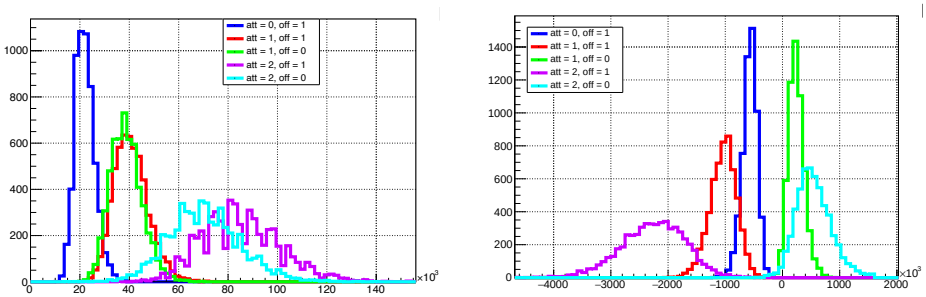

Figure 3.21: (Left) Distribution of the charges corresponding to one threshold step (Q_{th}) for a RICH1 column in different conditions of offset and attenuation. (Right) Distribution of the charges corresponding to the zero (Q_0) for a RICH1 column in different conditions of offset and attenuation. On the y-axis is reported the number of channels read (5632).

4. threshold scans for working points: given the results obtained in the test beam and in the Quality Assurance experiences, the working points are set 5 steps above the pedestal when operating at Attenuation=0. Since for most of the channels the pedestal is visible only when setting the offset bit to 1, tests with 1000 pulses per step with the following settings are performed:

   - Offset=1, Attenuation=0, HV=1000. In this case the WP is set 5 steps above pedestal;
   - Offset=1, Attenuation=1, HV=1000. In this case the WP is set 3 steps above pedestal.

   The case with Attenuation=1 is considered as alternative to the Attenuation=0. Indeed, even if the resolution in finding the WP is better when operating at Attenuation =0, there could be not optimal operating conditions given by possible CLARO saturation for large signals and not favoured CLARO time over threshold which could be mitigated by using the Attenuation =1. The WP are determined at 1000 V since they are determined by the CLARO pedestal and only minimal variation at different HV values are observed.

5. Test of working points: it's a short run to check that there are no noisy pixels after the loading of working points;

6. HV training: it is the most time consuming test since it requires the ramping up of the HV at 1050 V for eight hours. However the times are optimised since in the meantime the DAC scans analysis is running in background;

7. First dark counts run. The DCR of each MaPMT has been measured first at the PDQA and then at the ECQA. Another measurement is carried out during the column commissioning. Since during the assembly of the column and subsequent installation in the SSB the MaPMTs can be exposed to light, the column is first kept for an entire night in the dark, powered at 1050V. After the night the HV is set again to 1000 V. After 15 minutes a run without illumination (one time slot and 1M events, corresponding to a data acquisition time of $25ms$) is acquired in order to determine the DCR. The limits to define whether an MaPMT passed this test are the contractual limits defined with Hamamatsu:

   - DCR per pixel $<$ 1kHz (for R13742 and R13743);
   - total DCR R12742 $<$ 16kHz;
   - total DCR R13743 $<$ 72kHz.

   An automated check is performed to control that:

   - every pixel has less than 25 counts;
   - every R12742 MaPMT has less than 400 counts;
   - every R12743 MaPMT has less than 1800 counts.

8. Threshold scans for MaPMT gain measurement: to measure the MaPMT gain different threshold scans performed at various attenuation and HV values are acquired. The attenuation and offset bit settings used are the following:

   - Offset=1, Attenuation=1;
   - Offset=0, Attenuation=1;
   - Offset=0, Attenuation=2;
   - Offset=1, Attenuation=2.

   The HV, instead, spans from 800 to 1000 V in step of 50 V.

9. Second dark counts run;

10. SIN measurements: to characterise the SIN in the SSB 3 runs at different values of HV with TAE=1, by 23 M events each are performed:

    - time slot centered around the signal;
    - time slot delayed by $300ns$;
    - time slot delayed by $1\mu s$.

    A firmware is used to align the laser signal within the one time slot. The runs are repeated at different HV values from 800 to 100 V in step of 50 V, setting the WP found in the threshold scans with attenuation 0.

The column commissioning is considered completed when all the previous points have not failed, in case of failure of a single or multiple substeps the software developed give the chance to repeat the the corresponding steps by pressing the button "Repeat failed" runs present on the ComLab panel. Once the tests are finished, the HV and LV are switched OFF by using the related buttons on the TOP FSM panel, the data are copied on the storage server, and the column dismounted from the SSB and put it into the cabinet after purged the column from the gas coolant.

3.4 Installation in the LHCb cavern and current status

The installation at the LHCb site foresees not only the put in place of the PDM but also the set up of the gas enclosure, of the optics and the cabling with the services. The operations involved not only the column installation between February and mid April 2021 for the the A-side and C-side, respectively, but also some services work like: fibres connection to the Data centre, including their cleaning, LV switch on test, connectivity test like the ones performed to acquire the hitmap 3.22, and the HV cabling and installation. All the services related to the HV are placed in a sector of the LHCb cavern named D3. In particular, the racks of the A-side and C-side of RICH2 have been assembled. Each rack has been equipped with 2 HV-FanOut crate and 1 CAEN module, in each the CAEN module, 12 boards have been positioned,

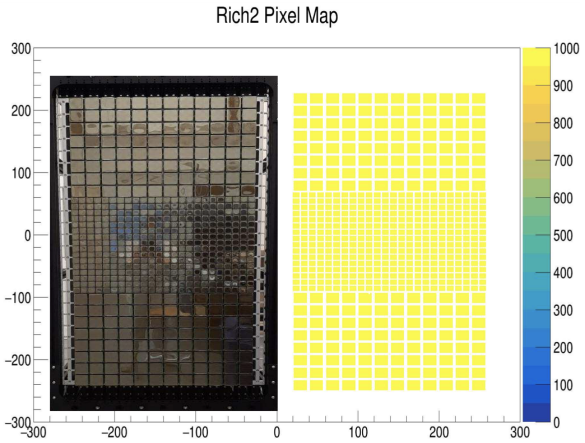

Figure 3.22: A-side RICH2 hitmap acquired programming all channels below zero. In the left part is shown the PDM while in the right the corresponding hitmap.

corresponding to the RICH2 columns. For the A-side, everything has been connected following the scheme shown in fig. 3.23. Then the crates have been connected to the online system and it has been possible to perform the first powering test thanks to the HV FSM to verify the mapping. A similar setup was provided also for the RICH1.

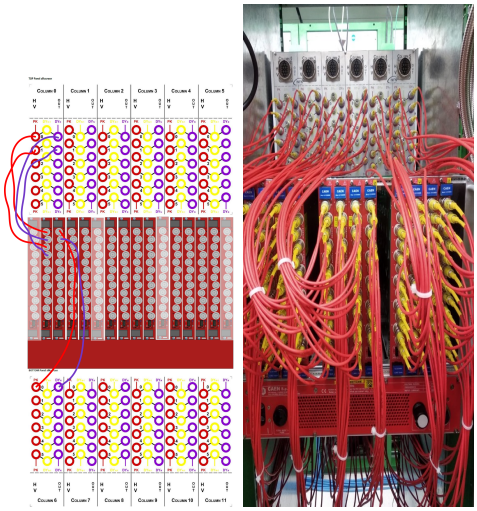

Figure 3.23: Fan-out crates and CAEN module connected, (Left) scheme (Right) real view.

3.4.1 Pilot test run

The status of the RICH2 installations allowed the subdetector to take part to the pilot test beam done in October-November 2021 with $\sqrt{s}$= 900GeV. During such test, the magnet was off and the RICH2 worked in a global configuration together with PLUME, ECAL, HCAL, MUON, and HLT1. The hitmap acquired with first HV tuning based on the gains measured during the PDQA, TAE half-window = 5, interlink alignment and working points determined in the columns commissioning, is shown in fig. 3.24. The first Cherenkov rings reconstructed using CO_2 as gas radiator are shown in fig. 3.25. Only few MaPMTs required a period of HV training

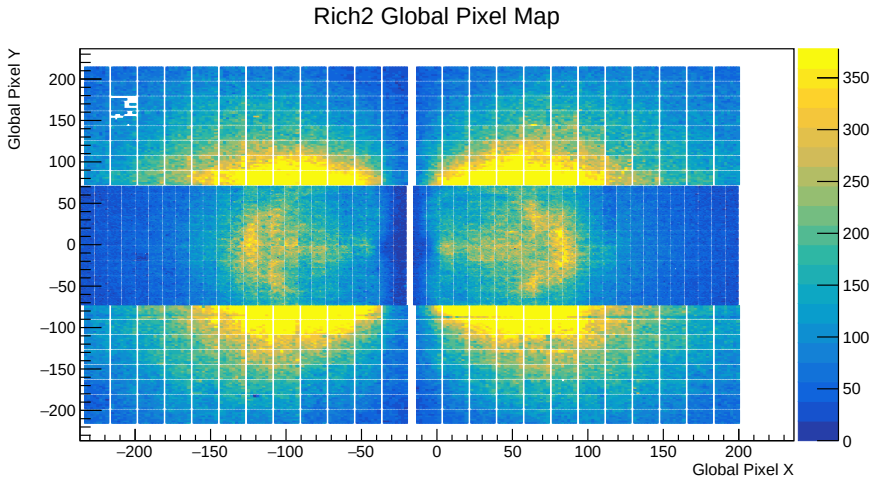

Figure 3.24: RICH2 global Pixel map. The map was acquired considering TAE half-window =5, interlink alignment, working points set from the column commissioning and HV tuned according to the average gain.

at 1050 V to reduce the dark counts rate and few instabilities in the data link and on the GBT server causing fake readings have been detected and are object of further investigations. The test beam was useful to check all the infrastructure and the capability of the RICH2 to run together with other subdetectors. After November 2021, the RICH1 also is being installed and its commissioning in the LHCb cavern is ongoing at the time of writing.

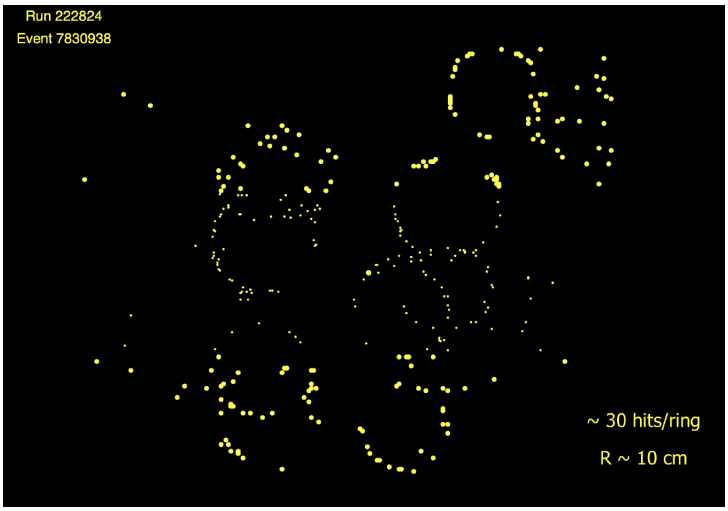

Figure 3.25: First Cherenkov rings reconstructed by RICH2 using WP determined in the column commissioning, HV tuned and from global running conditions.

Chapter 4

Lepton Flavour Universality: theoretical introduction and experimental overview

In this chapter are introduced the theoretical and the experimental frameworks behind the measurement described in this thesis. The underlying theory, the Standard Model (SM) of particle physics and its range of validity are treated in secs. 4.1 and 4.2. In sec. 4.3 an overview of the current experimental tests on Lepton Flavour Universality (LFU) using $b-$hadron decays and other measurements is given. Finally, in sec. 4.4, possible New Physics (NP) scenario that can explain the tensions with respect to the SM predictions arising from recent measurements are considered.

4.1 Standard Model overview

The SM describes three of the four known fundamental interactions in Nature, as it defines in a coherent model the unification of the electromagnetic and weak interaction [34–36], the strong interaction [43, 44] in the frame of the Quantum Chromodynamics (QCD) [40–42], and the Higgs mechanism [37–39]. It is a quantum field theory and it is invariant under transformations of the three gauge groups related to three of the four fundamental interactions. Each group is associated with a set of massless spin 1 vector fields, called bosons, which obey to the Bose-Einstein statistics: $U(1)_Y$ is associated to B_μ, $SU(2)_L$ to $W_\mu^{1,2,3}$, and $SU(3)_C$ to the eight $G_\mu^{1,\dots,8}$ vector fields. Then, three of these massless fields acquire mass with the spontaneous symmetry breaking and the Higgs mechanism, and become the known physics bosons: W^+, W^-, Z while the other nine fields, eight gluons and the photon, remain without mass. In total there are 12 vector fields associated with three gauge symmetries, all of which can be summarised by the tensor product of groups that defines the gauge symmetry of the Standard Model:

$$SU(3)_C \otimes SU(2)_I \otimes U(1)_Y \ .$$

The bosons are the mediators of the known forces and regulate the interactions among other

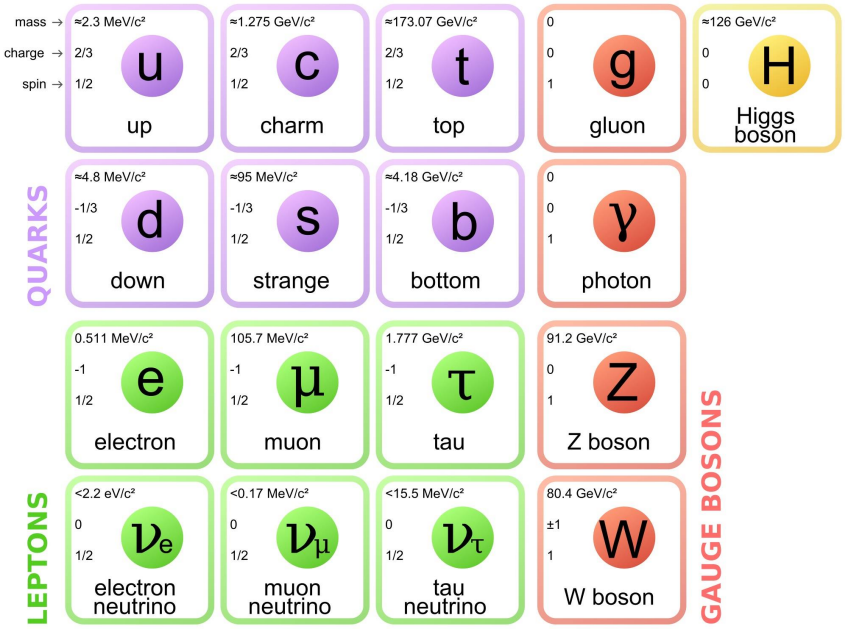

Figure 4.1: Standard Model particles: in violet the quarks, in green the leptons, in red the gauge bosons, and in yellow the Higgs boson.

spin 1/2 particles of the SM, called fermions. The SM, indeed, also foresees 12 fermions describing lepton and quark fields which obey the Fermi-Dirac statistics. Both leptons and quarks consist of three generations (families) of doublets. The SM takes also into account the Dirac equation associating to each fermion its anti-particle, defined as a particle with the same mass but with opposite quantum numbers. The last field predicted, which was recently discovered experimentally, is the complex scalar doublet named Higgs field from the name of one of the theorists who predicted its existence in 1964 [38]. In fig. 4.1 a schematic representation of the particles consisting the SM is shown.

4.1.1 Quantum electrodynamics

The first relativistic quantum field theory to be developed was the the Quantum Electrodynamics (QED), a gauge theory that describes the dynamics and interactions of fermions and the electromagnetic field. The QED lagrangian for a Dirac particle in a electromagnetic field can be obtained by adding the propagation term of free photons, to the lagrangian of the Dirac field ψ, with mass m, and the interaction term between the fermion field and the electromagnetic field:

$$\mathcal{L}_{QED} = \mathcal{L}_D + \mathcal{L}_\gamma + \mathcal{L}_{int} = i\bar{\psi}\gamma^\mu\partial_\mu\psi - m\bar{\psi}\psi - \frac{1}{4}F^{\mu\nu}F_{\mu\nu} - q\bar{\psi}\gamma^\mu A_\mu\psi\,, \tag{4.1}$$

with γ^μ the Dirac matrices, ψ and $\bar{\psi}$ the 4-components spinor and its adjoint, $F^{\mu\nu}$ is the field strength tensor, and A^μ is the electromagnetic four-potential. All the fundamental transition associated to the lagrangian in (4.1) can be seen in fig. 4.2.

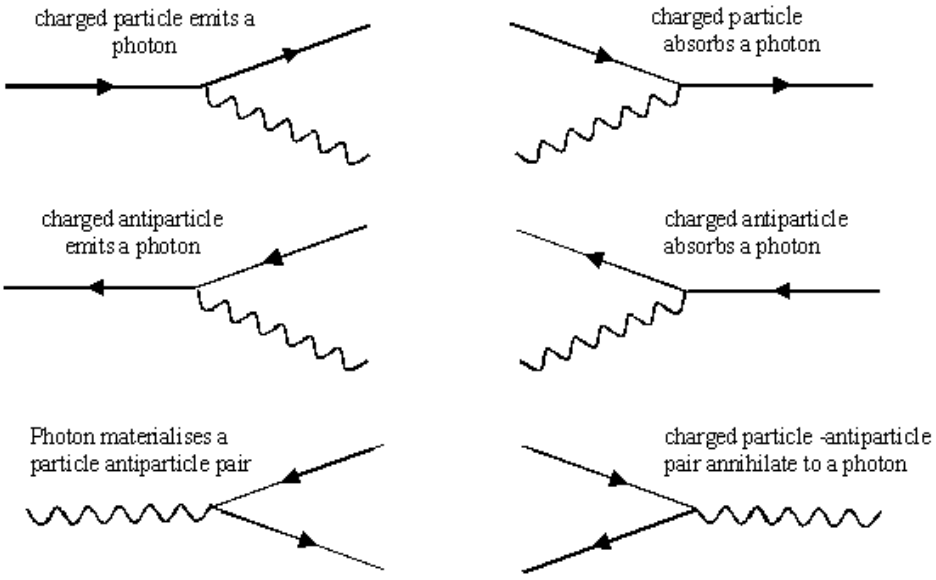

Figure 4.2: Basics vertices in Quantum Electrodynamics.

4.1.2 The Electroweak interaction

The Electroweak theory is the natural development of Fermi's theory, it has been proposed by S. Glashow, A. Salam and S. Weinberg [34–36], and it is also referred to as the GWS model of the weak interactions. The GWS Model is a quantum field theory based on the symmetry group $SU(2)_L$, where the subscript L means that only the left-handed chiral components of the fields can take part in the weak interactions. The generators of $SU(2)_L$ group are the Pauli 2×2 matrices σ_i (i = 1, 2, 3) and the particles, eigenstates of the weak interaction, are arranged in six doublets of weak isospin. The six doublets for leptons are:

$$I = 1/2 \qquad \begin{matrix} I_3 = +1/2 \\ I_3 = -1/2 \end{matrix} \qquad \begin{pmatrix} \nu_e \\ e \end{pmatrix}_L \begin{pmatrix} \nu_\mu \\ \mu \end{pmatrix}_L \begin{pmatrix} \nu_\tau \\ \tau \end{pmatrix}_L ,$$

and for quarks are:

$$I = 1/2 \qquad \begin{matrix} I_3 = +1/2 \\ I_3 = -1/2 \end{matrix} \qquad \begin{pmatrix} \mathrm{u} \\ \mathrm{d}' \end{pmatrix}_L \begin{pmatrix} \mathrm{c} \\ \mathrm{s}' \end{pmatrix}_L \begin{pmatrix} \mathrm{t} \\ \mathrm{b}' \end{pmatrix}_L .$$

being I the weak isospin and I_3 its observed component. The quark pairs, d′, s′ and b′ are the weak interaction eigenstates that are obtained as linear combination of mass eigenstates. The mixing of different flavours is given by:

$$\begin{pmatrix} \mathrm{d}' \\ \mathrm{s}' \\ \mathrm{b}' \end{pmatrix} = V \begin{pmatrix} \mathrm{d} \\ \mathrm{s} \\ \mathrm{b} \end{pmatrix},$$

where V is the complex unitary matrix named Cabibbo-Kobayashi-Maskawa (CKM) matrix:

$$V = \begin{pmatrix} \mathrm{V_{ud}} & \mathrm{V_{us}} & \mathrm{V_{ub}} \\ \mathrm{V_{cd}} & \mathrm{V_{cs}} & \mathrm{V_{cb}} \\ \mathrm{V_{td}} & \mathrm{V_{ts}} & \mathrm{V_{tb}} \end{pmatrix}.$$

As for the QED also in the GSW model a local gauge transformation invariance is required, and leads to the introduction of three isospin gauge fields which combined with the singlet, associated to the $U(1)_Y$ gauge field, gives the physics boson known as $W^{\pm}$ and Z. By requiring the invariance under local transformation of the $SU(2)_L$ it is possible to include the electromagnetic interaction in the weak one. The resulting quantum number is the weak hypercharge Y, that combined with I_3, member of a weak isomultiplet, determines the electric charge Q (in units of e) defined by Glashow as:

$$Q = I_3 + \frac{Y}{2}. \tag{4.2}$$

Eventually, the symmetry group of transformation is $SU(2)_I \otimes U(1)_Y$ and leads to 4 gauge fields, 3 associated to $SU(2)_L$ and 1 to $U(1)_Y$. The complete electroweak lagrangian is:

$$\begin{aligned} \mathcal{L}_{EW} = & - i\psi_L \gamma^\mu \left(\partial_\mu + ig\frac{\vec{\tau}}{2} \cdot W_\mu + ig' Y B_\mu \right) \psi_L + \\ & - i\psi_R \gamma^\mu \left(\partial_\mu + ig' Y B_\mu \right) \psi_R + \\ & - \frac{1}{4} W_i^{\mu\nu} W^i_{\mu\nu} - \frac{1}{4} B^{\mu\nu} B_{\mu\nu} + \\ & + \frac{1}{2} g\, \epsilon_{ijk} W_i^{\mu\nu} W_{j\mu} W_{k\nu} + \frac{1}{4} g^2\, \epsilon_{ijk} \epsilon_{imn} W_{j\mu} W_{k\nu} W_m^\mu W_n^\nu \,, \end{aligned} \tag{4.3}$$

where ψ_L and ψ_R are the left and right-handed chiral components of the particles, and the term in the last line describes the three and four-point self interactions of the vector bosons that arise because of the non-Abelian nature of the $SU(2)_I$ group. The four gauge fields can be combined to produce the physical vector fields for the $W^{\pm}, Z$ bosons and the photon. Two of the physical vector fields which can be obtained by the combination of the gauge fields, $W^{\pm}$, are electrically charged and can induce transitions between the members of the weak isospin doublets, while the Z boson is electrically neutral. The electromagnetic charge is then defined as:

$$q = g' \cos\theta_W = g \sin\theta_W \,, \tag{4.4}$$

being the parameter θ_W the Weinberg angle or weak mixing angle, to be determined experimentally, and g and g' two coupling constants.

4.1.3 Spontaneous symmetry breaking and Higgs mechanism

The gauge fields found within the GWS model are all massless; to give them mass it is necessary to introduce a spontaneous symmetry breaking and the Higgs mechanism. By introducing the Yukawa coupling between the fermion and the Higgs fields it is possible give mass to the fermions. This aspect of the SM theory is the less satisfactory part of the model because this coupling does not arise from a gauge principle but it is purely phenomenological and needs a specific coupling constant, g_f, for each fermion. Furthermore, the couplings are very different

given the wide range of fermion masses experimentally observed. In particular, in the quark sector, the charged current interactions are not diagonal in the mass eigentsates basis, as happens for the neutral current interactions. The results of this mismatch between the weak and the mass eigentsates for the charged current interactions is expressed by the 3×3 non diagonal complex unitary matrix, CKM [1]. Given that the matrix elements can be complex numbers, CP violation can be introduced resulting in different decay rates for particles and antiparticles. A popular parametrization of the CKM matrix is given by Wolfenstein:

$$V = \begin{pmatrix} 1-\lambda^2/2 & \lambda & A\lambda^3(\rho - i\eta) \\ -\lambda & 1-\lambda^2/2 & A\lambda^2 \\ A\lambda^3(1-\rho-i\eta) & -A\lambda^2 & 1 \end{pmatrix} + \mathcal{O}(\lambda^4) \ .$$

A graphical representation of the CKM matrix is given by the unitary triangle shown in fig. 4.3, where two sides and the apex of the triangle $(\bar{\rho}, \bar{\eta})$ depend on the CKM matrix elements, which are determined experimentally.

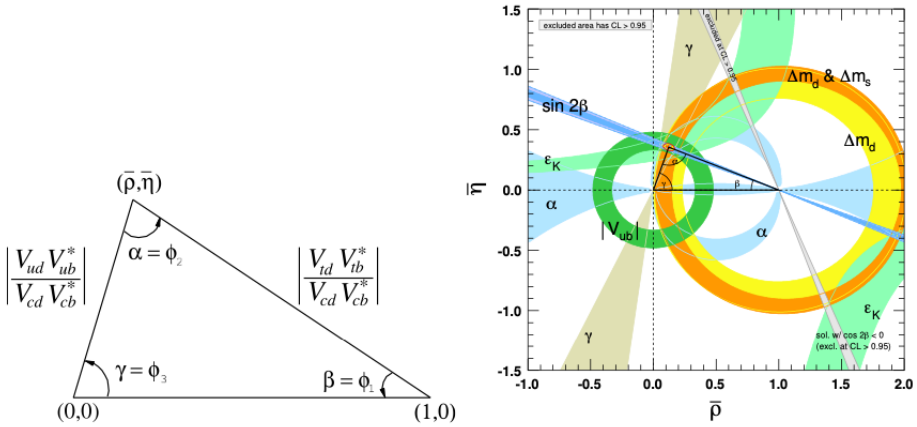

Figure 4.3: The unitary triangle (left) and the experimental constraints on the $(\bar{\rho}, \bar{\eta})$ plane (right) [56].

4.1.4 Quantum Chromodynamics

The Quantum Chromodynamics, QCD, is the gauge theory of strong interactions. Its symmetry group is $SU(3)_C$, where the subscript C stands for the charge associated with this symmetry, named colour. Since the generators of the $SU(3)_C$ do not commute, the QCD lagrangian contains interaction terms among gauge fields, called gluons, that bring the coloured charge. The lagrangian for the QCD is:

$$\mathcal{L}_{QCD} = \bar{\psi}\gamma^\mu \partial_\mu \psi - m\bar{\psi}\psi - ig_s \bar{\psi}\gamma^\mu \lambda_a \psi G^\alpha_\mu - \frac{1}{4} G^{\mu\nu}_\alpha G^\alpha_{\mu\nu} \, , \tag{4.5}$$

[1] Analogously a mixing matrix can be introduced also for the neutrino sector, the PMNS matrix from Pontecorvo, Maki, Nakagawa e Sakata.

where $G_\alpha^{\mu\nu}$ is the tensor field defined as

$$G_\alpha^{\mu\nu} = \partial^\mu G_\alpha^\nu - \partial^\nu G_\alpha^\mu - g_s f_{\alpha\beta\gamma} G^{\beta,\mu} G^{\gamma,\nu} \,, \tag{4.6}$$

and g_s is the strong coupling constant, G_μ^α are the 8 gluon fields and $f_{\alpha\beta\gamma}$ are the structure constants of the group $SU(3)_C$. The field ψ has three possible states labelled as red, green, and blue since the generators of the $SU(3)_C$ are represented by 3×3 matrices. As for the QED, it is possible to associate to each lagrangian interaction term a Feynman diagram. Fig. 4.4 shows all the fundamental transitions associated to the lagrangian in eq. (4.5). Two relevant properties,

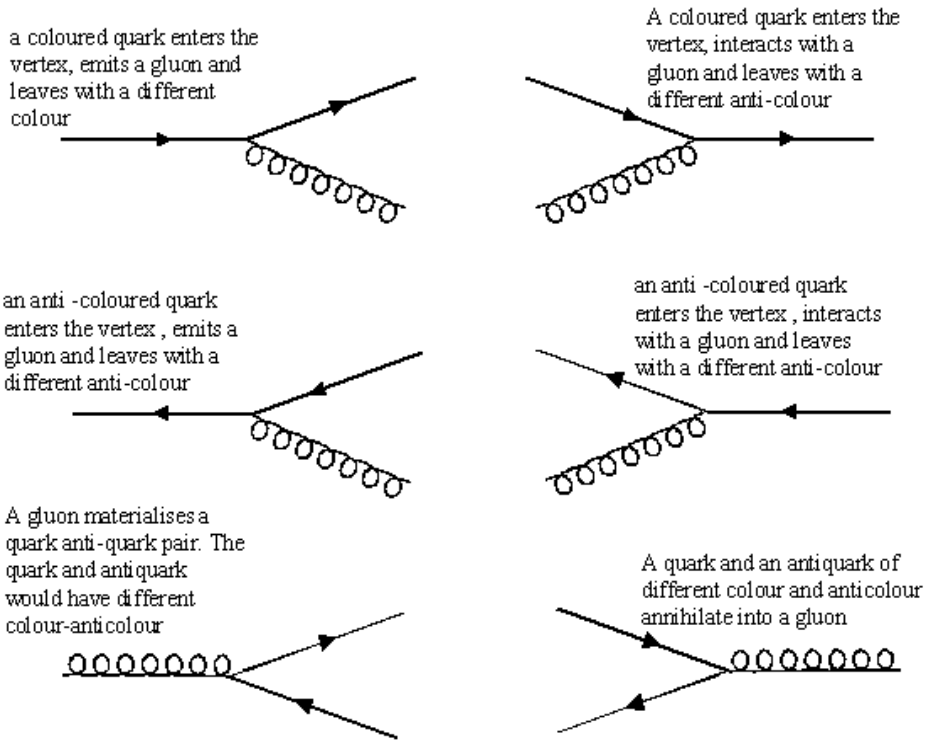

Figure 4.4: Basics vertices in Quantum Cromodynamics, QCD.

which stem from experimental evidence and are well described in SM in the strong interactions sector, significantly distinguish QCD from QED: colour confinement and asymptotic freedom. The asymptotic freedom has to cope with the experimental fact that no coloured hadrons are observed in nature. Hadrons, therefore, are colour singlets since they are interpreted as bound states of quarks in the QCD parton model. This imposes restrictions on the types of bound quark state configurations that can exist. All this can be summarised by saying that the quark colour degree of freedom must be confined. The colour confinement can be accounted by considering the running coupling constant of strong force that decreases as $|q^2|$ increases. Depending on the value of the coupling constant can be adopted a different approaches in the QCD calculations.

4.2 Limits and validity of the Standard Model

In the last 40 years many aspects of the SM theory have been tested: every predicted particle has been found, features of the electromagnetic and strong interactions have been described with accuracy, and in many cases predictions of the SM were verified experimentally with high precision. However, the SM is not sufficient to provide a full picture of the known universe, as it fails to explain several phenomena, like the different values of fermion masses spanning on 5 orders of magnitude due to the coupling constants (known as *naturalness* problem), the evidence of neutrino masses, dark energy and dark matter, and the impossibility to include the gravitational field. Much thought has been put into how the SM might be modified to solve these puzzles. Most of the possible answers fall into two proposals of New Physics (NP) scenarios:

- known fundamental fields with new interactions as foreseen by the Great Unification, Supersymmetry, string theories.
- new fundamental fields with new interactions ("compositeness", meaning that some of the known particles might be composites of still-smaller things, condensed fermion-antidermal, "technicolour", "extended technicolour", and more).

Therefore the experiments are trying to validate or discard these new theories. At the moment the theories which foresee new interactions with known fundamental fields are the most favoured when compared to the experimental results.

4.3 Lepton Flavour Universality

A way to test the SM validity is given by the the Lepton Flavour Universality. Indeed, according to the SM the photon, the W, and the Z bosons couple in the same manner to the three lepton generations therefore any departure from this identity, once considered all the corrections related to the kinematic differences due to the different lepton masses, could indicate the contribution of NP to the process. The best measurements to test the LFU within the SM are ratios of observables related to leptonic or semileptonic processes involving leptons of different generation but the same quark transition. Such ratios have precise theoretical predictions since terms related to the CKM matrix and the common hadronic form-factors cancel out. The use of the ratios brings also advantages from the experimental point of view reducing the size of the systematic uncertainties. In the following an overview of different LFU tests performed so far is given.

4.3.1 Precision tests

Precision measurement have been performed both at e^+e^- (LEP and SLC) both at $p\bar{p}$ (Tevatron), and pp (LHC) colliders.

Focusing on the Z boson, the measurements at LEP and SLC [55] of the partial widths of the $Z \to \ell^+\ell^-$, being ℓ the e, μ, τ leptons, are in agreement each other. Their ratios are measured

to be:

$$\frac{\Gamma_{Z\to\mu^+\mu^-}}{\Gamma_{Z\to e^+e^-}} = 1.0009 \pm 0.0028,$$

$$\frac{\Gamma_{Z\to\tau^+\tau^-}}{\Gamma_{Z\to e^+e^-}} = 1.0019 \pm 0.0032$$

in perfect agreement with the predictions of the SM that assume negligible lepton masses.

The rate of the W boson decays to leptons, when considering $W^- \to \ell^-\bar{\nu}_\ell$, depends on the coupling g_ℓ, which is the same for all the three lepton families according to the SM. The ratio of decay the rates $W \to e^-\bar{\nu}_e$ and $W^- \to \mu^-\bar{\nu}_\mu$ measured by several experiments at Tevatron [57], LEP [58] and LHC [59, 60] constrain the ratio $(g_e/g_\mu)^2$ to the value of 1.005±0.008, in excellent agreement with the SM expectations.

In general, the measurements performed considering the third lepton family are less precise than those involving the first two lepton families, due to the challenging reconstruction of the τ decays. Assuming that LFU holds between the first and the second families, the test performed by measuring:

$$\frac{2\Gamma_{W^-\to\tau^-\bar{\nu}_\tau}}{\Gamma_{W^-\to e^-\bar{\nu}_e} + \Gamma_{W^-\to\mu^-\bar{\nu}_\mu}} = 1.066 \pm 0.025$$

shows a tension with respect to the SM expectation at the level of 2.6σ [58].

Other tests of LFU can be done considering leptonic decays of pseudoscalar mesons. Such decays are helicity suppressed in the SM and therefore bring stringent constraints on the LFU tests. In the kaons sector, the most precise measurement of the ratio, considering the first two families, is provided by the NA62 experiment [61], and it is measured to be:

$$\frac{\Gamma_{K^-\to e^-\bar{\nu}_e}}{\Gamma_{K^-\to\mu^-\bar{\nu}_\mu}} = (2.488 \pm 0.009) \times 10^{-5}.$$

This measurement is in a good agreement with the SM expectation which is computed with high precision taking into account the meson and leptons masses, and the QED contribution.

Similarly, the measurement of the ratio using pions [62] is:

$$\frac{\Gamma_{\pi^-\to e^-\bar{\nu}_e}}{\Gamma_{\pi^-\to\mu^-\bar{\nu}_\mu}} = (1.230 \pm 0.004) \times 10^{-4}\,,$$

which is consistent with the corresponding SM prediction $(1.2352 \pm 0.0001) \times 10^{-4}$ [63], though with poorer precision. Further tests can be performed considering charmed-meson and quarkonia resonances. The measurement obtained using the charmed-meson [64] is:

$$\frac{\Gamma_{D_s^-\to\tau^-\bar{\nu}_\tau}}{\Gamma_{D_s^-\to\mu^-\bar{\nu}_\mu}} = 9.95 \pm 0.61,$$

in agreement with the SM prediction 9.76±0.10 at level of 6%.

Lastly, the most precise test of LFU is given by the measurement of quarkonia partial widths

ratio [56]:

$$\frac{\Gamma_{J/\psi\to e^+e^-}}{\Gamma_{J/\psi\to\mu^+\mu^-}} = 1.0016 \pm 0.0031\,,$$

that reaches a precision of 0.31%.

4.3.2 Tests using $b-$hadron decays

LFU can be tested in decays of $b-$hadrons by exploiting both $b \to c\ell^-\bar{\nu}_\ell$ flavour-changing-charged current (FCCC) and $b \to s\ell^+\ell^-$ flavour-changing-neutral current (FCNC) processes, that occur at tree and loop level, respectively.

$b \to s\ell^+\ell^-$ transitions

This type of decays are challenging both experimentally and theoretically with respect to the charged transitions since are highly suppressed. Such suppression is due to the fact that the FCNC transitions are considered rare in the SM frame while could have noticeable effects in any NP model. The related Feynman diagrams are shown in fig. 4.5 (Top) and proceed through so-called penguin or box diagrams, depending on the exchange of Z/γ or W^+W^-. Whereas in fig. 4.5 (Bottom) are shown examples of potential NP contributions occurring within tree diagrams.

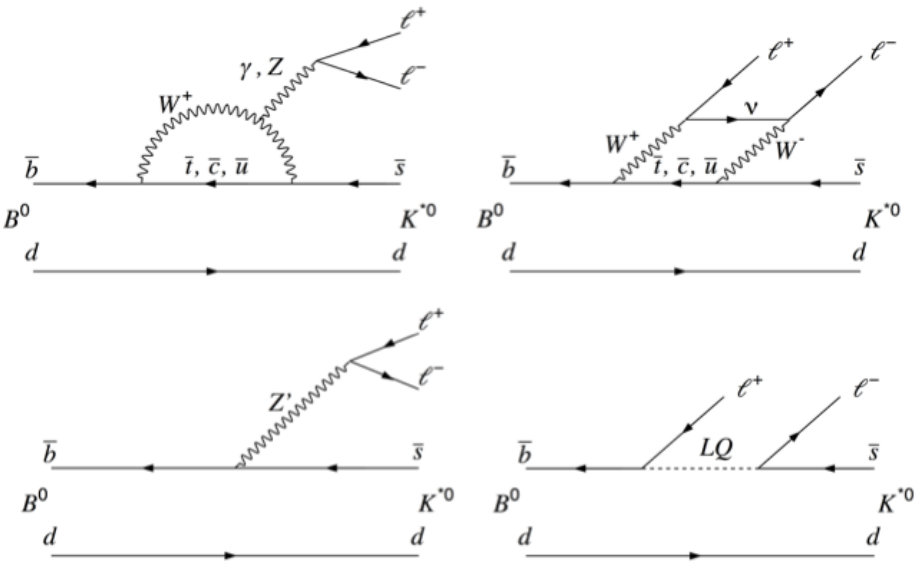

Figure 4.5: Feynman diagram penguin (Top Left) and box (Top Right) for the $B^0 \to K^{*0}\ell^+\ell^-$ decay within the SM, and tree level decays, within NP extension of the SM involving (Bottom Left) the Z' boson and (Bottom Right) a Leptoquark (LQ) exchange.

Sensitive probes to the LFU are the ratios defined as:

$$R(H_s) = \frac{\int_{q^2_{min}}^{q^2_{max}} \frac{d\Gamma(H_b\to H_s\mu^+\mu^-)}{dq^2} dq^2}{\int_{q^2_{min}}^{q^2_{max}} \frac{d\Gamma(H_b\to H_s e^+e^-)}{dq^2} dq^2}, \tag{4.7}$$

where H_b is a $b-$hadron (*e.g.* B^+, B^0, ...), H_s is an $s-$hadron (*e.g.* K, K^*..), q^2 is the invariant mass squared of the two leptons and q^2_{min} and q^2_{max} the integration limits. Due to the cancellation of hadronic uncertainties, common to both the numerator and the denominator, these ratios are predicted with high precision in the SM [69–71] and therefore represent excellent probes of NP effects. Indeed, NP contributions can induce a sizeable change of a particular decay rate. Moreover, such NP contributions can modify the angular distribution of the final-state particles providing a further test of LFU. Two ratios are particularly interesting: $R(K)$ and $R\left(K^{*0}\right)$ obtained considering the decays $B^+ \to K^+\mu^+\mu^-$ and $B^+ \to K^+e^+e^-$, for the first, and $B^0 \to K^{*0}\mu^+\mu^-$ and $B^0 \to K^{*0}e^+e^-$ for the latter. In fig. 4.6 are shown the measurements performed by BaBar, Belle and LHCb compared to the SM expectations. The value measured by LHCb [74] is the most precise of all three collaborations and is consistent with the SM at the level of 2.5 standard deviations.

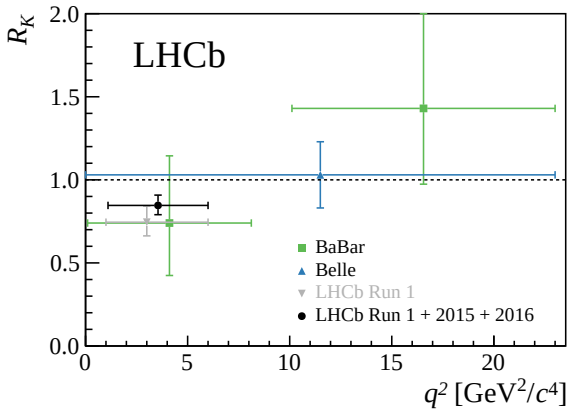

Figure 4.6: $R(K)$ measurements performed by BaBar [75], Belle [76] and LHCb [72–74] compared to the SM expectation. The LHCb Run1 result (in grey) is superseded by the new result.

Also $R\left(K^{*0}\right)$ has been measured by the three collaborations, the comparison of the measurements and the SM predictions is shown in fig. 4.7. Despite the previous results obtained by BaBar and Belle which agreed with the SM ($< 1\sigma$), the measurements performed by LHCb, in two bins of q^2, show deviations of 2.2–2.4 and 2.4–2.5σ with respect to the SM predictions.

A first test of lepton universality with $b-$baryons has been performed by LHCb using Λ_b decays [78]. The measurement of the R^{-1}_{pK} ratio is compatible with the SM prediction within one standard deviation.

Additional indications of tensions with the SM predictions arise from the study of the angular distribution of variables such as the P'_5 studied in the $B^0 \to K^{*0}\mu^+\mu^-$ decay [81], see fig. 4.8. In that case the tension with the SM is 2.5-2.9σ and when combined with other angular variables the global discrepancy reaches 3.3σ. Table 4.1 reports all the measurements related to the $b \to s\ell^+\ell^-$ transitions.

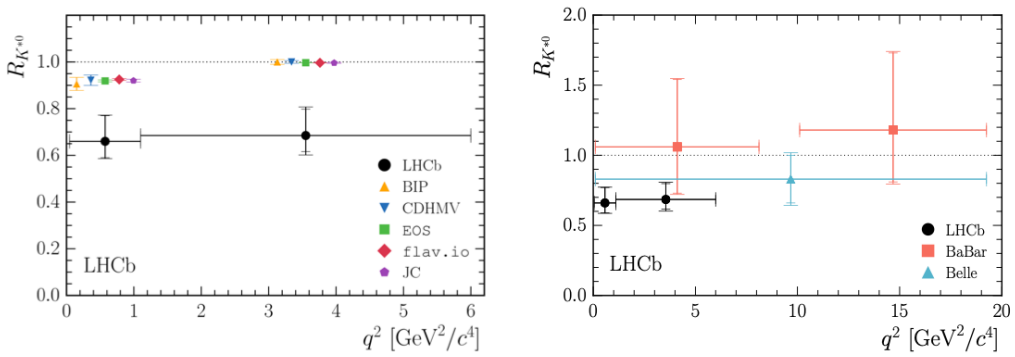

Figure 4.7: (Left) comparison of the $R\left(K^{*0}\right)$ measurement performed by LHCb with different available SM predictions. (Right) comparison of the measurements performed by Babar [75], Belle [76] and LHCb [73] with the SM prediction (grey horizontal dotted line) [77].

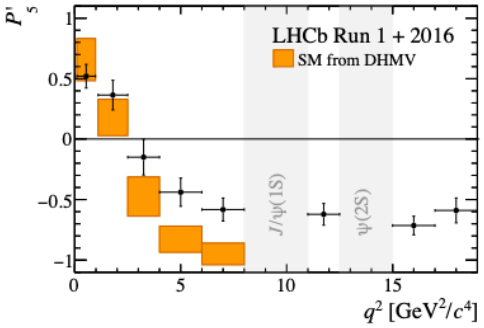

Figure 4.8: LHCb measurement of P_5' [81] in bins of q^2. The data are compared to SM predictions based on the prescription of Refs. [82, 83].

$b \to c\ell^-\bar{\nu}_\ell$ transitions

These type of transitions occur in the SM through tree-level diagrams, are referred to as semileptonic decays, and differ each other only because of the lepton mass involved in the decay. The semileptonic decays involving the first two lepton generation (*i.e.* e^- and μ^-) are consistent to each other within experimental uncertainties and in agreement with LFU. Whereas, the large τ mass, makes this kind of transitions more sensitive to the presence of NP effects. The useful observable to probe NP contributions are ratios of branching fractions defined as:

$$R(H_c) = \frac{\mathcal{B}(H_b \to H_c\tau^-\bar{\nu}_\tau)}{\mathcal{B}(H_b \to H_c\ell^-\bar{\nu}_\ell)}, \tag{4.8}$$

where H_b and H_c are hadrons containing a b and a c quark, respectively, and ℓ represents an electron or a muon. The ratio helps to cancel large part of theoretical uncertainties like $|V_{cb}|$ and form factors, as well as the experimental uncertainties given by the measurement of branching fractions, such as systematic uncertainties related to reconstruction efficiencies. The different τ decay modes exploited for the $R(H_c)$ measurements are enlisted in the table 4.2 together with

Table 4.1: Summary of the measurements related to the $b \to s\ell^+\ell^-$ transitions performed by BaBar, Belle, and LHCb experiments.

Experiment	Parameter	q^2 range	Value	SM consistency	Ref.
Belle	$R(K)$	[0.1,4.0]	$1.01^{+0.28}_{-0.25} \pm 0.02$	$< 1\sigma$	[79]
Belle	$R(K)$	[4.8,12]	$0.85^{+0.30}_{-0.24} \pm 0.01$	$< 1\sigma$	[79]
Belle	$R(K)$	[1,6]	$1.03^{+0.28}_{-0.24} \pm 0.01$	$< 1\sigma$	[79]
Belle	$R(K)$	[10.2,12.8]	$1.97^{+1.03}_{-0.89} \pm 0.02$	$< 1.1\sigma$	[79]
Belle	$R(K)$	>14.18	$1.16^{+0.30}_{-0.27} \pm 0.01$	$< 1\sigma$	[79]
Belle	$R(K)$	whole range	$1.10^{+0.16}_{-0.15} \pm 0.02$	$< 1\sigma$	[79]
BaBar	$R(K)$	[0.10,8.12]	$0.74^{+0.40}_{-0.31} \pm 0.06$	$< 1\sigma$	[75]
BaBar	$R(K)$	>10.11	$1.43^{+0.65}_{-0.44} \pm 0.12$	$< 1\sigma$	[75]
LHCb	$R(K)$	[1.1,6.0]	$0.846^{+0.042\ +0.039}_{-0.013\ -0.012}$	3.1σ	[72]
Belle	$R\left(K^{*0}\right)$	[0.045,1.1]	$0.52^{+0.36}_{-0.26} \pm 0.06$	$\approx 1\sigma$	[80]
Belle	$R\left(K^{*0}\right)$	[1.1,6]	$0.96^{+0.45}_{-0.29} \pm 0.11$	$< 1\sigma$	[80]
Belle	$R\left(K^{*0}\right)$	[0.1,8]	$0.90^{+0.27}_{-0.21} \pm 0.10$	$< 1\sigma$	[80]
Belle	$R\left(K^{*0}\right)$	[15,19]	$1.18^{+0.52}_{-0.32} \pm 0.11$	$< 1\sigma$	[80]
Belle	$R\left(K^{*0}\right)$	> 0.045	$0.94^{+0.17}_{-0.14} \pm 0.08$	$< 1\sigma$	[80]
BaBar	$R\left(K^{*0}\right)$	[0.10,8.12]	$1.06^{+0.48}_{-0.33} \pm 0.09$	$< 1\sigma$	[75]
BaBar	$R\left(K^{*0}\right)$	> 10.11	$1.18^{+0.55}_{-0.37} \pm 0.11$	$< 1\sigma$	[75]
LHCb	$R\left(K^{*0}\right)$	[0.045,1.1]	$0.66^{+0.11}_{-0.07} \pm 0.03$	2.2σ	[77]
LHCb	$R\left(K^{*0}\right)$	[1.1,6.0]	$0.69^{+0.11}_{-0.07} \pm 0.05$	2.4σ	[77]
LHCb	R_{pK}^{-1}	[0.1,6.0]	$1.17^{+0.18}_{-0.16} \pm 0.07$	1σ	[78]
LHCb	P_5'	[4,6]	*cf.* fig. 4.8	2.5σ	[81]
LHCb	P_5'	[6,8]	*cf.* fig. 4.8	2.9σ	[81]
LHCb	all angular observables	≈[0,19]	n/a	3.3σ	[81]

their branching fractions $\mathcal{B}$.

Both Belle and BaBar experiments have measured the $R(D)$ and $R(D^*)$ ratios [84, 86] by using different τ decay modes and different (B-tagging) techniques to fully reconstruct the signal candidate: hadronic and semileptonic. The LHCb collaboration, instead, performed the measurement of the ratios $R(D^*)$ and $R_{J/\psi}$ exploiting the leptonic τ decays [97, 98], and of the $R(D^*)$ ratio using the 3-prong hadronic τ decays [99, 100].

A summary of the measurements of $R(D)$ and $R(D^*)$ as well as their combination and comparison with SM prediction can be seen in fig. 4.9 while in table 4.3 are listed all the LFU measurements performed on the semitauonic B decays by the three collaborations. The SM predictions of $R(D)$ and $R(D^*)$ are estimated to be

$$R(D) = 0.298 \pm 0.003$$

and

$$R(D^*) = 0.252 \pm 0.005.$$

From the experimental side both the averages of $R(D)$ and $R(D^*)$ measurements exceed the SM prediction at 1.4σ and 2.9 σ, respectively. Considering a $R(D)$-$R(D^*)$ correlation of -0.38, the resulting difference with the SM predictions corresponds to about 3.4 σ. The deviation

Table 4.2: Branching fractions and classification modes of the τ decays that have been used to perform measurements in semitauonic H_b decays.

Decay	Mode	$\mathcal{B}$[%]
$\tau^- \to \mu^- \bar{\nu}_\mu \nu_\tau$	leptonic	17.39±0.04
$\tau^- \to e^- \bar{\nu}_e \nu_\tau$	leptonic	17.82±0.04
$\tau^- \to \pi^- \pi^0 \nu_\tau$	hadronic 1-prong	25.49±0.09
$\tau^- \to \pi^- \nu_\tau$	hadronic 1-prong	10.82±0.05
$\tau^- \to \pi^- \pi^+ \pi^- \pi^0 \nu_\tau$	hadronic 3-prong	9.02±0.05
$\tau^- \to \pi^- \pi^+ \pi^- \nu_\tau$	hadronic 3-prong	4.49±0.05

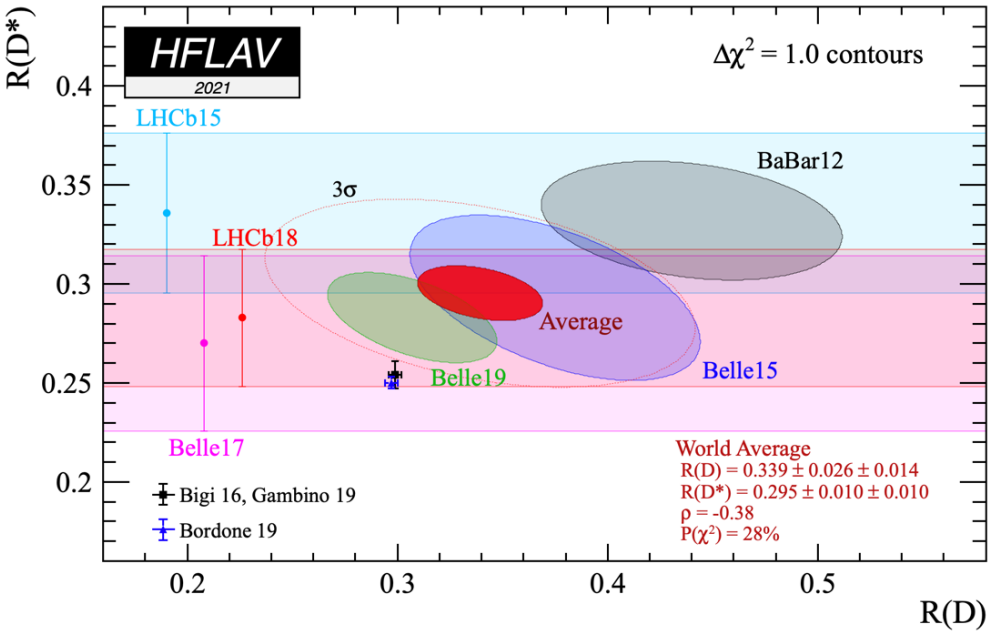

Figure 4.9: Current status of the combination of both $R(D)$ and $R(D^*)$ measurements and their comparison with the SM prediction [64].

from unity of both the ratios $R(D)$ and $R(D^*)$ is related to the different lepton masses and to the ratios of form factors when considering all the terms in eq. 4.8. Since this tension could be explained within NP processes, investigating more $R(D^*)$ and similar ratios involving the $b \to c\ell^- \bar{\nu}_\ell$ decays is crucial. With this purpose in mind has been possible to evaluate also other ratios such as $R_{J/\psi}$ taking advantage of the sizeable B_c^+ production at the LHC. Several other observables are currently being studied by the LHCb collaboration, like $R(D_s)$ and $R(\Lambda_c^{(*)})$.

4.4 New Physics in semitauonic b-hadron decays

The experimental picture has grown considerably in the recent years thanks to the different measurements possible at the LHC. Overall, it shows hints of tensions with respect to the SM

Table 4.3: Measurements performed by BaBar, Belle and LHCb collaborations to test the LFU in semitauonic H_b decays.

Experiment (year)	H_b-tag	τ decay	$R(D)$	$R(D^*)$	Ref.
BaBar (2012)	Had.	$\tau^- \to \ell^- \bar{\nu}_\ell \nu_\tau$	0.440±0.058 ± 0.042	0.332±0.024±0.018	[84, 85]
Belle (2015)	Had.	$\tau^- \to \ell^- \bar{\nu}_\ell \nu_\tau$	0.375±0.064 ± 0.026	0.293±0.038±0.015	[86]
Belle (2016)	SL	$\tau^- \to \ell^- \bar{\nu}_\ell \nu_\tau$	/	0.302±0.030±0.011	[87]
Belle (2017)	Had.	$\tau^- \to \pi^-(\pi^0)\nu_\tau$	/	$0.270 \pm 0.035^{+0.21}_{-0.16}$	[88]
Belle (2019)	SL	$\tau^- \to \ell^- \bar{\nu}_\ell \nu_\tau$	0.307±0.037 ± 0.016	0.283±0.018±0.014	[89]
LHCb (2015)	/	$\tau^- \to \mu^- \bar{\nu}_\mu \nu_\tau$	/	0.336±0.027±0.030	[97]
LHCb (2017)	/	$\tau^- \to \pi^-\pi^+\pi^-(\pi^0)\nu_\tau$	/	0.291±0.019±0.029	[99, 100]
Experiment (year)	H_b-tag	τ decay	$R_{J/\psi}$		Ref.
LHCb (2017)	/	$\tau^- \to \mu^- \bar{\nu}_\mu \nu_\tau$	0.71±0.17±0.18		[98]

predictions that boosted both the theoretical and the experimental community to improve the results in the field. To explain the deviations of measurements from the SM expectations, one can perform a model-independent analysis by considering the relevant effective Hamiltonian, determining the values of the short-distance Wilson coefficients from the data, and comparing them with respect to the SM computation. This method, referred to as Effective Field Theory (EFT), allows to separate effects from different energy scales and all the contributions are summed in series which comprises the SM effective Hamiltonian. The advantage to use this approach is that it accommodates NP effects by adding extra operators whose contributions are normalised by their coefficients. To better explain, for example, the EFT in the case of a weak decay mediated ignores the boson and assumes a four-fermion vertex, resulting in the operator $\mathcal{O}_{v\ell}$:

$$\mathcal{H}_{eff}(b \to c\ell^- \nu_\ell) = \frac{4G_F}{\sqrt{2}} V_{cb} \sum_i \mathcal{C}_i \mathcal{O}_i \,, \tag{4.9}$$

where the index i runs over the 4-fermion. The operator product expansion can be resumed in the $\mathcal{O}_{V\ell}$:

$$\mathcal{C}_{V\ell}\mathcal{O}_{V\ell} = (\bar{c}\gamma_\mu P_L b)(\bar{\ell}\gamma^\mu P_L \nu_\ell) \,, \tag{4.10}$$

being P_L function of the γ_5 Dirac matrix, ($P_L = (1-\gamma_5)/2$) and $\mathcal{C}_{V\ell}$ normalised to unity. Since there are no signs of LFU violation for the electron and muon $b \to c\ell^- \bar{\nu}_\ell$ decays, most of the EFT assume that NP is present only in $b \to c\tau^- \bar{\nu}_\tau$ decays. The most recent model-independent analysis [101] considers observables on both $b \to s\ell^+\ell^-$ and $b \to c\ell^- \bar{\nu}_\ell$ processes by exploiting NP Wilson coefficients. That analysis suggests the presence of right-handed couplings encoded in the Wilson coefficients $\mathcal{C}_{9'\mu}$ and $\mathcal{C}_{10'\mu}$, and reinforces the previous observation of lepton flavour universality violation (LFUV) in left-handed lepton coupling ($\mathcal{C}^V_{9\mu} = -\mathcal{C}^V_{10\mu}$), showing a better agreement to data in NP scenarios when considering $\mathcal{C}_{9\mu}$. Currently, in addition to the EFT, three models beyond the SM manage to account the anomalies found in the semitauonic b-hadron decays [102]: two-Higgs-doublet [103], heavy vector bosons [104] and leptoquark [105, 106]. The first two models are more discouraged nowadays since they would lead to a too large B_c^+ lifetime and a q^2 distribution different from the one observed, moreover the second will imply the presence of bosons with unnaturally large widths. The most favoured theory foresees the leptoquarks

(LQs) which are particles that carry both lepton and baryon numbers, allowing for transition between leptons and quarks. Such particles have properties that depends from the specific model and are classified as either scalar (spin 0) or vector (spin 1) particles. With a single vector LQ of mass around 1 TeV, it is possible to solve both $R\left(K^{*0}\right)$ and $R(D^*)$ puzzles simultaneously. Constraints might be obtained, in this sector, by LHCb and Belle II experiments. The ATLAS and CMS collaboration are performing direct searches of LQs. The analyses performed so far have excluded LQs of the first and second generations below the mass of 1.3-1.5 TeV [107–109] while the third generation LQs are excluded below the 740-1002 TeV [110–114]. The current measurements based on Run1 and Run2 datasets show no evidence of such particles.

Chapter 5

$R(D_s)$ measurement with three-prong τ decays

To shed light on the LFU puzzle described in the previous chapter, complementary measurements using additional b-hadron decays should be performed by exploiting the abundance of the different b-hadrons species produced in pp collisions at the LHC collider.

In particular, in this thesis I focused on the analysis of the decay $B_s^0 \to D_s^- \tau^+ \nu_\tau$, reconstructed through the decays $D_s^+ \to K^+K^-\pi^-$ and $\tau^+ \to \pi^+\pi^-\pi^+(\pi^0)\nu_\tau$, needed for the measurement of the $R(D_s)$ ratio, which is defined as:

$$R(D_s) = \frac{\mathcal{B}(B_s^0 \to D_s^- \tau^+ \nu_\tau)}{\mathcal{B}(B_s^0 \to D_s^- \mu^+ \nu_\mu)} \,. \tag{5.1}$$

The SM theoretical prediction of $R(D_s)$ is known with high accuracy $R(D_s)^{SM} = 0.2971 \pm 0.0034$ [121]. Measuring a deviation from this value would indicate possible NP contributions at quark level transitions in the $B_s^0 \to D_s^- \tau^+ \nu_\tau$ decay.

In sec. 5.1 is explained the measurement techniques, then in secs. 5.2 are considered the possible normalisation channels.

5.1 Measurement technique

In the ratio in eq. 5.1 the numerator is referred to as *signal* channel while the decay in the denominator is the *reference* channel. The branching fraction of the reference channel was recently measured by the LHCb collaboration [90] and is $(2.49 \pm 0.24)\%$. The hadronic τ decay mode, which characterise the signal channel decay is shown in fig. 5.1. The absence of charged leptons in the final state suppresses backgrounds originating from semileptonic $b-$ or $c-$hadron decays. Moreover, the three-pions τ decay allows to reconstruct both the τ and the B_s^0 decay vertices and the τ decay time, which is is a distinctive feature of the signal decay that helps to discriminate the signal from the $B_s^0 \to D_s^- \pi^+\pi^-\pi^+$ and other background contributions. The main background sources are due to inclusive $b-$hadron decays to a charmed hadron and three charged or more pions, and doubly-charmed decays, $H_b \to D_s H_c n\pi$, where the H_c decays to

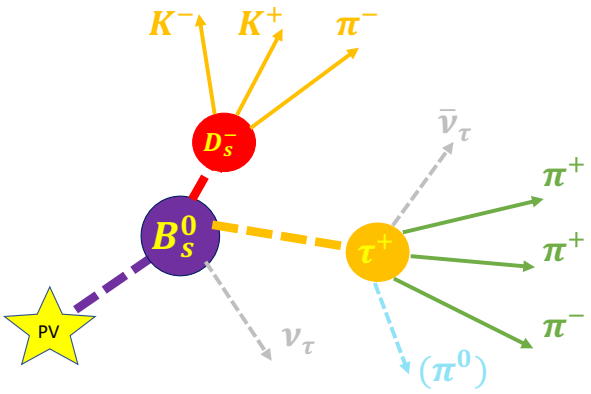

Figure 5.1: Schematic view of the signal decay.

three charged or more pions.

The presence of different final states in the numerator and in the denominator of eq. 5.1 is not ideal from the experimental point of view. Following a similar strategy already used in other analyses [99, 100], the $R(D_s)$ ratio is determined by measuring the $B_s^0 \to D_s^- \tau^+ \nu_\tau$ branching ratio relative to that of a decay with a same/similar topology and known branching fraction value (referred to as *normalisation* channel in the following, *norm*). In this way, in fact, many experimental uncertainties related to the final state reconstruction cancel out leading to a more precise measurement. Following this approach the $R(D_s)$ ratio is computed as:

$$R(D_s) = \frac{\mathcal{B}(B_s^0 \to D_s^- \tau^+ \nu_\tau)}{\mathcal{B}(norm)} \times \frac{\mathcal{B}(norm)}{\mathcal{B}(B_s^0 \to D_s^- \mu^+ \nu_\mu)} = \mathcal{K} \times \alpha \,, \tag{5.2}$$

with $\mathcal{K}$ and α defined as

$$\mathcal{K} = \frac{\mathcal{B}(B_s^0 \to D_s^- \tau^+ \nu_\tau)}{\mathcal{B}(norm)} \qquad \alpha = \frac{\mathcal{B}(norm)}{\mathcal{B}(B_s^0 \to D_s^- \mu^+ \nu_\mu)} \,, \tag{5.3}$$

where α term is a known factor computed using the values of the branching fraction, while $\mathcal{K}$ needs to be determined from data. Considering as signal the $B_s^0 \to D_s^- \tau^+ \nu_\tau$, the yields and the selection efficiencies of the signal and the normalisation channel, the ratio $\mathcal{K}$ can be rewritten as:

$$\mathcal{K} = \frac{N_{sig}}{\epsilon_{sig}} \frac{\epsilon_{norm}}{N_{norm}} \frac{1}{\mathcal{B}(\tau^+ \to \pi^+\pi^-\pi^+(\pi^0)\nu_\tau) \times \mathcal{B}(D_s^- \to K^+K^-\pi^-)} \,. \tag{5.4}$$

5.2 Possible normalisation channels

The choice of the normalisation channel is driven by the precision of the measurement. Indeed, by choosing a normalisation channel as much as similar to the signal and reconstructed in a similar way, a common selection can be implemented. Therefore, when measuring $\mathcal{K}$, the efficiency ratio is expected to be close to one, except for effects due to the different kinematics involved, but, more important, the uncertainties on the efficiency ratio should cancel as they are highly correlated.

Another requirement for the normalisation channel concerns the branching fraction: it should be as large as possible, in order to have large statistics of reconstructed normalisation channel decays, and be measured with as high precision as possible, in order to minimise its contribution to the $R(D_s)$ uncertainty. The possible normalisation channels which presents the same or similar topology with respect to the signal channel are enlisted in table 5.1.

Table 5.1: Possible normalisation channels presenting the same or similar topology with respect to the signal channel, their Branching Fractions, obtained by combining the values in ref. [56], and the relative error. In case of decays with B_d^0 instead of B_s^0 the Branching Fraction total is re-weighted for the f_d/f_s ratio [90, 91].

Decay type	Effective Branching Fraction	Relative error [%]
$B_s^0 \to D_s^-(\to K^+K^-\pi^-)\pi^+\pi^-\pi^+$	$(33.2 \pm 5.5)\times10^{-5}$	16.6
$B_s^0 \to D_s^-(\to \phi(\to K^+K^-)\pi^-)\pi^+\pi^-\pi^+$	$(13.8 \pm 2.3)\times10^{-5}$	16.7
$B_s^0 \to D_s^-(\to K^+K^-\pi^-)D_s^+(\to \pi^+\pi^-\pi^+)$	$(25.9 \pm 3.2)\times10^{-7}$	12.4
$f_d/f_s \times B_d^0 \to D^-(\to K^+K^-\pi^-)\pi^+\pi^-\pi^+$	$(24.2 \pm 3.0)\times10^{-4}$	12.4
$f_d/f_s \times B_d^0 \to D^-(\to K^+\pi^-\pi^-)\pi^+\pi^-\pi^+$	$(25.0 \pm 3.1)\times10^{-5}$	12.4
$f_d/f_s \times B_d^0 \to D^-(\to \phi(\to K^+K^-)\pi^-)\pi^+\pi^-\pi^+$	$(69.4 \pm 8.8)\times10^{-6}$	12.7
$f_d/f_s \times B_d^0 \to D^-(\to K^+K^-\pi^-)D_s^+(\to \pi^+\pi^-\pi^+)$	$(32.4 \pm 4.1)\times10^{-7}$	12.6
$f_d/f_s \times B_d^0 \to D^-(\to \pi^+\pi^-\pi^-)D_s^+(\to K^+K^-\pi^+)$	$(55.2 \pm 7.4)\times10^{-7}$	13.4

Among all the candidates reported in table 5.1, the $B_s^0 \to D_s^-(\to K^+K^-\pi^-)\pi^+\pi^-\pi^+$ and $B_s^0 \to D_s^-(\to K^+K^-\pi^-)\pi^+\pi^-\pi^+$ decays (fig. 5.2) are considered the best.

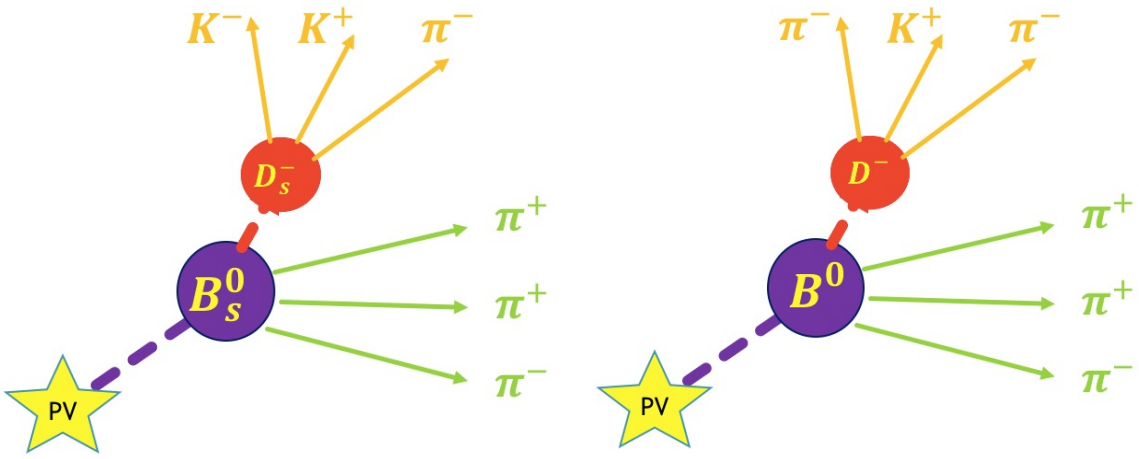

Figure 5.2: (Left) Schematic representation of the $B_s^0 \to D_s^-\pi^+\pi^-\pi^+$ and (Right) $B_d^0 \to D^-\pi^+\pi^-\pi^+$ decay.

The first decay has the same charged final state particles of the signal and the $R(D_s)$ ratio can be written as:

$$R(D_s) = \mathcal{K} \times \alpha = \frac{N_{sig}}{\epsilon_{sig}} \frac{\epsilon_{norm}}{N_{norm}} \frac{1}{\mathcal{B}(\tau^+ \to \pi^+\pi^-\pi^+(\pi^0)\nu_\tau)} \times \frac{\mathcal{B}(B_s^0 \to D_s^- 3\pi)}{\mathcal{B}(B_s^0 \to D_s^-\mu^+\nu_\mu)}. \tag{5.5}$$

The contribution to the relative uncertainty on the $R(D_s)$ measurement due to the measured

branching fractions, enlisted in table 5.2, is 19.10%.

Table 5.2: Values of the external input used to calculate $R(D_s)$ and the relative uncertainty. All the values are taken from refs. [56, 90]. The value of the τ Branching Fraction listed is obtained considering the combination of the two τ decays $\tau^+ \to \pi^+\pi^-\pi^+\nu_\tau$ and $\tau^+ \to \pi^+\pi^-\pi^+\pi^0\nu_\tau$.

External input	Value[%]	Relative uncertainty[%]
$\mathcal{B}(\tau^+ \to \pi^+\pi^-\pi^+(\pi^0)\nu_\tau)$	11.76±0.07	0.60
$\mathcal{B}(B_s^0 \to D_s^- 3\pi)$	0.61±0.10	16.4
$\mathcal{B}(B_s^0 \to D_s^- \mu^+\nu_\mu)$	2.49±0.24	9.64
$\mathcal{B}(B^0 \to D^- 3\pi)$	0.60±0.07	11.7
$\mathcal{B}(D^- \to K^+\pi^-\pi^-)$	9.38±0.16	1.71
$\frac{f_s}{f_d} \times \mathcal{B}(D_s^- \to K^+K^-\pi^-)$	1.26±0.05	3.97

The second normalization channel also has a topology similar to the signal, but involve B_d^0 and the D^- mesons instead of the B_s^0 and D_s^- mesons. Using a B_d^0 decay is advantageous as its production rate in the LHCb acceptance is enhanced with respect to that of the B_s^0 by a factor f_d/f_s larger than four [90, 91]. To maximize the yield, the favoured D^- decay to $K^+\pi^-\pi^-$ is considered instead of $K^+K^-\pi^-$, which is suppressed almost of a factor 10 [56]. The different masses of the particles involved lead to some differences in the kinematics of the decay. The ratio in this case can be written as:

$$\begin{aligned} R(D_s) &= \mathcal{K} \times \alpha \\ &= \frac{N_{sig}}{\epsilon_{sig}} \frac{\epsilon_{norm}}{N_{norm}} \frac{\mathcal{B}(D^- \to K^+\pi^-\pi^-)}{\mathcal{B}(\tau^+ \to \pi^+\pi^-\pi^+(\pi^0)\nu_\tau) \times \frac{f_s}{f_d} \cdot \mathcal{B}(D_s^- \to K^+K^-\pi^-)} \times \frac{\mathcal{B}(B^0 \to D^- 3\pi)}{\mathcal{B}(B_s^0 \to D_s^- \mu^+\nu_\mu)}. \end{aligned} \tag{5.6}$$

Despite the presence of additional contributions in the α term (f_s/f_d and the $\mathcal{B}(D_s^- \to K^+K^-\pi^-)$ $\mathcal{B}(D^- \to K^+\pi^-\pi^-)$) the resulting relative uncertainty on $R(D_s)$ due to external inputs is 14.3%[1], which is smaller than that of the $B_s^0 \to D_s^-\pi^+\pi^-\pi^+$ channel.

The additional contributions to the uncertainty on $R(D_s)$ related to the normalisation channels are related to the $\mathcal{K}$ term and will be extensively discussed in Chapter 6.

5.3 Data and simulation samples

The analysis discussed in this thesis is based on the data collected by the LHCb collaboration during 2012, corresponding to an integrated luminosity of 2 fb^{-1} of pp collisions events at $\sqrt{s} = 8$ TeV. The analysis developed uses several simulated samples to study the properties of the signal and of the normalization channels, and of the main background contributions. The background contributions given by decays to final states containing three pions and a D_s^- meson have been studied using simulated sample, incl_$H_b \to D_s 3\pi X$, where the events are produced inclusively from any source containing a $b-$hadron decay to a D_s^- and the three pions are required to be reconstructed in the LHCb acceptance and satisfy minimal requirements. These samples are

[1]The calculation includes the correlation between the measurements of $\frac{f_s}{f_d} \times \mathcal{B}(D_s^- \to K^+K^-\pi^-)$ and of the branching fraction $\mathcal{B}(B_s^0 \to D_s^-\mu^+\nu_\mu)$ [90], $\rho = -0.581$.

used to develop the selection and to model the relevant contributions.

The list of the simulated samples relevant for the analysis is given in table 5.3, where the statistics is also given in units of luminosity. Such statistics has been calculated considering the known branching fractions, the detector conditions, the fractions f_s and f_d, and the value of the $b\bar{b}$ cross section [92] at 7 TeV.

All the samples are generated, reconstructed, and selected following the 2012 detector conditions in order to reproduce the same processing flow of data. To save CPU time and disk space, events are filtered at generation level. For example, the charged final state particles from the decay chain are required to be in the LHCb acceptance

Table 5.3: Simulated samples produced for this analysis listed with Event type that is a eight digit number following the convention defined by LHCb collaboration, the number of events generated for the simulation and those saved by LHCb correspond to the Up/Down polarity of the magnetic field. The last line represents the inclusive sample of $b-$hadron decaying into D_s^- and three prompt pions.

Decay type	Event type	Generated events	saved events	eq. fb^{-1}
$B_s^0 \to D_s^-(\to K^+K^-\pi^-)\tau^+(\to \pi^+\pi^-\pi^+(\pi^0))\nu_\tau$	15363002	2M/2M	40k/40k	79.3
$B_s^0 \to D_s^{*-}(\to D_s^-\gamma/\pi^0)\tau^+(\pi^+\pi^-\pi^+(\pi^0))\nu_\tau$	13763200	4M/4M	80k/80k	88.9
$B_s^0 \to D_s^-(\to K^+K^-\pi^-)\pi^+\pi^-\pi^+$	13266069	3.2M/3.2M	61k/61k	9.3
$B_d^0 \to D^-(\to K^+\pi^-\pi^-)\pi^+\pi^-\pi^+$	11266009	41M/41M	425k/425k	10.9
incl_$H_b \to D_s 3\pi X$	23903000	625M/625M	2.5M/2.5M	8.8

Datasets collected with both the magnet polarities (Up/Down) are merged, this is also true for the simulation samples. As anticipated also in the sec. 1.2.2, the acquisition of data with different magnet polarities is done to avoid systematic effects related to candidates reconstruction and to take into account asymmetries in the detector.

Chapter 6

Selection of signal and normalisation channels

This chapter discusses how the signal and the normalisation channels are selected. The contents covered in this chapter follow and deepen the studies performed in the work [127]. The selection aims at reducing the different sources of background while maintaining the largest fraction of useful events and consists in several steps. Initial selection steps have been developed in common to both signal and normalisation channels in order to minimise differences in the corresponding efficiencies (secs. 6.1,6.2,6.3). Then, selections for signal and normalisation channels split to clearly identify the normalisation (sec. 6.4) and further improve the semileptonic signal decay selection (Chapter7).

A quantitative comparison between the two considered normalisation channels is made based on their statistical and systematic uncertainties contributions to the $R(D_s)$ uncertainty (sec. 6.5).

6.1 Stripping and Trigger Selections

According to the computing model the collision events that pass the trigger requirements are acquired as raw data, then are reconstructed offline and finally are saved on disk/tape after a further selection known as *Stripping*. The Stripping is a centralised selection of events of interest, it is implemented by stripping lines which contain the instructions for reconstructing the particles of interest from the reconstructed stable particles, and the corresponding selections to be applied. The signal and the normalisation channels are selected by the dedicated stripping lines `Bs2DsTauNuForB2XTauNu` (for the B_s^0 decays) and `B0d2DTauNuForB2XTauNu` (for the B_d^0 decays), and then refined with an offline selection. The cuts applied by the stripping selections are summarised in table 6.1 and are based on several geometrical and kinematic variables that discriminate between signal and background. For example the variable DIRA corresponds to the cosine of the angle between the $B_{(s)}$ particle's momentum and flight direction, computed from the positions of the origin and decay vertices, the variable DOCA represents the maximum distance of closest approach between all possible pairs of particles and IP χ^2 is the difference

between the χ^2 of the PV reconstructed with and without the track under consideration.

Table 6.1: Cuts implemented in the stripping selections `Bs2DsTauNuForB2XTauNu` and `B0d2DTauNuForB2XTauNu`. Both the selections apply minimal requirements on reconstructed events in order to retain only candidate good decays needed for the analysis.

Cut	Value
$B_{(s)}$	
$\Delta(M)$	(-2579)-300 or 720-1721 MeV/c^2
Max. DOCA	< 0.15 mm
DIRA	> 0.995
$D^+_{(s)}$	
p_T	> 1600 MeV/c
$\lvert M - M_{D^+_{(s)}} \rvert$	< 40.0MeV/c^2
DIRA	> 0.995
Vertex distance χ^2	> 36 if $D_s^+ > 50$ if D^+
Vertex $\chi^2/NDOF$	< 10
IP χ^2	> 10
K from $D_{(s)}$	
p_T	> 1500MeV/c
Track $\chi^2/NDOF$	< 30
IP χ^2	> 10
Ghost Probability	< 0.4
PIDK	> 3
π from $D_{(s)}$	
p_T	> 150 MeV/c
Track $\chi^2/NDOF$	< 3
IP χ^2	> 10
Ghost Probability	< 0.4
PIDK	< 50
τ	
$m(\pi\pi\pi)$	400-3500 MeV/c^2
$m(\pi_1\pi_2)$ or $m(\pi_2\pi_3)$	< 1670 MeV/c^2
Max. DOCA	< 0.15 mm
DIRA	> 0.99
Vertex χ^2	< 25
max 1 pion with p_T	< 300 MeV/c
min 2 pions with IP χ^2	> 5
π from τ	
p_T	> 150 MeV/c
Track $\chi^2/NDOF$	< 4
IP χ^2	> 4
Ghost Probability	< 0.4
PIDK	< 8

Since the final state of the decays of interest only involves hadrons, the trigger requirements

at L0 level (hadrware trigger) are `L0_hadron_TOS`[1], or `L0_Global_TIS`[2], while at the HLT1 level (software trigger) the requirement is `Hlt1TrackAllL0Decision_TOS`[3]. In this thesis, the requests on the Hlt2 trigger are not implemented, which means that it is considered the "OR" between all the available lines. A refinement of the Hlt2 trigger request will be the subject of an advanced study of this analysis. The efficiency of the trigger selection is evaluated using simulated samples. It amount to 96.9% on the signal and on the $B_s^0 \to D_s^- \pi^+ \pi^- \pi^+$ normalisation channel, while is about 97.3% on the $B_d^0 \to D^- \pi^+ \pi^- \pi^+$ simulated sample.

6.2 Decay reconstruction and preliminary selection

Candidate $B_{(s)}$ signal and normalisation decays are formed by the combination of three charged particles, compatible with the pion mass hypothesis, originated from a common vertex, and displaced from any PV, and a $D^+_{(s)}$candidate. The $D^+_{(s)}$candidate is formed by three particles originated from a common vertex, displaced from any PV, and consistent with the mass hypothesis of two kaons and one pion, in the D_s^- case, or one kaon and two pions of the same charge, in the D^- case. The candidate decays are formed and selected at stripping level and used in the offline selection described in the following.

To improve the purity of $D^+_{(s)}$signal a selection, referred to as *"Xc_selection"*, is applied. It is based on the reconstructed invariant mass of the $D^+_{(s)}$candidates, which is required to be within ± 20 MeV/c^2 the known value and on the identification of the final state particles, by applying different PID requirements to the final state particles depending on their kinematics and the D_s^- (D^-) dynamics. For the $D_s^- \to K^+K^-\pi^-$ decay, that is dominated by the $\phi(1020)\pi^+$ and $K^*(892)^0K^+$ decays (see fig. 6.1 (Left)) the selection cuts are shown in table 6.2 and supersede those of table 6.1.

Table 6.2: Cuts applied on the $D_s^- \to K^+K^-\pi^-$ decay considering the three mass region around $\Phi(1020)$, $K^*(892)^0$ and the non resonant.

Decay modes	Mass condition MeV/c^2	PID condition
$D_s^+ \to \phi(1020)\pi^+$	$\lvert m(K^+K^-) - 1020\rvert \leq 12$	K^+ PIDK> -2 K^- PIDK> -2
$D_s^+ \to K^*(892)^0K^+$	$\lvert m(K^+K^-) - 1020\rvert > 12$ $\lvert m(K^-\pi^+) - 892\rvert < 50$	K^+ PIDK> -2 K^- PIDK> 5
$D_s^+ \to K^+K^-\pi^+$ (non resonant)	$\lvert m(K^+K^-) - 1020\rvert > 12$ $\lvert m(K^-\pi^+) - 892\rvert > 50$	K^+ PIDK> 5 K^- PIDK> 5 π^+ PIDK< 10

In the case of the $D^- \to K^+\pi^-\pi^-$ decay, which dominated by the broad resonances $K^*(892)^0$ and $K^{*0}(1430)$ (see fig. 6.1 (Right)), the PID cuts are applied at the level of stripping line selection of table 6.1.

[1] the final-state hadrons of the signal B_s^0 decays are required to satisfy the trigger selection (Trigger-On-Signal)
[2] the trigger requirements are satisfied independently on the signal (Trigger-Independent-of-Signal)
[3] at least one track in the signal decay satisfies the requirements of IP > 0.1 mm with respect to each PV and $p_{\mathrm{T}} > 1.6 GeV/c$.

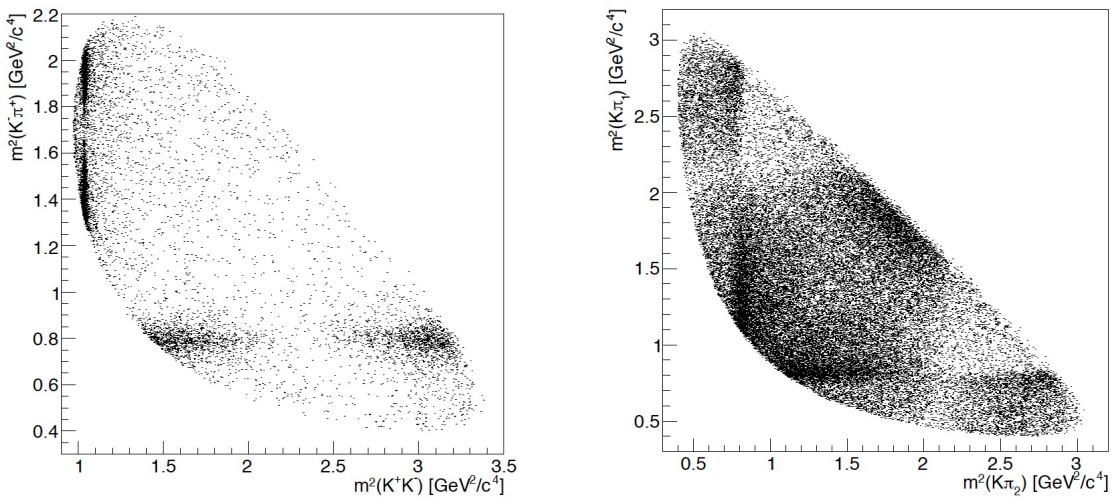

Figure 6.1: (Left) $D_s^+ \to K^+K^-\pi^+$ Dalitz plot of events selected in the ± 50MeV/c^2 B_s^0 mass range. The concentration of events in the vertical band at $m^2(K^+K^-) \sim 1$ GeV$^2/c^4$ corresponds to the $D_s^+ \to \phi(1020)\pi^+$ decays. Whereas the horizontal band at $m^2(K^-\pi^+) \sim 0.8$ GeV$^2/c^4$ corresponds to $D_s^+ \to K^*(892)^0K^+$ decays. The remaining decays are referred to as "non-resonant". (Right) $D^+ \to K^+\pi^-\pi^+$ Dalitz plot of events selected in the ± 50MeV/c^2 B^0 mass range. The concentration of events in the vertical and in the horizontal band at $m^2(K\pi_1) \sim 0.8$ GeV$^2/c^4$ or $m^2(K\pi_2) \sim 0.8$ GeV$^2/c^4$, respectively, corresponds to the $D^+ \to K^*(892)^0\pi^+$ and $D^+ \to K^*(1430)^0\pi^+$ decays whereas, the remaining decays are referred to as "non resonant".

Vetoes are applied to suppress c-hadron decays in three charged particles that can be selected as $D^+_{(s)}$candidates due to misidentification of the final state particles. In particular, the vetoes reported in table 6.3 are applied to suppress misidentified D^+ and Λ_c^+ in the $D_s^- \to K^+K^-\pi^-$ candidate selection, while in table 6.4 are reported those applied to veto the D_s^- and the Λ_c^+ while performing the $D^- \to K^+\pi^-\pi^-$ reconstruction. Moreover, a veto to reject $D^0 \to K^+K^-$ decays combined with an additional random pion is applied by requiring the K^+K^- invariant mass below the 1840 MeV/c^2. In the case of the $D^- \to K^+\pi^-\pi^-$ selection the D^0 veto is applied to both the combinations of the kaon with a potentially misidentified pion.

Table 6.3: Vetoes applied to suppress misidentified c-hadron in the $D_s^- \to K^+K^-\pi^-$ candidate selection.

Decay hypothesis	Mass cut MeV/c^2	PID cut
$D^+ \to K^-\pi^+\pi^+$	$\lvert m' - 1869\rvert < 30$	K^+ PIDK< 10
$\Lambda_c^+ \to pK^-\pi^+$	$\lvert m' - 2280\rvert < 30$	K^+ (PIDK-PIDp)< 5

6.3 Multivariate (BDT) selections

Different kinds of background need to be considered and reduced to improve the signal selection:

Table 6.4: Vetoes applied to suppress misidentified c-hadron in the $D^- \to K^+\pi^-\pi^-$ candidate selection.

Decay hypothesis	Mass cut MeV/c^2	PID cut
$D_s^+ \to K^+K^-\pi^+$	$\lvert m' - 1968\rvert < 30$	π^+ PIDK< 0
$\Lambda_c^+ \to pK^-\pi^+$	$\lvert m' - 2280\rvert < 30$	π^+ PIDp< 0

- $b-$hadron decays to final states with similar signal topology with final state particles misidentified as signal particles or with additional particles that may be not reconstructed, partially reconstructed;
- combinations of particles that belong to sources different from the signal or are combinations of part of the signal decay and particles from other sources, so called combinatorial background.

To suppress such backgrounds and enhance the signal contribution several selections based on multivariate analysis classification exploiting the ROOT Toolkit for Multivariate Analysis (TMVA) [125] are studied. The technique exploited is the Boosted Decision Tree (BDT). The BDTs are trained using samples of well-identified signal and background and exploit the discrimination power between signal and background of several input variables. In particular, three BDTs have been implemented to refine the selection of the $D^+_{(s)}$, 3π and $B_{(s)}$ candidates.

The BDT for the *"$D^+_{(s)}$ selection"* aims at reducing the background due to combinatorial. It is developed using as training samples for the *signal* D_s^- candidates from the simulation sample of $B_s^0 \to D_s^-\tau^+\nu_\tau$, where the reconstructed D_s^- are matched to the "true" $D_s^- \to K^+K^-\pi^-$ decays. The *background* sample consists of D_s^- candidates from data by requiring the reconstructed B_s^0 mass larger than 5200MeV/c^2 and $\lvert m(D_s) - 1968\rvert > 30$ MeV/c^2. The BDT relies on several input variables describing the properties of D_s^- and its decay products. Among the possible variables, those showing the larger discriminating power between signal and background are chosen. It is also checked that the inputs have similar distributions for the $B_s^0 \to D_s^-\tau^+\nu_\tau$, $B_s^0 \to D_s^-\pi^+\pi^-\pi^+$ and $B_d^0 \to D^-\pi^+\pi^-\pi^+$ samples. For the D_s^- the inputs are: transverse momentum, pseudorapidity, flight distance from primary vertex (FD_OWNPV), flight distance from the B_s^0 vertex (FD_ORIVX), χ^2 vertex reconstruction (ENDVERTEX_CHI2). For the D_s^- decay products the inputs are: transverse momentum, impact parameter χ^2 and the track ghost probability.

The effectiveness of the BDT selection can be appreciated from fig. 6.2 (left), where the BDT output response on the D_s^- candidate is shown for the signal (black), the background (red) and for the $B_s^0 \to D_s^-\pi^+\pi^-\pi^+$ simulation sample (green) as well as for the D^- candidate in the $B_d^0 \to D^-\pi^+\pi^-\pi^+$ simulation sample (blue). The similarity among the BDT output distributions of signal and normalisation channels indicate that the BDT performs in the same way on both D_s^- and D^- signals, addressing the requirement to perform a common selection. The different distribution of the background allows a good discrimination power between D_s^- and D^- signals from combinatorial background. Figure 6.2 (Right) shows the efficiency of the signal

and background as function of the cut on the BDT output. The cut value -0.0876, indicated by the vertical line, corresponds to an efficiency of 95% and a background rejection of 77%.

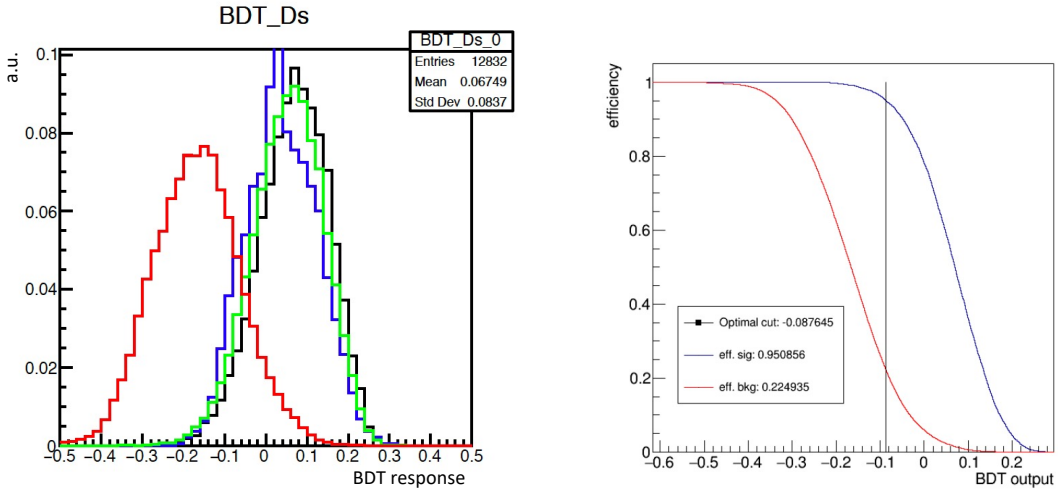

Figure 6.2: (Left) Distribution of the BDT output for the *"$D^+_{(s)}$ selection"* for the (red) background and D^-_s signal in (black) $B^0_s \to D^-_s \tau^+ \nu_\tau$ and (green) $B^0_s \to D^-_s \pi^+ \pi^- \pi^+$ and D^- signal in (blue) $B^0_d \to D^- \pi^+ \pi^- \pi^+$ simulation samples. (Right) Efficiency for (blue) signal and (red) background of the BDT *"$D^+_{(s)}$ selection"* as a function of the cut value. The vertical line indicate the cut to which the signal efficiency is 95% and the background rejection almost 77%.

The peculiarity of the signal and normalisation decays is also related to the topology of the three charged pions originated from a vertex displaced from the PV. To refine the selection of the three charged pions associated to the signal and normalisation $B_{(s)}$ decays and suppress the large contamination due to pions produced in the pp collisions a dedicated BDT selection has been developed using as training samples for the *signal* the three-pions candidates from the $B^0_s \to D^-_s \tau^+ \nu_\tau$ simulation sample, where the three pions are matched to the "true" pions from the τ decay in the signal decay chain. The *background* training sample is given by data with a reconstructed B^0_s mass larger than 5450 MeV/c^2, dominated by combinatorial background. The BDT inputs are variables related to the 3π vertex, such as the distance of closest approach (DOCA) between two tracks, the the vertex χ^2 (ENDVERTEX_CHI2), and to each pion, such as the pseudorapidity, the impact parameter χ^2 of the pion track from the primary vertex (IP_CHI2_OWNPV) and the track ghost probability.

The output of this BDT classifier is shown in fig. 6.3 left. Also in this case are shown the distribution of the two normalisation channels using the same code colors of fig. 6.2. The signal and background selection efficiencies as a function of the BDT cut are plotted in fig. 6.3 right. By choosing a cut at -0.0727 it is possible to select 95% of the signal and reject 87.9% of the background.

A further refinement of the selection is performed by another BDT that focuses on the inputs of the reconstructed $B_{(s)}$ candidates. In this case the *signal* training sample is given by the simulated sample of $B^0_s \to D^-_s \tau^+ \nu_\tau$, where the reconstructed B^0_s candidates are associated with the "true" signal decays. The *background* training sample is obtained by merging reconstructed

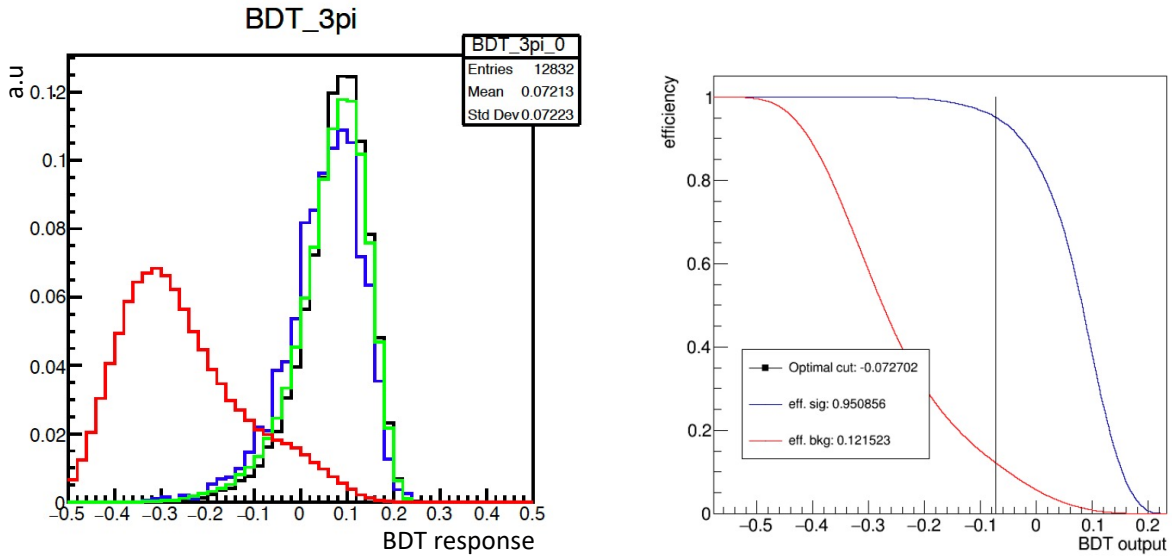

Figure 6.3: (Left) Distribution of the BDT output for the *"3π selection"* for the (red) background, (black) signal $B_s^0 \to D_s^- \tau^+ \nu_\tau$ and normalisation samples: (green) $B_s^0 \to D_s^- \pi^+ \pi^- \pi^+$ and (blue) $B_d^0 \to D^- \pi^+ \pi^- \pi^+$. (Right) Efficiency for (blue) signal and (red) background of the BDT *"3π selection"* as a function of the cut value. The vertical line indicate the cut to which the signal efficiency is 95% and the background rejection almost 88%.

B_s^0 candidates in data with mass larger than 5450 MeV/c^2 and reconstructed B_s^0 candidates from a "wrong-sign" data sample with mass larger than 5300 MeV/c^2. The latter sample is obtained applying the same selection cuts used for the signal selection on a combination of D_s^- and 3π candidates with the same (wrong) charge, selected by a dedicated stripping line (`Bs2DsTauNuWSForB2XTauNu`). The two samples show similar features and are merged to enrich the statistics of the background sample, that is necessary for a reliable training of the BDT. To gain signal-to-background discrimination power, a cut on the output of the BDT classifiers for the *"$D_{(s)}^+$ selection"* and *"3π selection"* is applied prior the training of the BDT for the *"$B_{(s)}$ selection"*.

The BDT inputs are the B_s^0 pseudorapity and flight distance from the primary vertex (FD_OWNPV), the BDT output responses of the "$D_{(s)}^+$" and "3π" selections.

The BDT output distribution for signal, normalisation and background samples are shown in fig. 6.4 left, where the same colour code of fig. 6.2 and 6.3 is used. The separation power between signal and background achieved in this case is smaller than the previous cases, mainly due to the cut on the BDT for the "$D_{(s)}^+$" and "3π" selections. The requirement on the similarity of the distributions for signal and $B_s^0 \to D_s^- \pi^+ \pi^- \pi^+$ is satisfied, while the $B_d^0 \to D^- \pi^+ \pi^- \pi^+$ distribution shows some deviations. This has some impact on the efficiency for the selection cuts as will be discussed later in sec. 6.5.3. Figure 6.4 right, shows the selection efficiency for (blue) signal and (red) background as function of the BDT cut. By choosing a cut at -0.0655 it is possible to select the 90% of the signal and reject about 65% of the background.

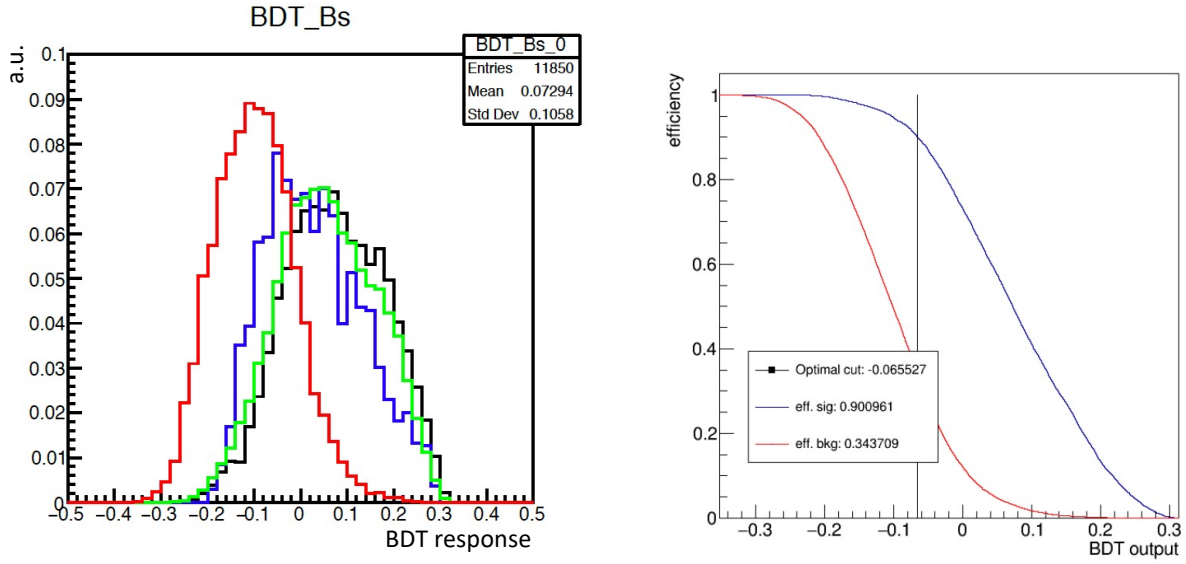

Figure 6.4: (Left) Distribution of the BDT output for the *"$B_{(s)}$ selection"* for the (red) background, (black) signal and normalisation samples: (green) $B_s^0 \to D_s^- \pi^+ \pi^- \pi^+$ and (blue) $B_d^0 \to D^- \pi^+ \pi^- \pi^+$. (Right) Efficiency for (blue) signal and (red) background of the BDT *"$B_{(s)}$ selection"* as a function of the cut value. The vertical line indicate the cut to which the signal efficiency is 90% and the background rejection almost 65%.

6.4 Separation of signal and normalisation channels

The three BDTs discussed so far allow to separate the signal from the background (mostly combinatorial) preserving similar distributions between the signal and normalisation samples. To separate the signal from the normalisation the differences in the three pions present in the final states can be exploited. Indeed in the signal case, the three pions originate from the τ vertex decay which is displaced from the B_s^0 vertex by about 90 μm in average, while in the normalisation samples they originate directly from the $B_{(s)}$ decay vertex. Figure 6.5 shows the distribution of the displacement along the z coordinate of the $\tau/3\pi$ system with respect to the $B_{(s)}$ decay vertex , normalised to its uncertainty, referred to as B_Y_SEP. The distributions for signal (in red) and normalisation channels (in black and green) are clearly different, though they have an overlapping region. By requiring B_Y_SEP> -4.5 (< -4.5) it is possible to select $B_{(s)}$ candidates with an efficiency of about 99.8% (36.2%) in the normalisation (signal) channels. More details on the B_Y_SEP discriminating variable are discussed in Chapter 7.

6.5 Yield of the normalisation channels

The impact of the different selection cuts (*"Xc_Selection"*, BDTs and the separation between the signal and the normalisation channels) are shown in fig. 6.6 for B_s^0 and B_d^0 candidates selected by the corresponding stripping lines (sec. 6.1) in data. The semileptonic signal channel candidates contribute to a continuous distribution below the $B_{(s)}$ mass, while the normalisation

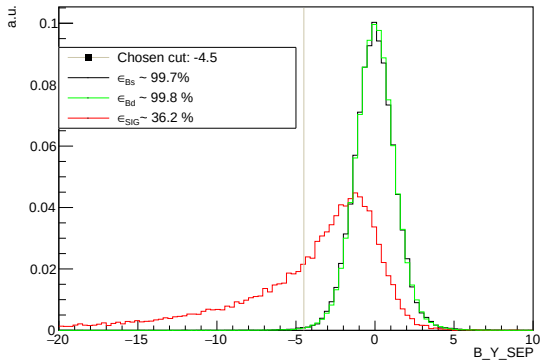

Figure 6.5: Separation between $B_{(s)}$ vertex with respect to the 3π vertex along z coordinate for the (red) signal, the (black) $B_s^0 \to D_s^- \pi^+ \pi^- \pi^+$ and the (green) $B_d^0 \to D^- \pi^+ \pi^- \pi^+$ normalisation channels. The red vertical line corresponds to an optimised separation cut (see Chapter 7).

channel candidates contribute to the peaking structure around the $B_{(s)}$ mass.

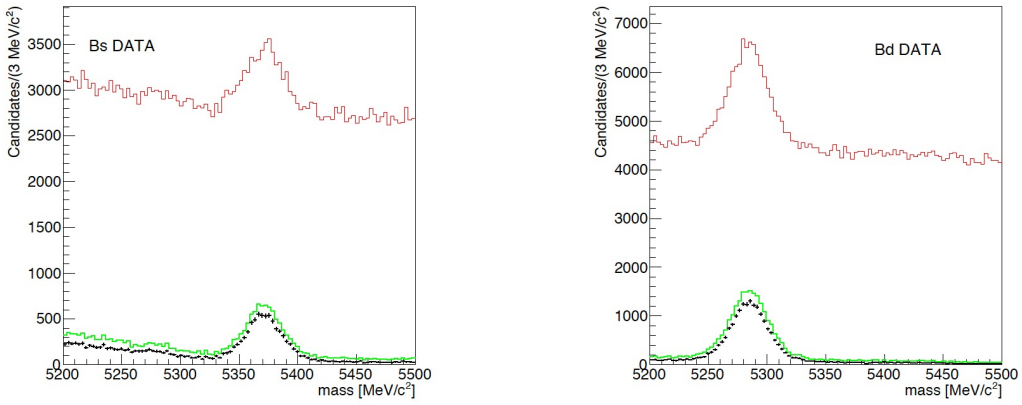

Figure 6.6: Invariant mass distribution for the (Left) B_s^0 and (Right)B_d^0 candidates after the (red) *"Xc_Selection"*, (green) BDT selections, and (black) after a preliminary cut to select the normalisation channels based on the distance between the $b-$meson and 3π vertices.

While the normalisation channels are clearly identified from the peak in the $D_{(s)}^+ 3\pi$ mass distribution, the semileptonic B_s^0 candidates decays need a further selection to suppress the background sources arising from b-hadron decays that are partially reconstructed. A detailed study on the background that affect the signal selection is treated in the next Chapter.

To achieve the final measurement of $R(D_s)$ is essential to measure the $\mathcal{K}$, in particular what are needed are the yields of signal and normalisation channels and their efficiencies. The yields of the normalisation channels are evaluated by means of a maximum-likelihood fit to the invariant-mass distributions of the B_s^0 and B_d^0 candidates selected in data by the different criteria described so far. The fit exploits the `RooFit` [126] libraries of the `ROOT` [124] package to model the probability density functions (PDFs) of the different contributions. The contribution due to the

normalisation channel decays is modelled by the sum of a Gaussian and a Crystal Ball or of two Crystal Ball functions; the combinatorial background is modelled by an exponential function; while the relevant background due to partially reconstructed and misidentified b-hadron decays are described by dedicated functions obtained from simulation.

6.5.1 Fit of the $B_s^0 \to D_s^- \pi^+ \pi^- \pi^+$ normalisation channel

The reconstructed B_s^0 mass distribution of the $B_s^0 \to D_s^- \pi^+ \pi^- \pi^+$ simulation sample is shown in fig. 6.7 (Left). Its shape is well described by the sum of a Gaussian function and a Crystal Ball with parameters μ and σ_{gauss}, and μ and σ_{CB} and n_{CB} respectively. While fitting data, all the parameters from the fit to simulation are fixed to their central values except for the mean, which is floated. Moreover, the parameters related to the mass resolution, σ_{gauss} and σ_{CB}, are multiplied by a common free scale factor to account for possible differences between data and simulation.

The main background due to b-hadron decays in the mass range of interest, (*i.e.* between 5250-5500MeV/c^2) are $B_s^0 \to D_s^- K^+ \pi^- \pi^+$, $B_s^0 \to D_s^{*-}(D_s^- \gamma)3\pi$, and $B_d^0 \to D^- \pi^+ \pi^- \pi^+$ decays. Their shapes are studied by means of a simplified simulation based on the `TGenPhaseSpace` class from the `ROOT` package [124] that accounts for the kinematics of the decay and for the detector resolutions. The $B_s^0 \to D_s^- K^+ \pi^- \pi^+$ decay contributes to the mass region of interest in case the kaon in the final state is misidentified as a pion. Its distribution is modelled by a Crystal Ball function. The $B_s^0 \to D_s^{*-}(D_s^- \gamma)3\pi$ decay, where the γ is not reconstructed, is modelled by an analytic function. The $B_d^0 \to D^- \pi^+ \pi^- \pi^+$ decays, where a π^- from the $D^- \to K^+ \pi^- \pi^-$ decay is misidentified as a kaon, is a potential background source which is highly suppressed thanks to the vetoes applied in the *"Xc_Selection"*. It is described with the sum of a Novosibirsk and a Crystal Balls functions. Its contribution is indeed found to be consistent with zero in the fit.

The resulting fit to the data distribution is shown in fig. 6.7 (Right). The resulting yield is

$$N_{norm} = 7969 \pm 166$$

which contributes to the statistical uncertainty on $\mathcal{K}$ due to the yield of the normalisation channel of 2.1%.

6.5.2 Fit of the $B_d^0 \to D^- \pi^+ \pi^- \pi^+$ normalisation channel

The yield of the $B_d^0 \to D^- \pi^+ \pi^- \pi^+$ normalisation decays is obtained similarly to what explained for the $B_s^0 \to D_s^- \pi^+ \pi^- \pi^+$. In this case the shape of the $B_d^0 \to D^- \pi^+ \pi^- \pi^+$ normalisation channel is modelled by the sum of two Crystal Ball functions, whose parameters are obtained from a fit to the invariant-mass distribution of the simulated sample. While fitting data, all the parameters from the fit to simulation are fixed to their central values, except for the mean and the resolution scale factor which are floated.

The fit, shown in fig. 6.8 is performed in the 5200-5450MeV/c^2 mass region, where the main

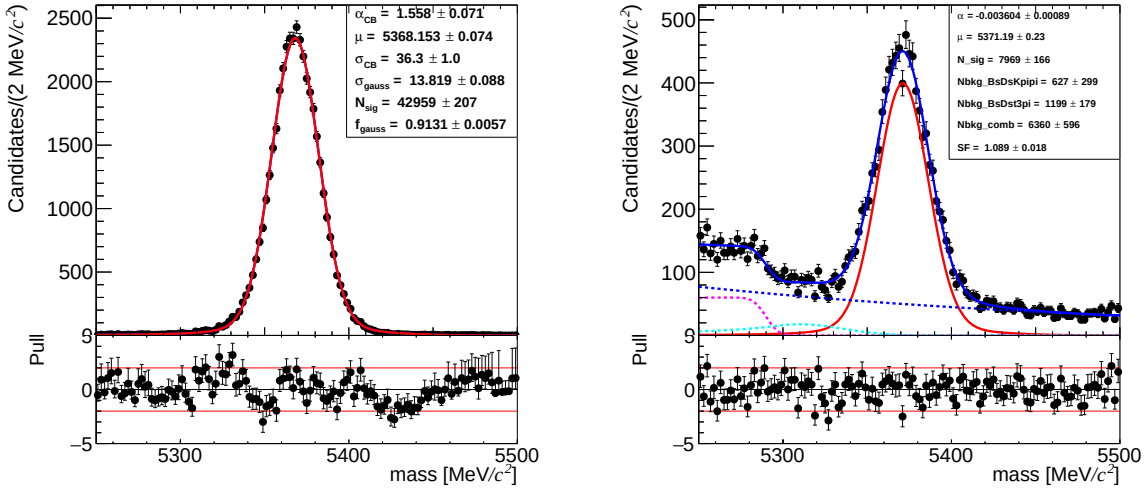

Figure 6.7: (Left) Fit to the invariant-mass distribution of the $B_s^0 \to D_s^- \pi^+ \pi^- \pi^+$ simulated sample after the full selection described above. In the legend are enlisted all the fit parameters. The bottom part of the plot represents the fit pulls which are defined as the difference between the data and the fit normalised by the statistical uncertainty. (Right) Invariant-mass distribution of the B_s^0 selected candidates in data. The fit function (blue line) accounts for several background components: combinatorial (dashed blue line), $B_s^0 \to D_s^- K^+ \pi^- \pi^+$ (dashed cyan), $B_s^0 \to D_s^{*-}(D_s^- \gamma) 3\pi$ (dashed magenta). The normalisation $B_s^0 \to D_s^- \pi^+ \pi^- \pi^+$ decays (red line) are described by the sum of a gaussian function and a Crystal Ball (dashed red lines).

source of background to be considered is due combinatorial. The yield obtained is

$$N_{norm} = 19092 \pm 169$$

which contributes to the statistical uncertainty on $\mathcal{K}$ of about 0.9%.

6.5.3 Efficiencies

As mentioned before, the determination of $R(D_s)$ depends on the efficiency ratio for the normalisation, ϵ_{norm}, and the signal channels, ϵ_{sig} (see eq. 5.4). Since two different normalisation channels are considered, two ratios are determined. The total efficiency of the signal and of the normalisation channels is obtained from simulation, considering all the selections applied from the simulation production till the offline selection described so far. Table 6.5 reports the corresponding values.

The efficiency ratio evaluated considering the $B_s^0 \to D_s^- \pi^+ \pi^- \pi^+$ normalisation channel, including the statistical uncertainty due to the limited size of the simulated samples, is 5.10±0.06, which corresponds to an uncertainty on the determination of $\mathcal{K}$ of 1.2%. In the case of the $B_d^0 \to D^- \pi^+ \pi^- \pi^+$, the efficiency ratio is 2.08 ± 0.02, and gives a contribution to the uncertainty of $\mathcal{K}$ of 0.9%.

As can be noticed, despite the selection is common to the signal and the normalisation

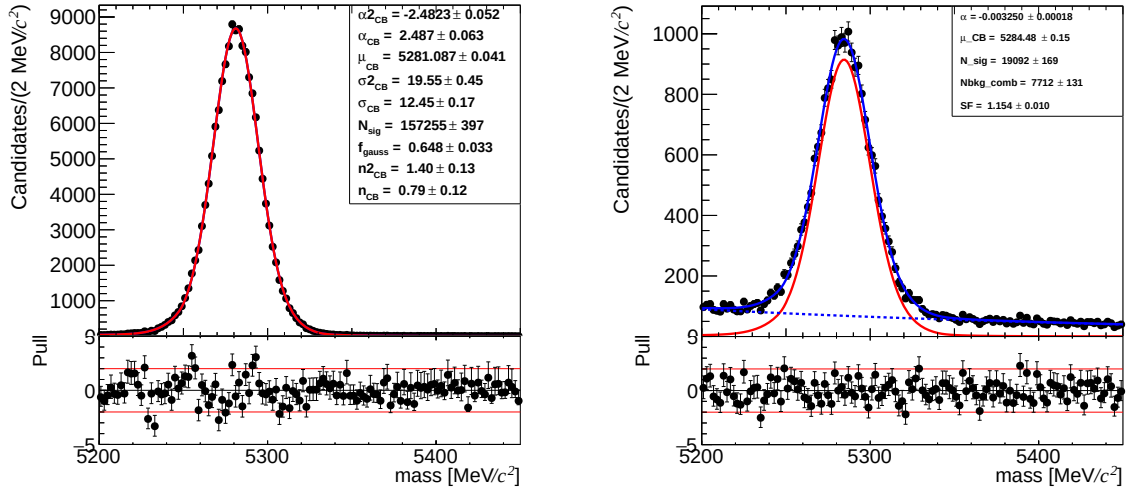

Figure 6.8: (Left) Fit to the invariant-mass distribution of the $B_d^0 \to D^-\pi^+\pi^-\pi^+$ simulated sample after the full selection described above. In the legend are enlisted all the fit parameters. The bottom part of the plot shows the fit pulls defined as the difference between the data and the fit normalised by the statistical uncertainty. (Right) Fit to the B_d^0 candidates mass spectrum after the application of the selection described above, (red) the function used to describe the $B_d^0 \to D^-\pi^+\pi^-\pi^+$ normalisation channel, (dashed blue) the combinatorial background.

Table 6.5: Efficiencies evaluated on simulated samples of signal and normalisation channels for each step of the selection. Each efficiency is computed with respect to the previous cut. Uncertainties are statistical only.

Step	$B_s^0 \to D_s^-\tau^+\nu_\tau$	$B_s^0 \to D_s^-\pi^+\pi^-\pi^+$	$B_d^0 \to D^-\pi^+\pi^-\pi^+$
	$\epsilon_{sig}[\%]$	$\epsilon_{norm}[\%]$	$\epsilon_{norm}[\%]$
Generation	2.331 ± 0.004	3.405± 0.005	14.51±0.02
Filtering	1.916± 0.007	2.459± 0.007	0.4725±0.0005
Stripping	74.58±0.15	75.67±0.12	70.50±0.05
Simulation truth	73.18± 0.18	75.16±0.14	68.38±0.06
Trigger	96.94± 0.08	96.91± 0.07	97.30± 0.02
Xc_selection	82.06± 0.18	81.43± 0.15	54.55±0.08
BDTs	81.14±0.21	77.93± 0.18	68.10± 0.10
B_Y_SEP cut	36.34± 0.28	99.67±0.03	99.78±0.01
Total	$(5.72 \pm 0.06) \times 10^{-5}$	$(29.19 \pm 0.15) \times 10^{-5}$	$(11.92 \pm 0.04) \times 10^{-5}$

channels, the efficiency for the signal decay is smaller than that of the normalisation channels. This is due to the different kinematic distributions of the final state particles that for the semileptonic signal decay, due to the presence of neutrinos, have lower momenta than those of the normalisation channels. The smaller efficiency ratio obtained considering the $B_d^0 \to D^-\pi^+\pi^-\pi^+$ channel is motivated by differences in the *"Xc_Selection"* and by kinematics, that impact the BDT B_s^0 distributions (see sec. 6.3 and fig. 6.4).

6.5.4 Systematics

Possible sources of systematic uncertainties can affect the determination of $\mathcal{K}$ are:

- related to differences between data and simulation: small deviations between data and simulation can affect the evaluation of the selection efficiency. As a cross-check, the distribution of the BDTs outputs for selected candidates of the two normalisation channels in simulation and in data, where the background is statistically subtracted by means of the "`sPlot`" method [128], are compared and found in reasonable agreement among each other. The relative difference between the selection efficiencies in data and simulation for the two normalisation channels is assigned as systematic uncertainty. Assuming the same systematic uncertainty of the $B_s^0 \to D_s^- \pi^+ \pi^- \pi^+$ also for the signal, since both the distributions are very similar, the resulting systematic uncertainty on the efficiency ratio is $< 0.1\%$ for the $B_s^0 \to D_s^- \pi^+ \pi^- \pi^+$ and about 1.9% for the $B_d^0 \to D^- \pi^+ \pi^- \pi^+$ normalisation channels, respectively;

- addressed to the selection applied on both signal and normalisation channels. In this case, possible sources of uncertainties are particle identification and trigger selection efficiencies, and a not precise momentum calibration which could lead to a biased measurement of the invariant mass.The systematic uncertainty related to the particle identification is computed as the difference of two efficiencies determined by the use different methods (PIDCalib and PIDGen [129]) and then is propagated to the efficiency ratio $\epsilon_{norm}/\epsilon_{sig}$. The relative systematic uncertainty is 0.3% for the $B_s^0 \to D_s^- \pi^+ \pi^- \pi^+$, and 4.4% for $B_d^0 \to D^- \pi^+ \pi^- \pi^+$. Such results are due to the fact that since the selection of the D_s is equal to the signal and in the $B_s^0 \to D_s^- \pi^+ \pi^- \pi^+$ channel, most of the uncertainties cancel out, whereas, in the case of the $B_d^0 \to D^- \pi^+ \pi^- \pi^+$ the selection is different and there's only a partial cancellation. The systematic uncertainty associated to the trigger efficiency, estimated on simulated samples, is defined as the expected deviation of the efficiencies from their nominal values based on previous analysis [99]. Lastly the ones associated to the momentum scale calibration are taken from the difference between the nominal values of the overall efficiencies and those recomputed for the signal and normalisation channels after the application of the momentum scale calibration, which is estimated by scaling the the $D_{(s)}^+$mass cut by the resolution scale factor found fitting data. As a result, the systematic uncertainties assigned to the efficiency ratios are $< 0.1\%$ for $B_s^0 \to D_s^- \pi^+ \pi^- \pi^+$ and 0.4% for $B_d^0 \to D^- \pi^+ \pi^- \pi^+$;

- due to possible mismodeling of the background sources and the normalisation contributions in the fit model that affect the yield. The uncertainty is estimated as the difference in the normalisation yield considering different assumptions on the fit model. The resulting uncertainties on the efficiency ratios is 1.2% for the $B_s^0 \to D_s^- \pi^+ \pi^- \pi^+$ and 0.9% for the $B_d^0 \to D^- \pi^+ \pi^- \pi^+$.

All the systematic uncertainties discussed so far are enlisted in the table 6.6 and deeply studied in [127].

Table 6.6: Summary of the systematic uncertainties to $\mathcal{K}$ ratio enlisted considering two different normalisation channels: $B_s^0 \to D_s^- \pi^+ \pi^- \pi^+$ and $B_d^0 \to D^- \pi^+ \pi^- \pi^+$

Contribution	$B_s^0 \to D_s^- \pi^+ \pi^- \pi^+$ [%]	$B_d^0 \to D^- \pi^+ \pi^- \pi^+$ [%]
Particle Identification	0.3	4.4
Trigger	1.0	1.0
Momentum Scale Calibration	< 0.1	0.4
Fit model	1.2	0.9
Data-simulation differences	< 0.1	1.9
Total	1.6	5.0

As a result, the overall uncertainties on the $R\,(D_s)$ measurement considering all the selection implemented, and the external branching fractions inputs, are reported in table 6.7. As can

Table 6.7: Summary of the main contribution to the overall uncertainty on $R\,(D_s)$ measurement given by the selection implemented and the external branching fractions inputs.

Contribution	$B_s^0 \to D_s^- \pi^+ \pi^- \pi^+$ [%]	$B_d^0 \to D^- \pi^+ \pi^- \pi^+$ [%]
Normalisation yield	2.1	0.9
Simulation statistics	1.2	0.9
Systematic uncertainties	1.6	5.0
External contributions	19.1	14.3
Total	19.3	15.2

be argued from the table 6.7, the best normalisation channel is the $B_d^0 \to D^- \pi^+ \pi^- \pi^+$ since it allows a more precise measurement of $R\,(D_s)$ measurement. Nevertheless, both the normalisation channels are going to be considered for the rest of this study as they provide a useful internal cross check for the measurement and can eventually be averaged. It should be emphasised that for the signal only the efficiency given by the first level selection was considered, which is common to both the signal and the normalisation channels. The signal efficiency, in fact, must be recalculated by adding also the second level selection efficiency which is specific to the semileptonic channel and is discussed in the next Chapter.

6.5.5 Cross-check on the normalisation channels

A useful cross-check to validate the analysis performed so far is the determination of ratio of the yields of the two normalisation channels corrected by the corresponding efficiencies which should coincide with the ratio of the measured branching fractions. Using the yields of sec.6.5 and the efficiencies of table 6.5 and taking into account the statistic and the systematic uncertainties, the ratio is :

$$\frac{N_{B_d^0 \to D^- \pi^+ \pi^- \pi^+}}{N_{B_s^0 \to D_s^- \pi^+ \pi^- \pi^+}} \times \frac{\epsilon_{B_s^0 \to D_s^- \pi^+ \pi^- \pi^+}}{\epsilon_{B_d^0 \to D^- \pi^+ \pi^- \pi^+}} = 5.9 \pm 0.7$$

while from the branching fractions of table 5.2 the ratio is

$$\frac{\mathcal{B}(B_d^0 \to D^- \pi^+ \pi^- \pi^+)}{\mathcal{B}(B_s^0 \to D_s^- \pi^+ \pi^- \pi^+)} \times \frac{\mathcal{B}(D^- \to K^+ \pi^- \pi^-)}{\mathcal{B}(D_s^- \to K^+ K^- \pi^-)} \times \frac{f_d}{f_s} = 7.3 \pm 1.5 \,.$$

The two ratios are consistent within 1σ, which represents a good cross-check of the analysis performed so far.

Moreover, it is possible to evaluate expected yield of the normalisation and signal channels in the 2012 data sample (2 fb^{-1}), taking into account the cross section [92] and the efficiencies related to the first level selection. The results are listed in table 6.8. The values found for the normalisation channels are consistent with the measurements within 1-2σ. For the signal the expected yield is 258 events, which will be further reduced once the selection is refined to suppress the remaining background sources. More considerations will be provided in the following Chapter.

Table 6.8: Number of events of signal and normalisation channels foreseen in the 2012 data sample. The uncertainty takes in account both the statistical and the systematic contributions.

Contribution	Yield
$B_s^0 \to D_s^-(\to K^+K^-\pi^-)\tau^+(\to \pi^+\pi^-\pi^+(\pi^0))\nu_\tau$	258±49
$B_s^0 \to D_s^-(\to K^+K^-\pi^-)\pi^+\pi^-\pi^+$	9129±1930
$B_d^0 \to D^-(\to K^+\pi^-\pi^-)\pi^+\pi^-\pi^+$	27155±4750

Chapter 7

Background composition and further selections

In this Chapter a detailed study of the remaining background contributions is presented. The study is performed on a sample of events containing inclusive $b-$hadron decays to D_s^- decaying to $K^+K^-\pi^-$ and three pions reconstructed in the LHCb acceptance that pass the selection described in the previous Chapter. By exploiting the truth information a categorisation of the different sources is possible (sec. 7.1). A selection is developed to suppress selected candidate of background decays containing extra charged particles originating from the same reconstructed vertices (sec. 7.2). A further selection allows to separate the signal from "prompt-3π-from-B" background decays exploiting the distance between the B_s^0 and the 3-π vertices (sec. 7.3).

7.1 Studies on the inclusive simulated sample

The inclusive simulated sample incl_$H_b \to D_s 3\pi$ has been specifically produced to study all possible sources of background in the reconstructed final state. At generation level the events are required to contain a $D_s^- \to K^+K^-\pi^-$ decay originated from a $b-$hadron decay and three pions reconstructed in the LHCb acceptance. The events passing the first level selection discussed in the previous Chapter are studied and classified by exploiting the simulation truth information. The list of categories is given in table 7.1.

The categories found among all the possible decays are listed in table 7.1. The categories take in account the possibility that the D_s^- is correctly reconstructed as a signal decay ("Xc_signal_XXX") or not ("Xc_background"). The "Xc_signal" category is split based on the 3-prongs origin (referred to as "Ypis"), which could be not matched ("_no_match"), or originated from different vertices ("_diffVertex"), or from the same. In the last case, the D_s^- and the 3-prongs could have a different ancestor ("_diffAncestorYXc"), or the same. In the last case the 3-prongs can be produced promptly from a $b-$hadron ("_B_vertex") or displaced from the B vertex ("_displaced"). Eventually the different cases of "B_vertex" from which the 3-prongs are produced have been classified, as well as in the case of the 3-prongs produced "_displaced" from the $b-$hadron.

Table 7.1: Categories of events in the inclusive simulated sample after the first level selection, with corresponding yield, percentage of the full sample and B/S ratio, where S is the yield of signal, corresponding to 'Xc_signal_Ypis_displaced_fromTau" row.

Category	Candidates	Percentage [%]	B/S
Xc_signal_Ypis_B_vertex_fromBs	497166	35.60	103
Xc_signal_Ypis_diffVertex	237635	17.01	49
Xc_background	214533	15.36	44
Xc_signal_Y_no_match	146006	10.45	30
Xc_signal_Ypis_displaced_fromD0	96237	6.89	20
Xc_signal_Ypis_displaced_fromDs	89399	6.40	18
Xc_signal_Ypis_displaced_fromDp	61396	4.40	13
Xc_signal_Ypis_B_vertex_fromOtherB	27945	2.00	5.8
Xc_signal_Ypis_displaced_fromLambdac	12471	0.89	2.6
Xc_signal_Ypis_diffAncestorYXc	8709	0.62	1.8
Xc_signal_Ypis_displaced_fromTau	4845	0.35	–
Xc_signal_Ypis_displaced_other	218	<0.10	0.05
Xc_signal_Ypis_displaced_fromXic	78	<0.10	0.02
Xc_signal_Ypis_B_vertex_fromHc	32	<0.10	0.007

As can be seen from the table 7.1 the signal is only the 0.35 % of the total sample while the most abundant contributions are the Xc_signal_Ypis_B_vertex_fromBs category (35%), to which the normalisation channel belong, categories with the 3-prongs arising from different vertices (17%), the D_s^- not correctly reconstructed (15%) and the doubly charmed $b-$hadron decays (Xc_signal_Ypis_displaced_fromX with X= D_s^-, D^0, D^-, Λ_c). It is evident that a further suppression of the background is needed to identify the signal.

7.2 Charged isolation

Among the possible background sources, partially reconstructed b-hadron decays where only part of the final state particles are considered for the candidate reconstruction represent an important contribution. Such background decays feature extra tracks consistent with the hypothesis of being originated from one of the vertices of the decay chain. To suppress this contribution, a specific BDT selection has been developed.

Given a selected signal candidate, the additional tracks reconstructed in the event are studied and classified in two categories according to their associated true information:

- isolated tracks: tracks that cannot be attached to any vertex of the signal candidate decay chain;
- non-isolated tracks: tracks consistent with being originated from one of the vertices of the signal candidate decay chain. Such tracks usually belong to the partially reconstructed b-hadron decays that needs to be suppressed.

Figure 7.1 shows both types of tracks: the isolated ones are in grey while the non-isolated are in red.

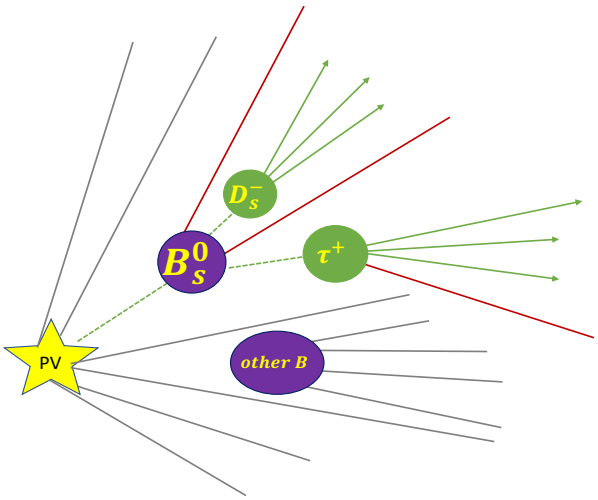

Figure 7.1: Schematic view of an event containing the signal decay. Isolated tracks are shown in grey, non-isolated tracks are represented in red and signal tracks are drawn in green.

The variables considered for the BDT training are based on the package `TupleToolIsoGeneric` that classifies all the tracks in the event in terms of its isolation property with respect to the signal candidate and identifies the non-isolated tracks. For each track of the signal candidate decay, the variables considered are:

- `IsoMinBDT`: the output response of a BDT classifier of the `TupleToolIsoGeneric` tool;
- `NIsoTr`: the number of non-isolated tracks;
- `ConeIso`: the variable defined as the ratio $I = \frac{p_{\mathrm{T}}(B)}{p_{\mathrm{T}}(B)+\sum_i p_{\mathrm{T,i}}}$, obtained considering the $i-$th non-isolated tracks in a cone with $\Delta R = \sqrt{\delta\phi_i^2 + \delta\eta_i^2} < 1$ around the B_s^0 candidate;
- `PAIR_M`: invariant mass of the pair given by the particle considered and the non-isolated track with the lowest IsoMinBDT value.

The variables associated to the final track with the minimum IsoMinBDT are considered, in addition to the output of the BDT "Bs selection" (BDT_Bs). The BDT is trained using as *signal* selected candidate decays from the simulation sample of $B_s^0 \to D_s^-\tau^+\nu_\tau$ decays, where the reconstructed B_s^0 are matched to the "true" decays. The *background* sample consists of selected candidates from the inclusive sample $H_b \to D_s 3\pi X$ containing a "true" non-isolated track. The distributions of the BDT inputs are shown in fig. 7.2. The distributions of the BDT output for signal and background are shown in fig. 7.3 (Left). Since they are quite separated, it is possible to apply a cut that highly suppresses the background while preserving most of the signal. For example, by applying a cut corresponding to 90% efficiency on the signal a background rejection of about 7% can be achieved, as shown in fig. 7.3 (Right).

By applying the cut on the "BDT_Iso" on the inclusive sample incl_$H_b \to Ds3\pi X$ (see table 7.2) the signal contribution passes from 0.35% to almost 1%, the Xc_background reduces its impact on the full sample as well as the background given by 3-prongs no matched or coming

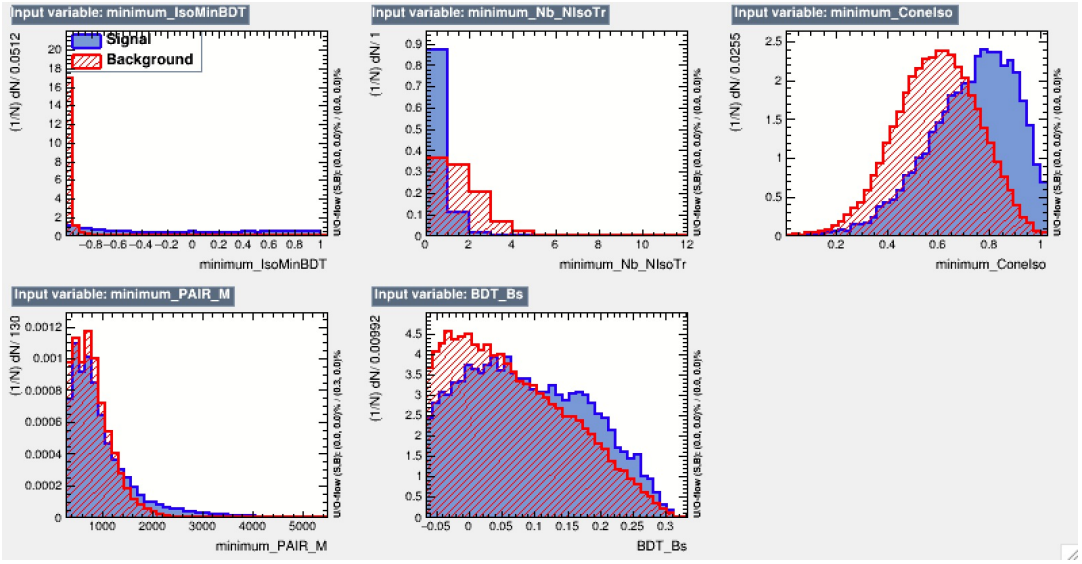

Figure 7.2: Distribution of the input variables used in the BDT to discriminate between signal tracks and non-isolated tracks. The signal is in blue the background in red.

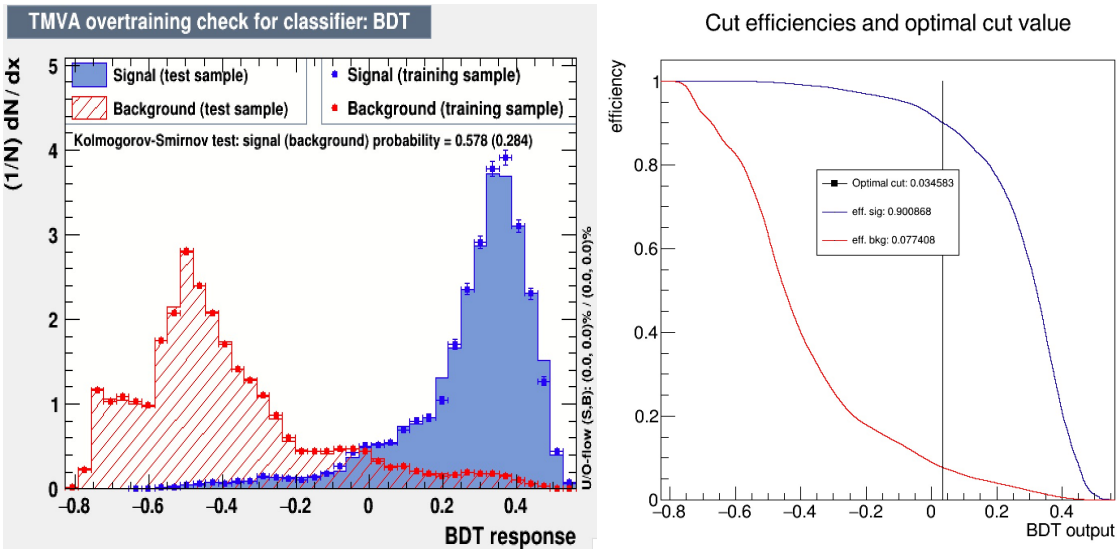

Figure 7.3: (Left) Distribution of the BDT output response to discriminate between signal tracks and non-isolated tracks. The signal is in blue the background in red. (Right) Cut efficiencies to signal and background as a function of the BDT cut.

from different vertices. Also the contributions of the backgrounds with 3-prompt prongs, and the double charmed decays, is reduced but a further suppression is needed.

7.3 Discrimination between signal and normalisation channels with the B_Y_SEP cut

Given the results shown in the previous section, a further request is implemented on the inclusive sample considering the displacement of the $b-$hadron from the 3 π decay vertex.

Table 7.2: Categories found in the inclusive simulated sample, their percentage with respect to the full sample after the cut on the "BDT_Iso", and the ratio B/S.

Category	Candidates	Percentage [%]	B/S
Xc_signal_Ypis_B_vertex_fromBs	176041	42.76	43
Xc_signal_Ypis_diffVertex	67030	16.25	16
Xc_background	41716	10.11	10
Xc_signal_Ypis_displaced_fromDp	33278	8.07	8.0
Xc_signal_Ypis_displaced_fromDs	32299	7.83	7.9
Xc_signal_Y_no_match	29652	7.19	7.2
Xc_signal_Ypis_displaced_fromD0	13951	3.38	3.4
Xc_signal_Ypis_displaced_fromLambdac	8595	2.08	2.1
Xc_signal_Ypis_B_vertex_fromOtherB	4455	1.08	1.1
Xc_signal_Ypis_displaced_fromTau	4099	0.99	–
Xc_signal_Ypis_diffAncestorYXc	1242	0.30	0.3
Xc_signal_Ypis_displaced_fromXic	64	<0.10	0.02
Xc_signal_Ypis_displaced_other	61	<0.10	0.01
Xc_signal_Ypis_B_vertex_fromHc	21	<0.10	0.005

To suppress the large background due to 3-prong produced promptly from the B (Xc_signal_Ypis_from_B_vertex, also referred to as "Prompt" in the following), to which the normalisation channels belong to, the distance along z coordinates of the B and 3π vertices (B_Y_SEP) is considered:

$$B\_Y\_SEP = \frac{(B_{ENDVERTEX_Z} - Y_{ENDVERTEX_Z})}{\sqrt{(\sigma_{B_{ENDVERTEX_Z}})^2 + (\sigma_{Y_{ENDVERTEX_Z}})^2}}.$$

The optimal cut is found by maximising the figure of merit $FOM \equiv \mathrm{S}/\sqrt{\mathrm{S}+\mathrm{B}}$, with S and B the signal (Xc_signal_Ypis_displaced_fromTau) and the prompt background (Xc_signal_Ypis_from_B_vertex) yields, respectively, and corresponds to the value -4.5. Even if this cut is quite

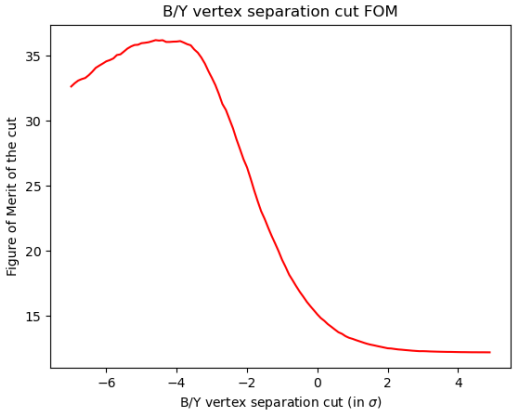

Figure 7.4: Distribution of the figure of merit in function of the variable B_Y_SEP.

aggressive on the signal (36% of efficiency), it is very efficient in reducing the prompt background

(by more than 90%).

Table 7.3 summarises the background composition in the inclusive sample after the cut. The B/S ratio is reduced not only for the prompt background, but also for Xc_background, Y_nomatch, and diff_Vertex categories. The doubly charm contributions, instead, remains almost unaffected by this cut since, like for the signal, the three pions originate from a long lived particle.

To suppress the doubly charm background contributions a further selection still needs to be developed. Like for the $R(D^*)$ analysis, it should rely on the different kinematic correlations of the three pions originated from the τ or the D_s^-/D^- and D^0 decays. Such study could not be performed during the PhD term, due to lack of time and low statistics of the simulation sample, and will be done in the next future.

Table 7.3: Categories found in the inclusive simulated sample, their percentage with respect to the full sample after the cut B_Y_SEP< -4.5, and the ratio B/S.

Category	Candidates	Percentage [%]	B/S
Xc_signal_Ypis_displaced_fromDp	24059	27.34	14
Xc_signal_Ypis_displaced_fromDs	19907	22.62	12
Xc_signal_Ypis_diffVertex	16719	20.00	10
Xc_signal_Ypis_displaced_fromD0	8762	9.97	5.2
Xc_signal_Y_no_match	6884	7.82	4.1
Xc_background	5892	6.70	3.5
Xc_signal_Ypis_displaced_fromLambdac	2539	2.88	1.5
Xc_signal_Ypis_displaced_fromTau	1672	1.90	–
Xc_signal_Ypis_diffAncestorYXc	801	0.91	0.5
Xc_signal_Ypis_B_vertex_fromBs	643	0.73	0.4
Xc_signal_Ypis_displaced_other	49	< 0.10	0.3
Xc_signal_Ypis_B_vertex_fromOtherB	29	< 0.10	0.02
Xc_signal_Ypis_displaced_fromXic	28	< 0.10	0.02
Xc_signal_Ypis_B_vertex_fromHc	18	< 0.10	0.01

Chapter 8

D_s^- and D_s^{*-} separation

To measure $R(D_s)$ it is important to separate the contribution of the signal $B_s^0 \to D_s^- \tau^+ \nu_\tau$ from the $B_s^0 \to D_s^{*-} \tau^+ \nu_\tau$ decay, where the D_s^{*-} decays to $D_s^- \gamma$ or $D_s^- \pi^0$ with a Branching Fraction of 93.5% and 5.8% respectively (fig. 8.1). A discrimination between the two channels is possible in case the neutral particle emitted in the D_s^{*-} decay is detected. The small Q-value of the D_s^{*-} decay implies that the neutral particle is emitted in a cone close to the flight direction of the D_s^-. A multivariate analysis has been developed using the information from the calorimeter system and the neutral cone isolation tool, as explained in the following section.

The branching fraction of the $B_s^0 \to D_s^- \tau^+ \nu_\tau$ and $B_s^0 \to D_s^{*-} \tau^+ \nu_\tau$ can be calculated by using the theoretical prediction of $R(D_s)$ and $R(D_s^*)$ [121] and the measured values of $B_s^0 \to D_s^- \mu^+ \nu_\mu$ and $B_s^0 \to D_s^{*-} \mu^+ \nu_\mu$ [56], and are $\mathcal{B}(B_s^0 \to D_s^- \tau^+ \nu_\tau) = (7.5 \pm 0.7) \times 10^{-3}$ and $\mathcal{B}(B_s^0 \to D_s^- \tau^+ \nu_\tau) = (13.3 \pm 6.5) \times 10^{-3}$.

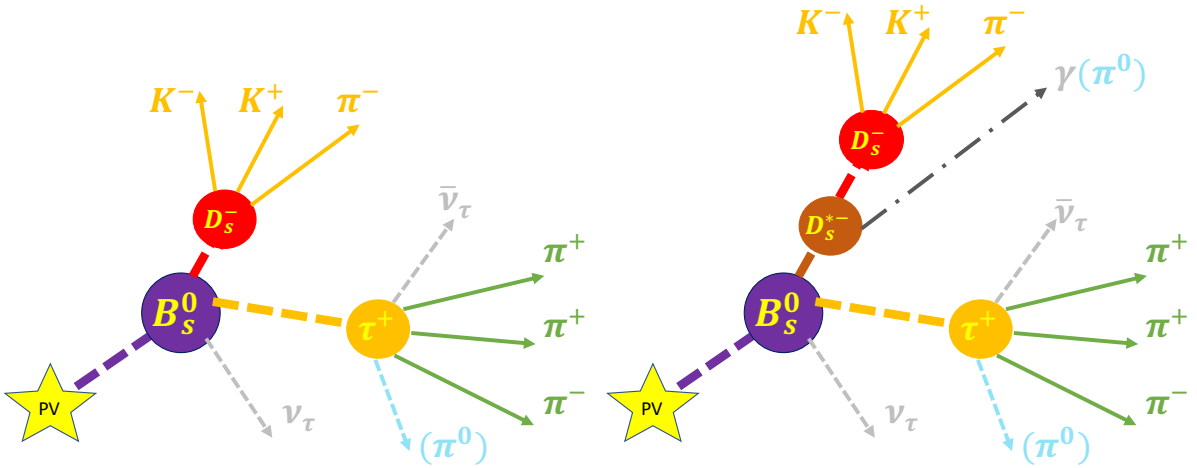

Figure 8.1: Schematic representation of the $B_s^0 \to D_s^- \tau^+ \nu_\tau$ and of $B_s^0 \to D_s^{*-} \tau^+ \nu_\tau$ decays with D_s^- meson decaying to $K^+ K^- \pi^-$ and D_s^{*-} decaying into $D_s^- \gamma$ or $D_s^- \pi^0$.

8.1 Neutral Isolation Tool

The selection described in the previous chapter is efficient to select events with D_s^- and 3π coming from B_s^0 and to reject the combinatorial background containing the same final state particles. Among the channels that present the same final state topology of the signal, the semileptonic decay $B_s^0 \to D_s^{*-}\tau^+\nu_\tau$ differs from the $B_s^0 \to D_s^-\tau^+\nu_\tau$ for the further D_s^{*-} decay into a D_s^- plus a neutral particle (γ or π^0) which can be taken into account using a specific tool. In particular, the neutral isolation tool considers the reconstructed photons from the *StdLooseAllPhotons* particle container and then selects those within a cone around the D_s^- flight direction. The algorithm allows to choose the aperture of the cone, defined as $\Delta R \equiv \sqrt{\Delta\eta^2 + \Delta\phi^2}$, between 0.1 and 1.0 around the D_s^- direction and then to compute different variables that can help to separate the two semileptonic decays $B_s^0 \to D_s^-\tau^+\nu_\tau$ and $B_s^0 \to D_s^{*-}\tau^+\nu_\tau$. In this study case, the neutral isolation variables are all reconstructed in a cone of 0.2 opening around the D_s^- flight direction since this configuration corresponds to the one that provides the best discrimination power between D_s^- and D_s^{*-}.

8.2 Multivariate analysis

Due to the large number of reconstructed photons in the calorimeter, the discrimination between D_s^- and D_s^{*-} suffers from the contamination of combinatorial. For this reason, to best discriminate between D_s^- and D_s^{*-} a composite multivariate analysis (MVA) exploiting the variables provided by the neutral isolation tool and both the candidates with or without a reconstructed photon inside the cone has been developed. The MVA is trained on 2012 simulation samples of $B_s^0 \to D_s^-\tau^+\nu_\tau$ (referred to as *signal*) and $B_s^0 \to D_s^{*-}\tau^+\nu_\tau$ (referred to as *background*) candidates passing the signal selection of sec. 6 with cuts reported in table 8.1, except for the B_Y_SEP cut, which is too aggressive on the signal (with an efficiency of about 36%) and is not convenient for this study. Among all the possible variables provided by the

Table 8.1: Cuts applied on $B_s^0 \to D_s^-\tau^+\nu_\tau$ and $B_s^0 \to D_s^{*-}\tau^+\nu_\tau$

Variable	Cut
Xc_Selection	> 0
BDT_3pi	> -0.0727
BDT_Ds	> -0.0876
BDT_Bs	> -0.0655

neutral isolation tool, those showing a good discriminating power between D_s^- and D_s^{*-} are used as input of the MVA classifier. Even if the multiplicity of photons inside the cone around the D_s^- candidate, in principle, should discriminate between the contribution of D_s^- from the one of D_s^{*-} it's not possible to consider such cut without loosing efficiency. Table 8.2 reports the efficiencies for $B_s^0 \to D_s^-\tau^+\nu_\tau$ and $B_s^0 \to D_s^{*-}\tau^+\nu_\tau$ for the requirement multiplicity > 0 and the figure of merit S/B.

Table 8.2: Relative efficiencies for multiplicity of photons > 0 for different cone sizes around the D_s^- candidate in $B_s^0 \to D_s^- \tau^+ \nu_\tau$ and $B_s^0 \to D_s^{*-} \tau^+ \nu_\tau$ simulated samples. S/B ratio computed as the ratio between the total efficiencies corrected by the ratio of branching fractions.

Cone Size	efficiency for multiplicity > 0		FoM
	$B_s^0 \to D_s^- \tau^+ \nu_\tau$	$B_s^0 \to D_s^{*-} \tau^+ \nu_\tau$	S/B
0.2	33%	47%	0.38
0.3	56%	70%	0.43
0.4	72%	83%	0.47

As a consequence, after choosing the cone size 0.2, depending on the multiplicity of photons found in the cone around the D_s^- candidate, Xc_0.2_nc_mult $= 0$ or > 0, two classifiers are defined. In the first case a Fisher discriminant [120] is used, by exploiting only the variable Xc_pT_Breco_Yreco, representing the reconstructed transverse momentum of the D_s^- with respect to the B_s^0 flight direction. In the second case a BDT is used, by exploiting the following input variables:

- Xc_0.2_nc_maxPt_PT: maximum transverse momentum of the photons inside the cone;
- Xc_0.2_nc_avCL: average value of the photon confidence level (CL) for the photons inside the cone. The CL variable is the output of a multivariate algorithm that uses among the input variables the shape of the cluster in the electromagnetic calorimeter.
- Xc_0.2_nc_asy_P: asymmetry between the D_s^- momentum and that of the photons inside the cone defined as: $(|P_{D_s^-}| - |\sum P_\gamma|)/(|P_{D_s^-}| + |\sum P_\gamma|)$
- Xc_0.2_nc_deltaEta: difference between the D_s^- pesudorapidity and the that of the photons inside the cone;
- Xc_0.2_nc_deltaPhi: difference between the D_s^- azimuthal angle and that of the photons inside the cone;
- Delta_ms_020_maxPt: the difference in mass between the D_s^- and D_s^{*-} computed with the information coming from the photon with the maximum transverse momentum among the photons reconstructed inside the cone;
- Xc_pTreco_Breco_Yreco: reconstructed transverse momentum of the D_s^- with respect to the B_s flight direction.

To develop and study the performance of the classifiers, both the D_s^- and the D_s^{*-} simulated samples are split in two: one is used to train the MVA classifier, the other is used to check the results. In both cases the information about the true identity of the reconstructed candidate (being D_s^- or D_s^{*-}) is exploited. Figures 8.2 and 8.3 show the distributions of the inputs of the two MVA classifiers (see table 8.3) for the D_s^- and D_s^{*-} training samples in blue and red, respectively.

Table 8.3: Input variables for MVA analysis listed with their ranking. The category 1 takes into account the Fisher method used for events with Xc_0.20_nc_mult = 0, while the category 2 refers to the events with Xc_0.20_nc_mult > 0 which have been studied with the BDT method.

Category	% of D_s^-	% of D_s^{*-}	MVA method	Variable	Ranking
(1)	67%	53%	Fisher	Xc_pT_Breco_Yreco	2.6×10^{-2}
(2)	33 %	47%	BDT	Delta_ms_020_maxPt	1.9×10^{-1}
				Xc_0.2_nc_avCL	1.5×10^{-1}
				Xc_pT_Breco_Yreco	2.2×10^{-1}
				Xc_0.2_nc_maxPt_PT	1.4×10^{-1}
				Xc_0.2_nc_deltaEta	1.2×10^{-1}
				Xc_0.2_nc_deltaPhi	1.2×10^{-1}
				Xc_0.2_nc_asy_P	1.2×10^{-1}

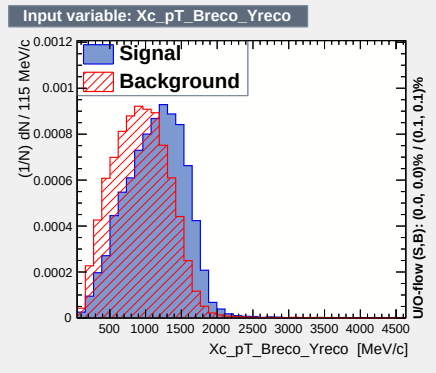

Figure 8.2: Distribution of the input variable of the Fisher discriminant for category 1.

The output of the BDT and Fisher methods are shown in fig. 8.5. The discrimination power of the two classifiers is limited due to the large overlap of the D_s^- (signal shown in blue) and D_s^{*-} (background shown in red) distributions. Moreover also studying different Figures of Merit(FoM), Fig. 8.4, like S/B, $\epsilon_S \times S/B$, $S/(S+B)$ and $S/\sqrt{(S+B)}$ is not possible to select a specific cut which at the same time gives the maximum value of the FoM and avoid to loose in efficiency. As a consequence, for the $R(D_s)$ and, possibly, the $R(D_s^*)$ measurements it is better to exploit the MVA output values to separate the D_s^- and D_s^{*-} contribution on a statistical basis rather than selecting D_s^- and D_s^{*-} candidates based on a cut on the MVA outputs. In particular, the final fit to determine the signal yield (see Chapter 9), could be extended to be a 4D fit of the observables q^2, τ decay time (t_τ), BDT and the Multidimensional MVA output discussed above. In this view, a validation of the MVA distributions on a data control channel is needed.

8.3 Validation of the MVA on a control sample

The validation of the MVA classifiers described in the previous section has been performed on data samples of $B_s^0 \to D_s^-\pi^+$ and $B_s^0 \to D_s^{*-}\pi^+$ decays which are reconstructed in the

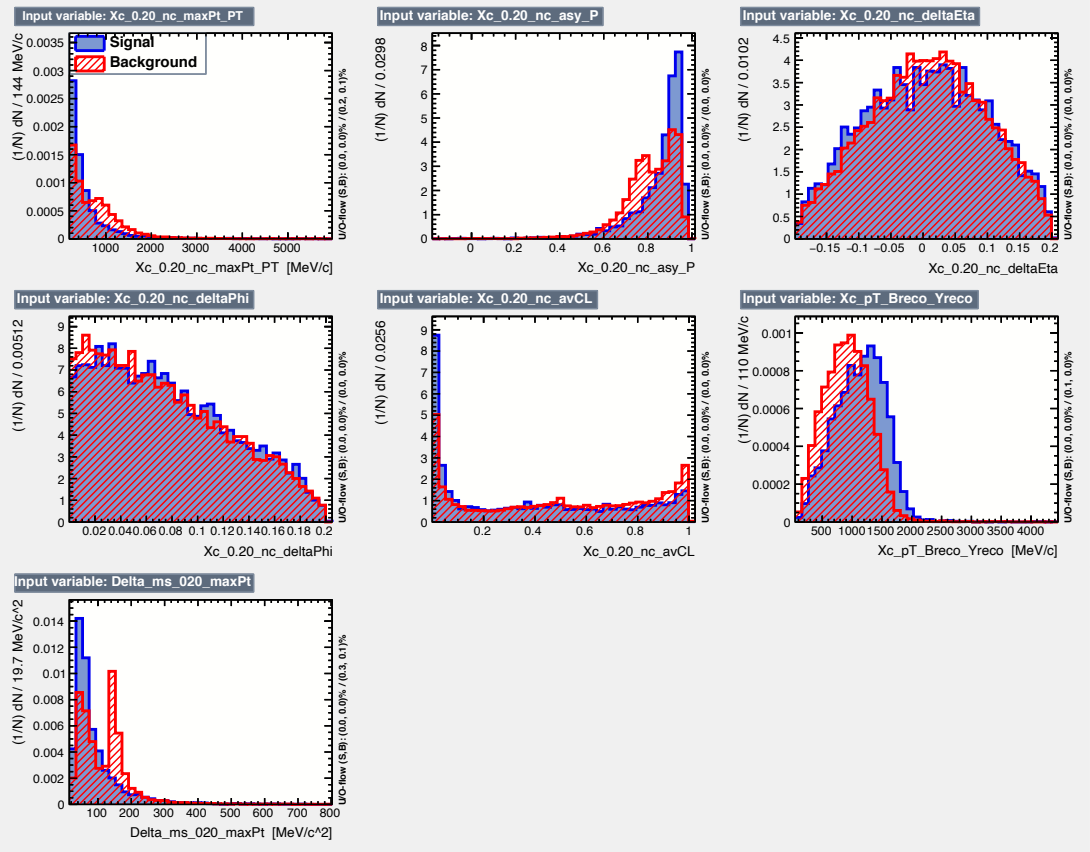

Figure 8.3: Distributions of the input variables for the BDT classifier for category 2.

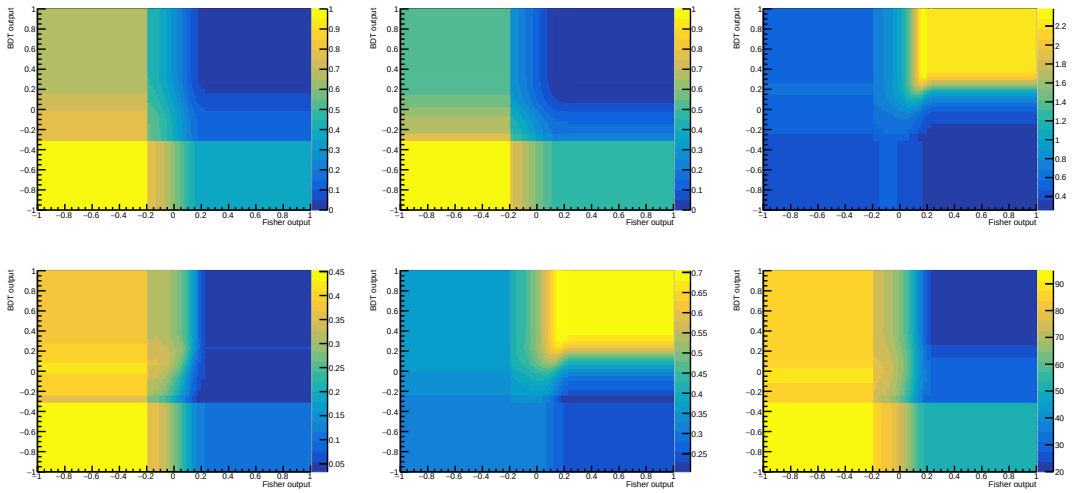

Figure 8.4: Efficiencies of (top left) Signal, ϵ_S, and (top middle) Background, ϵ_B, and different Figure of Merit: (top right) S/B, (bottom left) $\epsilon_S \times S/B$, (bottom middle) $S/(S+B)$ and (bottom right) $S/\sqrt{(S+B)}$.

$B_s^0 \to D_s^- \pi^+$ final state with $D_s^- \to K^+K^-\pi^-$ (see fig. 8.6). The main advantages of using these control channels is that they have large Branching Fractions (0.3% and 0.2%, respectively) and they contain a D_s^- and D_s^{*-} like for the semileptonic signals, so the same D_s^- selection can be

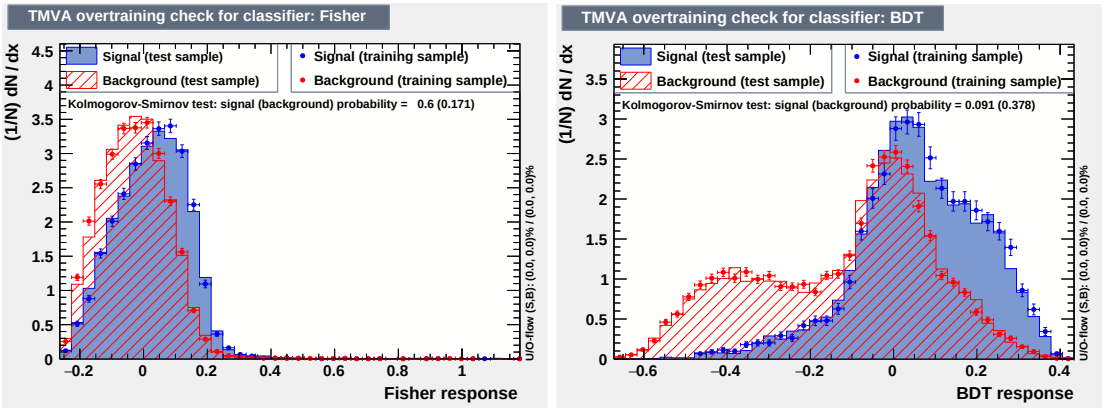

Figure 8.5: Output of the (left) Fisher and (right) BDT classifiers developed for the discrimination between $B_s^0 \to D_s^- \tau^+ \nu_\tau$ (signal) and $B_s^0 \to D_s^{*-} \tau^+ \nu_\tau$ (background) for category 1 and 2, respectively.

applied. Moreover, the exclusive reconstruction of the $B_s^0 \to D_s^- \pi^+$ decay allows the selection of a clean sample of candidates. Regarding the $B_s^0 \to D_s^{*-} \pi^+$, even if it is reconstructed inclusively, ignoring the neutral final state particles, the background level is limited, thanks to the D_s^- selection, and can be separated from the signal.

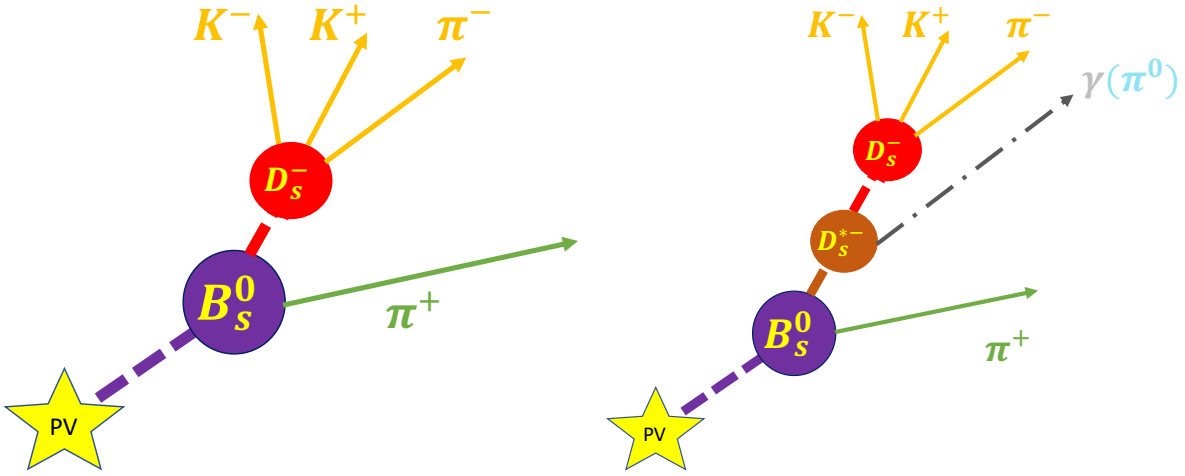

Figure 8.6: Schematic representation of the $B_s^0 \to D_s^- \pi^+$ and of $B_s^0 \to D_s^{*-} \pi^+$ decays with D_s^- meson decaying to $K^+K^-\pi^-$ and D_s^{*-} decaying into $D_s^- \gamma$ or $D_s^- \pi^0$.

8.3.1 Selection of the control channel

The validation of the MVA distribution is performed using a data sample collected in 2012. Signal candidates are selected by the `B02DPiD2HHHBeauty2CharmLine` stripping line (version v21), which is different from that used for the semileptonic signal channel $B_s^0 \to D_s^- \tau^+ \nu_\tau$ (see table 8.4 for the list of all the cuts applied). In addition to the stripping selection, the cuts listed in table 8.5 are applied to further reduce the background contamination. In particular, by selecting the $D_s^- \to \Phi(1020)\pi^-$ decay mode with $\phi(1020) \to K^+K^-$ by means of appro-

priate kinematic and PID cuts, a clean sample of D_s candidates with very little background contamination is obtained.

Table 8.4: Summary of the stripping line `B02DPiD2HHHBeauty2CharmLine` (version 21) selection cuts. The pion from the B_s^0 decay is referred to as "bachelor".

	Variable	Cut
Each event	#long tracks	< 500
Each particle	Track χ^2/ndf	< 3.0
	Track χ^2_{IP}	> 4
	Track ghost probability	< 0.4
	p_T	> 100 MeV/c
	p	> 1000 MeV/c
Bachelor particle	Track χ^2/ndf	< 2.5
	p_T	> 500 MeV/c
	p	> 5000 MeV/c
$D^{\pm}_{(s)}$ candidate	invariant mass	[1769.6; 2068.5] MeV/c^2
	p_T	> 1800 MeV/c
	DOCA cut	< 0.5 mm
$D^{\pm}_{(s)}$ has a daughter with	Track χ^2/ndf	< 2.5
	p_T	> 500 MeV/c
	p	> 5000 MeV/c
$B^0_{(s)}$ candidate	invariant mass	[4750; 7000] MeV/c^2
	proper lifetime	> 0.2 ps
	χ^2_{IP} w.r.t. PV	< 25
$B^{\pm}_{(s)}$ has a daughter with	Track χ^2_{IP}	> 16
	Track IP	> 0.1 mm
	p_T	> 1700 MeV/c
	p	> 10 GeV/c

Figure 8.7 shows the invariant-mass distribution of the 84106 B_s^0 selected candidates, where the peak due to $B_s^0 \to D_s^- \pi^+$ decays around 5370 MeV/c^2 is clearly visible. The region below 5300 MeV/c^2 receives the contributions from different partially reconstructed or mis-identified b-hadron decays. Among these, the contribution due to the $B_s^0 \to D_s^{*-} \pi^+$ is identified in the region between 5000 and 5300 MeV/c^2.

The background contributions can be classified in three categories:

- fully reconstructed background from $B_d^0 \to D_s^- \pi^+$ decays. This background contributes with a peaking distribution around 5270 MeV/c^2 of low yield, due to the small $\mathcal{B}$ (Cabibbo suppressed decay).

- partially reconstructed $b-$hadron decays, where one or more final state particles of the decay are not reconstructed. These background populate the region below the $b-$hadron mass and contribute with broad distributions whose shape depends on the number of missing particles and the kinematics of the decay. In the considered range of $[4900; 5250]$ MeV/c^2 such contributions are mainly due to $B_s^0 \to D_s^- \rho^+$ decays, with $\rho \to \pi^- \pi^0$, where

Table 8.5: Cuts applied to $B_s^0 \to D_s^{(*)-}\pi^+$ to reduce the background contribution.

	Variable	Cut
B_s^0 candidate	DOCA cut	< 0.15 mm
	BDT_Ds	$>$ -0.15
	p_T	> 1600 MeV/c
	DIRA	> 0.995
D_s^- candidate	χ^2_{IP} w.r.t. PV	> 10
	$\lvert m(KK) - 1020\rvert$	≤ 12 MeV/c^2
	kaons PIDK	$>$ -2
	χ^2_{IP} w.r.t. PV	> 10
Bachelor particle	PIDK	< 0
	isMuon	= false
Composite	$\chi^2_{vtx}(B_s^0) < 1$ OR $\log(\chi^2_{IP}(Xc)) > 4.5$ OR $\log(\chi^2_{IP}(Y)) > 4.5$	

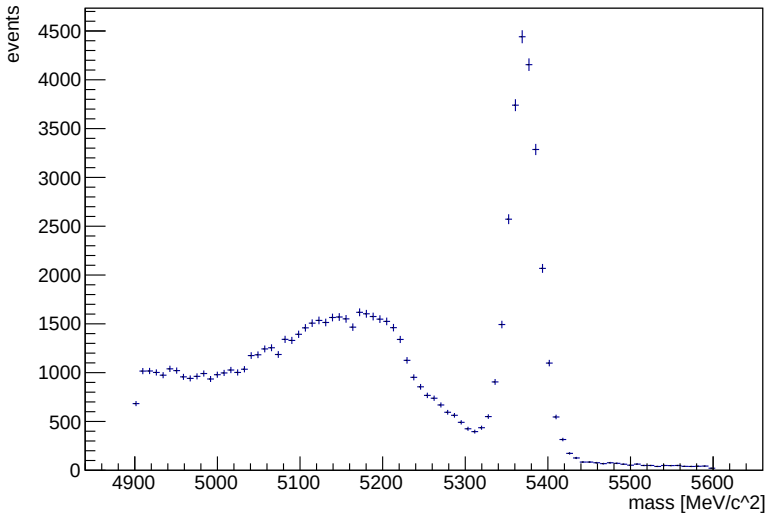

Figure 8.7: Invariant-mass distribution of the selected $B_s^0 \to D_s^{(*)-}\pi^+$ candidates for the 2012 data sample.

the π^0 is not reconstructed; $B_s^0 \to D_s^{*-}\rho^+$ and $B_s^0 \to D_s^{*-}\pi^+$ decays with D_s^{*-} decays to $D_s^-\gamma$ or $D_s^-\pi^0$, where the neutral particle is not reconstructed.

- combinatorial background, due to random combinations of reconstructed particles passing the $B_d^0 \to D_s^-\pi^+$ candidate selection. These can be due to combination of real D_s^- with a random pion, or random combination of $K^+K^-\pi^-$ forming a D_s^- combined with an additional pion.

- misidentified background: $b-$hadron decays with a similar topology of the signal that could pass the selection due to the wrong identification of the final state particles (*i.e.* $B^0 \to D^-(\to K^+\pi^-\pi^-)\pi^+$, $B_s^0 \to D_s^-(\to K^-K^+\pi^+)K^-$ or $\Lambda_b^0 \to \Lambda_c^+(\to pK^-\pi^+)\pi^-$). This kind of background is suppressed by vetoes implemented in the Xc_Selection also

exploiting the PID information coming from the RICH detectors.

8.3.2 Mass fit to data

To perform the validation of the MVA analysis using data, a fit to the invariant-mass distribution of the selected candidates is performed. This allows the determination of the yields of $B_s^0 \to D_s^-\pi^+$, $B_s^0 \to D_s^{*-}\pi^+$ and of the other background contributions, as well as the signal *sWeights* that are used for the $B_s^0 \to D_s^-\pi^+$ channel to produce the input and output distributions of the MVA by means of the *sPlot* technique.

Figure 8.8 shows the result of the fit to the invariant-mass distribution of the $B_s^0 \to D_s^-\pi^+$ decays in the range $[4900; 5600]$ MeV/c^2 selected from the 2012 data sample.

In the fit, all the contributing PDFs have been parametrised as discussed in the appendix 9.3 with parameters fixed to the values of the best fit on simulation except for the $B_s^0 \to D_s^-\pi^+$ component, in which the mean parameter and a scale factor (SF) on the mass resolution parameter, included to account for possible differences between data and simulation, are left free to vary. The fit determines the yield of each contributing component: $N_{\rm sig}$, $N_{B_d^0\to D_s^-\pi^+}$, $N_{B_s^0\to D_s^{*-}\pi^+}$, $N_{B_s^0\to D_s\rho^+}$, $N_{B_s^0\to D_s^{*-}\rho^+}$ and $N_{\rm comb}$.

The invariant-mass fit is then repeated in the restricted mass range of $[5280; 5550]$ MeV/c^2 ($[5000; 5300]$ MeV/c^2) around the $B_s^0 \to D_s^-\pi^+$ ($B_s^0 \to D_s^{*-}\pi^+$) in order to determine the yields and the signal *sWeights* in a region with reduced background contribution. [1] In this fit all the parameters are fixed to the values obtained from the previous fit, except for the yields of $B_s^0 \to D_s^-\pi^+$ ($B_s^0 \to D_s^{*-}\pi^+$) signal and total background contribution. The relative fractions of the different background sources have been recomputed in the restricted mass range and fixed.

Table 8.6 shows the results obtained for the yields of signal and background in the two regions highlighted in Fig. 8.8.

Table 8.6: Yields of signal and background extracted from the fit in the $[5280; 5500]$ MeV/c^2 region for the $B_s^0 \to D_s^-\pi^+$ and in the $[5000; 5300]$ MeV/c^2 region for the $B_s^0 \to D_s^{*-}\pi^+$.

Sample	Signal yield	Background yield
$B_s^0 \to D_s^-\pi^+$	25256± 170	3268±80
$B_s^0 \to D_s^{*-}\pi^+$	23322± 360	20956±350

8.3.3 Data/Simulation comparison of the MVA analysis in the $B_s^0 \to D_s^-\pi^+$ and $B_s^0 \to D_s^{*-}\pi^+$ control channels

The validation of the MVA analysis in the $B_s^0 \to D_s^-\pi^+$ and $B_s^0 \to D_s^{*-}\pi^+$ control channels consists in comparing the distributions of the output and input variables of the MVA classifiers for the selected signal decays in data and simulation.

For data, the signal distributions can be obtained with the *sPlot* technique, using either $B_s^0 \to D_s^-\pi^+$ or $B_s^0 \to D_s^{*-}\pi^+$ signal *sWeights* to subtract the background. This cancellation

[1] This approach has been adopted in order not to encounter numerical problems in the representation of the *sPlot*s due to large background contribution.

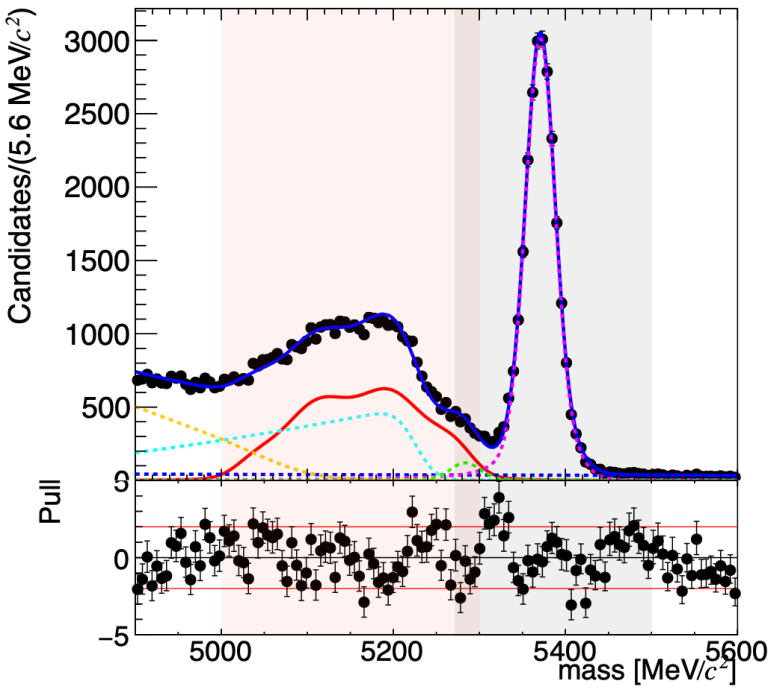

Figure 8.8: Invariant-mass distribution of $B_s^0 \to D_s^{(*)-} \pi^+$ selected candidates in data in the range [4900; 5600] MeV/c^2. The best fit is overlaid (blue line), while the fit components are: $B_s^0 \to D_s^{*-} \rho^+$ (dashed orange), $B_s^0 \to D_s^- \rho^+$ (dashed cyan), $B_s^0 \to D_s^{*-} \pi^+$ (red), $B_d^0 \to D_s^- \pi^+$ (dashed green), $B_s^0 \to D_s^- \pi^+$ (dashed magenta) and combinatorial (dashed blue) background. Highlighted in red is the region used to extract the yields related to the $B_s^0 \to D_s^{*-} \pi^+$, while in grey is the region used to determine the $B_s^0 \to D_s^- \pi^+$ contribution.

is proved to be valid for distributions of observables that are uncorrelated to the variable used to extract the *sWeights*, i.e. the invariant mass. Figure 8.9 shows the distributions of the Xc_pT_Breco_Yreco versus the invariant mass for the $B_s^0 \to D_s^- \pi^+$ (left) and $B_s^0 \to D_s^{*-} \pi^+$ (right) simulation samples. While the correlation is negligible in the case of the $B_s^0 \to D_s^- \pi^+$, this is not true for the $B_s^0 \to D_s^{*-} \pi^+$ channel, where correlation factor of ∼20% is found. This correlation is due to the kinematics of the decay with the missing neutral particle from the D_s^{*-} decay. As a consequence, the *sPlot* technique can only be applied to the $B_s^0 \to D_s^- \pi^+$ channel to compare the distributions of the Xc_pT_Breco_Yreco input and of the MVA outputs in data and simulation. For the case of the $B_s^0 \to D_s^{*-} \pi^+$ a different strategy has been adopted.

In all cases, simulation needs to be corrected to account for known differences between data and simulation in the event multiplicity. The event multiplicity is well represented by the number of reconstructed long tracks (nTracks) and of the SPD hit (nSPDHits), which are systematically smaller in simulation with respect to data. While nSPDHits distribution is adjusted by applying a scale factor of 1.3 to simulation to correct for inaccuracy in the modelling of M1 muon station, the nTrack distribution is corrected by applying a weight to each event. Since the corrections for

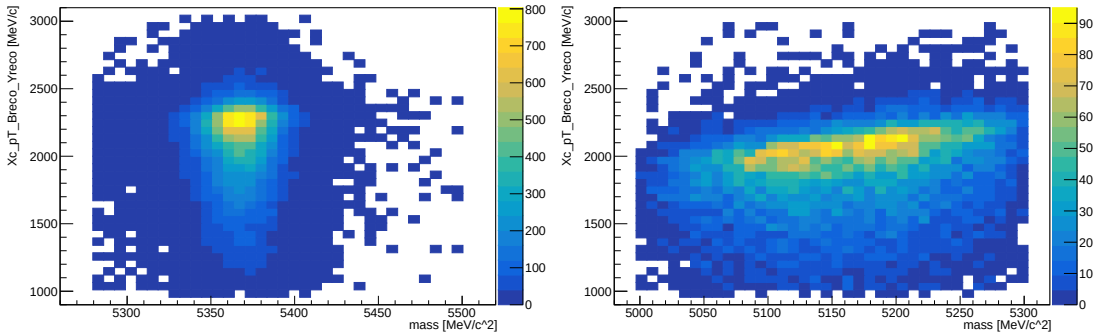

Figure 8.9: Distributions of the Xc_pT_Breco_Yreco in function of the invariant mass. Left for the $B_s^0 \to D_s^- \pi^+$, right for the $B_s^0 \to D_s^{*-} \pi^+$.

$B_s^0 \to D_s^- \pi^+$ and $B_s^0 \to D_s^{*-} \pi^+$ are both consistent within their errors, the two contributions have been summed. From the ratio of the log(nTracks) distributions in data and simulation a first weight function to apply to simulation is obtained. Then, the weighted distribution of nSPDhits in simulation is scaled by a factor 1.3 in order to match the data distribution. A cut on the rescaled number of nSPDhits(<600) is then applied to reproduce the L0-hadron trigger requirement. Finally, the a new weight function is applied to simulation in order to match the updated log(nTracks) distribution in data. The distributions of the log(nTracks) and log(nSPDhits) are shown in Fig. 8.10, where it can be appreciated the good level of agreement between data and simulation after the weighting procedure.

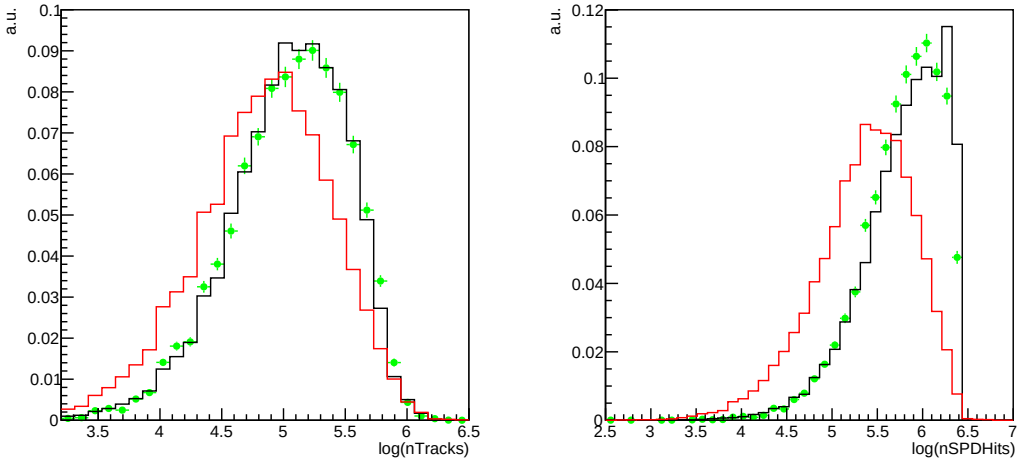

Figure 8.10: Distribution of (left) log(nTracks) and (right) log(nSPDhits) for $B_s^0 \to D_s^{(*)-} \pi^+$ decays. Data (*sPlots*) and simulation before and after correction are shown in green, red and black, respectively.

Figure 8.11 shows the distributions of the MVA classifiers input variables for the two categories of events of the $B_s^0 \to D_s^- \pi^+$ decay while the corresponding outputs are shown in Fig. 8.12 All the input and output distributions for both the categories show a good agreement between

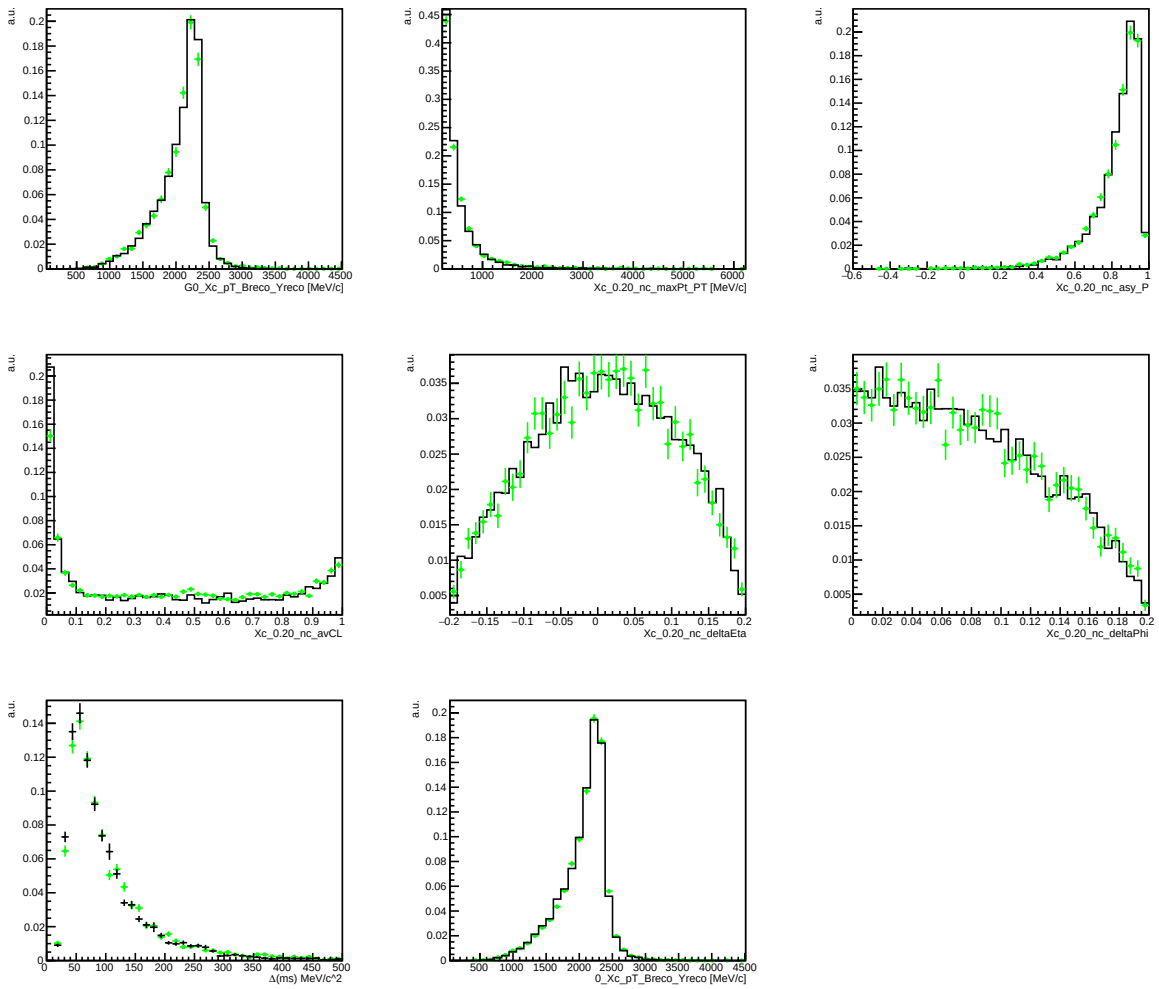

Figure 8.11: Distributions of the MVA classifiers input variables for the two categories of events of the $B_s^0 \to D_s^- \pi^+$ decay. Data *sPlots* and simulation after reweight are shown in green and black, respectively.

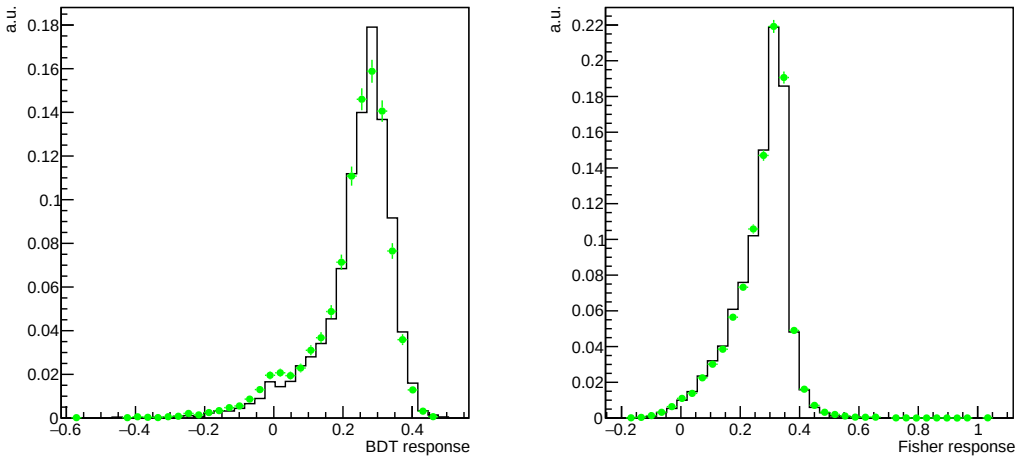

Figure 8.12: Distributions of the MVA classifier output for the two categories of events of the $B_s^0 \to D_s^- \pi^+$ decay. Data *sPlots* and simulation after reweight are shown in green and black, respectively.

data and simulation.

For the $B_s^0 \to D_s^{*-} \pi^+$, since the *sPlot* technique cannot be applied, a different strategy has been adopted. Instead of comparing background-subtracted data with the simulated signal $B_s^0 \to D_s^{*-} \pi^+$ decay, the data distributions in the mass range $[5000; 53000]$ MeV/c^2 are compared to the corresponding distributions obtained by adding the different signal and background contributions according to the fitted yields.[2] The distribution of each contribution has been extracted from the respective simulation sample except for the combinatorial background, which has been extracted from data for values of the invariant mass > 5500 MeV/c^2. Each simulation plot has been reweighted to match the distributions of nTracks and nSPDHits between data and simulation. Table 8.7 shows the fitted yields used for the validation of the MVA analysis in the $B_s^0 \to D_s^{*-} \pi^+$ decay.

Table 8.7: Yields of contributing signal and background components in the $[5000; 5300]$ MeV/c^2 invariant-mass region obtained from the fit to data distribution for the two categories of events.

Sample	Yields	
	category 1	category 2
$B_s^0 \to D_s^- \pi^+$	580± 26	200±15
$B_s^0 \to D_s^{*-} \pi^+$	15850 ± 550	5930±360
$B_s^0 \to D_s^- \rho^+$	9525±570	6075±380
$B_s^0 \to D_s^{*-} \rho^+$	2243±82	905±55
$B_d^0 \to D_s^- \pi^+$	625±70	220±49
Combinatorial	1229±56	876±45

Figures 8.13 and 8.14 show the input and the output distributions of the MVA classifiers for the two categories of events of the $B_s^0 \to D_s^{*-} \pi^+$ decays. Also in this case a good agreement

[2]Due to the low yield, the $B_d^0 \to D_s^- \pi^+$ component has been neglected.

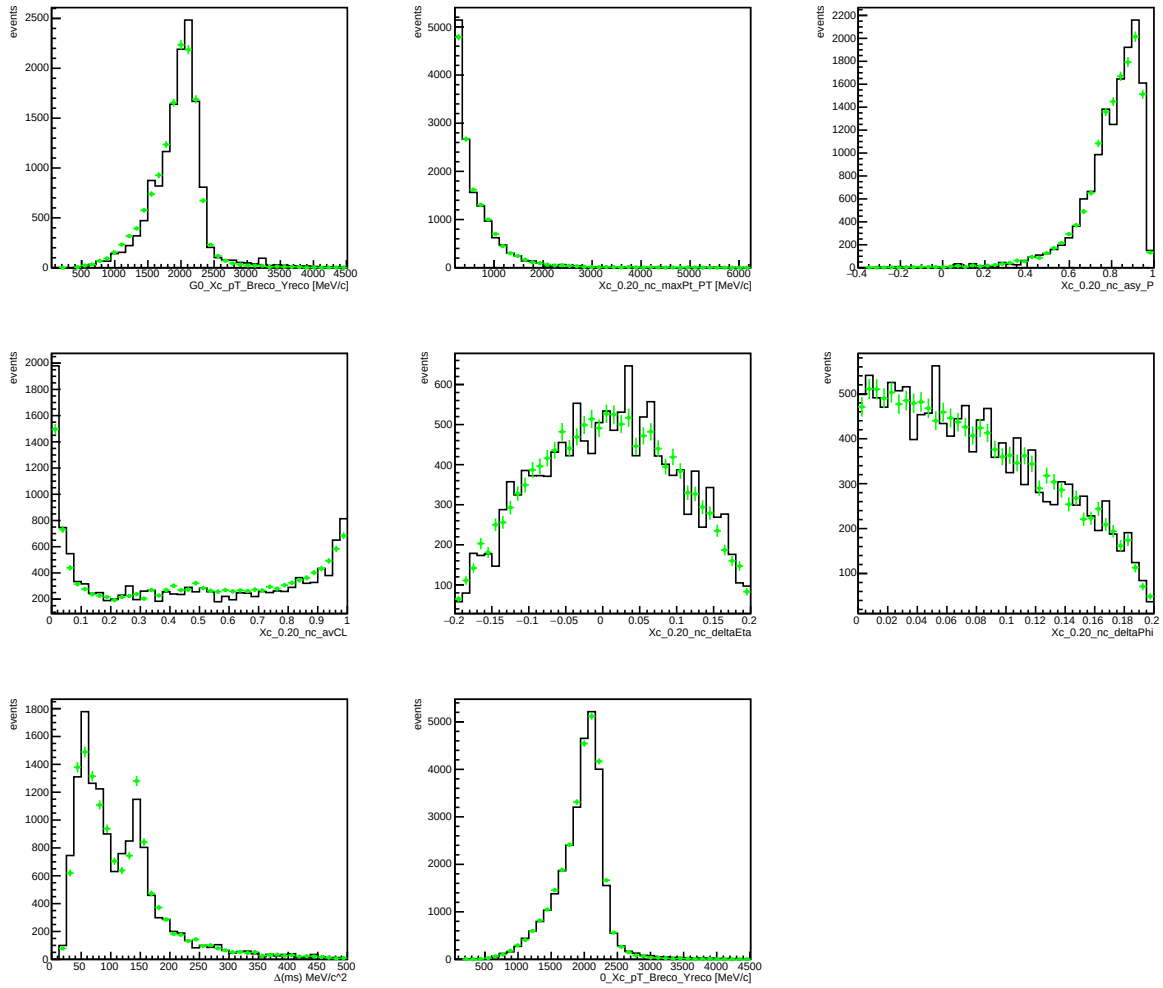

Figure 8.13: Distributions of the MVA classifiers input variables for the two categories of events of the $B_s^0 \to D_s^{*-} \pi^+$ decay. Data and simulation are shown in green and black, respectively. The simulation plots have been built by adding the different signal and background contributions taken from simulation and from data (combinatorial background only) according to the fitted yields. Each simulation plot has been reweighted to match the distributions of nTracks and nSPDHits between data and simulation.

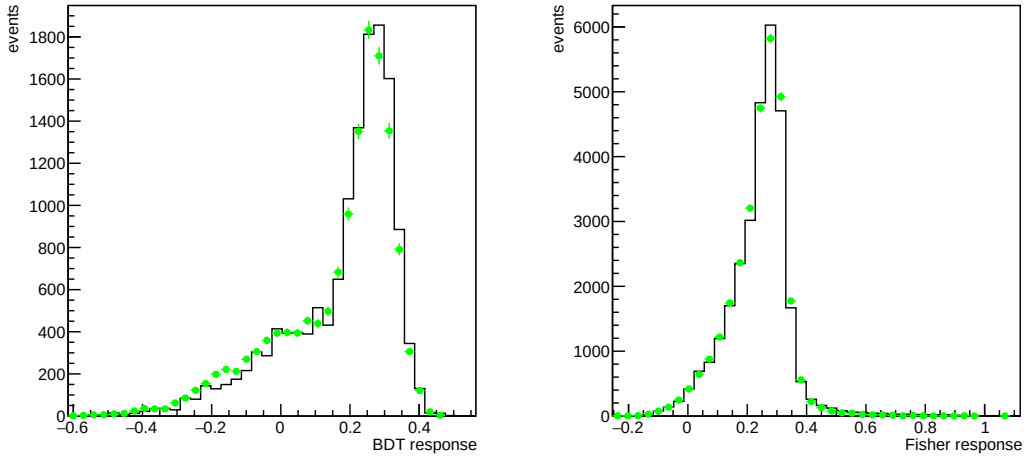

Figure 8.14: Distributions of the MVA classifier output for the two categories of events of the $B_s^0 \to D_s^{*-} \pi^+$ decay. Data and simulation are shown in green and black, respectively. The simulation plots have been built by adding the different signal and background contributions taken from simulation and from data (combinatorial background only) according to the fitted yields. Each simulation plot has been reweighted to match the distributions of nTracks and nSPDHits between data and simulation.

between data and simulation is obtained. Given the agreement reached between data and simulation in the control channel, the validation can be considered concluded. The final information that can be extracted to complete the validation of the MVA analysis in data is the comparison of the fraction of candidates for each category. Table 8.8 shows the results: for simulation the fractions are computed after weighting the events in order to match the event multiplicity observed in data, while for data they are computed from the mass fit results in each category. The

Table 8.8: Fraction of candidates in each category of neutral cone isolation for $B_s^0 \to D_s^- \pi^+$ and $B_s^0 \to D_s^{*-} \pi^+$ decays in data and simulation.

Decay	Sample	category 1	category 2
$B_s^0 \to D_s^- \pi^+$	simulation	73.4±0.3%	26.6±0.3%
	data	73.8±0.7%	26.2±0.7%
$B_s^0 \to D_s^{*-} \pi^+$	simulation	64.8±0.5%	35.2±0.5%
	data	73±3 %	27±6 %

agreement between data and simulation is very good for $B_s^0 \to D_s^- \pi^+$ decay, while a significative difference of about 11% is present for the $B_s^0 \to D_s^{*-} \pi^+$ decay. The different values found for the efficiency in the two samples don't compromise the analysis strategy because the yields of the $B_s^0 \to D_s^{(*)-} \tau \nu_\tau$ will be free parameters in both the categories. At this point, it is possible to extract the template from the simulated sample $B_s^0 \to D_s^{(*)-} \tau \nu_\tau$ that will be considered to distinguish the signal components of $B_s^0 \to D_s^- \tau^+ \nu_\tau$ and $B_s^0 \to D_s^{*-} \tau^+ \nu_\tau$ in the final fit to reach the measurement of $R(D_s)$ and $R(D_s^*)$. However due to time constraints this part is not treated in the preliminary attempt to fit the signal yield.

Chapter 9

Determination of the signal yield

Though the analysis still needs to be finalised to further suppress the background contributions, an explorative study on how to estimate the signal yield from a fit to the meaningful distributions is performed. This study has been developed in analogy to the one of the $R(D^*)$ with 3-prongs analysis [99, 100] concerning the definition of the fitting observables (sec. 9.1) and of the fit model (sec. 9.2). The study is performed on a pseudo data sample, exploiting different configurations of B/S and luminosities (sec. 9.3).

9.1 Fitting observables

Following the analysis of $R(D^*)$ the signal yield is obtained from a fit to the distributions of different observables. The observables are chosen based on their discrimination power between signal and background. Physics quantities like the momenta transfer to the leptons, q^2, and the tau decay time, t_τ, are the best candidates, as they specifically describe the features of the semileptonic signal decay. In addition to that, a BDT output discriminating between signal and background was used. In this study the BDT is initially replaced by the BDT_Iso output, that has some discrimination power between signal from background of partially reconstructed decays. In a second step the BDT is generated according to distributions that provide a better discrimination of the background.

9.1.1 Reconstruction of the decay kinematics

The exclusive reconstruction of the signal decay is not possible given the presence of two neutrinos in the final state. As a consequence the reconstruction of the B_s^0 and τ momenta based only on the visible final state particles is affected. With some approximation, it is possible to improve the kinematic reconstruction of the B_s^0 and τ particles by exploiting the full information of the reconstructed decay, in particular of the decay vertices.

The information related to the two missing neutrinos in the signal decay can be retrieved from the B_s^0 and the τ flight directions (defined by the vectors joining the B_s^0 vertex to the PV and the 3π vertex to the B_s^0 vertex, respectively), together with the known B_s^0 and τ masses. Then, the complete decay kinematics of both the B_s^0 and the τ decays can be determined up to

a two-fold ambiguity. The absolute value of the τ momentum in the laboratory frame, $|\vec{p}_\tau|$, is:

$$|\vec{p}_\tau| = \frac{(m_{3\pi}^2 + m_\tau^2)|\vec{p}_{3\pi}|\cos\theta_{\tau,3\pi} \pm E_{3\pi}\sqrt{(m_\tau^2 - m_{3\pi}^2)^2 - 4m_\tau^2|\vec{p}_{3\pi}|^2\sin^2\theta_{\tau,3\pi}}}{2(E_{3\pi}^2 - |\vec{p}_{3\pi}|^2\cos^2\theta_{\tau,3\pi})}\,, \tag{9.1}$$

with:

- $\theta_{\tau,3\pi}$ the angle between τ line of flight and 3π system three-momentum;
- $m_{3\pi}$, $|\vec{p}_{3\pi}|$, and $\mathrm{E}_{3\pi}$ the invariant mass, the three momentum and the energy of the 3π system;
- m_τ the known τ mass.

By choosing $\theta_{\tau,3\pi}$ to its maximum allowed value defined as

$$\theta_{\tau,3\pi}^{max} = \arcsin\left(\frac{m_\tau^2 - m_{3\pi}^2}{2m_\tau|\vec{p}_{3\pi}|}\right),$$

the two solutions degenerate to a single value for the τ momentum. Similarly, identifying with ξ the system made up of D_s^- and τ, the B_s^0 momentum can be obtained from:

$$|\vec{p}_{B_s^0}| = \frac{(m_\xi^2 + m_{B_s^0}^2)|\vec{p}_\xi|\cos\theta_{B_s^0,\xi} \pm E_\xi\sqrt{(m_{B_s^0}^2 - m_\xi^2)^2 - 4m_{B_s^0}^2|\vec{p}_\xi|^2\sin^2\theta_{B_s^0,\xi}}}{2(E_\xi^2 - |\vec{p}_\xi|^2\cos^2\theta_{B_s^0,\xi})}\,, \tag{9.2}$$

by imposing

$$\theta_{B_s^0,\xi}^{max} = \arcsin\left(\frac{m_{B_s^0}^2 - m_\xi^2}{2m_{B_s^0}|\vec{p}_\xi|}\right)$$

where $\vec{p}_\xi$ and E_ξ are the three-momentum and the mass of the D_s^-. Whereas, the energies and the three-momenta of the D_s^- and the τ can be written as:

$$\vec{p}_\xi = \vec{p}_{D_s} + \vec{p}_\tau$$

$$E_\xi = E_{D_s} + E_\tau.$$

The possibility to reconstruct both the τ and the B_s^0 momenta allows to compute the mass of the virtual W boson (M_W) and the momentum transferred to the τ-ν_τ system referred to as q^2 and defined as: $q^2 \equiv (p_{B_s} - p_{D_s})^2 = (p_\tau + p_{\nu_\tau})^2$.

In addition, the τ decay time, t_τ, can be obtained from the τ distance of flight from the B_s^0, L, and the reconstructed momenta as

$$t_\tau = \frac{m_\tau L}{p_\tau c}\,. \tag{9.3}$$

In fig. 9.1 the differences between the reconstructed and the true values of τ decay time (Left) and q^2 (Right) on the simulated events are shown. In both cases the kinematic correction improve the resolution and reduce the bias between the measured and the true value.

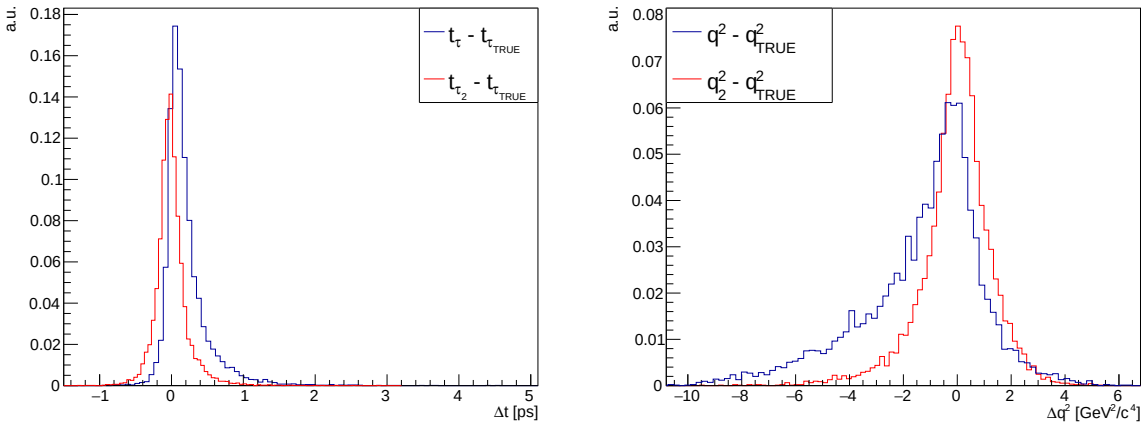

Figure 9.1: Distribution of the difference between (Left) the measured and the true τ decay time and (Right) the measured and true q^2 value using (blue) uncorrected and (red) corrected kinematics with the approximation described in the text.

9.2 Fit Model

The fit is performed by means of the maximum likelihood method on binned pseudo-data. The choice of performing a binned fit is related to the expected large statistics of data and on the modelling of the Probability Density Functions (PDF) for the different components, that are based on 3D templates determined from data and simulation that in this way also account for correlations among observables. The range of the observable, as well the binning scheme used has been chosen in order to avoid empty bin and to reflect the physics scenario.

In the studies performed, pseudo-data samples are generated using the same model that is used for fitting.

The fit maximise the likelihood function that can be written as product of Poissonian Probability Density Functions corresponding to each bin whose number of entries is given by n_i. The expected number of entries in each bin depends on some unknown parameters: $\mu_i = \mu_i(\theta_1, ..., \theta_m)$. To avoid numerical problems, instead of maximising the extended likelihood function [119] it is more convenient to use $-2ln\mathcal{L}$. The function being minimised, in order to fit $\theta_1, ..., \theta_m$ is the sum of the following:

$$-2ln\mathcal{L}(\vec{n};\vec{\theta}) = -2\sum_{i}^{n_{bins}}(n_i\, ln\mu_i(\theta_1, ..., \theta_m) - \mu_i(\theta_1, ..., \theta_m))$$

with i an index running over the bins, n_i, the number of observed events in the i^{th} bin, and $\mu_i(\vec{\theta})$ the number of expected events in the i^{th} bin. This number depends on $\vec{\theta}$, a vector of nuisance parameters and on the parameter of interest, *i.e.* the yield of signal and of each background component, which are free to vary in the fit. The expected number of entries in each bin, μ_i, is given by the superposition of the templates.

The templates for signal and different background categories are determined from simulation and data. The background categories analysed in Chapter 7 are grouped according some general

criteria discussed in the following. All the background categories of table 7.3 with less than 100 events are not considered because of the poor statistics. Among the others, the category "diffAncestorYXc" collects D_s and 3π not coming from a common ancestor. This background source and the purely combinatorial background can be described to a good level of approximation by the Wrong-sign data, where the D_s^- and the 3π have the same charge ("WS background"). The category "Xc background" represents the background given by D_s candidates not correctly reconstructed, while the category "Prompt" is given by the different cases where the 3π originate promptly from a $b-$hadron. The remaining background categories are found to be related to 3π originated from a $c-$hadron and thus are grouped together in the "Doubly charm" category. The templates are obtained from the inclusive $b-$hadron background simulated sample, except for the "Signal", which is determined from the signal simulation sample and for the "WS background" that is defined using the Wrong-Sign data sample.

Table 9.1: Final list of categories contributing to the fit studies. The percentage is referred to the abundance of each category in the inclusive simulated sample after all the selection described in Chapter 7. The third column shows the expected yield in 2 fb^{-1}.

Category	Percentage [%]	yield in 2 fb^{-1}
Signal	2.0	232
Doubly charm	90.2	10304
Xc background	6.7	766
Prompt	0.8	90
WS background	0.3	29

Figure 9.2 shows the results of a fit to a pseudo-data sample corresponding to 2 fb^{-1}, where the different contributions are listed 9.1 together with their expected yields extracted from the inclusive $b-$hadron background simulated sample after the selection of Chapter 6 and 7. Despite the huge background contamination (98% of the sample) the fit converges and finds a signal yield consistent with the input value $N_{sig} = (1.25 \pm 1.19) \times 10^2$. The relative uncertainty is more than 90% due to both the huge background contamination and the limited discrimination power of the considered BDT (see next sections).

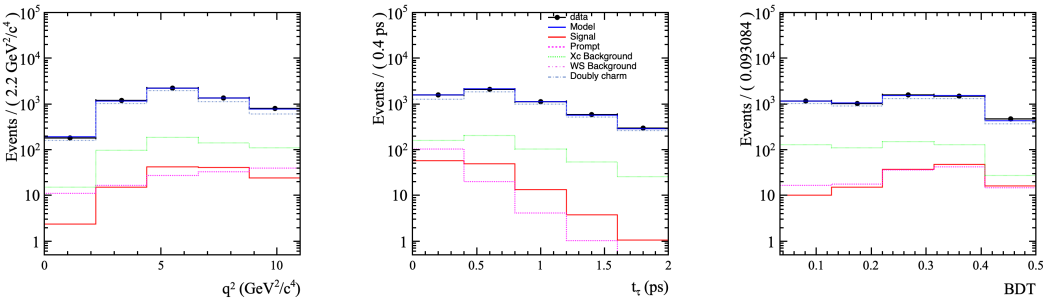

Figure 9.2: Results of the 3D binned extended maximum likelihood fit to pseudo-data. Fit projections on (Left) q^2, (Center) t_τ, and (Right) BDT_Iso.

9.2.1 Fit Validation

To validate the reliability of the results, the fit is performed on several ($\mathcal{O}(100)$) statistically independent samples of pseudo-data (TOYs) and the results are compared with the input values. A reliable fit should find a solution in 100% of cases (converge) and the fit parameters should be consistent with the inputs within the uncertainties, *i.e.* the pull[1] distributions should be normal Gaussian.

Figure 9.3 shows the results of the toys for the signal nominal inputs relative to 2fb^{-1}. The pull distribution of the signal yield deviates from the normal Gaussian distribution, and in particular the mean presents significative bias with respect to zero of about 9σ.

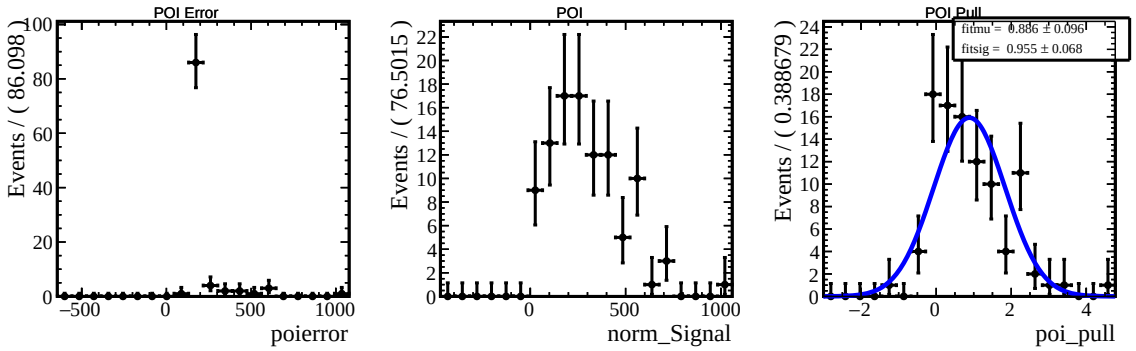

Figure 9.3: Results of the toys for the nominal inputs. (Left) Error distribution, (Center) Yield distribution and (Right) Pull distribution of N_{sig}.

This bias is present also in toys where the fraction of the background is scaled to lower values or the luminosity is doubled. The suspect is that the bias is related to the small discrimination power of the templates.

To better understand the origin of the observed bias the validation has been performed replacing the BDT_Iso distributions with shapes with a better discrimination power between different contributions. New templates are generated preserving the original information on the q^2 and t_τ observables and their correlation, and generating the BDT observable using different PDFs for each fit component.

Figure 9.4 shows the results of a fit and the pull distributions for a set of 100 toys.

The pull are normal Gaussian distributed with the mean and standard deviation compatible with zero and unity, respectively. Therefore, in case the BDT discriminates better among the different contributions, the fit result on signal yield is reliable.

[1]The pull quantity for a fit parameter is defined as

$$pull(N) = \frac{N_{fit} - N_{input}}{\sigma_{N_{fit}}}$$

where N_{fit} and $\sigma_{N_{fit}}$ are the fit value and its uncertainty and N_{input} is the input value.

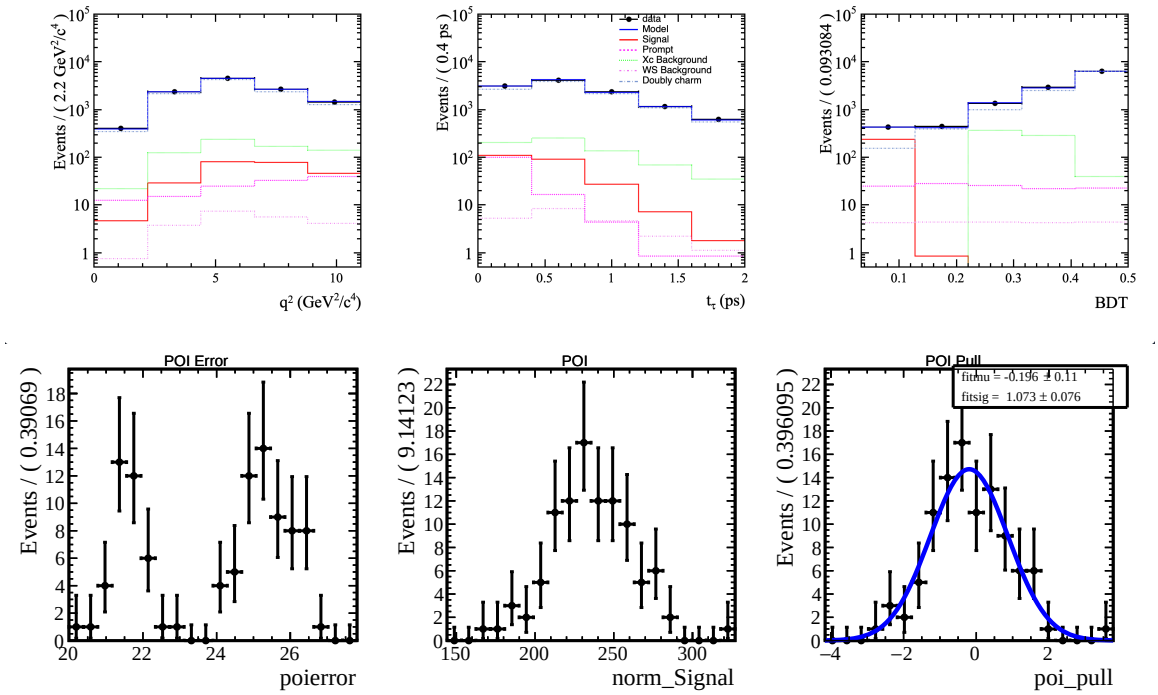

Figure 9.4: (Top) Results of the 3D binned extended maximum likelihood fit to pseudo-data. Fit projections on (Left) q^2, (Center) t_τ, and (Right) BDT. (Bottom) (Left) Error distribution and (Center) Yield distribution from a toy study with a statistic of each sample corresponding to 2 fb^{-1}. (Right) Pull distribution of N_{sig}.

9.3 Studies on the signal yield

By using the latter configuration of templates a study is performed to test the results in different scenarios of luminosity and background contamination, B/S. The scan in luminosity considers the luminosities delivered at LHCb in the 2011, 2012, in the full Run1 and full Run1+Run2 being 1,2,3 and 9 fb^{-1}, respectively. The scan in background contamination considers the cases where the relative contribution of the doubly charm background with respect to the signal is set to 1 (nominal condition) or suppressed by the factors 0.75, 0.50, 0.25, and 0.10. Also in this case each scan has been validated using 100 toys and evaluating the pull mean and sigma distributions of the signal yield. Figure 9.5 shows the results of the pulls mean (Left) and of the pulls sigma (Right) which are consistent with zero and one within 3σ.

The results of the studies are reported in fig. 9.6. The signal yield scales linearly with the luminosity (Left) while the relative uncertainty scales as the inverse of the luminosity squared (Right) as expected. Moreover the yield uncertainty depends on the B/S ratio, as also expected, and approaches the statistical limit given by $1/\sqrt{N_{\rm sig}}$ (6.5% and 3% at 2 and 9 fb^{-1}, respectively).

This study has underlined once more the key role of a good discrimination between the signal and the various background contributions. Since no further improvements are expected on the q^2 and t_τ observables, the BDT plays the key role.

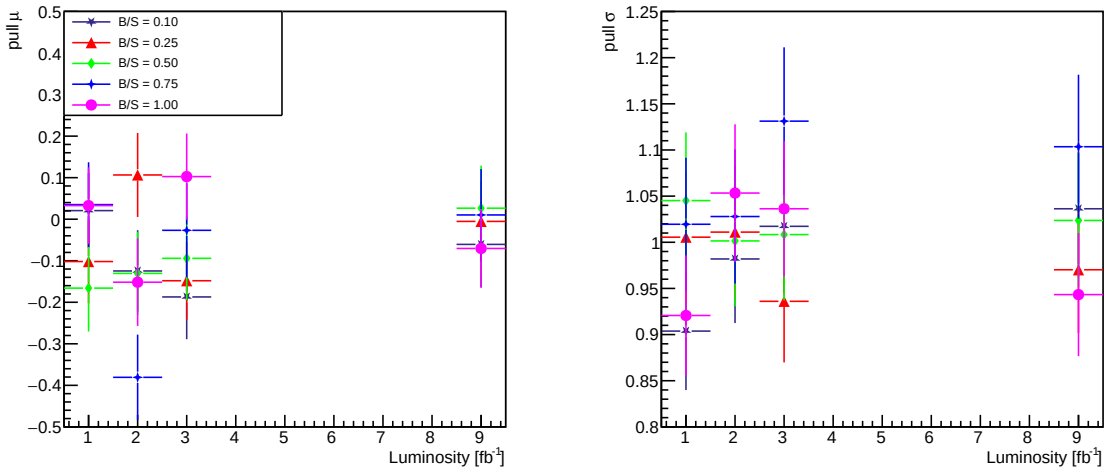

Figure 9.5: (Left) Pulls mean and (Right) pulls sigma referred to the signal yield, N_{sig} at different values of luminosity and of B/S.

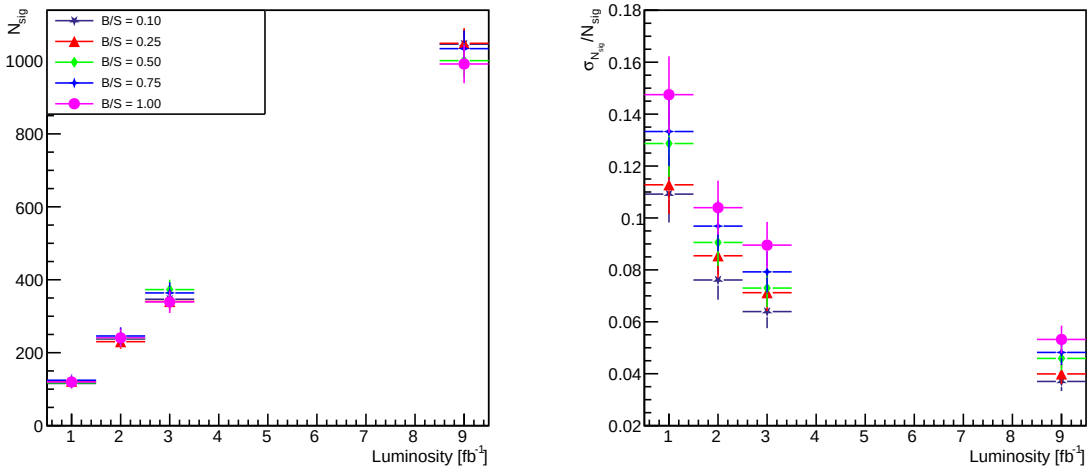

Figure 9.6: (Left) Signal yield, N_{sig} and (Right) relative uncertainty at different values of luminosity and of B/S.

Conclusions

This thesis reports on the activities I did during the PhD within the LHCb experiment.

The first part of the thesis concerns an hardware activity on the RICH detector for the LHCb upgrade, and in particular the Quality Assurance test and the commissioning activities performed in Ferrara and at CERN, respectively. The Quality Assurance tests have been performed to validate the core of the RICHs upgrade represented by the Elementary Cells. A total number of 387 R-Type and 194 H-type have been mounted and tested at the Ferrara site following a precise test protocol defined by the LHCb collaboration. Different measurements to characterised the opto-electronics have been performed, some of the measurements required a dedicated analysis to study of the so called Signal Induced Noise effect. This kind of noise originates from combined effects of internal light emission and ion feed-back and is localised in external region of the Multianode Photomultiplier Tubes (MaPMTs) used for the LHCb RICH upgrade. The result of the studies performed has been summarised in mitigation strategies adopted to reduce this effect [30]: the use of an appropriate high-voltage operating point, the implementation of a nanosecond time gate in the digital readout board firmware to improve the signal-to-noise ratio, and the installation new MaPMTs with new internal mechanics in the region of RICH1 which present high occupancy. The commissioning activities, instead, regarded the assembling and the testing of the RICH1 columns in the ComLab in Meyrin, and the installation of the commissioned RICH2 columns in the LHCb site. The column commissioning, as the quality assurance tests, followed a specific test protocol defined by the LHCb collaboration and deeply illustrated in the thesis. The installation at the LHCb site has implied also some services work like: fibres connection to the Data centre, LV switch on test, connectivity test to check the correct mapping, and the HV cabling and installation of the crates. The preparatory work has allowed the RICH2 to take part in the pilot test beam done in October-November 2021 with pp collisions at a centre-of-mass energy of $\sqrt{s} = 900$ GeV. The test beam was useful to check all the infrastructure functionalities and the capability of the RICH2 to run together with other subdetectors. After November 2021, the RICH1 also is being installed and its commissioning in the LHCb cavern is ongoing at the time of writing.

The second part of this thesis concerns a physics measurement to test the Lepton Flavour Universality in semileptonic decays foreseen by the Standard Model. The goal is to determine the ratio

$$R(D_s) = \frac{\mathcal{B}(B_s^0 \to D_s^- \tau^+ \nu_\tau)}{\mathcal{B}(B_s^0 \to D_s^- \mu^+ \nu_\mu)}$$

which is predicted by the SM with high precision, $R(D_s)^{SM} = 0.2971 \pm 0.0034$ [121], and has never been measured. Observing a deviation from the predicted value would indicate possible NP contributions at quark level transitions in the $B_s^0 \to D_s^- \tau^+ \nu_\tau$ decay.

The measurement exploits the large B_s^0 meson production at the LHC, the reconstruction of the $B_s^0 \to D_s^- \tau^+ \nu_\tau$ decays (referred to as *signal* channel) using the $D_s^- \to K^+ K^- \pi^-$ and $\tau^+ \to \pi^+ \pi^+ \pi^- \bar{\nu}_\tau$ decays and the recent LHCb measurement of the $B_s^0 \to D_s^- \mu^+ \nu_\mu$ branching fraction [90]. Following the analysis strategy developed for the measurement of $R(D^*)$ [99, 100] the $R(D_s)$ ratio is determined experimentally by measuring the ratio relative to a *normalisation* channel with the same or a similar topology to the signal and a known branching fraction. In this way, in fact, many experimental uncertainties related to the reconstruction of the different final states in the $R(D_s)$ ratio cancel allowing a more precise measurement.

In the thesis, different normalisation channels suitable for the $R(D_s)$ measurement are compared. A common selection for the signal and the normalisation channels based on simulated samples and 2012 data collected by the LHCb experiment has been developed following what was done in ref. [127]. It is based on simple cuts and a multivariate classifiers. The selection efficiencies related to the signal and the normalisation channels have been determined from simulated samples while the normalisation yields have been extracted from fits to the invariant mass distributions of the candidates passing the selection in data. Finally the contributions to the uncertainty on $R(D_s)$ due to the choice of the normalisation channel have been evaluated.

To improve the signal purity, the further selection has been developed. It is based on the analysis of the inclusive $b-$hadron background simulated sample and the identification of the different sources of background. This this study has allowed to optimise a cut to discriminate between the signal and the normalisation channels and to develop a BDT (BDT_Iso) to suppress the background due to partially reconstructed $b-$hadron decays. Further studies will be needed to suppress the dominant background of $b-$hadron decays to two $c-$hadrons that have similar features to the signal.

A study on the separation of $B_s^0 \to D_s^- \tau^+ \nu_\tau$ and $B_s^0 \to D_s^{*-} \tau^+ \nu_\tau$ decays is also performed. The $B_s^0 \to D_s^{*-} \tau^+ \nu_\tau$ channel in fact would contaminate the signal given the D_s^{*-} decay to D_s^- and a neutral particle (γ/π^0). A multivariate analysis has been developed and shows some discrimination power of the two contributions that can be eventually used in the final fit to determine the signal yield.

Finally, an explorative study on how to estimate the signal yield from a fit to the distributions of meaningful observables is performed. Following the same technique of the $R(D^*)$ analysis [99, 100], the signal yield is from a maximum likelihood binned fit to the distributions of the observables q^2, t_τ and BDT. Since the signal selection is not complete, as a first attempt the BDT_Iso is used, however, given its poor discrimination power among the different contributions, a more discriminating variable generated from ad-hoc distributions has been used. A validation of the fit results has been performed using several samples ($\mathcal{O}(100)$) of pseudo-data generated in nominal conditions and for different values of luminosity and background contamination (B/S ratio). The fit is biased in case the discrimination between the different contribution is poor, as in the case the BDT_Iso is used, while it is reliable when the discrimination is good.

In the latter case the results on the signal yields and the relative uncertainty follow the expected dependency on the luminosity and background contribution and approach the statistical limit. This study has underlined once more the key role of a good discrimination between the signal and the various background contributions.

Acknowledgements

The PhD has been a fantastic journey, sometimes tough but I have always found a way to see things from a good perspective thanks to the people I have found along my way.

Despite the hard time we lived in the past years, I've always had the chance to conduct my research in a collaborative environment and this work has been possible also because of the efforts of the people I've worked with. I would like to express my deep gratitude to Dr. Stefania Vecchi, for her guidance, patience, and motivation which never missed in these three years, and carried me through all the stages of the PhD. My sincere thank goes to Prof. Massimiliano Fiorini, for introducing me to the LHCb RICH family, for his advice and availability. I would also like to thank my referees: Prof. Antonio Romero Vidal, Prof. Silvia Gambetta, and Prof. Gabriele Simi for their suggestions and comments, and for the improvements they have made to my thesis. I want to thank Benedetto, Concezio, Ben, Edoardo, Ilaria and Luca for the always fruitful collaboration, and for their constant presence.

Last but not least there are no words to express my deep and sincere gratitude to my parents Maria Neve and Pasquale for giving me the opportunity to study and to achieve this important result.

To all my Family and Friends the biggest thank for being always by my side.

Appendix A

In the following are reported all the studies performed to determine the PDFs of each sample used to fit the invariant mass distribution of $B_s^0 \to D_s^{(*)-}\pi^+$ for the validation of the MVA developed to separate the $B_s^0 \to D_s^-\tau^+\nu_\tau$ from the $B_s^0 \to D_s^{*-}\tau^+\nu_\tau$ in sec.8.3.2.

To perform the fit, each contribution needs to be described by means of appropriate PDFs. Such PDFs are determined from samples of simulated decays generated, reconstructed and selected similarly to the 2012 data sample. The full list of simulation samples used can be found in table A.1.

Table A.1: Simulation samples used in the analysis of the $B_s^0 \to D_s^-\pi^+$ and $B_s^0 \to D_s^{*-}\pi^+$ control channels for the validation of the MVA analysis in data.

Sample	EvtType
$B_s^0 \to D_s^-\pi^+$	13264021
$B_s^0 \to D_s^{*-}\pi^+$	13264221
$B_s^0 \to D_s^-\rho^+$	13264421
$B_s^0 \to D_s^{*-}\rho^+$	13264631

$B_s^0 \to D_s^-\pi^+$ component

The invariant-mass distribution of selected $B_s^0 \to D_s^-\pi^+$ candidate decays from simulation, where the identification of the true signal decay is also requested, is shown in Fig. A.1. Its PDF can be described by the sum of two Crystal Ball functions, each one consisting in a Gaussian with an exponential tail on one side defined by the equation:

$$CB(x;\mu,\sigma,\alpha,n) = \begin{cases} A\cdot\left(B-\frac{x-\mu}{\sigma}\right)^{-n}, \text{for } \frac{m-\mu}{\sigma} \leq -\alpha \\ exp\left(-\frac{(x-\mu)^2}{2\sigma^2}\right), \text{for } \frac{m-\mu}{\sigma} > -\alpha \end{cases} \tag{A.1}$$

$$\text{with } A = \left(\frac{n}{|\alpha|}\right)^n \cdot exp\left(-\frac{|\alpha|^2}{2}\right) \text{ and } B = \frac{n}{|\alpha|} - |\alpha| \,,$$

where (μ,σ,α,n) are function's parameters. In particular, the two Crystal Balls share the same mean (μ) and have tails on both sides of the peak to account for nongaussian contributions to the mass resolution and (the left tail) to describe the radiative $B_s^0 \to D_s^-\pi^+$ decay contribution. The best fit and the corresponding parameters are shown in fig. A.1 and in table A.2. The normalised residuals in fig. A.1 have been evaluated in each bin as the difference between the

simulation and the fit value over the error: in most cases, they are within ±2 times the error except a few points which are instead within ±5 times but in any case all the values indicate a good fit.

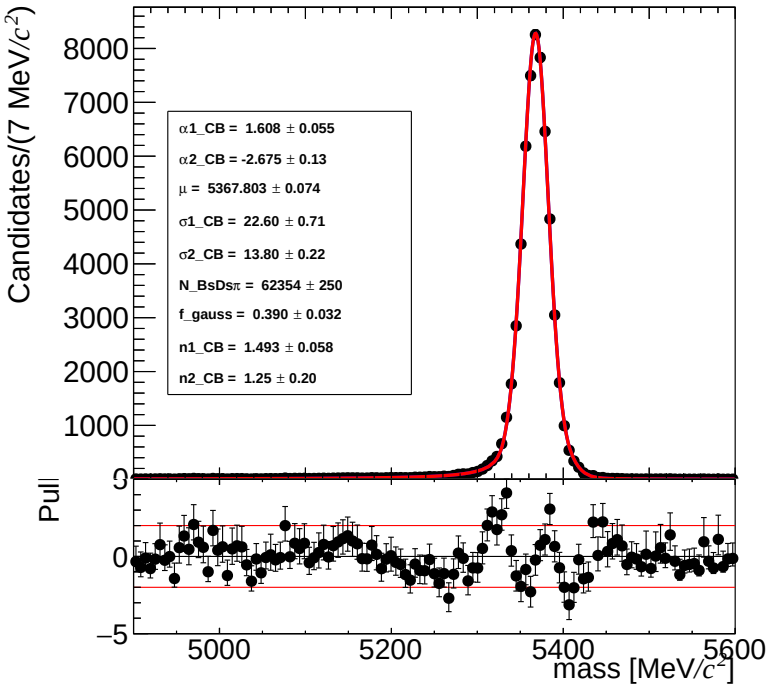

Figure A.1: Invariant-mass distribution of selected $B_s^0 \to D_s^- \pi^+$ decays from $B_s^0 \to D_s^- \pi^+$ simulation sample (data points) with the result of the best fit (red line) and the normalised residuals (pull).

Table A.2: Double Crystal Ball parameters obtained from the fit to the $B_s^0 \to D_s^- \pi^+$ simulation sample.

Parameters	Fit values for $B_s^0 \to D_s^- \pi^+$
μ [MeV/c^2]	5367.80 ± 0.07
σ1_CB [MeV/c^2]	22.6 ± 0.7
α1_CB	1.61 ± 0.05
n1_CB	1.49 ± 0.06
σ2_CB [MeV/c^2]	13.8 ± 0.2
α2_CB	-2.7 ± 0.1
n2_CB	1.2 ± 0.2
f_gauss	0.39 ± 0.03

$B_d^0 \to D_s^- \pi^+$ component

This background component arises from fully reconstructed final state $D_s^- \pi^0$ from a B_d^0 decay. Since the final-state reconstruction is identical to that of the B_s^0 and the kinematics is similar, the PDF is assumed to be the same as the $B_s^0 \to D_s^- \pi^+$, except for the mean value, which is shifted by -87.26 MeV/c^2, *i.e.* the difference between the known B_d^0 and B_s^0 masses.

Partially-reconstructed background components (with a missing photon or pion)

The invariant-mass distribution of partially reconstructed backgrounds have peculiar shapes that depend whether a photon or a pion is not reconstructed. Their shapes can be described by a `RooHILLdini` or a `RooHORNSdini` PDF, respectively [130] which are parametrised by the following functions: These two PDFs are of the form:

$$\texttt{RooHORNSdini}(\mu) = \int_a^b \left(x - \frac{a+b}{2}\right)^2 D(x|\mu,\sigma,f_g,R_\sigma)\left(\frac{1-\xi}{b-a}x + \frac{b\xi - a}{b-a}\right)dx \tag{A.2}$$

$$\texttt{RooHILLdini}(\mu) = \int_a^b -(x-a)(x-b)\, D(x|\mu,\sigma,f_g,R_\sigma)\left(\frac{1-\xi}{b-a}x + \frac{b\xi - a}{b-a}\right)dx \tag{A.3}$$

where $D(x|\mu,\sigma,f_g,R_\sigma)$ is a double Gaussian function defined as:

$$D(x|\mu,\sigma,f_g,R_\sigma) = (1-f_g)G(x|\mu,\sigma) + f_g G(x|\mu,R_\sigma\sigma)$$

where each of the PDF parameters are briefly discussed in the 9.3.

The PDF for the $B_s^0 \to D_s^- \rho^+$ background contribution is given by the `RooHORNSdini` function, while for $B_s^0 \to D_s^{*-}\pi^+$ and $B_s^0 \to D_s^{*-}\rho^+$ background contributions a combination of `RooHILLdini` and `RooHORNSdini` functions has been considered to account for both the $D_s^{*-} \to D_s^-\gamma$ and $D_s^-\pi^0$ decays.

The best fit to the invariant-mass distribution of the three decay channels from simulation and the corresponding parameters are shown in figures A.2,A.3,A.4 and table A.3.

Combinatorial background

The combinatorial background contributes to the full mass range with a regular, decreasing shape which becomes evident in the high-mass region (> 5350MeV/c^2), where it dominates. In this region, the data distribution is compatible with both a linear and an exponential function.

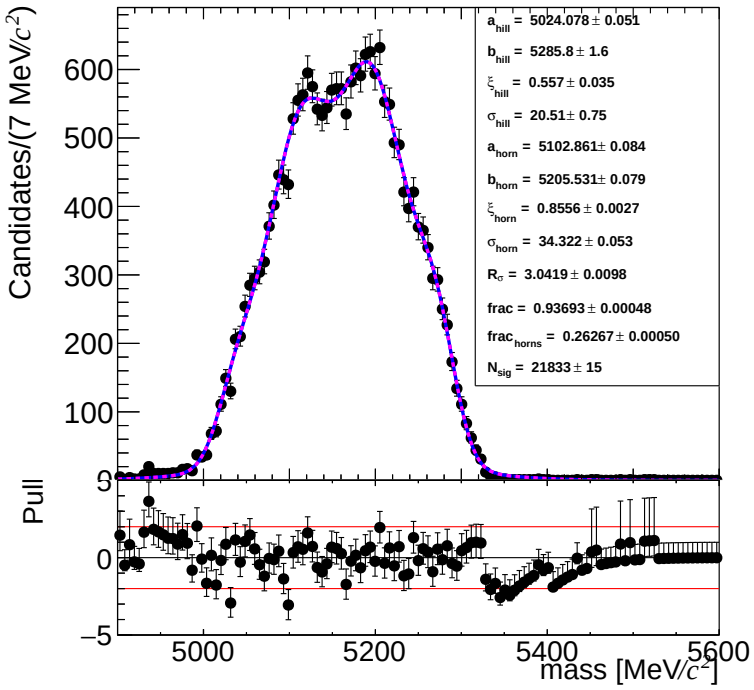

Figure A.2: Fit to the invariant mass of the $B_s^0 \to D_s^{*-}\pi^+$ simulation sample.

Table A.3: Parameters obtained from the fit to the $B_s^0 \to D_s^{*-}\pi^+$, $B_s^0 \to D_s^{*-}\rho^+$ and $B_s^0 \to D_s^-\rho^+$ simulation samples.

Parameters	Fit values		
	$B_s^0 \to D_s^{*-}\pi^+$	$B_s^0 \to D_s^{*-}\rho^+$	$B_s^0 \to D_s^-\rho^+$
a_{hill} [MeV/c^2]	5024.08 ± 0.05	4748 ± 18	–
b_{hill} [MeV/c^2]	5285.8 ± 1.6	4400	–
ξ_{hill}	0.55 ± 0.03	2.0 ± 1.1	–
σ_{hill} [MeV/c^2]	20.5 ± 0.7	12.3 ± 1.9	–
a_{horn} [MeV/c^2]	5102.86 ± 0.08	4900 ± 9.6	3620 ± 125
b_{horn} [MeV/c^2]	5205.531 ± 0.003	5020.5 ± 7.1	5225.5 ± 1.3
ξ_{horn}	0.855 ± 0.003	1.0 ± 0.6	1.2 ± 0.7
σ_{horn} [MeV/c^2]	34.32 ± 0.05	58.2 ± 4.4	18.9 ± 1.2
R_σ	3.042 ± 0.009	10.0 ± 1.6	6.1 ± 1.5
$frac$	0.9369 ± 0.0005	0.991± 0.005	0.982 ± 0.009
$frac_{horns}$	0.2627 ± 0.0005	0.36 ± 0.06	–

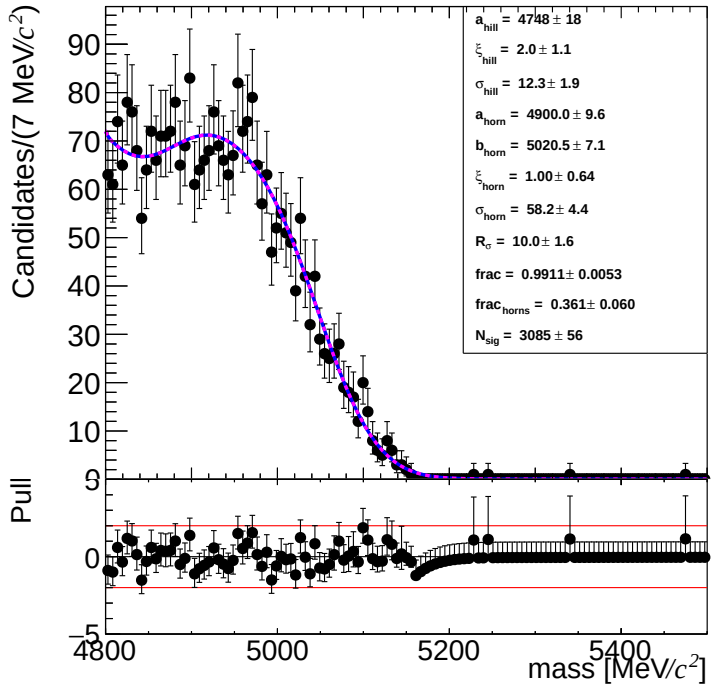

Figure A.3: Fit to the invariant mass distribution of the $B_s^0 \to D_s^{*-}\rho^+$ simulation sample.

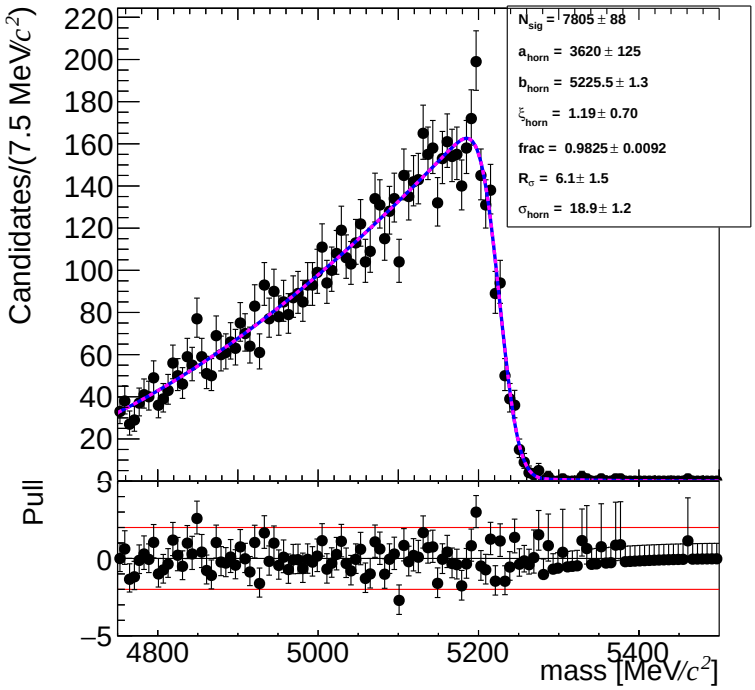

Figure A.4: Fit to the invariant mass distribution of the $B_s^0 \to D_s^{-}\rho^+$ simulation sample.

Appendix B

TheRooHORNSdini and RooHILLdini are defined as:

$$\texttt{RooHORNSdini}(\mu) = \int_a^b \left(x - \frac{a+b}{2}\right)^2 D(x|\mu,\sigma,f_g,R_\sigma)\left(\frac{1-\xi}{b-a}x + \frac{b\xi - a}{b-a}\right)dx \tag{B.1}$$

$$\texttt{RooHILLdini}(\mu) = \int_a^b -(x-a)(x-b)\, D(x|\mu,\sigma,f_g,R_\sigma)\left(\frac{1-\xi}{b-a}x + \frac{b\xi - a}{b-a}\right)dx \tag{B.2}$$

where $D(x|\mu,\sigma,f_g,R_\sigma)$ is a double Gaussian function defined as:

$$D(x|\mu,\sigma,f_g,R_\sigma) = (1-f_g)G(x|\mu,\sigma) + f_g G(x|\mu,R_\sigma\sigma)$$

Those functions are parametrised using the following list of parameters:

- x [MeV/c^2] - fit variable, is the reconstructed invariant mass.
- a [MeV/c^2] - lower kinematic endpoint. Fully determined by the specific particle masses in the decay chain.
- b [MeV/c^2] - upper kinematic endpoint, also fully determined by the specific particle masses in the decay chain.
- ξ - relative height of the two peaks, allowing for invariant mass dependent selection effects that remove more of one peak than the other. When $\xi = 1$, both peaks are equal height, while when $\xi > (<)1$, the lower (upper) peaks is largest.
- σ [MeV/c^2] - width of the core resolution Gaussian. The core Gaussian is the Gaussian of narrowest width in the overall double Gaussian convolution.
- f_σ - fraction of yield contained in the core Gaussian.
- R_σ - ratio wide Gaussian and core Gaussian widths in the double Gaussian resolution function.

Bibliography

[1] "LHC machine", Journal of Instrumentation 3 no.8, (2008) S08001. http://iopscience.iop.org/1748-0221/3/08/S08001.

[2] The LHCb Collaboration et al,2015, "LHCb detector performance, http://dx.doi.org/10.1142/S0217751X15300227, DOI=10.1142/s0217751x15300227

[3] "Christian Elsässer","LHCb collaboration", "$\bar{b}b$ production angle plots",https://lhcb.web.cern.ch/lhcb/speakersbureau/html/bb_ProductionAngles.html

[4] The LHCb Collaboration *et al.*, "The LHCb Detector at the LHC", 2008 JINST 3 S08005

[5] R. Aaij, A. Affolder, K. Akiba, M. Alexander, S. Ali, R. B. Appleby, M. Artuso, A. Bates, A. Bay and O. Behrendt, *et al.* "Performance of the LHCb Vertex Locator", JINST **9**, P09007 (2014) doi:10.1088/1748-0221/9/09/P09007 [arXiv:1405.7808 [physics.ins-det]].

[6] ,L.S.T.Group, "LHCb Silicon Tracker - Material for Publications",https://lhcb.physik.uzh.ch/ST/public/material/index.php

[7] LHCb Outer Tracker group,"Performance of the LHCb Outer Tracker",JINST 9 (2014) P01002,https://arxiv.org/abs/1311.3893

[8] M. Adinolfi, G. Aglieri Rinella, E. Albrecht,et al., "Performance of the LHCb RICH detector at the LHC",Eur. Phys. J. C 73 (2013) 2431,https://arxiv.org/abs/1211.6759

[9] Irina Machikhiliyan and the LHCb calorimeter group, "Current status and performance of the LHCb electromagnetic and hadron calorimeters",https://iopscience.iop.org/article/10.1088/1742-6596/293/1/012052

[10] V. Khachatryan *et al.* [CMS and LHCb], "Observation of the rare $B_s^0 \to \mu^+\mu^-$ decay from the combined analysis of CMS and LHCb data", Nature **522**, 68-72 (2015) doi:10.1038/nature14474 [arXiv:1411.4413 [hep-ex]].

[11] R. Aaij *et al.* [LHCb], "Measurement of the $B_s^0 \to \mu^+\mu^-$ decay properties and search for the $B^0 \to \mu^+\mu^-$ and $B_s^0 \to \mu^+\mu^-\gamma$ decays", Phys. Rev. D **105**, no.1, 012010 (2022) doi:10.1103/PhysRevD.105.012010 [arXiv:2108.09283 [hep-ex]].

[12] R. Aaij *et al.* [LHCb], "Angular Analysis of the $B^+ \to K^{*+}\mu^+\mu^-$ Decay", Phys. Rev. Lett. **126**, no.16, 161802 (2021) doi:10.1103/PhysRevLett.126.161802 [arXiv:2012.13241 [hep-ex]].

[13] LHCb, R. Aaij et al., "Implications of LHCb measurements and future prospects", Eur. Phys. J. C73 (2013), no. 4 2373, arXiv:1208.3355.

[14] R. Aaij *et al.* [LHCb], "Observation of a narrow pentaquark state, $P_c(4312)^+$, and of two-peak structure of the $P_c(4450)^+$", Phys. Rev. Lett. **122**, no.22, 222001 (2019) doi:10.1103/PhysRevLett.122.222001 [arXiv:1904.03947 [hep-ex]].

[15] R. Aaij *et al.* [LHCb], "Observation of an exotic narrow doubly charmed tetraquark", [arXiv:2109.01038 [hep-ex]].

[16] R. Aaij *et al.* [LHCb], "Study of the doubly charmed tetraquark T_{cc}^+", [arXiv:2109.01056 [hep-ex]].

[17] LHCb detector performance. International Journal of Modern Physics A, 30.07 (Mar. 2015), p. 1530022. issn: 1793-656X. doi: 10.1142/s0217751x15300227. url: http://dx.doi.org/10.1142/S0217751X15300227

[18] LHCb muon system," Technical Design Report", `CERN-LHCC-2001-010`

[19] R.Frühwirth, "Application of Kalman filtering to track and vertex fitting", `https://doi.org/10.1016/0168-9002(87)90887-4`

[20] Particle Data Group,"Passage of Particles Through Matter",`https://pdg.lbl.gov/2019/reviews/rpp2018-rev-passage-particles-matter.pdf`

[21] M. Bellato et al.,"A PCIe gen3 based readout for the LHCb upgrade", Journal of Physics: Conference Series 513 (2014) 012023.

[22] J. P. Cachemiche et al.," The PCIe-based readout system for the LHCb experiment", JINST 11 (2016), no. 02 P02013. 12 p.

[23] J. Mitra et al.," GBT link testing and performance measurement on PCIe40 and AMC40 custom design FPGA boards", JINST 11 (2016), no. 03 C03039. 12 p

[24] LHCb Collaboration," LHCb VELO Upgrade Technical Design Report", Tech. Rep. CERN-LHCC-2013- 021. LHCB-TDR-013, Nov, 2013

[25] LHCb Collaboration, "LHCb Tracker Upgrade Technical Design Report", Tech. Rep. CERN-LHCC-2014- 001. LHCB-TDR-015, Feb, 2014.

[26] LHCb Collaboration," LHCb PID Upgrade Technical Design Report", Tech. Rep. CERN-LHCC-2013-022. LHCB-TDR-014, Nov, 2013

[27] M. Baszczyk, P. Carniti *et al.*, " CLARO: an ASIC for high rate single photon counting with multi-anode photomultipliers", Journal of Instrumentation, 2017, doi = 10.1088/1748-0221/12/08/p08019, https://doi.org/10.1088/1748-0221/12/08/p08019.

[28] LHCb Collaboration, "Experimental studies for the validation of the opto-electronic components for the LHCb RICH Upgrade", 2020, https://cds.cern.ch/record/2715879

[29] https://fluka.cern

[30] M. Andreotti *et al.* [LHCb], "Characterisation of signal-induced noise in Hamamatsu R11265 Multianode Photomultiplier Tubes,"JINST **16** (2021), P11030, doi:10.1088/1748-0221/16/11/P11030 [arXiv:2110.00831 [physics.ins-det]].

[31] https://jcop.web.cern.ch/jcop-framework/.

[32] https://www.winccoa.com/.

[33] Easo Sajan,"LHCb RICH","Overview of LHCb-RICH upgrade","Nucl. Instrum. Meth. A",v "876", 2017, doi :"10.1016/j.nima.2017.02.061",https://www.sciencedirect.com/science/article/pii/S0168900217302565.

[34] S. Glashow, "Partial-symmetries of weak interactions", Nuclear Physics, 22:579-588, (1961).

[35] S. Weinberg, "A model of leptons", Phys. Rev. Lett., 19:1264-1266, (1967).

[36] A. Salam, N. Svalthrom ed., "Elementary particle theory: relativistic groups and analyticity", Nobel symposium. (1968)

[37] F. Englert and R. Brout, "Broken Symmetry and the Mass of Gauge Vector Mesons", Phys. Rev. Lett., 13:321-323, (1964).

[38] P.W. Higgs, "Broken Symmetries and the Masses of Gauge Bosons", Phys. Rev. Lett., 13:508-509, (1964).

[39] G.S. Guralnik, C.R. Hagen and T.W.B. Kibble, "Global Conservation Laws and Massless Particles", Phys. Rev. Lett., 13: 585–587, (1964).

[40] G. Zweig, "An SU(3) model for strong interaction symmetry and its breaking", Technical Report CERN-TH-401, CERN, Geneva, (1964).

[41] M.Y. Han and Y. Nambu, "Three-triplet model with double SU(3) symmetry", Phys. Rev., 139:B1006-B1010, (1965).

[42] O.W. Greenberg, "Spin and Unitary Spin Independence in a Paraquark Model of Baryons and Mesons", Phys. Rev. Lett., 13:598-602, (1964).

[43] H.D. Politzer, "Reliable perturbative results for strong interactions", Phys. Rev. Lett., 30:1346–1349, (1973).

[44] D.J. Gross and F. Wilczek, "Ultraviolet behavior of non-abelian gauge theories", Phys. Rev. Lett., 30:1343–1346, (1973).

[45] G. Arnison et al., Phys.Lett. 122B (1983) 103; 126B 398, (1983).

[46] M. Banner et al., Phys. Lett. 122B 476, (1983).

[47] P. Bagnaia et al., Phys. Lett. B129 130, (1983).

[48] Abe F. et al, CDF Collaboration, Phys Rev. D50 2966 and Phys. Rev. Lett. 73 225, (1994).

[49] ATLAS Collaboration, "Observation of a new particle in the search for the Standard Model Higgs boson with the ATLAS detector at the LHC". Phys.Lett.B, (2012).

[50] CMS Collaboration, "Observation of a new boson at a mass of 125 GeV with the CMS experiment at the LHC". Phys.Lett.B, (2012).

[51] P. Langacker, "Introduction to the Standard Model and Electroweak Physics", Phys.Lett. High Energy Physics-Phenomenology, (2009), `http://arxiv.org/abs/0901.0241`.

[52] B. Odom et al., "New Measurement of the Electron Magnetic Moment Using a One-Electron Quantum Cyclotron", Phys. Rev. Lett. 97 (3 2006) 030801, `http://link.aps.org/doi/10.1103/PhysRevLett.97.030801`

[53] ALEPH Collaboration, DELPHI Collaboration, L3 Collaboration, OPAL Collaboration, LEP Working Group for Higgs Boson Searches, Phys. Lett. B, 565 (2003), `http://arXiv:hep-ex/0306033`

[54] Tevatron, " New Phenomena and Higgs Working Group for the CDF and DØ Collaborations", FERMILAB-PUB-09-060-E, `http://arXiv:0903.4001`

[55] S. Schael *et al.* [ALEPH, DELPHI, L3, OPAL, SLD, LEP Electroweak Working Group, SLD Electroweak Group and SLD Heavy Flavour Group], "Precision electroweak measurements on the Z resonance," Phys. Rept. **427**, 257-454 (2006) doi:10.1016/j.physrep.2005.12.006, `https://arxiv.org/abs/hep-ex/0509008`.

[56] Review of Particle Physics, Tanabashi, M. and Hagiwara, K. et Al., Particle Data Group, Phys. Rev. D, 98, 3, 030001, 1898,2018,Aug,American Physical Society, doi = 10.1103/PhysRevD.98.030001, `https://link.aps.org/doi/10.1103/PhysRevD.98.030001`

[57] CDF Collaboration, "Measurements of Inclusive W and Z Cross Sections in p-$\bar{p}$ Collisions at $\sqrt{s}$ =1.96 TeV", J.Phys.G34:2457-2544,2007, `https://arxiv.org/abs/hep-ex/0508029`.

[58] S. Schael *et al.* [ALEPH, DELPHI, L3, OPAL and LEP Electroweak], "Electroweak Measurements in Electron-Positron Collisions at W-Boson-Pair Energies at LEP," Phys. Rept. **532**, 119-244 (2013) doi:10.1016/j.physrep.2013.07.004, `https://arxiv.org/abs/1302.3415`.

[59] LHCb collaboration, "Measurement of forward $W \to e\nu$ production in pp collisions at $\sqrt{s}$=8 TeV",JHEP 10 (2016) 030, DOI: 10.1007/JHEP10(2016)030, `https://arxiv.org/abs/1608.01484`.

[60] ATLAS Collaboration, "Precision measurement and interpretation of inclusive W^+, W^- and Z/γ^* production cross sections with the ATLAS detector", Eur. Phys. J. C 77 (2017) 367, DOI: 10.1140/epjc/s10052-017-4911-9, `https://arxiv.org/abs/1612.03016`.

[61] NA62 collaboration, C. Lazzeroni et al., "Precision Measurement of the Ratio of the Charged Kaon Leptonic Decay Rates", Phys. Lett. B719 (2013) 326, arXiv:1212.4012.

[62] A. Aguilar-Arevalo et al., "Improved Measurement of the $\pi \to e\nu$ Branching Ratio", Phys. Rev. Lett. 115 (2015), no. 7 071801, arXiv:1506.05845.

[63] V. Cirigliano and I. Rosell, "Two-Loop Effective Theory Analysis of $\pi(K) \to e\bar{\nu}_e[\gamma]$ Branching Ratios", Phys. Rev. Lett. 99 (2007) 231801, arXiv:0707.3439.

[64] HFLAV collaboration, Y. Amhis et al., "Averages of b-hadron, c-hadron, and τ-lepton properties as of summer 2016", Eur. Phys. J. C77 (2017) 895, arXiv:1612.07233.

[65] G. D'Ambrosio, G. Ecker, G. Isidori, and J. Portoles, The Decays $K \to \pi\ell^+\ell^-$ beyond leading order in the chiral expansion, JHEP 08 (1998) 004, arXiv:hep-ph/9808289.

[66] S. Fajfer, S. Prelovsek, and P. Singer, Rare charm meson decays $D \to P\ell^+\ell^-$ and $c \to u\ell^+\ell^-$ in SM and MSSM, Phys. Rev. D64 (2001) 114009, arXiv:hep-ph/0106333.

[67] F. Mescia, C. Smith, and S. Trine, $K_{\rm L}^0 \to \pi^0 e^+ e^-$ and $K_{\rm L}^0 \to \pi^0 \mu^+ \mu^-$: A Binary star on the stage of flavor physics, JHEP 08 (2006) 088, arXiv:hep-ph/0606081.

[68] L. Cappiello, O. Cata, and G. D'Ambrosio, Standard Model prediction and new physics tests for $D^0 \to {\rm h}^+{\rm h}^-\ \ell^+\ell^-$ (h = π,K: $\ell = e, \mu$), JHEP 04 (2013) 135, arXiv:1209.4235.

[69] G. Hiller and F. Kruger, More model-independent analysis of $b \to s$ processes, Phys. Rev. D69 (2004) 074020, arXiv:hep-ph/0310219.

[70] C. Bobeth, G. Hiller, and G. Piranishvili, Angular distributions of $\bar{B} \to \bar{K}\bar{\ell}\ell$ decays, JHEP 12 (2007) 040, arXiv:0709.4174.

[71] C. Bouchard et al., Standard Model predictions for $B \to K\ell^+\ell^-$ with form factors from lattice QCD, Phys. Rev. Lett. 111 (2013) 162002, arXiv:1306.0434.

[72] R. Aaij et al. "Test of lepton universality in beauty-quark decays", `https://arxiv.org/abs/2103.11769`

[73] R. Aaij et al., Test of lepton universality using $B^+ \to K^+\ell^+\ell^-$ decays. Phys. Rev. Lett., 113 (2014), p. 151601. doi: 10.1103/PhysRevLett.113.151601. arXiv: 1406.6482 [hep-ex]

[74] R. Aaij et al., "Search for Lepton-Universality Violation in $B^+ \to K^+\ell^+\ell^-$ Decays ",Phys. Rev. Lett. 122, 191801, DOI:10.1103/PhysRevLett.122.191801 , https://arxiv.org/abs/1903.09252.

[75] J. P. Lees et al. Measurement of Branching Fractions and Rate Asymmetries in the Rare Decays $B \to K^{(*)}\ell^+\ell^-$. Phys. Rev., D86 (2012), p. 032012. doi: 10.1103/ PhysRevD.86.032012. arXiv: 1204.3933 [hep-ex]

[76] J.-T. Wei et al., Measurement of the Differential Branching Fraction and Forward-Backward Asymmetry for $B \to K^{(*)}\ell^+\ell^-$. Phys. Rev. Lett., 103 (17 Oct. 2009), p. 171801. doi: 10.1103/PhysRevLett.103.171801. https://link.aps.org/doi/10.1103/PhysRevLett.103.171801

[77] R. Aaij et al., Test of lepton universality with $B^0 \to K^{*0}\ell^+\ell^-$ decays. JHEP , 08 (2017), p. 055. doi:10.1007/JHEP08(2017)055. arXiv: 1705.05802 [hep-ex]

[78] R. Aaij et al., Test of lepton universality with $\Lambda_b^0 \to pK^-\ell^+\ell^-$ decays. Journal of High Energy Physics, 2020.5 (May 2020). issn: 1029-8479. doi: 10.1007/ jhep05(2020)040. http://dx.doi.org/10.1007/JHEP05(2020)040

[79] A. Abdesselam et al., Test of lepton flavor universality in $B \to K\ell^+\ell^-$ decays (Aug. 2019). arXiv: 1908.01848 [hep-ex]

[80] A. Abdesselam et al., Test of lepton flavor universality in $B \to K^*\ell^+\ell^-$ decays at Belle (Apr. 2019). arXiv: 1904.02440 [hep-ex]

[81] LHCb collaboration et al., "Measurement of CP-averaged observables in the $B^0 \to K^{*0+-}$ decay. 2020." arXiv:2003.04831[hep-ex]

[82] S. Descotes-Genon, L. Hofer, J. Matias, and J. Virto, "On the impact of power corrections in the prediction of $B \to K^*\mu^+\mu^-$ observables", JHEP 12 (2014) 125, arXiv:1407.8526.

[83] A. Khodjamirian, T. Mannel, A. A. Pivovarov, and Y.-M. Wang, "Charm-loop effect in $B \to K^{(*)}\ell^+\ell^-$ and $B \to K^*\gamma$", JHEP 09 (2010) 089, arXiv:1006.4945.

[84] BaBar collaboration, J. P. Lees et al., Evidence for an excess of $\bar{B} \to D^{(*)}\tau^-\bar{\nu}_\tau$ decays, Phys. Rev. Lett. 109 (2012) 101802, arXiv:1205.5442.

[85] BaBar collaboration, J. P. Lees et al., "Measurement of an Excess of $\bar{B} \to D^{(*)}\tau^-\bar{\nu}_\tau$ Decays and Implications for Charged Higgs Bosons", Phys. Rev. D88(2013) 072012, arXiv:1303.0571.

[86] Belle collaboration, M. Huschle et al., Measurement of the branching ratio of $\bar{B} \to D^{(*)}\tau^-\bar{\nu}_\tau$ relative to $\bar{B} \to D^{(*)}\ell^-\ \bar{\nu}_\ell$ decays with hadronic tagging at Belle, Phys. Rev. D92 (2015) 072014, arXiv:1507.03233

[87] Belle collaboration, Y. Sato et al., "Measurement of the branching ratio of $\bar{B}^0 \to D^{*+}\tau^-\bar{\nu}_\tau$ relative to $\bar{B}^0 \to D^{**}\ell^-\bar{\nu}_\ell$decays with a semileptonic tagging method", Phys. Rev. D94 (2016) 072007, arXiv:1607.07923.

[88] S. Hirose et al., "Measurement of the τ lepton polarization and $R(D^*)$ in the decay $\bar{B}^0 \to D^{*+}\tau^-\bar{\nu}_\tau$", Phys. Rev. Lett. 118 (2017) 211801, arXiv:1612.00529.

[89] G. Caria et al. (Belle Collaboration), "Measurement of $R\,(D)$ and $R(D^*)$ with a Semileptonic Tagging Method", Phys. Rev. Lett. 124, 161803 – Published 24 April 2020.

[90] LHCb collaboration, R. Aaij et al., " Measurement of $|V_{cb}|$ with $B_s^0 \to D_s^{(*)-}\mu^+\nu$ decays", doi: 10.1103/PhysRevD.101.072004 `https://link.aps.org/doi/10.1103/PhysRevD.101.072004`.

[91] LHCb collaboration, R. Aaij et al., " Measurement of $b-$ hadron production fractions in 7 TeV pp collisions", Phys. Rev. D 85, 032008, `https://doi.org/10.1103/PhysRevD.85.032008`.

[92] R. Aaij *et al.* [LHCb],'Measurement of the b-quark production cross-section in 7 and 13 TeV pp collisions", Phys. Rev. Lett. **118**, no.5, 052002 (2017) [erratum: Phys. Rev. Lett. **119**, no.16, 169901 (2017)] doi:10.1103/PhysRevLett.118.052002, [arXiv:1612.05140 [hep-ex]].

[93] S. Aoki et al., FLAG Review 2019. The European Physical Journal C, 80.2 (Feb. 2020). issn: 1434-6052. doi: 10.1140/epjc/s10052-019-7354-7. `http:dx.doi.org/10.1140/epjc/s10052-019-7354-7`

[94] Jon A. Bailey et al., Update of $|V_{cb}|$ from the $\bar{B} \to D^*\ell\bar{\nu}_\ell$ form factor at zero recoil with three-flavor lattice QCD. Phys. Rev. D, 89 (11 June 2014), p. 114504. doi: 10.1103/PhysRevD.89.114504. `https://link.aps.org/doi/10.1103/PhysRevD.89.114504`

[95] Judd Harrison, Christine T. H. Davies, and Matthew Wingate, Lattice QCD calculation of the $B_{(s)} \to D^*_{(s)}\ell\nu_\ell$ form factors at zero recoil and implications for $|V_{cb}|$. Phys. Rev. D, 97 (5 Mar. 2018), p. 054502. doi: 10.1103/PhysRevD.97.054502. `https://link.aps.org/doi/10.1103/PhysRevD.97.054502`

[96] T. Kaneko et al., $B \to D^{(*)}\ell\nu$ form factors from lattice QCD with relativistic heavy quarks. 2019. arXiv: 1912.11770 [hep-lat]

[97] R. Aaij et al., Measurement of the ratio of branching fractions $\mathcal{B}(B^0 \to D^{*+}\tau^-\bar{\nu}_\tau)/\mathcal{B}(B^0 \to D^{*+}\mu^-\bar{\nu}_\mu)$. Phys. Rev. Lett., 115 (2015), p. 111803. doi: 10.1103/PhysRevLett.115.111803. arXiv: 1506.08614 [hep-ex].

[98] R. Aaij et al., Measurement of the ratio of branching fractions $\mathcal{B}(B_c^+ \to J/\psi\tau^+\nu_\tau)/\mathcal{B}(B_c^+ \to J/\psi\mu^+\nu_\mu)$. Phys. Rev. Lett., 120 (2018), p. 121801. doi: 10.1103/PhysRevLett.120.121801. arXiv: 1711.05623 [hep-ex]

[99] R. Aaij et al. [LHCb], "Test of Lepton Flavor Universality by the measurement of the $B^0 \to D^{*-}\tau^+\nu_\tau$ branching fraction using three-prong τ decays," Phys. Rev. D **97** (2018) no.7, 072013 doi:10.1103/PhysRevD.97.072013 [arXiv:1711.02505 [hep-ex]].

[100] R. Aaij *et al.* [LHCb Collaboration], "Measurement of the ratio of the $B^0 \to D^{*-}\tau^+\nu_\tau$ and $B^0 \to D^{*-}\mu^+\nu_\mu$ branching fractions using three-prong τ-lepton decays," Phys. Rev. Lett. **120**, no. 17, 171802 (2018) doi:10.1103/PhysRevLett.120.171802 [arXiv:1708.08856 [hep-ex]].

[101] Marcel Algueró et al., "Emerging patterns of New Physics with and without Lepton Flavour Universal contributions." The European Physical Journal C, 79.8 (Aug. 2019). issn: 1434-6052. doi: 10.1140/epjc/s10052-019-7216-3. http://dx.doi.org/10.1140/epjc/s10052-019-7216-3

[102] Andreas Crivellin, Dario Müller, and Toshihiko Ota, "Simultaneous explanation of $R(D^{(*)})$ and $b \to s\mu^+\mu^-$: the last scalar leptoquarks standing". Journal of High En- ergy Physics, 2017.9 (Sept. 2017). issn: 1029-8479. doi: 10.1007/jhep09(2017) 040. http://dx.doi.org/10.1007/JHEP09(2017)040

[103] Andreas Crivellin, Julian Heeck, and Peter Stoffer," Perturbed Lepton-Specific Two-Higgs-Doublet Model Facing Experimental Hints for Physics beyond the Standard Model." Physical Review Letters, 116.8 (Feb. 2016). issn: 1079-7114. doi: 10.1103/physrevlett.116.081801. http://dx.doi.org/10.1103/PhysRevLett.116.081801

[104] Admir Greljo, Gino Isidori, and David Marzocca, "On the breaking of Lepton Flavor Universality in B decays." 2015. arXiv: 1506.01705 [hep-ph]

[105] S. Fajfer and N. Košnik. Vector leptoquark resolution of $R(K)$ and $R(D^{(*)})$ puzzles. Physics Letters B, 755 (Apr. 2016), pp. 270–274. issn: 0370-2693. doi: 10.1016/j.physletb.2016.02.018. http://dx.doi.org/10.1016/j.physletb.2016.02.018

[106] Damir Bećirević et al., "Leptoquark model to explain the B-physics anomalies, $R(K)$ and $R(D)$ ". Physical Review D, 94 (Aug. 2016). doi:10.1103/PhysRevD.94.115021

[107] M. Aaboud et al., "Searches for scalar leptoquarks and differential cross-section measurements in dilepton–dijet events in proton–proton collisions at a centre-of- mass energy of $\sqrt{s}$ =13 TeV with the ATLAS experiment." The European Physical Journal C, 79.9 (Sept. 2019). issn: 1434-6052. doi:10.1140/epjc/s10052-019- 7181-x. http://dx.doi.org/10.1140/epjc/s10052-019-7181-x

[108] A. M. Sirunyan et al., "Search for pair production of first-generation scalar leptoquarks at $\sqrt{s}$ =13 TeV." Phys. Rev. D, 99 (5 Mar. 2019), p. 052002. doi: 10.1103/PhysRevD.99.052002. https://link.aps.org/doi/10.1103/PhysRevD.99.052002

[109] A. M. Sirunyan et al., "Search for pair production of second-generation leptoquarks at $\sqrt{s}$ =13 TeV." Phys. Rev. D, 99 (3 Feb. 2019), p. 032014. doi: 10.1103/ PhysRevD.99.032014. https://link.aps.org/doi/10.1103/PhysRevD.99.032014

[110] M. Aaboud et al., " Searches for third-generation scalar leptoquarks in $\sqrt{s}$ =13 TeV pp collisions with the ATLAS detector." Journal of High Energy Physics, 2019.6 (June 2019). issn: 1029-8479. doi: 10.1007/jhep06(2019)144. http://dx.doi.org/10.1007/JHEP06(2019)144

[111] A. M. Sirunyan et al., "Search for heavy neutrinos and third-generation leptoquarks in hadronic states of two leptons and two jets in proton-proton collisions at $\sqrt{s}$ =13 TeV." Journal of High Energy Physics, 2019.3 (Mar. 2019). issn: 1029- 8479. doi: 10.1007/jhep03(2019)170. http://dx.doi.org/10.1007/JHEP03(2019)170

[112] A. M. Sirunyan et al., " Search for third-generation scalar leptoquarks decaying to a top quark and a τ lepton at $\sqrt{s}$ =13 TeV." The European Physical Journal C , 78.9 (Sept. 2018). issn: 1434-6052. doi: 10.1140/epjc/s10052-018-6143-z. http://dx.doi.org/10.1140/epjc/s10052-018-6143-z

[113] A. M. Sirunyan et al., " Search for a singly produced third-generation scalar leptoquark decaying to a lepton and a bottom quark in proton-proton collisions at $\sqrt{s}$ =13 TeV." Journal of High Energy Physics, 2018.7 (July 2018). issn: 1029- 8479. doi: 10.1007/jhep07(2018)115. http://dx.doi.org/10.1007/JHEP07(2018)115

[114] A. M. Sirunyan et al., "Constraints on models of scalar and vector leptoquarks decaying to a quark and a neutrino at $\sqrt{s}$ =13 TeV." Phys. Rev. D, 98 (3 Aug. 2018), p. 032005. doi: 10.1103/PhysRevD.98.032005. https://link.aps.org/doi/10.1103/PhysRevD.98.032005

[115] Luciano Maiani, "The GIM Mechanism: origin, predictions and recent uses", https://arxiv.org/abs/1303.6154.

[116] A. Navada, A. N. Ansari, S. Patil and B. A. Sonkamble, "Overview of use of decision tree algorithms in machine learning," 2011 IEEE Control and System Graduate Research Colloquium, 2011, pp. 37-42, doi: 10.1109/ICSGRC.2011.5991826.

[117] S. Agostinelli et al., "Geant4. A simulation toolkit", Nuclear Instruments and Methods in Physics Research Section A: Accelerators, Spectrometers, Detectors and Associated Equipment, no. 3, volume 506 (pag. 250−303), 2003, https://www.sciencedirect.com/science/article/pii/S0168900203013688.

[118] T. Sjostrand, S. Mrenna, and P. Z. Skands, "A Brief Introduction to PYTHIA 8.1", Comput.Phys. Commun. 178 (2008) 852–867, https://arxiv.org/abs/0710.3820.

[119] L. Lista, "Practical Statistics for Particle Physicists", https://arxiv.org/pdf/1609.04150.pdf

[120] G. Cowan, "Statistical Data Analysis", Oxford science publications, Clarendon Press, 1998

[121] Bordone, M., Gubernari, N., van Dyk, D. et al.," Heavy-Quark expansion for $\bar{B} \to D_s^{(*)}$ form factors and unitarity bounds beyond the $SU(3)_F$ limit.", Eur. Phys. J. C 80, 347 (2020). https://doi.org/10.1140/epjc/s10052-020-7850-9.

[122] Anders Ryd, David Lange, Natalia Kuznetsova, Sophie Versille, Marcello Rotondo, David P. Kirkby, Frank K. Wuerthwein, and Akimasa Ishikawa. "EvtGen: A Monte Carlo Generator for B-Physics" (2005)

[123] I. M. Nugent, T. Przedziński, P. Roig, O. Shekhovtsova, and Z. Wa, " Resonance chiral Lagrangian currents and experimental data for $\tau^- \to \pi^-\pi^-\pi^+\nu_\tau$",Phys. Rev. D 88, 093012, doi = 10.1103/PhysRevD.88.093012, https://link.aps.org/doi/10.1103/PhysRevD.88.093012

[124] N. Dawe et al., scikit-hep/root numpy: "The interface between ROOT and NumPy." Zenodo, 2018. , https://github.com/scikit-hep/root_numpy/tree/4.8.0.

[125] A. Hoecker, P. Speckmayer, J. Stelzer, J. Therhaag, E. von Toerne, and H. Voss, "TMVA: Toolkit for Multivariate Data Analysis", PoS A CAT 040, https://arxiv.org/abs/physics/0703039, (2007).

[126] Wouter Verkerke, David Kirkby, "The RooFit toolkit for data modeling",https://arxiv.org/abs/physics/0306116.

[127] LHCb Collaboration, "Test of Lepton Flavour Universality using Bs semileptonic decays",https://cds.cern.ch/record/2724839/

[128] M. Pivk and F. R. Le Diberder, "sPlot: A statistical tool to unfold data distributions", Nucl. Instrum. Meth. A555 (2005) 356, arXiv:physics/0402083.

[129] L. Anderlini, A. Contu *et al.*, "The PIDCalib package", CERN-LHCb-PUB-2016-021, http://cds.cern.ch/record/2202412.

[130] Donal Hill, Paolo Gandini; "PDFs for partially recon- structed B → DX decays: RooHORNSdini and RooHILLdini"; https://indico.cern.ch/event/283973/contributions/1633715/attachments/523911/722643/CTSmeeting51213.pdf#search=roohornsdini